EXPERIMENTAL AND NUMERICAL STUDIES ON SAVONIUS ROTOR FOR HYDROPOWER UTILIZATION

Thesis

Submitted in partial fulfillment of the requirement for the degree of

DOCTOR OF PHILOSOPHY

by

SHASHIKUMAR C M

Reg. No. 155042ME15F02

DEPARTMENT OF MECHANICAL ENGINEERING

NATIONAL INSTITUTE OF TECHNOLOGY KARNATAKA

SURATHKAL, MANGALORE – 575025

JULY 2021

EXPERIMENTAL AND NUMERICAL STUDIES ON SAVONIUS ROTOR FOR HYDROPOWER UTILIZATION

Thesis

Submitted in partial fulfillment of the requirement for the degree of

DOCTOR OF PHILOSOPHY

by

SHASHIKUMAR C M

Under the Guidance of

Dr. VASUDEVA MADAV
Assistant Professor

DEPARTMENT OF MECHANICAL ENGINEERING

NATIONAL INSTITUTE OF TECHNOLOGY KARNATAKA

SURATHKAL, MANGALORE – 575025

JULY 2021

DECLARATION

I hereby *declare* that the Research Synopsis entitled "**EXPERIMENTAL AND NUMERICAL STUDIES ON SAVONIUS ROTOR FOR HYDROPOWER UTILIZATION**" which is being submitted to the **National Institute of Technology Karnataka, Surathkal** in partial fulfilment of the requirements for the award of the Degree of **Doctor of Philosophy** in **Mechanical Engineering** is a *bonafide report of the research work carried out by me.* The material contained in this Research Synopsis has not been submitted to any University or Institution for the award of any degree.

Register Number: **155042ME15F02**

Name of the Research Scholar: **SHASHIKUMAR C M**

Signature of the Research Scholar:

Department of Mechanical Engineering

Place: NITK, Surathkal

Date: 04-08-2021

C E R T I F I C A T E

This is to *certify* that the Research Thesis entitled **"EXPERIMENTAL AND NUMERICAL STUDIES ON SAVONIUS ROTOR FOR HYDROPOWER UTILIZATION"** submitted by **SHASHIKUMAR C M (Register Number: 155042ME15F02)** as the record of the research work **c**arried out by him, is *accepted as the Research Synopsis submission* in partial fulfilment of the requirements for the award of degree of Doctor of Philosophy.

R e s e a r c h   G u i d e

Dr. VASUDEVA MADAV
Assistant Professor
Department of Mechanical Engineering
National Institute of Technology Karnataka, Surathkal

Chairman-DRPC
Department of Mechanical Engineering
National Institute of Technology Karnataka, Surathkal

Date: 04-08-2021

DEDICATED TO

MY BELOVED PARENTS AND

FAMILY MEMBERS

ACKNOWLEDGEMENT

This thesis becomes a reality with the kind support and help of many individuals. I would like to thank all of them at this moment.

It is a great pleasure for me to express my deep sense of gratitude to my supervisor **Dr. Vasudeva Madav** for their excellent inspiring guidance, valuable suggestions and encouragement rendered throughout the course of my thesis work. I am thankful to Professor **Dr. Kulkarni S M,** Professor and Head, Department of Mechanical Engineering, for support and providing facilities required to successfully complete this research work. I take this opportunity to acknowledge the former HODs, Mechanical engineering, **Dr. Shrikantha S. Rao, Dr. Narendranath S and Dr. Gangadharan K.V**, for their support and encouragement. I wish to thank my RPAC members **Dr. Veershetty G** and **Dr. Pruthivi Raju U** for their valuable suggestions during my project assessment.

My deepest gratitude to my previous research guide **Dr. Vijayakumar H** for his valuable guidance and piece of advice.

I am extremely grateful to **Dr. Ramesh H Associate professor, Department of Water Resources & Ocean Engineering,** and non-teaching staff for helping me to carry out the experimental investigation at the Fluid mechanics and hydraulics laboratory.

I am very much thankful to **Dr. Kumar G N, Associate professor Department of Mechanical Engineering,** for carrying out numerical simulations in the CFD laboratory using the high-end workstation.

I acknowledge my parents, **Manjunatha B** and **Suguna B** for their inspiration and support throughout my studies. Words cannot explain my gratitude to my wife **Lakshmi R N** and daughter **Chinmayi C S** for supporting me and staying pleasant. I am grateful to my brothers **Srikanth C M**, **Darshan C M,** and cuisine **Ganesh C, Assistant Engineer, Irrigation Department, Government of Karnataka** for their valuable suggestions.

My special thanks to my friends **Dr. Anil R Kadam, Dr. Nuthan R Prasad, Dr. Praveen T R, Lieutenant commander Dr. Ritesh Parida, Vasishta Ademane, Dr. Kotresha, Jagdish C, Rudramurthy B V, Madagonda Biradar, Narendran, Dr. Kesava Rao, Dr. Vasu M, Assistant professor, NIT Trichy, Department of**

Production Engineering Department, Manu J, Gopi Krishna, Sudeep N S and list seems to be endless.

I am extremely thankful to the Department of Mechanical Engineering, NITK, Faculty and non- teaching staff for providing all the facilities to carry out my research work.

I acknowledge with gratitude to all others who have helped directly or indirectly in completing my thesis successfully.

Finally, I am greatly indebted to almighty for giving me this opportunity.

Shashikumar C M

ABSTRACT

Hydrokinetic technologies harvest renewable power by harnessing the kinetic energy of water from free-flowing rivers, streams, dam head/tailrace, and irrigation channels. Savonius rotor is one of the simple and low-cost vertical drag type devices used for the extraction of hydrokinetic power. In the present study, various experimental and numerical investigations were carried out to enhance the performance of the Savonius hydrokinetic turbine. Initially, the effect of bed slope on the performance of the modified Savonius turbine were carried out experimentally. An in-house fabricated scale-down model of the Savonius rotor is tested in a multipurpose tilting flume at $0°$, $0.5°$, $1.0°$, $1.5°$ and $2.0°$ channel inclination to determine performance under controlled conditions. It is observed that at the tip speed ratio of 0.92 and channel inclination of $0.5°$ compared to $0°$ inclination, the C_P and C_T improved to 40% and 10%, respectively. It is found that the torque and power developed by the turbine are maximum at a bed slope of $2.0°$, owing to the maximum available energy. Further, the effect of taper on conventional Savonius turbine is studied numerically with zero bed slope, aspect ratio, and inlet velocity of 1.0 and 0.5 m/s. The results show a 5% increase in the performance of a conventional turbine compared to the tapered turbine with a taper angle of $5°$ and zero bed slope.

In order to enhance the performance of the turbine blade by reducing the negative torque developed by the returning blade profile, the semi-circular blade profile is reformed into a modified V-shaped blade profile. The experimental and numerical investigation is carried out in a multipurpose tilting water flume using V-shaped rotor blade profiles by maintaining a fixed V-angle of $90°$, varying length of V-edges, arc radius, with a constant aspect ratio of 0.7, without taper and zero bed slope at an inlet water velocity of 0.3090 m/s. From the experimental and numerical results, it was found that, the optimum blade profile (V_4) has developed a C_{Pmax} of 0.22 and 0.21 respectively, at a tip speed ratio of 0.87. It was found that the C_{Pmax} of the optimal V-shaped blade profile (V_4) is 19.3% higher than the semi-circular blade profile. Further, the effect of overlap ratio ranging from 0.0-0.3 using optimum rotor blade (V_4) were studied numerically. The results reveal that the turbine's performance with a zero overlap ratio is higher than the turbine blade with an overlap ratio ranging from 0.05 to

0.3. The rotor blade V_4 is further investigated by varying the V-angle ranging from 90° to 40° numerically. The results show that, for 80° V-angle rotor blade, the C_{Pmax} was found to be 0.23 at a tip speed ratio of 0.9. This rotor blade is used for experimental analysis to study the effect of aspect ratio ranging from 0.7 to 1.75 using top, middle, and bottom plates with an inlet velocity of 0.513 m/s. The rotor blade with two endplates and one mid-plate with an aspect ratio of 1.75 has shown a significant increase of performance by 86.13% at a tip speed ratio of 0.86 compared to the turbine blade with two endplates. It is recommended to have two endplates and one mid-plate for the turbine blade with an aspect ratio of 1.75 for better performance. The outcome of the parametric studies carried out in the present research work establishes a key technical basis for enhancing the efficiency of hydrokinetic power generation.

Keywords: Aspect ratio, Coefficient of power, Endplates, Savonius hydrokinetic turbine, Overlap ratio, Tip speed ratio

TABLE OF CONTENTS

iii

LIST OF FIGURES

iv

ix

LIST OF TABLES

NOMENCLATURE

Aw	Wetted area of the flume (m^2)
A_R	Area of the turbine blade (m^2)
AR	Aspect ratio (Height of the turbine (H_R)/Diameter of the turbine (D_r))
BR	Blockage ratio (Dimensionless)
C_d	Coefficient of discharge (Dimensionless)
C_T	Coefficient of torque (Dimensionless)
C_P	Coefficient of power (Dimensionless)
C_{Tmax}	Maximum coefficient of torque (Dimensionless)
C_{Pmax}	Maximum coefficient of power (Dimensionless)
D_r	Diameter of the turbine blade (mm)
D_{ep}	Diameter of the endplates (mm)
D_{Bottom}	Bottom side diameter of the turbine (mm)
D_{Top}	Top side diameter of the turbine (mm)
D_D	Depth of the domain (mm)
D_V	Width of arc on V-blade (mm)
d	Blade chord distance (mm)
d_T	Top diameter of advancing/returning blade bucket (mm)
d_B	Bottom diameter of the advancing/returning blade bucket (mm)
Fr	Froude number (Dimensionless)
g	Acceleration due to gravity (m/s^2)
H_R	Height of the rotor (mm)
H_w	Depth of water in the channel (mm)
H_C	Height of the channel (mm)
H	Distance between the advancing/returning blade midpoint to V-edge (mm)

H_1, H_2, H_3 and H_4 = Heights on advancing and returning blades (mm)

L	Length of V-edge (mm)
L_D	Length of the domain (mm)
OR	Overlap ratio (OR) (Dimensionless)

p	Radius of the straight edge (mm)
P_{Rotor}	Power developed by the rotor (W)
$P_{Available}$	Power available (W)
Q_{Actual}	Actual discharge (m³/s)
q	Radius of the arc (mm)
R_{Shaft}	Radius of the rotor shaft (mm)
R_{Rope}	Radius of the rope (mm)
Re	Reynolds number (Dimensionless)
R_r	Radius of the turbine blade (mm)
S_{SB}	Spring balance (g)
SMT	Sliding mesh technique
S_{SB}	Spring balance (g)
TSR (λ)	Tip speed ratio (Dimensionless)
T_{Rotor}	Rotor torque (N-m)
$T_{Available}$	Available torque (N-m)
TSS	Time step size (s)
TST	Total simulation time (s)
t	Thickness of the turbine blade/ top, bottom and endplates (mm)
V_w	Velocity of the water (m/s)
W_L	Weighing pan load (g)
V_W	Velocity of the water (m/s)
W_C	Width of the channel (mm)
W_D	Width of the domain (mm)
W_R	Width of the rotor (mm)

Greek symbols

ω	Angular velocity (rad/s)
μ_w	Absolute viscosity of water (N-s/m²)
ρ_w	Density of water (kg/m³)
ψ	Blade arc angle (Degree)
θ	Bed slope inclination of the channel (Degree)

Chapter 1

INTRODUCTION

In recent years the demand for renewable energy sources has grown substantially due to an increase in global energy demand, increased dependability and cost of fossil fuels, and the unforeseen environmental threat from fossil fuel consumption (Hand and Cashman 2020; Khan et al. 2009a; Loots et al. 2015; Moghimi and Motawej 2020; Puri et al. 2017). These crisis have led to a shift in our focus on renewable resources such as solar, wind, hydropower, geothermal, and biomass. Hydropower is one of the cleanest, most efficient, and predictable sources (Chen et al. 2017; Uchiyama et al. 2020; Zhou et al. 2019; Zhou and Deng 2017). Hydrokinetic energy is the economically most valued option for green energy production. The principle of hydrokinetic energy conversion involves the use of kinetic energy available in rivers, ocean tides, ocean water currents, and irrigation canals for small-scale hydropower generation (Patel et al. 2017; Zhou et al. 2019). This technology has immense potential to generate hydropower from water flowing with low velocity and a small head (Khan et al. 2009a; Kumar and Saini 2016; Loots et al. 2015; Salleh et al. 2019; Zhou et al. 2019). The turbines that transform the kinetic energy of flowing water into mechanical power are called hydrokinetic turbines; such turbines are also known as water current turbines, ultra-low head hydro turbines, free flow/stream turbines, and zero head hydro turbines (Güney and Kaygusuz 2010).

The Savonius hydrokinetic turbine is one of the innovative solutions for electricity generation in remote regions (Antheaume et al. 2008). Savonius hydrokinetic turbine is a vertical axis turbine, and it is a unique mechanical device that works on the mechanism of drag effect rather than lifting mechanism. The rotor has a high starting torque and is thus ideal for hydrodynamic application and operates at much lower flow rates. The main reason for using this turbine is that it offers a simple design, resulting in lower costs than other vertical axis turbines. In addition, the Savonius turbine has a simple blade profile compared to the more complex design requirements of the Darrieus turbine with airfoil-shaped blades.

The simpler construction criteria of the Savonius blade helps to reduce the development and maintenance cost of the entire system. The concept of a Savonius hydrokinetic turbine is equivalent to a Savonius wind turbine system since both the systems derive kinetic energy from free-flowing streams. Compared with the wind turbine system, the Savonius hydrokinetic turbine system has a higher energy density, mainly due to the direction and speed of the incoming water and good predictability (Khan et al. 2008; Kumar and Saini 2016).

The Savonius turbine consists of two semi-circular blade profiles such as convex and concave blade profiles, which is considered as advancing and returning blades. The basic theory of the Savonius turbine is based on the difference in drag force between advancing and returning blade profiles. As the turbine rotates, the advanced blade absorbs the incoming free stream into its concave surface, whereas the convex surface of the return blade deflects the flow. The advanced blade therefore, has more drag force than the return blade from the incoming flow. This drag force develops a positive torque on the advancing blade and a negative torque on the returning blade, which prevents the turbine rotation. Savonius hydrokinetic turbine is more suitable for supplying sustainable energy for remote areas using hydrokinetic energy available in irrigation channels.

While resource assessments have been carried out for wave, ocean current, tidal, and river sites, there is uncertainty about the potential of hydrokinetic energy production in canals and waterways. Some channels, particularly irrigation and power generation, have water flow rates, depths, and site features that are advantageous for producing economic hydrokinetic resources as the flow is constrained to one definite path (Gunawan 2017). The Savonius rotor was developed in the year 1920 for converting wind energy into electrical energy. Savonius turbine is one of the oldest vertical axis wind turbines widely studied to generate energy since 1920 by many researchers. However, its extensive application is obstructed due to its low power generation. Table 1.1 shows the values of hydrokinetic power capacity, head range, and operating concept of the various hydrokinetic energy available.

Table 1.1 Classification of hydropower plants based on the power output capacity, head range, and operating concepts (Doso and Gao 2020; Herman Jacous Vermaak, Kazumba Kusakana n.d.; Khan et al. 2008; Kumar and Saini 2016; Rumpfkeil et al. 2015; Salleh et al. 2019; Yah et al. 2017).

Sl. No	Classification	Description
Power capacity		
1.	Large	>100MW
2.	Medium	10–100MW
3.	Small	1–10MW
4.	Mini	100 kW–1MW
5.	Micro	5–100 kW
6.	Pico	<5kW
Head range		
1.	High head	$\geq$ 100m
2.	Medium head	30–100m
3.	Low head	2–30m
Theory of operation		
1.	Water reservoir (conventional)	It holds a large amount of water from rivers and regulates electricity generation based on load demands.
2.	Pump storage (conventional)	Pumps water sources from a water reservoir at a lower level to the top of the water reservoir using off-peak electricity.
3.	Run of the river (unconventional)	It is based on the natural flow rates of rivers and has no control over them.

1.1 Development of small-scale hydrokinetic turbines

The turbines that transform the kinetic energy of the moving water current into mechanical power are referred to as hydrokinetic turbines and these kinds of turbines are also known as ultra-head turbines, water current turbines (WCT), free flow/stream turbines and zero head hydro turbines (Khan et al. 2009a; Kumar and Saini 2016). The quantity of hydrokinetic energy in water masses depends on the speed of motion. The theoretical hydrokinetic power developed by the turbine can be written as.

3

$$P_{\text{Theoritical}} = \frac{1}{2} \rho_W A_C V_W^3$$

Only a small fraction of hydrokinetic energy can be stored in the water flowing through a turbine cross-section and this part of kinetic energy is known as the coefficient of power (C_P). By considering the C_P, the hydrokinetic energy taken by the turbine can be written as.

$$P_{\text{Turbine}} = C_P \frac{1}{2} \rho_W A_C V_W^3$$

Similar to the wind turbine, the Savonius hydrokinetic turbine C_P depends on TSR, which is defined as the ratio of velocity of the turbine blade to the velocity of the water flowing and it is written as (Akwa et al. 2012b; Roy and Saha 2013a);

$$TSR(\lambda) = \left(\frac{\omega\left(\dfrac{D_r}{2}\right)}{V_W} \right) = \frac{\text{Velocity of the turbine blade}}{\text{Velocity of the water}}$$

For non-ducted turbines, the theoretical limit for the coefficient of power is 0.59. As seen in Figure 1.1, this limit is generally used as the Betz limit. In ducted turbines, a large amount of water is forced to flow into the turbine through the duct (Khan et al. 2009b; Kumar and Saini 2016). The velocity of water at the turbine blade increases and the C_P is efficiently increased to reach the Betz limit (Kumar and Saini 2016). Figure 1.1 shows the C_{Pmax} values for different kinds of turbines. It can be noticed that at TSR between 0.7-0.8, the Savonius rotor has an approximately C_{Pmax} value of 0.3. The C_P of the turbine is decreased due to its own losses of the turbine which is installed in the river.
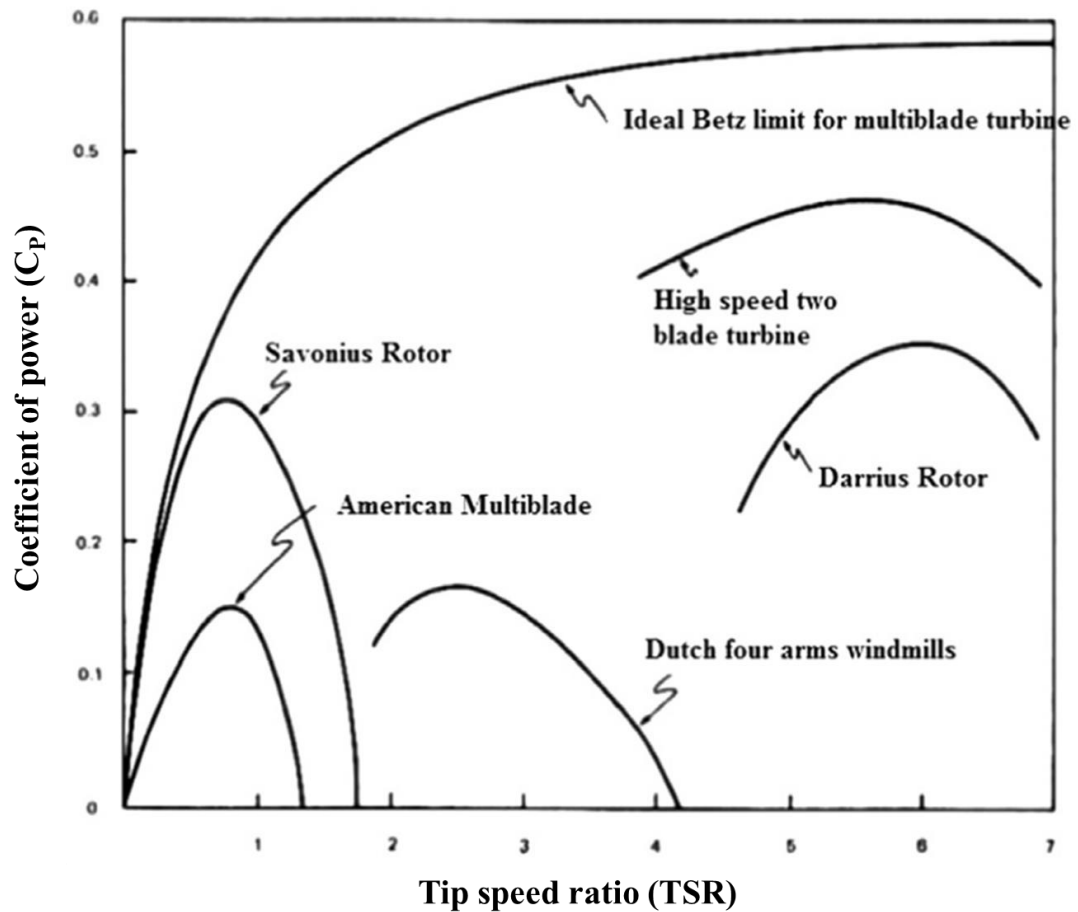
Figure 1.1 Variation of coefficient of power with respect to tip speed ratio for various types of turbine blades (Khan et al. 2009a; Kumar and Saini 2016).

1.2 Types of hydrokinetic turbines

As described above, hydrokinetic technology absorbs the kinetic energy of water flowing in river and irrigation channels without huge civil structures. Hydrokinetic turbines are distinct from traditional turbines, such as Pelton, Francis, and Kaplan. In recent years, principles of numerous hydrokinetic conversions, such as piezopolymer conversion, vortex-induced vibration, oscillating hydrofoil, etc., have been developed to generate electricity from free-flowing water. These turbines are commonly used due to their economic viability for real-world implementation and commercialization. For rivers, this technology is called RCT or the River Current Energy Conversion Device (Khan et al. 2008, 2009a).

Similar to wind turbines, numerous forms of hydrokinetic turbine designs are reported in the literature (Gorban' et al. 2001; Herman Jacous Vermaak, Kazumba Kusakana

n.d.; Iio et al. 2011; Khan et al. 2008, 2009a; Pham Long n.d.; Rourke et al. 2010). The turbines are mainly categorized into two groups, i.e., axial-flow and cross-flow turbines, depending on the axis of orientation with respect to the direction of water flow. Flow type, speed, and the desired system performance are the vital factors in hydrokinetic turbine selection (Herman Jacous Vermaak, Kazumba Kusakana n.d.) as shown in Figure 1.2.
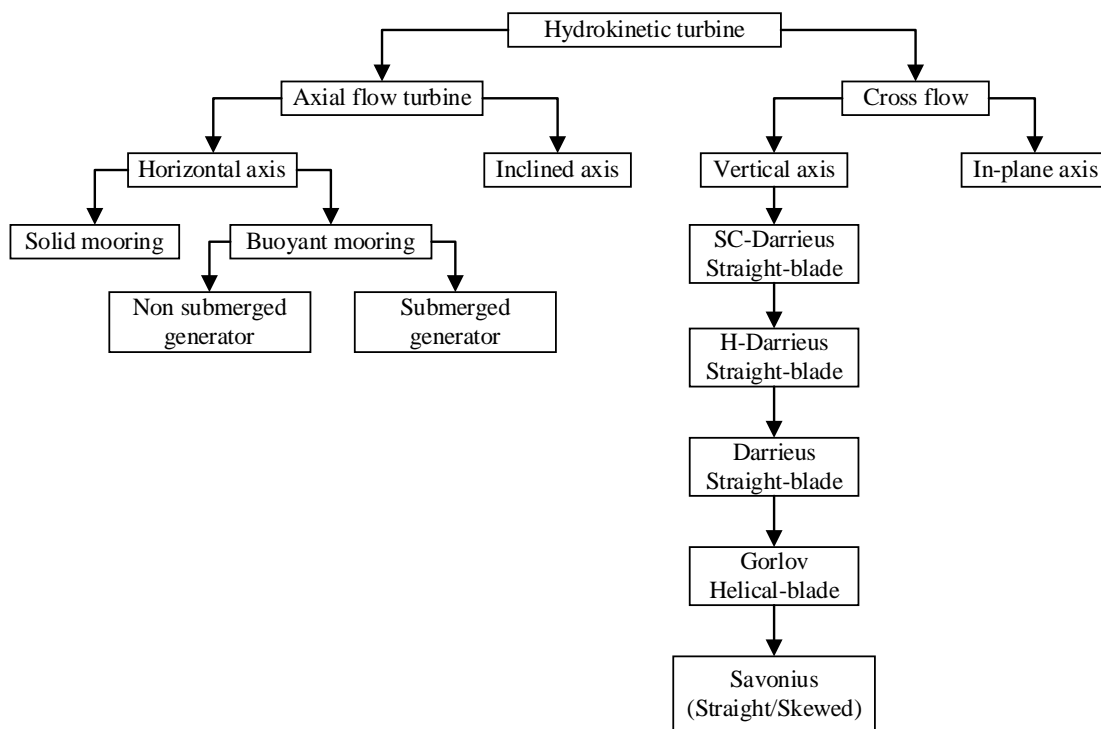
Figure 1.2 Classification of hydrokinetic turbines (Khan et al. 2009a; Kumar and Saini 2016).

Axial flow turbines are turbines in which the turbine's axis is parallel to water flow and can be constructed using two, three, and multi-blades. The cross-flow turbines have an orthogonal rotor axis to the flow of water but parallel to the surface of water. The cross-flow turbines are further classified into vertical and in-plane axis turbines. In the case of vertical axis turbines, the axis of the turbine blade is perpendicular to the water plane, and it is in a horizontal plane for the case of in-plane axis case. The in-plane turbines are typically drag-type devices and are less effective than the lift-type turbine (Khan et al. 2008). The Darrieus type of turbine is used as a vertical axis turbine for river energy applications (Khan et al. 2008). Darrieus straight-bladed turbines (type H or type

Squirrel Cage) are considered as a feasible choice for hydro applications (Khan et al. 2008).

There are two types of designs for vertical axis turbines: turbines based on the Darrieus system and turbines based on the Savonius model. The main driving force for the working of Darrieus design is lift force, and for the Savonius design drag force is caused by the inlet water velocity and the turbine blade (Kumar and Saini 2016). Güney and Kaygusuz 2010 studied a comprehensive assessment of different types of hydrokinetic turbines and reported that a vertical axis turbine is more appropriate for the case where water velocity is comparatively restricted. Authors have stated that horizontal axis turbines (HAT) are more efficient and self-starting and capable of being used but have higher production and transport costs. Authors have stated that horizontal turbines have higher performance and self-start capabilities, but production and transport costs are also higher. Axial flow turbines are primarily used in ocean and tidal applications because of their high performance.

Khan et al. 2009a stated that about one-third of the horizontal axis turbines are being considered for this type of arrangement, while approximately half of the vertical axis turbines are being considered for duct development. It is also suggested that vertical axis turbines can be coupled as a single unit in small rivers, water streams, or they can be conveniently mounted together in large rivers. The cylindrical profile of the rotor is a real benefit over the axial flow turbine shape of the rotor disk. Khan et al. 2008 also reviewed various river current energy transfer schemes and explored the benefits and drawbacks of different types of turbines.

It was found that the study of vertical axis turbines is easier, but not automatically self-starting. Rourke et al. 2010 reviewed marine current energy equipment and stated that only horizontal turbines are mounted and constructed in Ireland to produce tidal and marine current energy (Khan et al. 2009a). Boyle 2007; Vimal Patel, Ganapathi Bhat, T. I. Eldho 2016s claimed that the generator and bearings will be used above the water level due to the vertical shaft. Kassam 2009 stated that the vertical flow turbine can deflect entering debris rather than injecting it, lowering maintenance costs and not having expensive hydrofoil design blades. Based on the above discussion, a distinction

between horizontal and vertical turbines suggests that vertical axis turbines are beneficial for free flow applications to extract energy from the river, irrigation channels. Due to the prevailing advantages of small blades, lower construction costs, lower shipping costs and lower operating costs, the vertical axis turbine is considered as a favourable option for generating electricity to remote villages using free stream water.

Darrieus and Savonius type turbines are widely used in river energy applications in the field of vertical axis turbines. Straight-bladed Darrieus turbines (type H or type Squirrel Cage) is being considered as an option for hydro applications. Various research articles are available about the information on design, development, functional, and effectiveness problems related to Darrieus turbines (Liu and Xiao 2015; Power et al. 1996; Qasemi and Azadani 2020; Shaheen and Abdallah 2017). The Darrieus turbine blade design is driven primarily by the lifting force formed by the incoming water interaction with the blades. The Gorlov turbine blade's profiles are made of helical structure (Gorban' et al. 2001), whereas the Savonius turbines are built of straight or helical blades of drag form devices (S. J. Savonius 1931). Gorlov hydrokinetic turbine with 1 m diameter and 2.5 m height was built by GCK technology limited (USA) on the coast of Korea (Gorban' et al. 2001).

The Gorlov vertical axis turbine (Iio et al. 2011) having helical blade profile with the decreased relative diameter and increasing length of the blade was studied and found that C_{Pmax} of 0.35. To achieve improved performance, various types of rotors (such as Darrieus –Savonius Hybrid) can be hybridized (Power et al. 1996). Due to its simple design, easy fabrication with minimal cost, the Savonius turbine is still not as common as associated to the horizontal axis turbine because of its lower efficiency. The detailed literature review on Savonius turbines reveals that it has lower efficiency, large static torque variation. The basic form of the Savonius rotor is the 'S' type with a small overlap between two semi-circular blade profiles (S. J. Savonius 1931).

The Savonius hydrokinetic turbine is very simple in building with lower cost and low noise. It has the capability to receive fluid from any direction with better starting characteristics. It has low aerodynamic performance as compared to the Darrieus

8

turbine (Kamoji et al. 2008). The Savonius rotor working principle is based on the drag force between concave (advancing) and convex (returning) blade profiles as they are rotating around a vertical shaft. The drag force acting on the concave blade profile is higher than that of the convex blade profile. Therefore, an advanced blade profile (concave) will experience greater drag than returning blade profile (convex) (Kamoji et al. 2008). Savonius turbine consists of two semi-circular blade profiles, as shown in Figure 1.3 (a-c) and Figure 1.4. From Figure 1.3 (a-c) and Figure 1.4, H_R is the height of the turbine blade, D_r is the diameter of the turbine blade, and D_{ep} is the endplate diameter of the turbine blade.

The diameter of the endplate is 1.1 times the diameter of the turbine blade. The important geometric parameters of the Savonius turbine blade are aspect ratio (AR), overlap ratio (OR) and blade arc angle. The ratio of height of the turbine blade (H_R) to the diameter of the turbine blade (D_r) is known as aspect ratio (AR). Similarly, the definition of overlap ratio (OR) is the ratio of overlap distance (e) between the advancing and returning blades to the blade chord distance ($0.5D_r$) as per the literature (Akwa et al. 2012b; Roy and Saha 2013a; b; Sharifian 2014). During the Savonius turbine blade rotation, advancing blade profile (concave) develops positive torque and returning blade profile (convex) develops negative torque. The Savonius hydrokinetic turbine is similar to the Savonius wind turbine in terms of working principle.
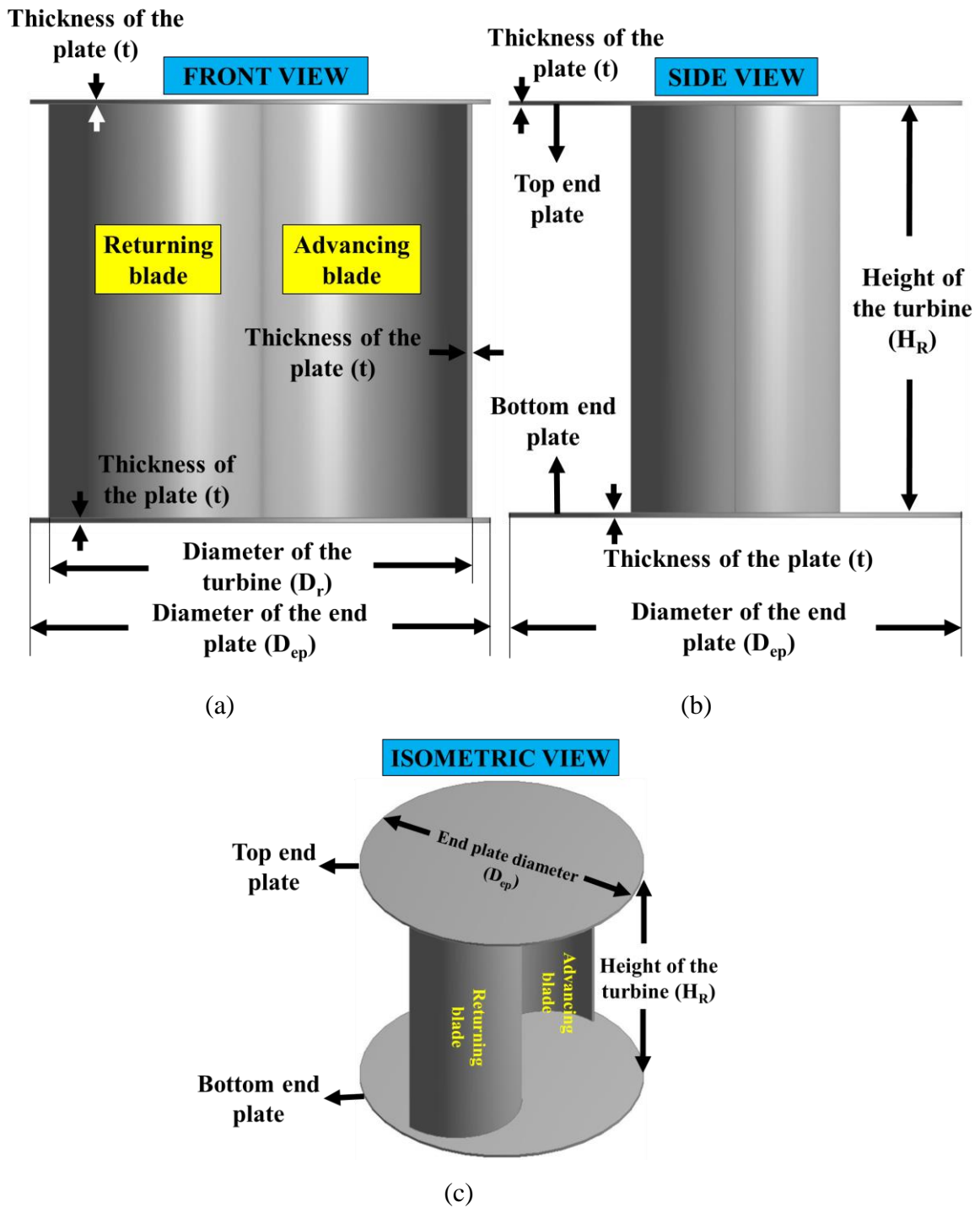
Figure 1.3 Geometric parameters of conventional Savonius hydrokinetic turbine (a) front, (b) side view and (c) isometric view
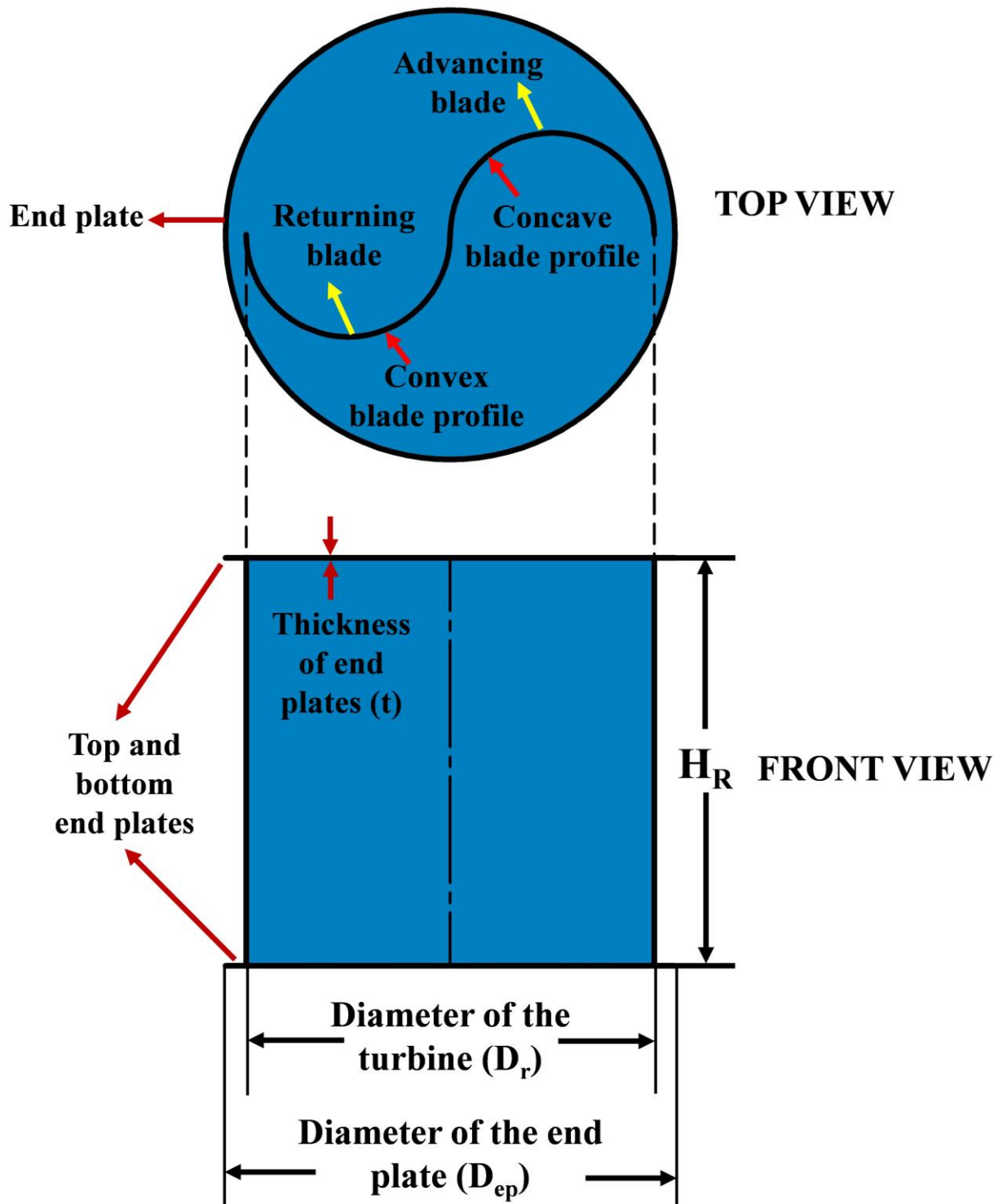
Figure 1.4 Geometric dimensions of a Savonius hydrokinetic turbine

Compared with the Savonius wind turbine system, the Savonius hydrokinetic turbine has a higher energy density since the density of water is 850 times more massive than air. Therefore, Savonius hydrokinetic turbines extract enough energy even at low speed due to higher specific gravity, higher momentum than air for the similar velocity of air (Herman Jacous Vermaak, Kazumba Kusakana n.d.; Sarma, N. K. Biswas and Misra 2014). A water velocity range of 0.5 m/s and above, Savonius hydrokinetic turbines can be installed to extract Savonius hydrokinetic turbines (Khan et al. 2008, 2009a; b). To enhance the efficiency of the Savonius hydrokinetic turbine blades, various parametric studies were carried out using experimental, numerical techniques in recent years (Akwa et al. 2012b; Roy and Saha 2013a; b).

Similar to wind turbines, various augmentation methods used to increase the efficiency of the Savonius turbine such as nozzle duct (Elbatran et al. 2017; Shikha et al. 2003, 2005), deflector plates (Golecha et al. 2011; Kailash et al. 2012; Mosbahi et al. 2019; Payambarpour et al. 2020) modified thick deflector plate (Kerikous and Thévenin 2019a), obstacle plate (Mohamed et al. 2011), curtain plate (Altan and Atilgan 2012), controlling the fluid direction (El-Askary et al. 2015), V-shaped deflector (Shaughnessy and Probert 1992), circular windshield (Hu et al. 2009), guide-box tunnel (Irabu and Roy 2007), conveyor-deflector curtain system (Tartuferi et al. 2015), partially-blocked Savonius rotor (Shaughnessy and Probert 1992), porous deflector (Eshagh et al. 2020) and wind booster (Korprasertsak and Leephakpreeda 2015). The results obtained by varying the various geometric parameters using experimental and numerical investigations by various researchers showed that geometrics parameters and inlet velocity flow also impact the efficiency of the Savonius turbine blades.

1.3 Benefits of irrigation channel over river flow for installation of Savonius hydrokinetic turbine

Figure 1.5 shows the schematic of Savonius hydrokinetic turbine in an irrigation channel to utilize hydrokinetic energy available in an irrigation channel. The following are the benefits of the irrigation channel over river flow to install Savonius hydrokinetic turbines.
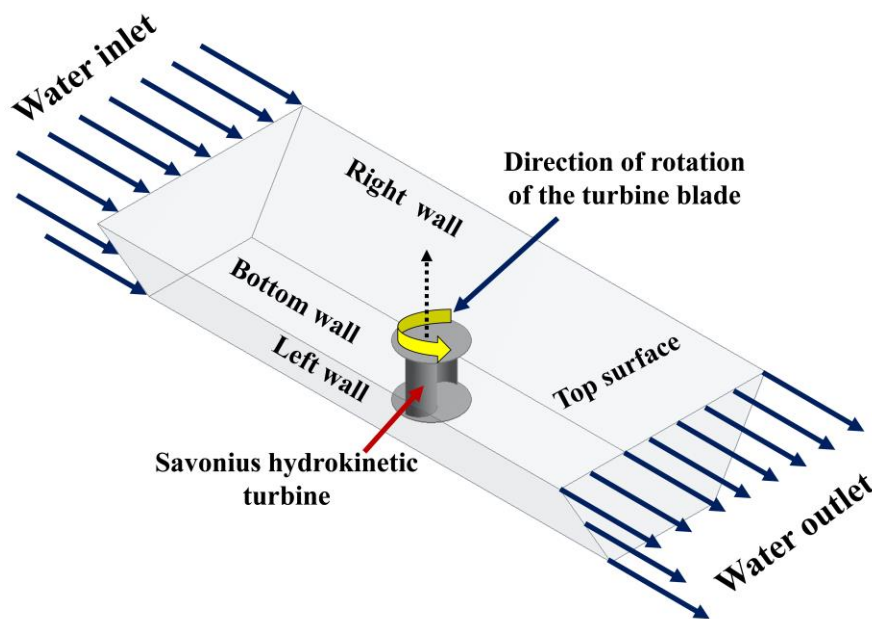
Figure 1.5 Schematic of Savonius hydrokinetic turbine in an irrigation channel

Savonius turbines, on the other hand, have many advantages, including rotational independence from fluid flow direction, strong starting characteristics, ease of design and construction, low cost, and less vibrational strain on the supporting structure.

1.4 Closure

The efficiency of the drag-type vertical axis Savonius hydrokinetic turbines is lower than lift-type turbines due to the negative torque developed by the returning blade profile. But the Savonius turbines have many advantages such as, rotational independence from fluid flow direction, good starting characteristics, simple design, and low cost. Based on the above benefits of the Savonius turbine, it is necessary to improve the performance of the turbine by modifying the various geometric parameters of the Savonius turbine using experimental, numerical, and optimization techniques,

the performance of the Savonius turbine can be increased. The organization and road map of the thesis are presented in section 1.5. The next chapter presents the detailed literature review, research gap, and objectives of the present research work.

1.5 Organization of thesis

This thesis is organized into five chapters to help the reader understand the nature of the present work.

Chapter-1: This chapter describes the detailed introduction about various vertical axis hydrokinetic turbines used for hydropower generations. This chapter also includes explanations for the use of the Savonius turbines in irrigation channels for hydropower generation by utilizing hydrokinetic energy.

Chapter-2: The detailed literature review on Savonius hydrokinetic turbine blades based on various geometric parameters using experimental and numerical approaches is presented. The summary and objectives of the present research work are also presented.

Chapter-3: The experimental setup, instruments used, and methodology using multipurpose tilting water flume using various geometric blade profiles and three-dimensional numerical methodology using ANSYS FLUENT by sliding mesh technique are presented.

Chapter-4: The results and discussion of the various parametric investigation of the present research work using experimental and numerical studies are presented in detail.

Chapter-5: The conclusions of research work using experimental and numerical investigation, key contribution, and scope of future work are presented. The list of references used for the present research work is included after chapter-5.

The various experimental and numerical investigations carried out to compute the performance parameters of the Savonius hydrokinetic turbine of the present research work are summarised as a road map, as shown in Figure 1.6.

14

Literature review on performance parameter of Savonius hydrokinetic turbine blade profiles using experimental and numerical investigation (Chapter-1)

Parametric investigation of Savonius hydrokinetic turbine blades to enhance the performance using numerical and experimental investigation. Summary and objectives of the present investigation (Chapter-2)

Experimental methodology for effect of bed slope on the performance of modified Savonius rotor blade (Chapter-3)

Results and discussion of effect of bed slope on the performance of modified Savonius rotor blade (Chapter-4)

Numerical methodology for the effect of taper on conventional Savoinius hydrokinetic turbine blade (Chapter-3)

Results and discussion of effect of taper on conventional Savoinius hydrokinetic turbine blade (Chapter-4)

Experimental and numerical methodology for the development of Novel V-shaped rotor blade profile (Chapter-3)

Results and discussion of development of Novel V-shaped rotor blade profile (Chapter-4)

Numerical methodology for the effect of overlap ratio on optimum Novel V-shaped blade profile (Chapter-3)

Results and discussion of effect of overlap ratio on optimum Novel V-shaped blade profile (Chapter-4)

Numerical methodology for the effect of V-angle, Experimental methodology for the effect of aspect ratio, end plates using optimum blade profile (Chapter-3)

Results and discussion of effect of V-angle, effect of aspect ratio, end plates using optimum blade profile (Chapter-4)

Conclusions of all the parametric studies using experimental and numerical investigation (Chapter-5)

Figure 1.6 Road map of the research work carriedout in the present study

Chapter 2

LITERATURE REVIEW

Hydrokinetic turbines harness the kinetic energy of water in free-flowing rivers, lakes, dam heads/tailrace, and irrigation channels to generate renewable energy. The hydrokinetic turbine technology is one of the interesting techniques adopted in recent times in the field of renewable energy sources (Gunawan 2017) and has enormous potential to generate electricity from water bodies such as irrigation channels where the direction of flow is uniform with low velocity and low head (Kumar and Saini 2016; Loots et al. 2015; Salleh et al. 2019). Due to the availability of sufficient water velocity, depth of water, and less debris, the man-made irrigation channel is ideal for hydrokinetic power generation (leaves, branches, logs) (Shashikumar C M et al. 2021).

The Savonius turbine is a vertical axis drag-type turbine suitable for low flow velocity as compared to other standard water turbines. It can accept fluid from any direction and generate power at low speed and with better starting characteristics (Jaohindy et al. 2013; Kumar and Saini 2016, 2017a). It can be manufactured by using two half-circular blades attaching to the rotating central shaft. Savonius turbine can be easily mounted in rivers or tiny irrigation channels, which makes them best suited for electricity generation for remote areas in developing nations like India (Kumar and Saini 2016). The two main advantages of vertical axis turbines (Savonius hydrokinetic turbines) for the generation of electricity are: (i) it eliminates the use of yaw control, improving reliability, (ii) reduce maintenance cost (Vimal Patel, Ganapathi Bhat, T. I. Eldho 2016). The Savonius turbine can also be used to generate electricity for domestic applications such as pumping water, charging battery and support broadcast communication systems (Roy and Saha 2013a; Vimal Patel, Ganapathi Bhat, T. I. Eldho 2016).

This chapter presents the detailed literature review on Savonius turbine blade performance parameters using various geometric parameters carried out by various researchers using experimental and three-dimensional numerical investigation. The summary of the literature review and objectives of the present research work is presented in this chapter.

2.1 Working of Savonius hydrokinetic turbine

The Savonius hydrokinetic turbine works on drag difference between concave (advancing blade), and convex (returning blade) blade profiles, and they rotate around a vertical shaft. The geometric dimension of the Savonius hydrokinetic turbine are height of the turbine (H_R), diameter of the turbine (D_r) and endplate diameter of the turbine (D_{ep}). Figure 2.1 (a and b) shows the important geometric dimensions of three dimensional Savonius hydrokinetic turbine with and without overlap ratio (OR). The various design parameters of the Savonius hydrokinetic turbines for the enhancement of performance are aspect ratio (AR), overlap ratio (OR), separation gap (SG), different blade profile, number of blades, augmentation technique, and number of stages.
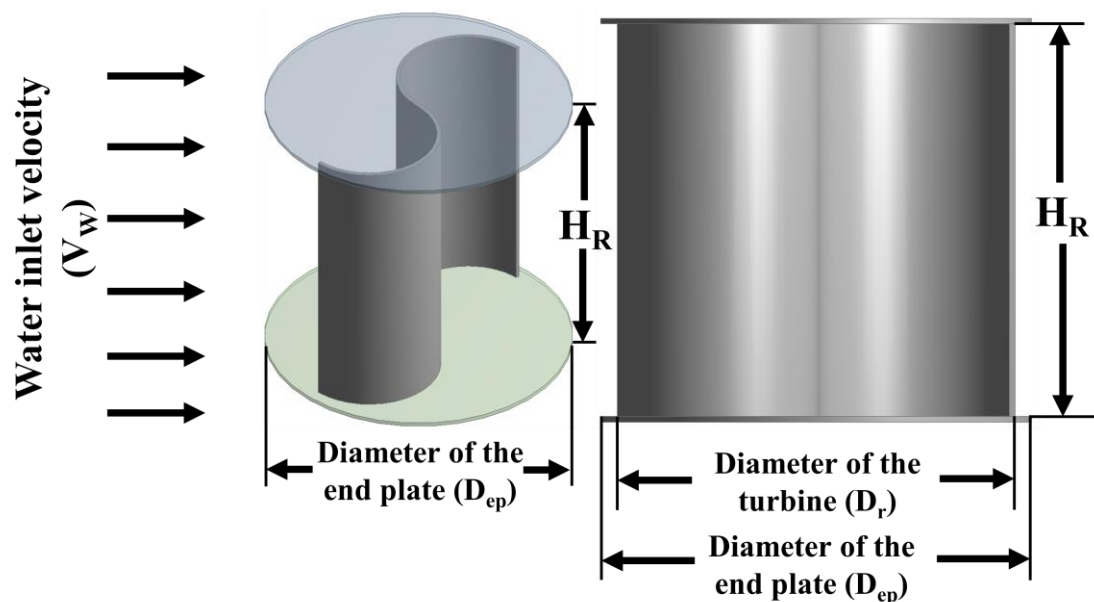
Figure 2.1 Three dimensional geometric parameters of Savonius turbine (a) without overlap ratio (OR) and (b) with overlap ratio (OR) (Roy and Saha 2013b)

2.2 Important performance parameters of a Savonius hydrokinetic turbine

The various performance parameters of Savonius hydrokinetic turbines, such as the coefficient of power (C_P), coefficient of torque (C_T), and tip speed ratio (TSR) are expressed by the following equations (Golecha et al. 2011).

$$\textbf{Coefficient of torque (C}_\textbf{T}) = \frac{T_{Rotor}}{T_{Available}} = \frac{T_{Rotor}}{\left(\frac{1}{2}\rho_W A_r (V_W)^2\right)\frac{D_r}{2}} \qquad (2.1)$$

Where A_R is the area of the rotor blade ($H_R D_r$), H_R is the height of the turbine, D_r is the diameter of the turbine, V_W is the velocity of water, and ρ_W is the density of water.

$$\textbf{Rotor torque T}_\textbf{Rotor} = (W_L - S_{SB})g(R_{Shaft} + R_{Rope}) \qquad (2.2)$$

W_L is the load acting on the shaft, S_{SB} is the spring balance reading, R_{Shaft} is the radius of the shaft, and R_{Rope} is the radius of the rope

$$\textbf{Coefficient of power (C}_\textbf{P}) = \frac{P_{Rotor}}{P_{Available}} = \frac{(T_{Rotor} \times \omega)}{\left(\frac{1}{2}\rho_W (A_R)(V_W)^3\right)} \qquad (2.3)$$

$$\textbf{P}_\textbf{Rotor} = T_{Rotor} \times \omega$$

Where, ω is the angular velocity

$$\textbf{Tip speed ratio (TSR)} = \frac{\omega D_r}{2V_W} \qquad (2.4)$$

2.3 Design parameters of Savonius hydrokinetic turbines

To design an efficient Savonius hydrokinetic turbine, the most important design parameters are aspect ratio (AR), overlap ratio (OR), separation gap (SG), endplates (D_{ep}), blade shape, and various augmentation techniques for the enhancement performance parameters such as C_T and C_P. Figure 2.2 shows the different design parameters used for the development of Savonius hydrokinetic turbine blades.

```
┌─────────────────────────────┐
│  Different design parameters of  │
│  Savonius hydrokinetic turbines  │
└─────────────────────────────┘
              │
              ▼
      ┌──────────────────┐
      │   Aspect ratio   │
      │   AR=$H_R/D_r$   │
      └──────────────────┘
              │
              ▼
      ┌──────────────────┐
      │   Overlap ratio  │
      │    OR=e/d        │
      └──────────────────┘
              │
              ▼
      ┌──────────────────┐
      │  Separation gap  │
      │      (SG)        │
      └──────────────────┘
              │
              ▼
      ┌──────────────────┐
      │    End plates    │
      └──────────────────┘
              │
              ▼
      ┌──────────────────┐
      │ Staging of Savonius │
      │       rotor      │
      └──────────────────┘
              │
              ▼
      ┌──────────────────┐
      │ Number of blades │
      └──────────────────┘
              │
              ▼
      ┌──────────────────┐
      │ Different blade  │
      │     profiles     │
      └──────────────────┘
              │
              ▼
      ┌──────────────────┐
      │   Augmentation   │
      │    techniques    │
      └──────────────────┘
```
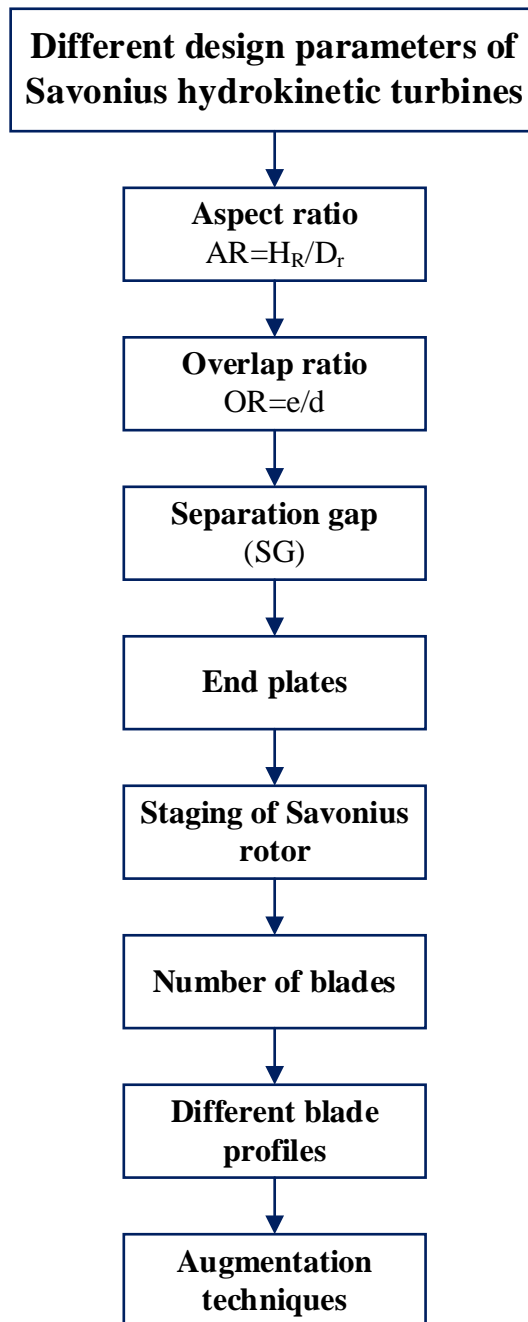
Figure 2.2 Different design parameters of Savonius hydrokinetic turbines

2.4 Aspect ratio (AR)

The aspect ratio (AR) of the Savonius hydrokinetic turbine is a dimensionless quantity and is defined as the ratio of the height of the turbine blade (H_R) to the diameter of the turbine blade (D_r) (Akwa et al. 2012b; Kumar and Saini 2016; Roy and Saha 2013b). It is a significant geometric parameter for enhancing performance parameters such as C_T and C_P of the Savonius hydrokinetic turbine. The aspect ratio is expressed as:

$$\text{Aspect ratio } (AR) = \frac{\text{Height of the turbine blade}}{\text{Diameter of the turbine blade}} = \frac{H_R}{D_r} \qquad (2.7)$$

The Savonius hydrokinetic turbine blade with a varying aspect ratio (AR) ranging from 0.5-2.0 is shown in Figure 2.3. Smaller the diameter of the turbine blade always produces sharp turns with respect to the direction of the fluid flow that increases the RPM of the turbine blade. The torque produced by the turbine blade increases at the price of lower rotational speed with the increase in diameter of the turbine blade. (Patel et al. 2016) reported that the performance of turbine blade always increases when the aspect ratio of the turbine blade is greater than 1.8. The values of C_T and C_P of the turbine blade with respect to aspect ratio by various researchers are presented in Table 2.1.

AR=0.5   AR=0.75   AR=1.0   AR=1.25   AR=1.5   AR=1.75   AR=2.0
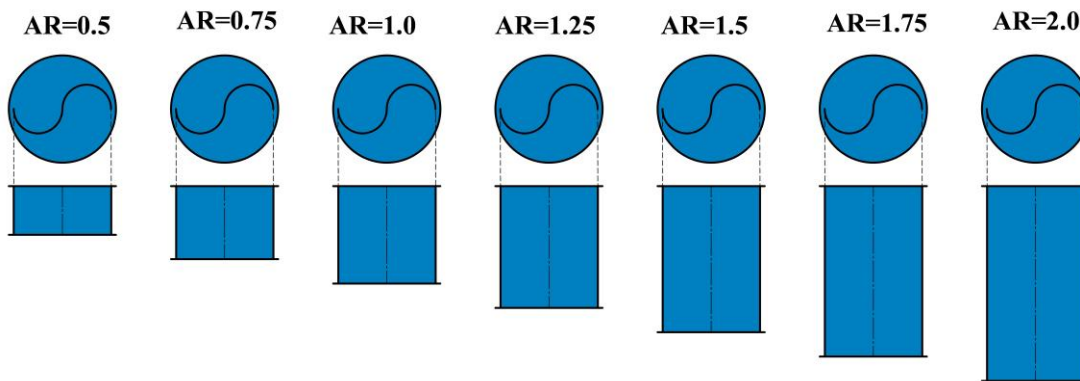
Figure 2.3 Examples of Savonius-style wind turbines with different aspect ratios (Akwa et al. 2012b)

Table 2.1: Values of the aspect ratio of Savonius hydrokinetic turbine by various researchers.

Sl. No	Researcher	AR=$H_R D_r$	C_{Pmax}	TSR
1.	Golecha et al. 2011	0.7	0.14	0.7
2.	Elbatran et al. 2017	0.7	0.25	0.73
3.	Kumar and Saini 2017b	1.58	0.39	0.9
4.	Kumar and Saini 2017a	1.58	0.426	0.9
5.	Talukdar et al. 2018	1.0	0.28	0.89
6.	Mosbahi et al. 2019	0.88	0.14	0.7
7.	Mosbahi et al. 2020a	0.88	0.191	0.63
8.	Mosbahi et al. 2020b	0.88	0.166	0.78
9.	Alipour et al. 2020	1.0	0.28	0.98

2.5 Overlap ratio (OR)

Another important dimensionless parameter to optimize the blade profile is the overlap ratio (OR). It is defined as the ratio of overlap distance (e) between the advancing and returning blade profiles to the blade cord length (d) (diameter of the advancing/ returning blade profiles) and is given by,

$$\text{Overlap ratio}\left(\text{OR}\right) = \frac{\text{Overlap distance}}{\text{Blade chord length}} = \frac{e}{d} \tag{2.8}$$

The conventional Savonius hydrokinetic turbine blade with an overlap ratio has better starting characteristics than without overlap ratio between the advancing and returning blade profiles (Akwa et al. 2012; Roy and Saha 2013; Patel et al. 2016). The Savonius hydrokinetic turbine blade schematic with varying overlap ratios ranging from 0.0-0.3 is shown in Figure 2.4.

During the turbine blade rotation with overlap ratio, the jet type flow is developed between the advancing and returning blade and is known as overlap jet (Kacprzak et al. 2013). The overlap jet flow developed between the turbine blades is the key cause for the improvement in starting characteristics. This overlap jet flow reduces the negative torque developed by the returning blade profile by introducing an opposite effect on the concave side of the returning blade profile. By reducing the turbine blade's negative torque, the net power developed by the turbine blade is improved. It is evident that as the overlap ratio (OR) increases beyond the optimum value, the net pressure acting on the concave side of the advancing blade decreases. Therefore, an optimum value of overlap ratio is required between the advancing and returning blade profiles. The optimum range of overlap ratio (OR) of 0.1 to 0.25 is always recommended to enhance the performance of the Savonius hydrokinetic turbine based on the previous researchers (Akwa et al. 2012; Roy and Saha 2013; Talukdar et al. 2018; Patel et al. 2016). Table 2.2 shows the C_{Pmax} values of Savonius hydrokinetic turbine blades with and without overlap ratio by various researchers.

Table 2.2 C_{Pmax} values of Savonius hydrokinetic turbine blades with respect to overlap ratio by various researchers.

Sl. No	Researcher	OR	C_{Pmax}	TSR
1.	Golecha et al. 2011	0.0	0.14	0.7
2.	Talukdar et al. 2018	0.15	0.28	0.89
3.	Kerikous and Thévenin 2019b	0.15	0.238	1.02
4.	Kerikous and Thévenin 2019a	0.15	0.219	1.0
5.	Alipour et al. 2020	0.15	0.28	0.98
6.	Ramadan et al. 2020	0.2	0.18	0.8
7.	Basumatary et al. 2021	0.23	0.268	0.549
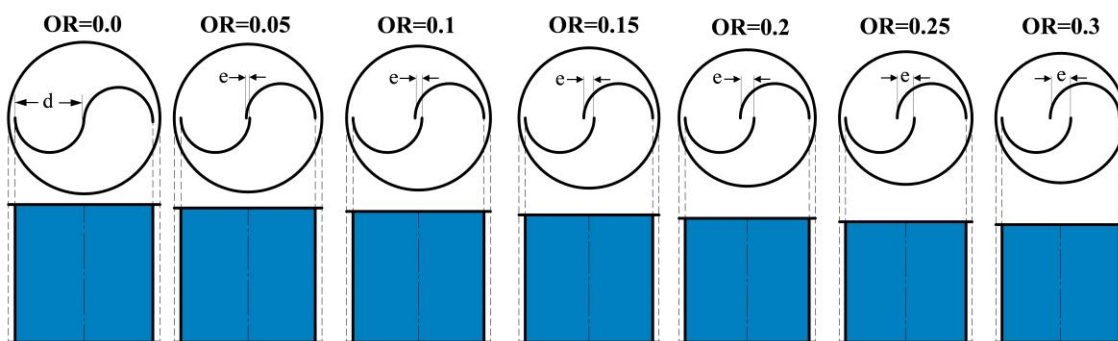
Figure 2.4 Examples of Savonius turbines with different aspect ratios and overlap ratios (Akwa et al., 2012)

2.6 Separation gap (SG)

Another design parameter for the effective design of Savonius hydrokinetic turbine blade is the separation gap (SG). It is the gap between the advancing and returning blade profiles. The separation gap (SG) is responsible for the flow of fluid through the gap between the advancing and returning blade profiles, as shown in Figures 2.5 (a) and (b). The water cannot concentrate on the concave side of returning blade profile with the inclusion of a separation gap (SG). This results in restoring pressure drag on the returning blade profile through the overlapping flow, and dragging flow is greatly reduced. Various researchers carried out most of the research investigation showed better results with zero separation gap between the advancing and returning blade

profile (Akwa et al. 2012b). Therefore, the net power developed by the turbine blade is decreased.

Separation gap

Without separation gap

Gap

H_R

H_R

Diameter of the turbine (D_r)

Diameter of the end plate (D_{ep})

Diameter of the turbine (D_r)

Diameter of the end plate (D_{ep})

(a)

(b)
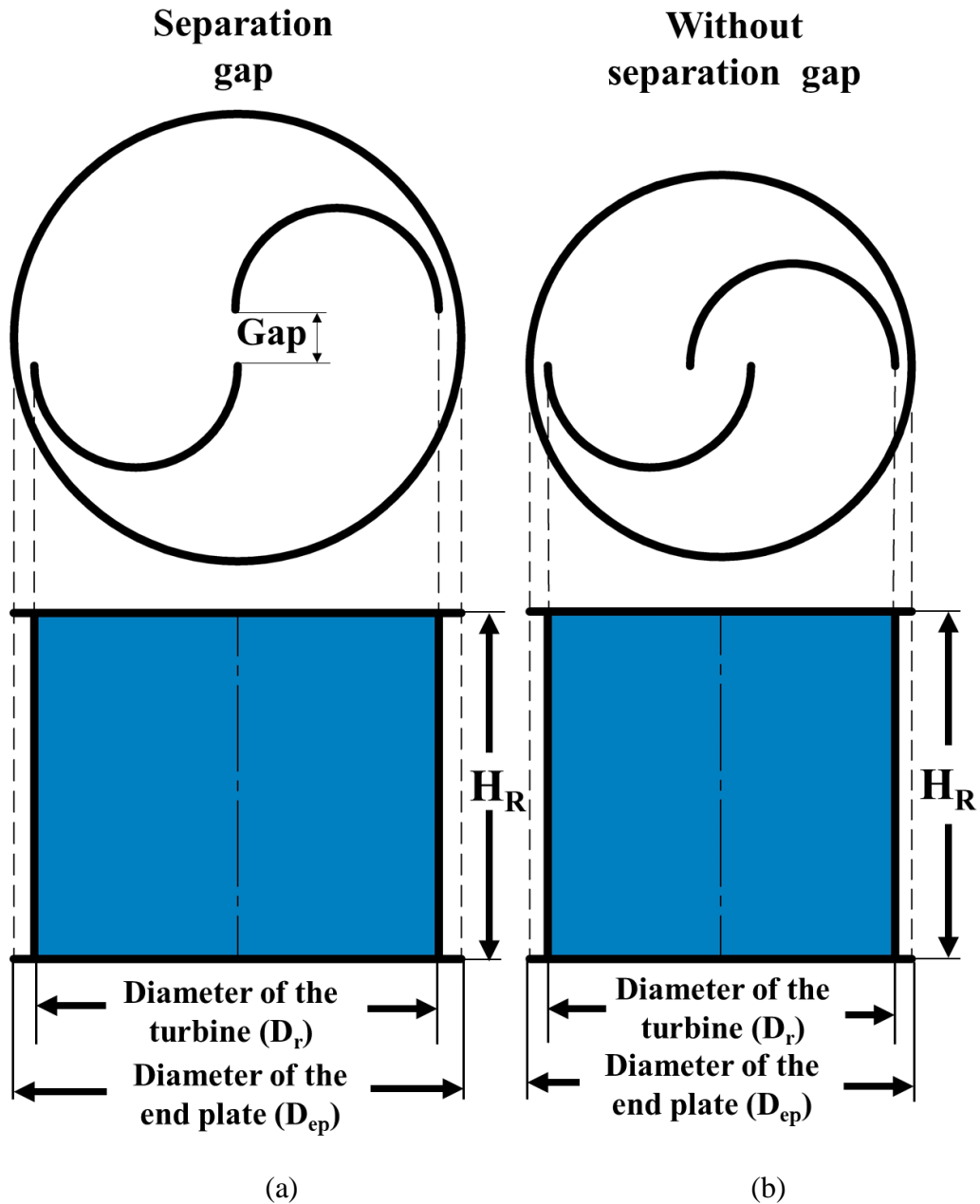
Figure 2.5 Savonius turbines (a) with and (b) without separation gap

2.7 Endplates (D_{ep})

The endplates are the thin circular plates that are fixed at the top and bottom end of the Savonius hydrokinetic turbine blades, as shown in Figures 2.6 (c and d). The importance of the endplate is to enhance the performance parameters. The inclusion of

endplates enhances the net power developed by the Savonius hydrokinetic turbine as compared to the without endplate case (Patel et al, 2016). This may be because fluid may flow from the top and bottom of the turbine blade in the case of without endplate case. Consequently, this does not contribute to the increase in the upstream stagnation pressure of the advanced turbine blade. Therefore, in the case of open-ended vanes, the amount of torque developed by stagnation pressure is lower than the endplate case (Patel et al, 2016). That is mainly due to the inhibition of air outflow from the advancing (concave) side of the blade profile by the endplates, which maintains the pressure difference between the advancing (concave) and returning (convex) sides of the blades at acceptable levels along with the turbine height. The recommended geometric dimension of the endplate diameter is 1.1 times the diameter of the turbine blade (Abraham et al. 2012; Akwa et al. 2012; Roy and Saha 2013b; Patel et al, 2016).
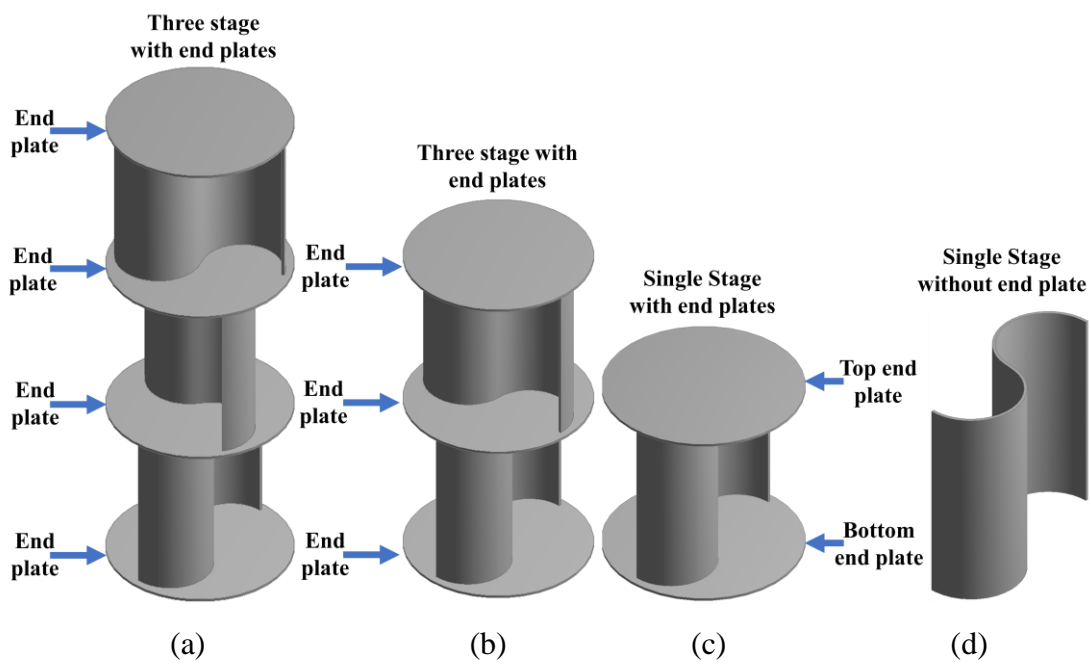
Figure 2.6 Use of endplates and multi-staging, (a) three stages, (b) two-stage, (c) sing stage, (d) single-stage without endplate

2.8 Staging of Savonius turbines

Savonius hydrokinetic turbines having high starting torque is the main advantage as reported in the previous section. But, at some angular positions ($\theta =110°–170°$), it is observed that changes in the direction of the fluid lead to lower starting torque. Therefore, the turbine cannot start on its own. To overcome this difficulty, the use of

multi-stage Savonius hydrokinetic turbines has shown a significant improvement over single-stage Savonius hydrokinetic turbines. A two-stage design of this style is achieved by aligning the top and bottom blade pairs at 90° to each other, while a three-stage design aligns them at 120° to each other. Figure 2.7 (a, b, and c) shows the schematic arrangement of stage-1, stage-2, and stage-3 Savonius hydrokinetic turbine.

Khan et al. 2009 conducted experimental studies on a single stage, two stages, and three-stage Savonius water turbine in a channel with a dimension of 5×3 m^2, having a turbine blade aspect ratio of 1.82 and an overlap ratio of 0.207. The test trials were conducted for three different Reynolds numbers, namely 0.98×10^5, 1.52×10^5, and 1.96×10^5. The study concluded that two-stage rotor blades having better performance as compared to single and three staged rotors. Nakajima, Miyoshi et al. 2008b examined the horizontal axis Savonius water turbine, with an overlap ratio (OR) and an aspect ratio (AR) of 0.36 and 1.48, respectively. They found that the C_{Pmax} of 0.25 at 1.1×10^5 Reynolds number. Nakajima, Miyoshi et al. 2008a extended his study on Savonius turbine with distinct models such as single-stage and double stage with 0° and 90° phase shift. Using the double phase rotor, they examined the flow field visually around the rotor to reveal the C_P enhancement processes.

It was found that the turbine's performance was improved approximately by 10 percent for a phase difference of 90°. Multi-staging decreases excessive torque variation without sacrificing the turbine's performance (Hayashi et al. 2005; Saha et al. 2008). Golecha et al. 2011 reported that the performance of two-stages modified Savonius hydrokinetic turbine with a 90° phase shift has a slightly higher C_{Pmax} compared to the rotor with a 0° phase shift.

2.9 Number of blades

Depending on the operating conditions, the number of blades for Savonius turbines is an effective parameter. The performance of two-bladed turbines of this type has been superior than that of three-bladed turbines (Talukdar et al. 2018). This is due to the approaching blade's angular locations being reduced, resulting in a "cascade effect" in which each blade impacts the performance of the next blade. As a result, higher-bladed devices convert a smaller portion of the energy released by moving fluid into

mechanical energy. A two-bladed turbine's C_P is about 1.5 times that of a three-bladed turbine (Ben F. Blackwell, Robert E. Sheldahl 1977). The two-bladed system has a greater performance (Talukdar et al. 2018). However, as previously mentioned, a multi-staging system can be used to improve the beginning capabilities of a two-bladed turbine. Figure 2.7 shows the schematic diagram of two and three-bladed Savonius turbine.

| (a) | (b) |
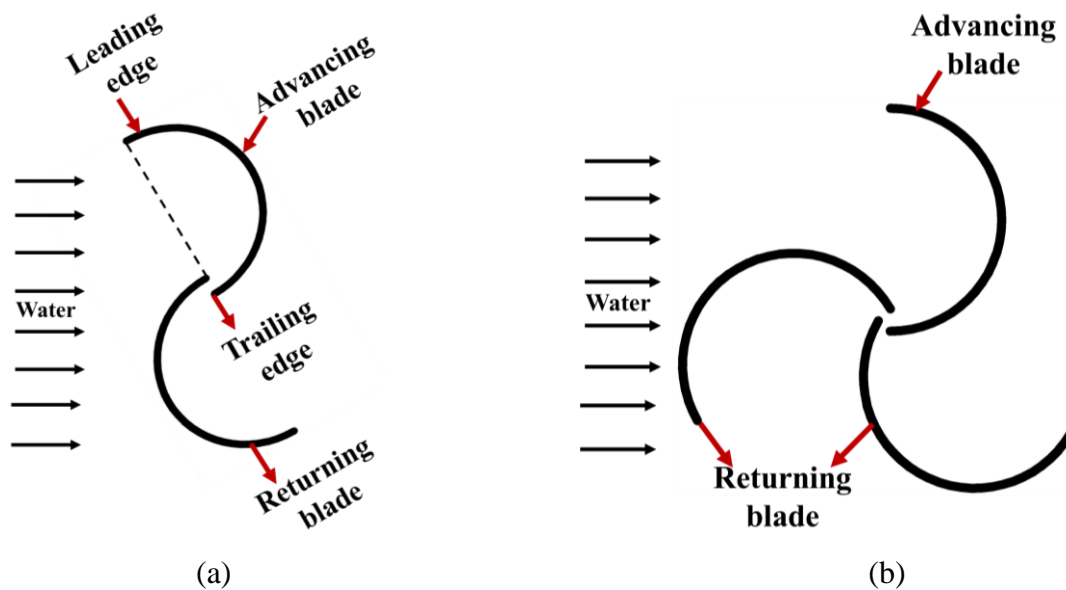
Figure 2.7 Two and three bladed Savonius hydrokinetic turbine blades

2.10 Different blade shapes

The advantage of using a basic blade profile for Savonius wind turbines is that variable blade profile optimization is possible. Savonius patented the first "S"-shaped Savonius turbine in 1929 (Savonius 1929). Thereafter, he improved the design to boost the efficiency of the turbine 1930 (Savonius 1930). These designs were further modified to enhance the performance parameters by various researchers by using experimental and numerical investigations (Kamoji et al. 2009c; Mohamed et al. 2011; Ramadan et al. 2018). These modified blade profiles are reported to be more efficient than the semi-circular blade profile. The various blade profiles used for SSWTs are shown in Figure 2.8. Apart from these "S" or "hook" profiles, twisted blades are another sort of profile that can be encountered in specific applications. According to open literature, twisted and helical bladed turbines have slightly enhanced the performance and starting characteristics of these turbines (Grinspan et al. 2001; Kamoji et al. 2009a; Kumar and

26

Saini 2017a; b; Mosbahi et al. 2019, 2020a; b; Saha et al. 2008). The influence of helical designs decreases the huge fluctuations in a single-stage Savonius turbine's torque characteristic (Kamoji et al. 2009a). The C_{Pmax} values of various blade profiles developed by previous researchers with different geometric parameters, inlet conditions are presented in Table 2.3.

Table 2.3 C_{Pmax} values of the rotor blade with varying the number of blades by previous researchers.

Sl.NO	Researcher	Rotor blade profile	Parameters	C_{Pmax}
1.	Golecha et al. 2011	Modified Savonius turbine	AR=0.7, V_W=0.45 m/s, and Re= 1.32×10^5	0.14 at 0.7 TSR
2.	Kumar and Saini 2017b	Helical blade profile	AR=1.58, OR=0.0, Blade shape factor=0.0-0.6, twist angle 0°-25°, V_W=0.5-2 m/s and Re=8.9× 10^4 to 35.9×10^4	0.39 at 0.9 TSR, twist angle =12.5°, V_W=2m/s and Re=35.9× 10^4
3.	Kumar and Saini 2017a	Helical blade profile	AR=1.58, Blade shape factor=0.0-0.6, twist angle 12.5°, blade arc angle=110°-150°, V_W=0.5-2 m/s and Re=7.36× 10^4 to 37.52×10^4	0.41 at 0.9 TSR, blade arc angle =150°, and V_W=2m/s
4.	Talukdar et al. 2018	Semi-circular blade profile	AR=1.0, OR=0.15, V_W= 0.8 m/s and Re= 2.25×10^5	0.28 at 0.89 TSR

5.	Talukdar et al. 2018	Elliptical blade profile	AR=1.0, OR=0.15, V_W= 0.8 m/s and Re=2.25×10^5	0.17 at 0.71 TSR
6.	Kerikous and Thévenin 2019b	Thick blade profile	AR=1.0 and OR=0.15	15% increase at a TSR of 1.2.
7.	Mosbahi et al. 2019	Helical Savonius hydrokinetic turbine (Three bladed)	AR=0.87, Twist angle 90° and V_W=0.86 m/s and Re=2.82×10^5	0.14 at 0.7 TSR
8.	Ramadan et al. 2020	New design	OR=0.2, V_W=0.5-3 m/s and Re= 2.7×10^5, 5.42×10^5, 1.08×10^6 and 1.62×10^6	0.24 at 0.8 TSR, and V_W=3m/s
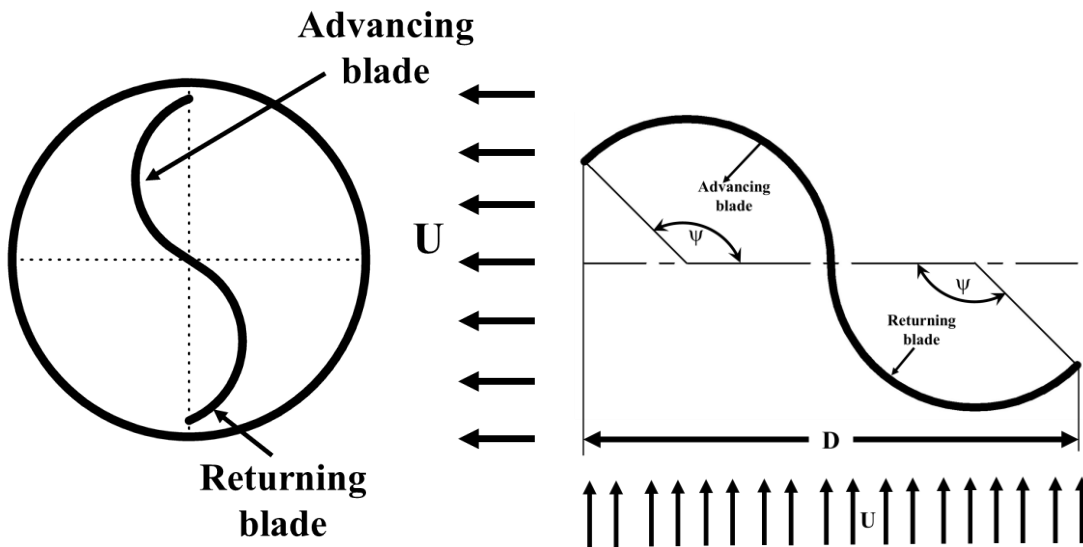
Modified Savonius rotor

(Golecha et al. 2011)

Twisted blade

(Kumar and Saini 2017b)

Two bladed
(Talukdar et al. 2018)

Three bladed turbine
(Talukdar et al. 2018)

Elliptical turbine blade
(Talukdar et al. 2018)

New design
(Ramadan et al. 2020)
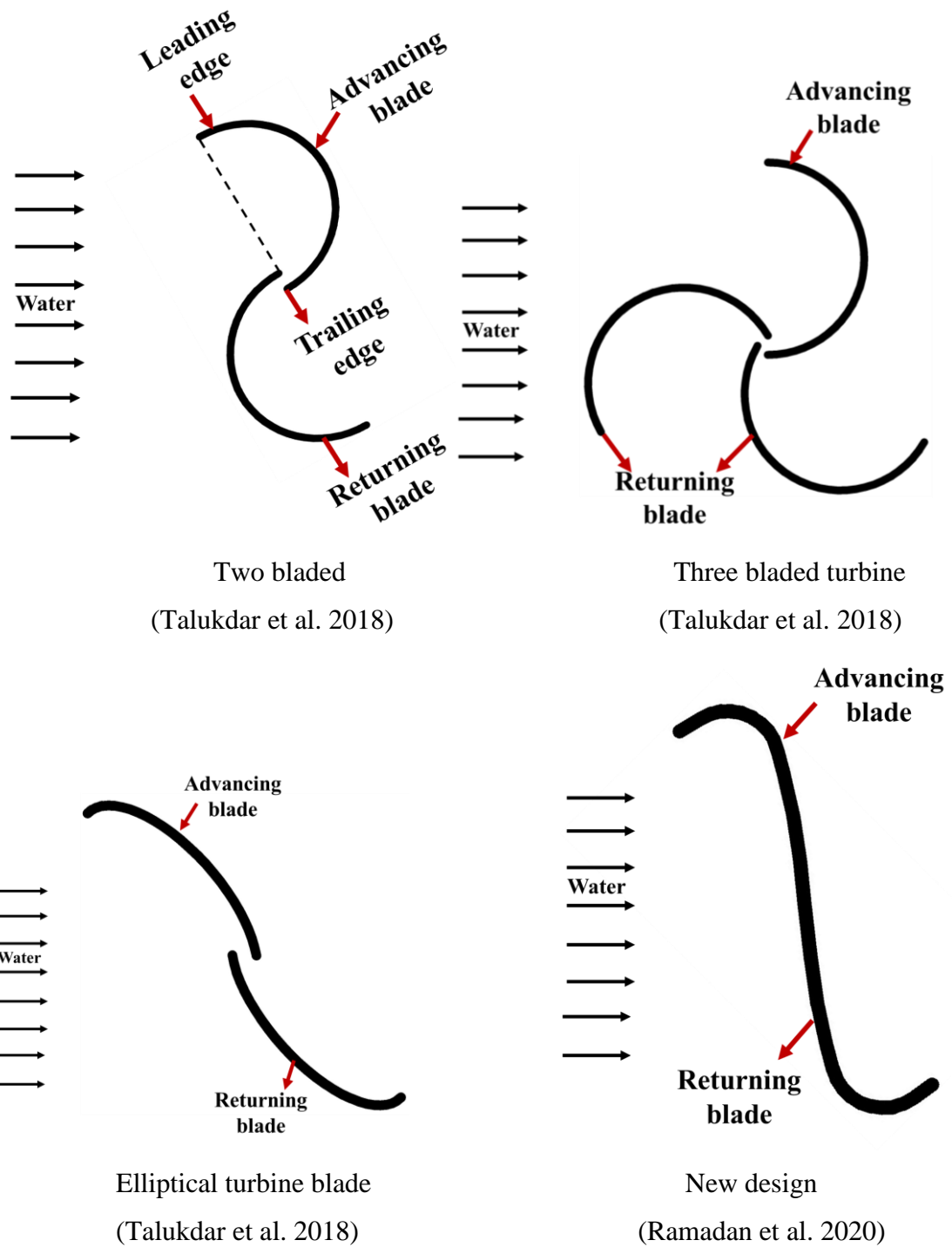
Figure 2.8 various blade profiles used for the enhancement of performance parameters
of conventional Savonius turbine blades

2.11 Augmentation techniques

According to open literature, the performance of a Savonius turbine blade can be greatly
improved by installing various power augmenters in front of the turbine blades, such as

curtains (Altan and Atilgan 2010), windshields (Hu et al. 2009), single and deflector plates (Golecha et al. 2011; Kailash et al. 2012), ducted nozzle (Elbatran et al. 2017), obstacle plate (Mohamed et al. 2011), wind booster (Korprasertsak and Leephakpreeda 2015), and conveyer deflector (Tartuferi et al. 2015) as shown Figures 2.9. It should be noted that the fluid pressure imposed on this turbine's returning blade causes a large negative torque, which reduces its total output. The net power output and beginning characteristics of the Savonius turbine can be increased in two ways using various augmentation approaches, namely.

1. Reduction of fluid resistance on the returning blade profile, and

2. Local acceleration of fluid flow impinging on the advancing blade profile. The C_{Pmax} values of various augmentation techniques used for the performance enhancement of the Savonius turbine by various researchers are presented in Table 2.4.

Table 2.4 Percentage increase of C_{Pmax} values by using various augmentation techniques.

Sl. No	Researchers	Augmentation type	C_{Pmax}	TSR
1.	Takenori Ogawa 1986	Deflector plate	24%	0.8
2.	Shaughnessy and Probert 1992)	V-shaped deflector	20%	0.22
3.	Altan and Atilgan 2010	Curtains	140.6%	0.35
4.	Mohamed et al. 2011	Obstacle shielding	38.9%	0.7
5.	M.H. Mohamed, G. Janiga, E. Pap 2010	Obstacle shielding	27.3%	0.8
6.	Golecha et al. 2011	Deflector plate	50.0%	0.7
7.	Roy et al. 2014	Oriented jet	32.3%	0.8
8.	Kailash et al. 2012	Two deflector plates	150%	1.08
9.	Elbatran et al. 2017	Ducted nozzle	78%	0.73
10.	Mosbahi et al. 2019	New deflector system	12%	0.7
11.	Tartuferi et al. 2015	Curtain system	22%	0.7
12.	Kerikous and Thévenin 2019a	Thick deflector plate	15%	1.2
13.	Alizadeh et al. 2020	Using barrier	18%	0.8
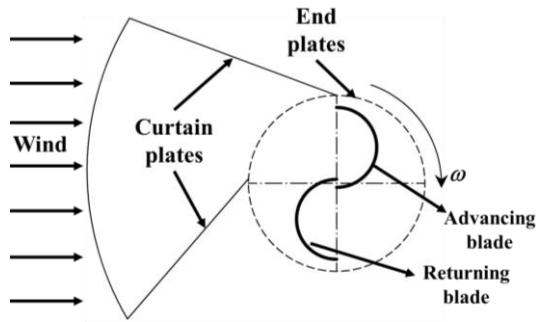
Curtains

(Altan and Atilgan 2012)
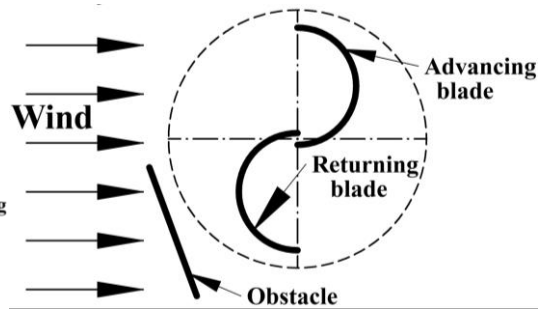
Obstacle plate

(Mohamed et al. 2011)
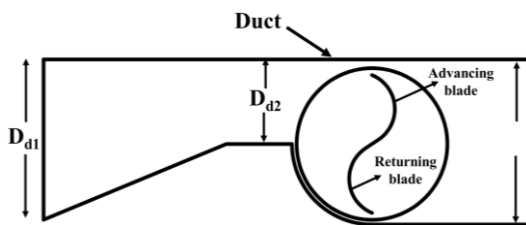
Duct configuration

(Elbatran et al. 2017)
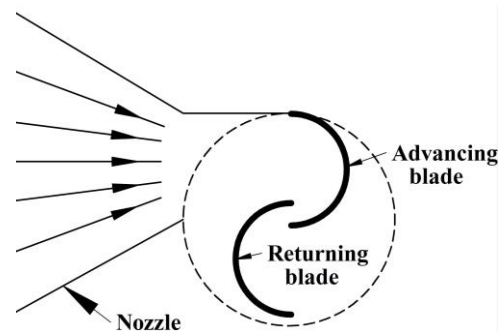
Nozzle

(Shikha et al. 2003)
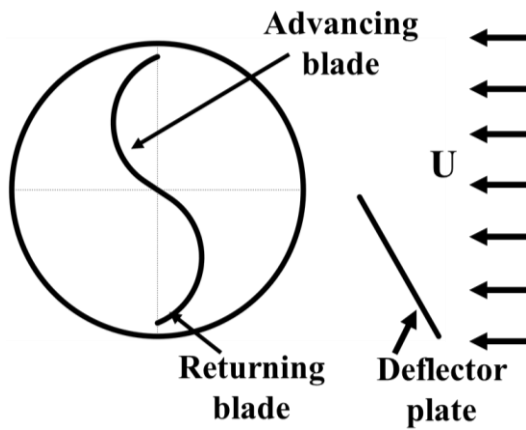
Single deflector plate

(Golecha et al. 2011)
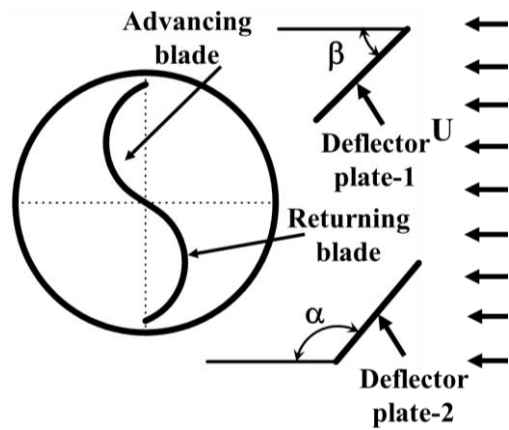
Double deflector plate

(Kailash et al. 2012)

Deflector system
(Mosbahi et al. 2019)

Conveyor-deflector
(Tartuferi et al. 2015)

Circular wind shield
(Yonghai et al. 2009)

Guide-box tunnel
(Irabu and Roy 2007)

Control of wind direction
(El-Askary et al. 2015)

Deflector plate
(Kerikous and Thevenin 2019)
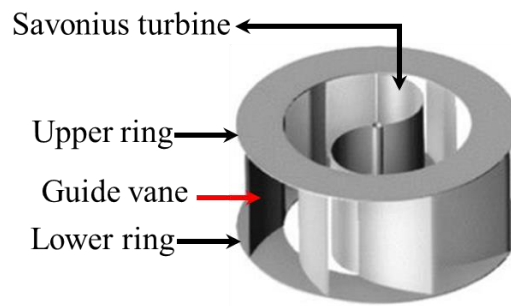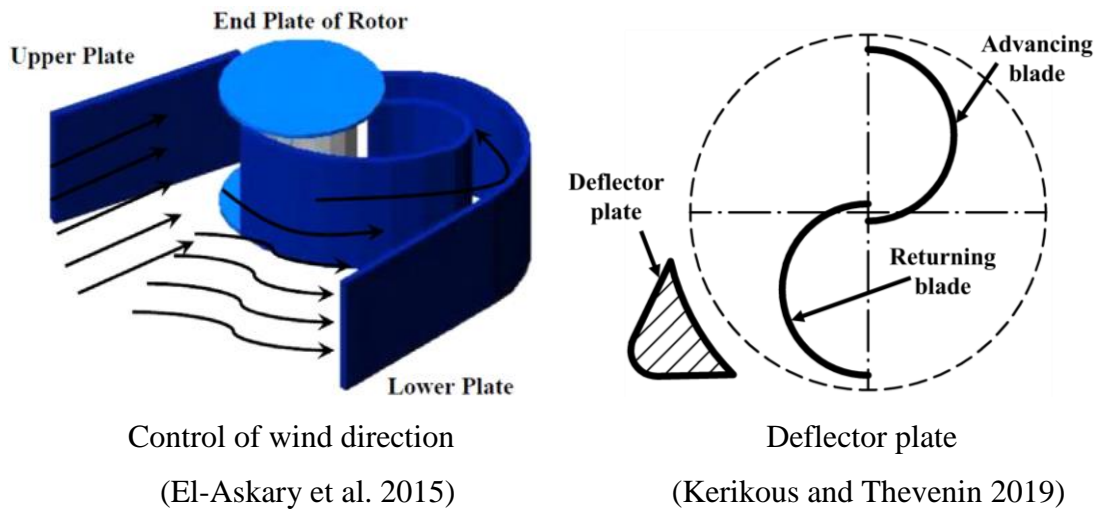
Wind booster (Korprasertsak and Leephakpreeda 2015)

Figure 2.9 Power augmentation techniques used for Savonius wind turbines

2.12 Influence of bed slope on the performance of the turbine

It has been observed that some of the irrigation channels available in the rural areas are having enough bed slope to generate kinetic energy, which can be harnessed through a Savonius rotor. Sivakumar et al. 2018 carried out the numerical investigation using MATLAB for different bed slopes to study the performance of the turbine. The authors reported that the overall power generation increased at the highest bed slope due to the increase in water velocity.

Table 2.5 shows the C_{Pmax} values of the Savonius hydrokinetic turbines by various researchers in the different axis of orientation with respect to dimensions of the water tunnel by using experimental, numerical investigation, without bed slope and taper (top and bottom diameter of the turbine blade are maintained similar).

Table 2.5 Summary of experimental and numerical investigation carried out by various researchers using different Savonius hydrokinetic turbine blade profiles.

Author	Axis of orientation and water tunnel dimensions (m × m)	Blade profile with stages	Performance of the turbine (C_{Pmax})
Nakajima, Miyoshi et al. 2008a	Horizontal 0.6 × 0.5, without bed slope and taper	Stage-1, semi-circular	0.25 at TSR=1.1
Nakajima, Miyoshi et al. 2008b	Horizontal 0.6 ×0.5, without bed slope and taper	Stage-1, 2 and semi-circular	0.275 at TSR=1.3
Khan et al. 2009b	Vertical 5 × 3, without bed slope and taper	Stage-1,2 and 3, semi-circular	0.038, 0.049 and 0.04
Golecha et al. 2011	Vertical 0.73 × 0.33, without bed slope and taper	Stage-1,2 and 3, modified type with and without defector type	50% improvement for the single-stage with deflector at an optimal position
Golecha et al. 2012	Vertical 0.73 × 0.33, without bed slope and taper	Stage-1 investigated the influence of separation gap ratio on the interaction between 2 rotors placed in an inline manner.	C_P increases with the interaction and reduces the performance as compared to keeping the turbine far away from the first turbine.
Sarma, N. K. Biswas and Misra 2014	Vertical 0.17×0.26, without bed slope and taper	Stage-1, semi-circular, three-bladed Savonius water turbine	0.39 at TSR=0.7
Patel et al. 2016	Vertical 0.75×0.27, without bed slope and taper	Stage-1, semi-circular blade with endplates, varying overlap ratio, and overlap ratio	C_P increases for turbine blade fixed overlap ratio, aspect ratio greater than 1.8 and by using top and bottom plates

Elbatran et al. 2017	Vertical 0.73 × 0.33, without bed slope and taper	Stage-1, modified Savonius rotor using the ducted shape of nozzle	0.27 at TSR=0.7
Kumar and Saini 2017b	Vertical 0.65 × 0.55, without bed slope and taper	Stage-1, twisted blade with different twist angle and different flow rate	0.39 at TSR=0.9
Kumar and Saini 2017a	Vertical 0.65 × 0.55, without bed slope and taper	Stage-1, twisted blade with different blade arc angle	0.426 at TSR=0.9
Talukdar et al. 2018	Vertical 10D×6D, without bed slope and taper	Stage-1, semi-circular blade profile	0.28 at TSR=0.89
Talukdar et al. 2018	Vertical 10D×6D	Stage-1, elliptical blade profile	0.17 at TSR=0.77 *TSR*
Sivakumar et al. 2018	Vertical 50X10, with bed slope and without taper	Stage-1, by varying the bed slopes of the irrigation channel by using numerical investigation	0.34 to 10.79MW
Mosbahi et al. 2019	Vertical 0.6X0.5, without bed slope and taper	Stage-1, helical turbine	0.14 at TSR=0.7
Mosbahi et al. 2020a	Vertical 0.6X0.5, without bed slope and taper	Stage-1, helical Savonius and delta bladed Darrieus turbines	0.232 at TSR= 0.63
Mosbahi et al. 2020b	Vertical 0.6X0.5, without bed slope and taper	Stage-1, twisted Savonius hydrokinetic turbine using deflector plate	17.47% increase in C_{Pmax} using deflector at TSR= 0.78

2.13 Summary of literature review

The detailed numerical and experimental research on Savonius hydrokinetic turbine blade is covered in the literature. A broad overview from all the perspectives is presented, covering all the parameters affecting the performance of the Savonius hydrokinetic turbines by using various geometric parameters in varying inlet conditions. Based on the literature review, the following observations are made:

1. Several experimental and numerical studies have been performed by different authors, using different types of turbines in a laboratory-scale open channel with a horizontal bed (bed slope $\theta = 0$). The only reported study by Sivakumar et al. 2018 on varying bed slopes was carried out by numerical simulation. The authors predicted that the total power generation increased at the highest slope due to the increase in flow velocity. There are no experimental studies reported in the literature on the performance of the Savonious rotor in an open channel with varying slopes.

2. The above literature review also highlights the performance studies of the Savonius hydrokinetic turbine by maintaining a similar diameter along with the height of the turbine blade, i.e., both the top and bottom diameter of the turbine blade are identical. However, there is no literature available on tapered Savonius hydrokinetic turbine blades, consisting of varying the diameter at the top and bottom side of the turbine blade. The diameter of taper turbine blade at the top is same as that of the conventional blade and bottom diameter is lower than the conventional turbine with respect to taper angle.

3. Various researchers' main limitations are that Savonius hydrokinetic turbines have lower efficiency due to negative torque developed by the returning blade without augmentation techniques. Literature review reveals that several experimental and numerical studies have been performed by different authors, using conventional (Patel et al. 2016), elliptical (Talukdar et al. 2018), helical (Mosbahi et al. 2020a),

and modified Savonius rotor blade profiles (Golecha et al. 2011) in a laboratory-scale open channel with curved or semi-circular shaped blade profiles.

4. The studies on performance evaluation of conventional Savonius rotor with V-shaped blade profiles with varying straight edges, arc radius, varying overlap ratio, V-angles, and aspect ratio using top middle and bottom endplates are not reported in the open literature. Based on the research gap identified through the detailed literature review, the objectives of the research work are as follows:

2.14 Objectives of the present investigation:

1. To determine the effect of bed slope inclination of the irrigation channel on the performance of the modified Savonius hydrokinetic turbine.

2. To study the effect of taper on conventional Savonius hydrokinetic turbine performance numerically with zero bed slope.

3. To carry out the experimental and numerical investigation of different V-shaped rotor blade profiles with zero bed slope and without taper and also to study the effect of overlap ratio (0.0-0.3) on the performance of modified V-shaped rotor blades.

4. To carry out the experimental and numerical investigation of modified V-shaped rotor blades with different V-angles (90°-40°), aspect ratio (AR=0.7-1.75) and using top, middle and bottom plates.

2.15 Closure

A detailed analysis of the literature is carried out in this chapter. Fundamental as well as parametric issues, were observed. Based on the research gaps, objectives are enlisted. The experimental setup, instruments used for experimentation, and three-dimensional numerical methodology using commercial software ANSYS Fluent used for various parametric investigations are explained in the next chapter.

Chapter 3

EXPERIMENTAL AND NUMERICAL METHODOLOGY

This chapter describes the experimental setup and the instruments used to perform the experimental investigation using different blade profiles. The discussion includes the various parametric studies carried out using experimental and three-dimensional computational fluid dynamics investigation using ANSYS FLUENT by sliding mesh technique adopted in the present work is also explained in brief.

3.1 Experimental and numerical investigations

3.1.1 Experimental investigation: Effect of bed slope

In the present study, an experimental investigation is conducted on a modified Savonius rotor (Golecha et al. 2011) to study the influence of inclination of bed slope in a laboratory-scale multipurpose tilting flume with various angles of inclination of the channel ranging from $\theta = 0^o$ to 2° with an increment of $0.5°$ and the effect of the Froude number (Fr) on the performance of the turbine with respect to different bed slope inclination (θ) of the channel were also studied. Figure 3.1 describes the geometric parameters which are considered for the present experimental investigation. Furthermore, geometric parameters of the modified Savonius turbine blade (Golecha et al. 2011) are straight edge, circular arc (p), arc angle (q), diameter of the rotor (D_r), height of the rotor (H_R), and endplate diameter (D_o) of the rotor are also shown in Figure 3.1.
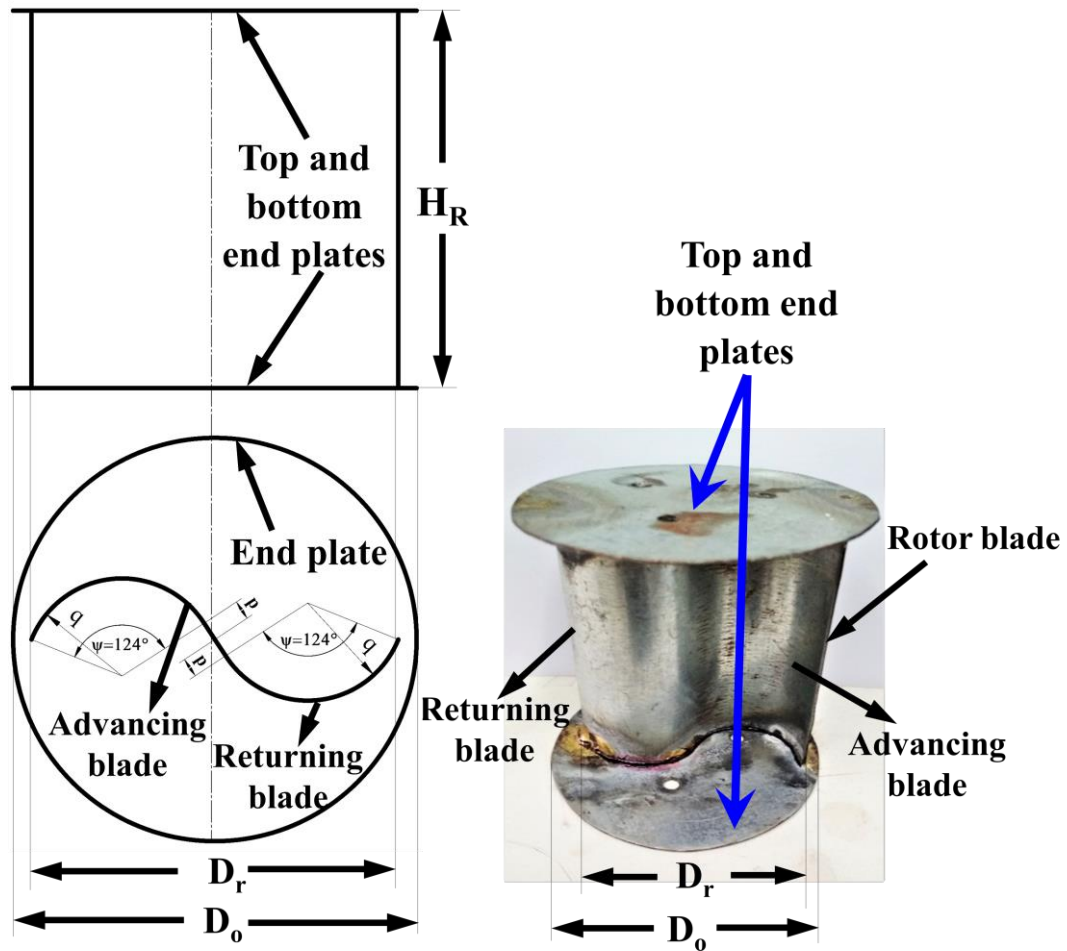
Figure 3.1 Geometric parameters of Savonius rotor (Golecha et al. 2011) (a) schematic of Savonius hydrokinetic turbine and (b) pictorial view of Savonius hydrokinetic turbine

3.1.2 Dimensions of scaled model and procedure

Golecha et al. 2011 carried out the experimental investigations in an open channel having a cross-sectional area of 730 mm x 330 mm to study the influence of the deflector plate on the performance of modified Savonius hydrokinetic turbine. In the present study, experiments were performed in laboratory-scale water re-circulating indoor flume with a flatbed having a cross-sectional area of 215 mm x 350 mm using a scale-down model of Savonius hydrokinetic turbine used by Golecha et al. 2011. The cross-sectional area of the experimental setup used by Golecha et al. 2011 and the present study are different. Therefore, scaled-down dimensions are calculated and

presented in Table 3.1. Figures 3.2 (a and b) show the schematic view of tilting flume in horizontal condition as well as inclined to an angle of (θ) to the horizontal, where H_C and H_W are the height of the channel and height of the water, respectively.

Table 3.1 The details of experimental setup and dimensions of modified Savonius hydrokinetic turbine.

Sl. No	Parameter	Golecha et al. 2011	Present Study
1.	Diameter of the rotor (D_r) mm	245	72
2.	Endplate Diameter (D_o) mm	269.5	79.2
3.	Height of the actual turbine (H_R) mm	170	51
4.	Aspect ratio (AR)	0.7	0.7
5.	Blade arc angle (ψ) Degree	124	124
6.	Blade shape factor (p/q)	0.2	0.2
7.	Width of the channel (W_C) mm	730	215
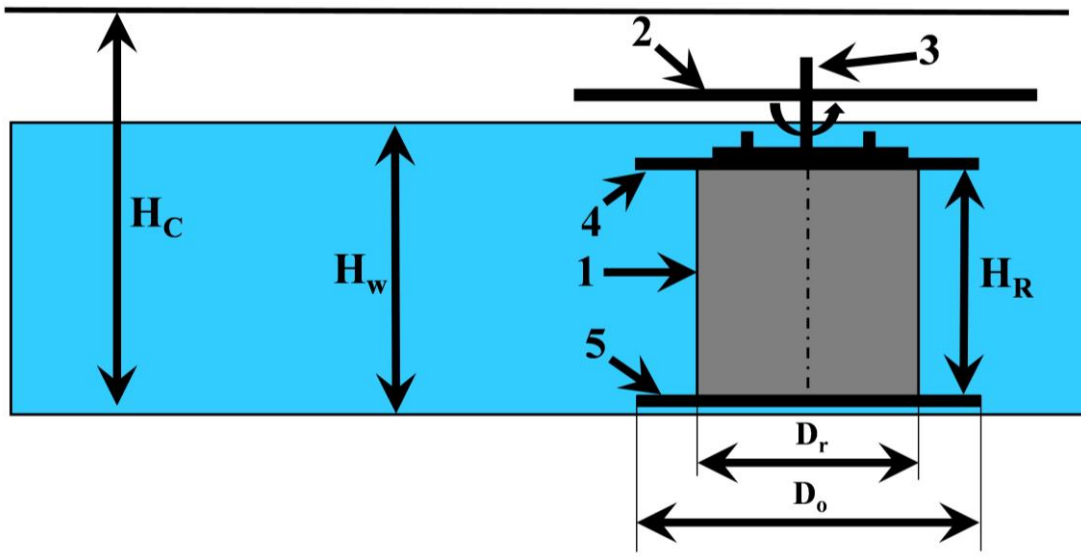
(a)
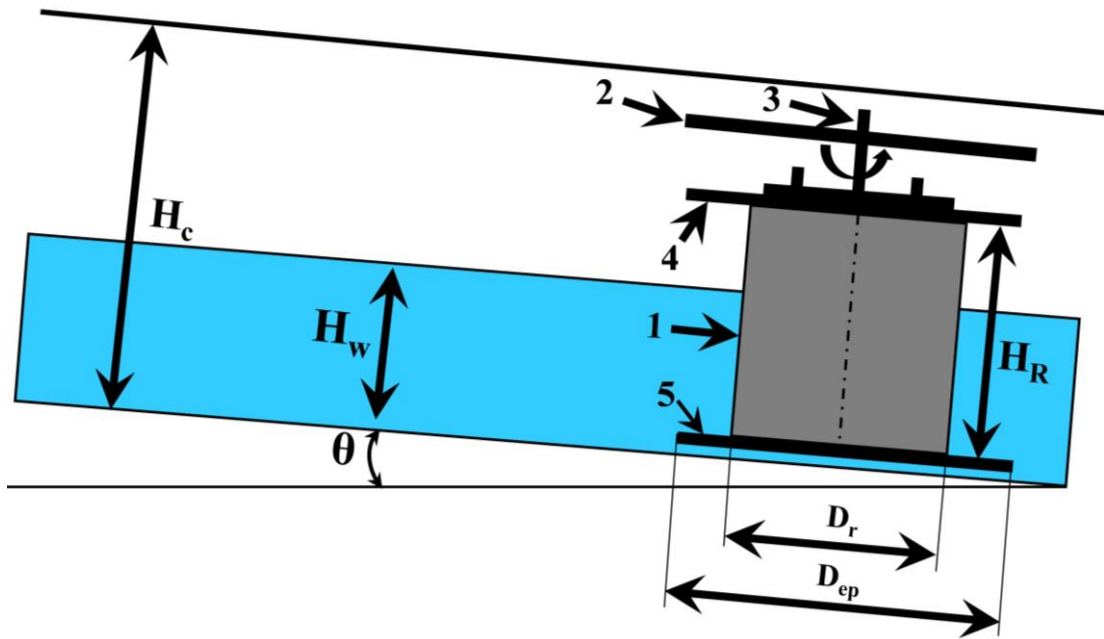
(b)

Figure 3.2 (a) Schematic of experimental setup in a horizontal and (b) inclined flume

1. Savonius rotor, 2. Top plate, 3. Rotor shaft, 4. Rotor upper-endplate, 5. Rotor bottom endplate

3.2 Geometric parameters for the effect of taper on conventional and tapered Savonius turbine blade

Figure 3.3 (a-d) shows a schematic diagram of conventional (a and c) and tapered (b and d) Savonius hydrokinetic turbine blades. The conventional Savonius hydrokinetic turbine blade consists of two semi-circular blade profiles, such as concave and convex profile known as advancing and returning blade profiles (Figures 3.3 (a-d)). The various geometric dimensions such as height (H_R), diameter of the turbine blade (D_r) and two plates, which is placed at top and bottom of the turbine blade known as endplates and its diameter is $1.1D_r$, and it is represented as D_{ep} for both conventional and tapered turbine blade.

Figure 3.3 (b and d) shows the turbine blade with a tapered design. The geometric dimensions of tapered turbine blade are: diameter at the top side (D_{Top}), bottom side (D_{Bottom}) of the turbine blade, height of the turbine blade (H_R) and endplate diameter (D_{ep}). The aspect ratio (AR) and overlap ratio (OR) of the conventional and tapered turbine blades are maintained same. The inside angle between height of the turbine (H_R)

41

and bottom diameter of the turbine (D_{Bottom}) for conventional and tapered turbine blades are 90° (without taper) and 95° (with taper) respectively, and the geometric dimensions of conventional and tapered blade are presented in Table 3.2.

Table 3.2 Important geometric dimension of conventional and tapered Savonius hydrokinetic turbine

Sl. No	Details	Conventional turbine	Tapered turbine
1.	Aspect ratio (H_R/D_r) (Dimension less)	1.0	1.0
2.	Overlap ratio (Dimension less)	0.0	0.0
3.	Inside angle between H_R and D_{Bottom} (Degrees)	90°	95°
4.	Taper angle (Degrees)	0°	5°
5.	Top side diameter of the turbine (D_{Top}) mm	72	72
6.	Bottom side diameter of the turbine (D_{Bottom}) mm	72	60
7.	Height of the turbine blade (H_R) mm	72	72
8.	Top and bottom endplate diameter of the turbine blade ($D_{ep}=1.1D_{Top}$) mm	79.2	79.2
9.	Top diameter of advancing blade bucket (d_T) mm	36	36
10.	Top diameter of returning blade bucket (d_T) mm	36	36
11.	Bottom diameter of advancing blade bucket (d_B) mm	36	30
12.	Bottom diameter of returning blade bucket (d_B) mm	36	30
13.	Thickness of the endplate (t) mm	1	1
14.	Thickness of the turbine blade (t) mm	1	1
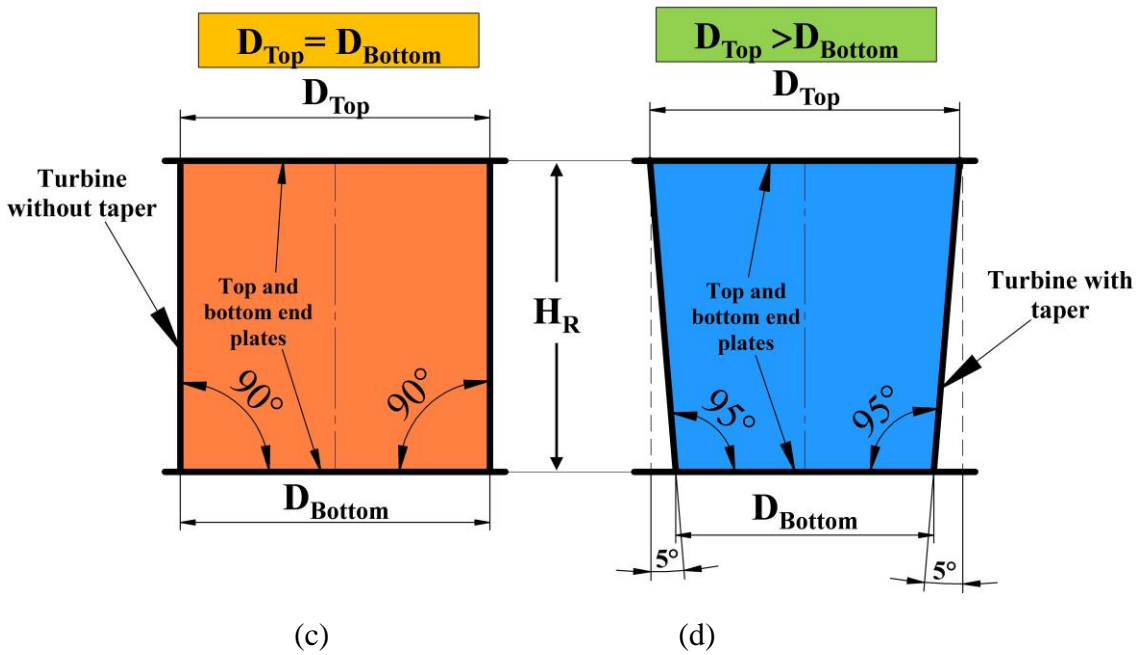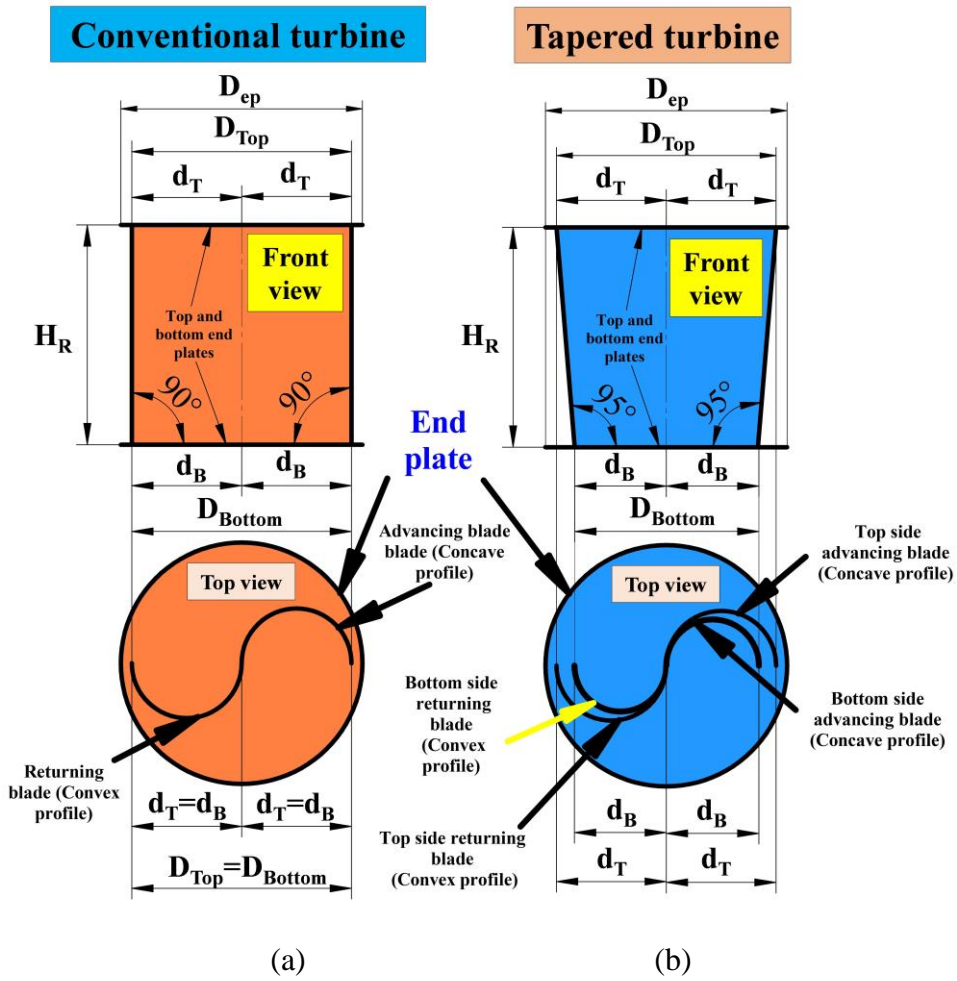
Figure 3.3 Important geometric parameters of the conventional (a and c) and tapered (b and d) turbine blade

3.3 Details of the development of novel V-shaped rotor blade profiles (V₁-V₅)

The various researchers carried out experimental and numerical studies on different rotor blade profiles, such as semi-circular (conventional Savonius rotor), elliptical, modified Savonius rotor, and helical rotor blades using wind and water as a working medium (Akwa et al. 2012b; Al-Bahadly 2009; Alizadeh et al. 2020; Chen et al. 2015; Golecha et al. 2011; Kang et al. 2014; Kumar and Saini 2016; Roy and Saha 2013b; a; Salleh et al. 2019; Wong et al. 2017). The conventional type of Savonius rotor consists of two semi-circular rotor blades known as (advancing blade) concave and (returning blade) convex blade profiles, as shown in Figure 3.4 (a) (dashed line). Precisely at the center of the returning (convex) and advancing side (concave) of the blade profiles (semi-circular blade), two straight lines are drawn with a V-angle of 90°. The blade is designated as V_1 having length two lines named L and 2L.

The first blade is having three straight lines (L and 2L) without any arc or curved shaped profile for the development of 2nd (V_2), 3rd (V_3), 4th (V_4), and 5th (V_5) blades at the height of H_1, H_2, H_3, and H_4 a small fillet is applied in between the two straight lines. Figure 3.4 (b) shows the different configurations from V_1-V_5 at various angular positions.
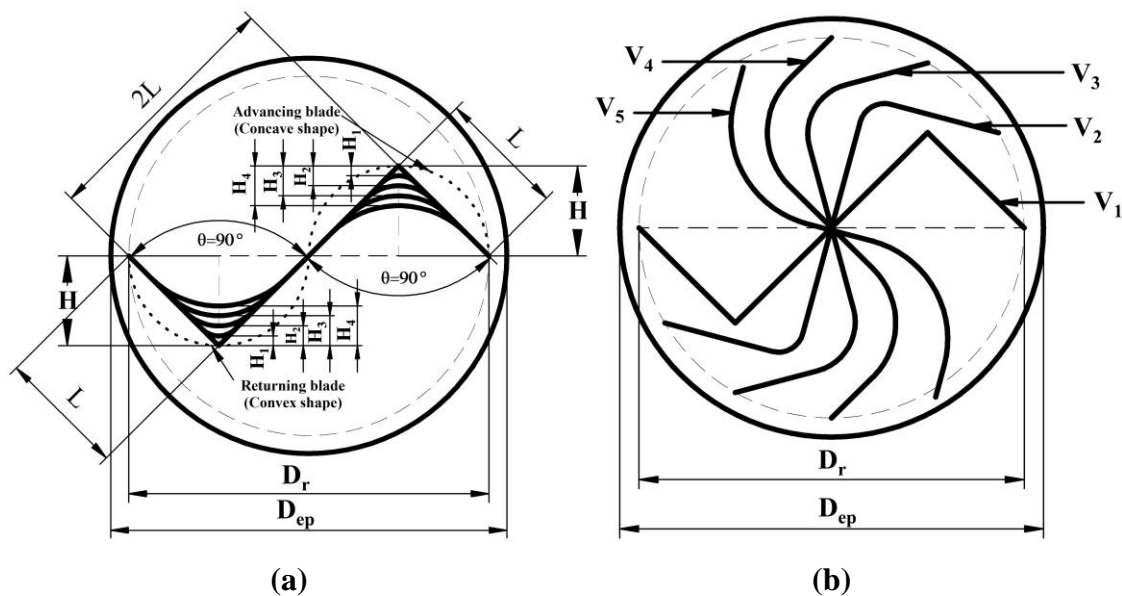
Figure 3.4 (a) Geometrical parameters of different V-shaped rotor blade profiles, (b) rotor blades (V_1-V_5) at different angular positions

44
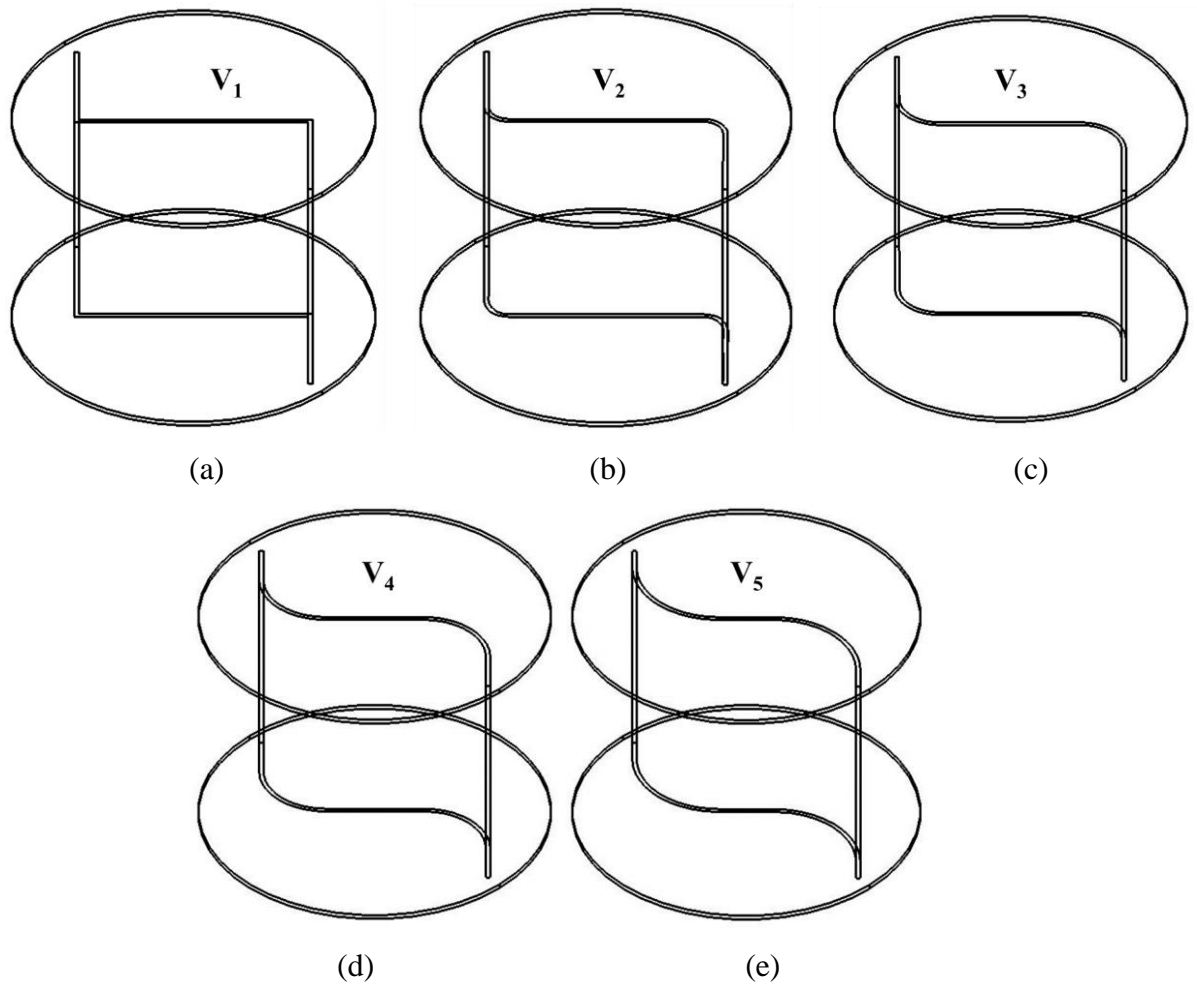
Figure 3.5 (a-e) Wireframe geometry of rotor blades for different blade configurations (V_1-V_5)

The final three-dimensional view of the rotor blade (V_1-V_5) configurations in the wireframe geometry are shown in Figures 3.5 (a-e). The dimensions of all the rotor blade profiles expressed in terms of L are shown in Figures 3.5 (b-f).In Figure 3.6 (a), the schematic diagram of (top view and front view) rotor blade with geometric parameters such as the diameter of the rotor (D_r), endplate diameter (D_{ep}), Height of the turbine (H_R), and all the blade profile dimensions are shown. Figure 3.6 (b) shows the pictorial view of fabricated rotor blades for experimentation named V_1, V_2, V_3, V_4, and V_5.
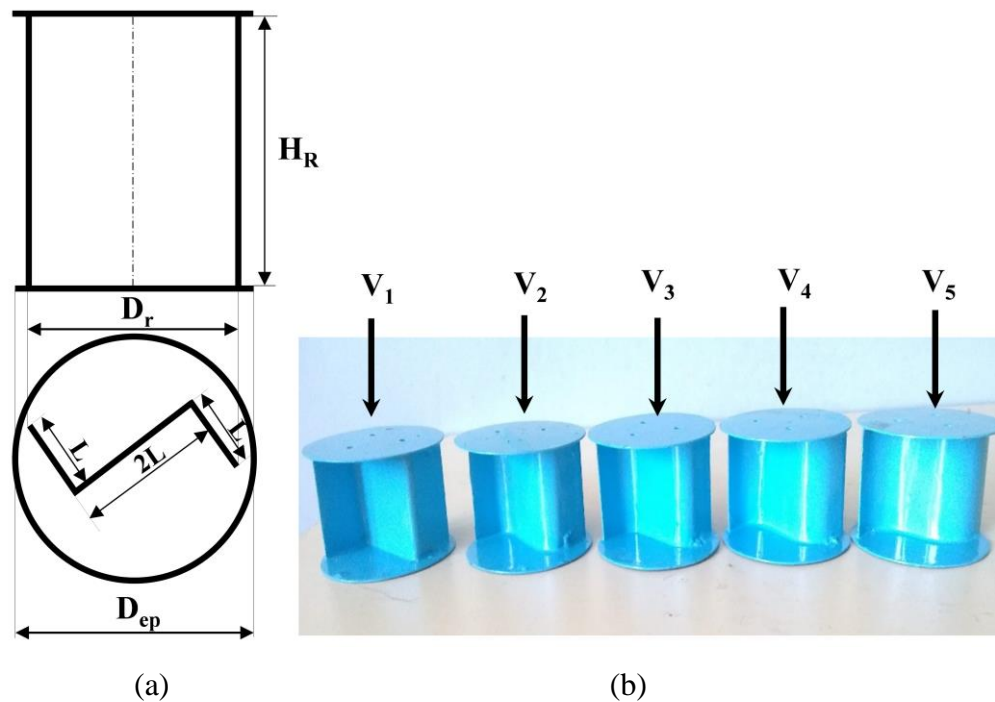
Figure 3.6 (a) Schematic of V-shaped rotor blade (front view and top view) and (b) pictorial of V-shaped rotor blades

Figures 3.7 (a-f) shows the line diagram of different V-shaped rotor blade configurations with all the essential geometric parameters. Figure 3.7 (a) is the general V-shaped rotor (V_{Rotor}) with horizontal lines having different heights (H_1-H_4) on the advancing and returning blades of the turbine. The rotor blades in Figures 3.7 (b-f) named as V_1, V_2, V_3, V_4, V_5, and all the geometrical parameters are given in terms of the length of the short line L. D_r is the diameter of the V-shaped rotor blade, and D_{ep} is the diameter of the endplate provided at the top and bottom of the rotor blades. In this rotor blade configurations, there is no overlap (gap) between the advancing and returning blade profiles, and the optimum aspect ratio (AR) of the rotor blade is taken from the published work of (Golecha et al. 2011, 2012; Sarma, N. K. Biswas and Misra 2014). The dimensions of various geometrical parameters such as height (H_R), diameter (D_r), aspect ratio (AR), and diameter of the endplate (D_{ep}) of V-shaped rotor blades (V_1-V_5) are presented in Table 3.3.
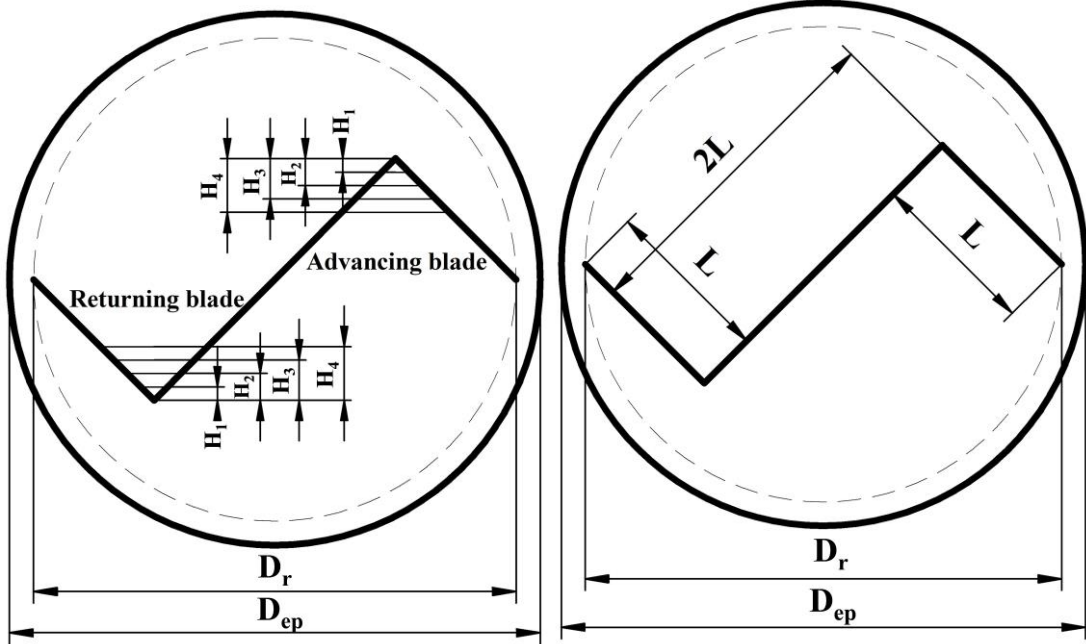
(a) (V_{Rotor})

(b) (V_1)

(c) (V_2)

(d) (V_3)

(e) (V$_4$) (f) (V$_5$)
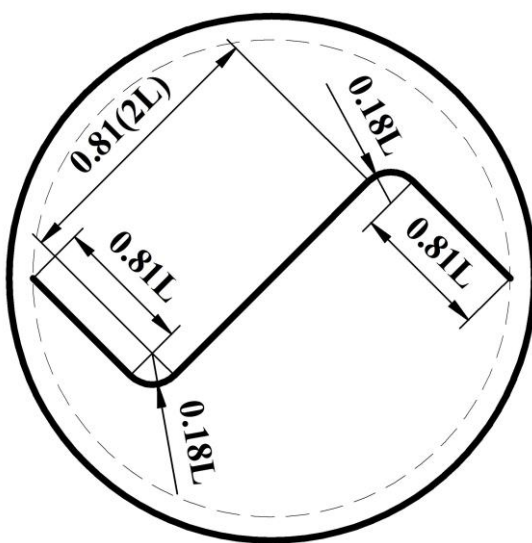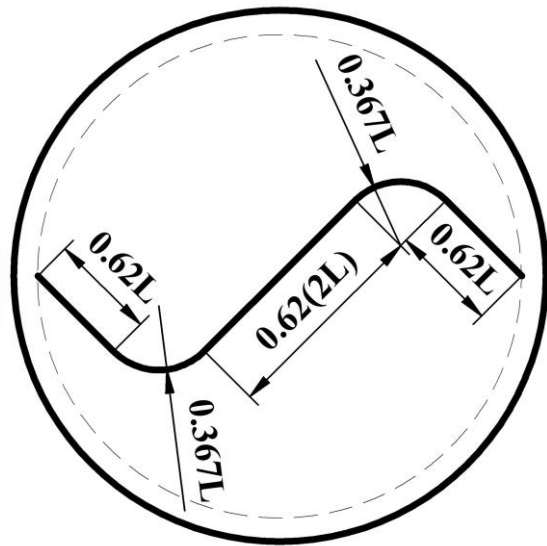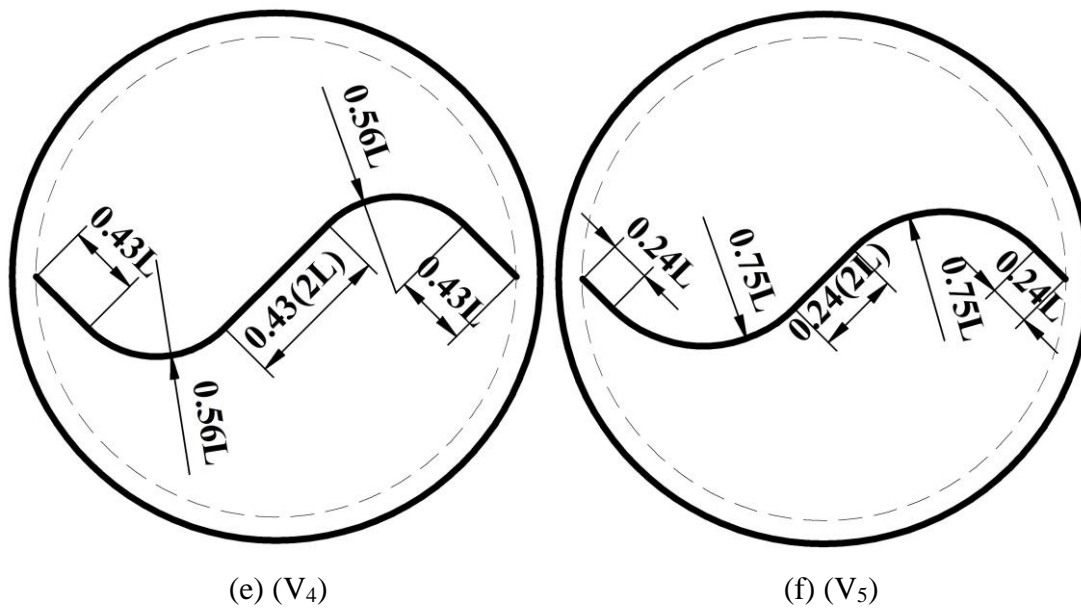
Figure 3.7 (a) Geometric parameters of general V-shaped rotor blade (V$_{Rotor}$) with different heights (H$_1$-H$_4$), (b-f) different configurations of rotor blades with varying geometric parameters (V$_1$-V$_5$)

Table 3.3 Geometrical specification of rotor blades (V$_1$-V$_5$)

Sl. No	Description	Values
1.	Height of the turbine blade (H$_R$) (mm)	50.4
2.	Diameter of the turbine blade (D$_r$) (mm)	72
3.	Endplate diameter of the turbine blade (D$_{ep}$=1.1D$_r$) (mm)	79.2
4.	Aspect ratio (H$_R$/D$_r$) (Dimensionless)	0.7
5.	Overlap ratio (OR) (Dimensionless)	0.0
6.	H$_1$, H$_2$, H$_3$, and H$_4$ (mm)	2, 4, 6 and 8
7.	H (mm)	18
8.	L (mm)	25.46

3.4 Effect of overlap ratio on the performance of modified V-shaped rotor blade with a V-angle of 90°

The overlap ratio (OR) is defined as the ratio of overlap distance between (e) the advancing and returning blades to the blade chord distance (d) as per the literature

48

(Akwa et al. 2012b; Roy and Saha 2013b; a; Sharifian 2014).In the present study, the optimum modified V-shaped blade profile (V_4) developed from the previous section is shown in Figure 3.8 is used to study the influence of overlap ratio. The diameter (D_r) and height (H_R) of the modified V-shaped blade profile (V_4) are 72 and 50.4 mm. The modified V-shaped rotor blade profile (V_4) with different overlap ratios (OR) ranging from (OR=0.0-0.3) with an increment of 0.05 is shown in Figures 3.9 (a-g). The turbine blade is having a diameter (D_r) and thickness (t) of 72 mm and 1 mm, respectively for an overlap ratio (OR) of 0.0 and turbine blade dimensions for various overlap ratios (OR 0.0-0.3) shown in Table 3.4. The dimension of the bottom and top endplates (D_{ep}) is 1.1 times the diameter of the turbine blades (D_r) based on previous literature (Akwa et al. 2012b; Roy and Saha 2013b; a).
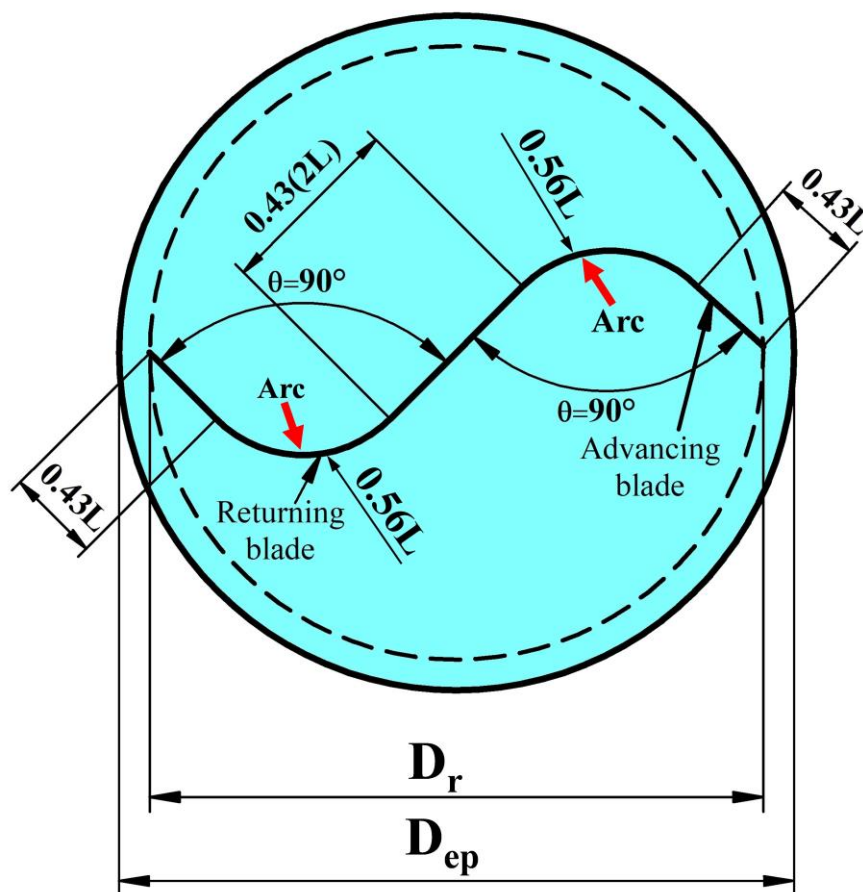
Figure 3.8 Schematic of important geometric parameters of modified V-shaped rotor blade (V_4) with zero overlap ratio (OR)

(a)

(b)

(c)

(d)

50
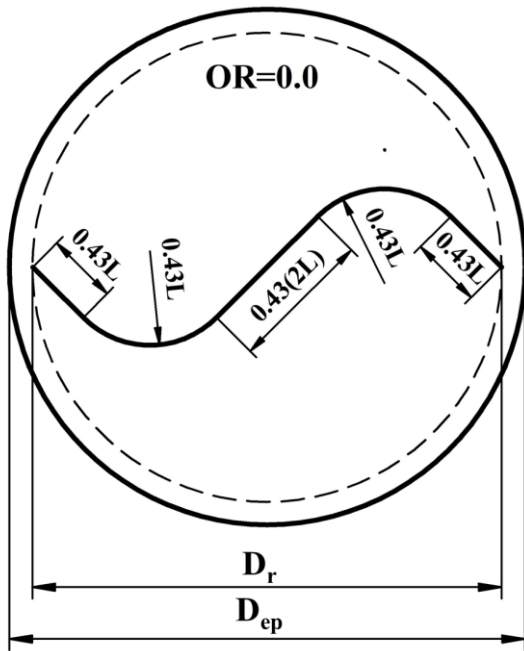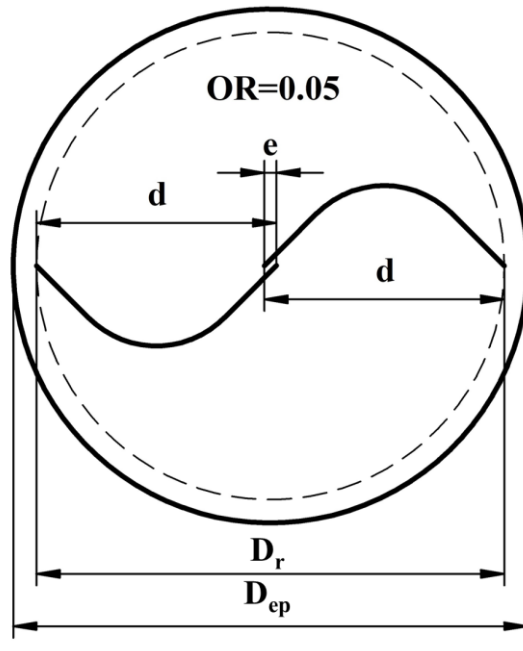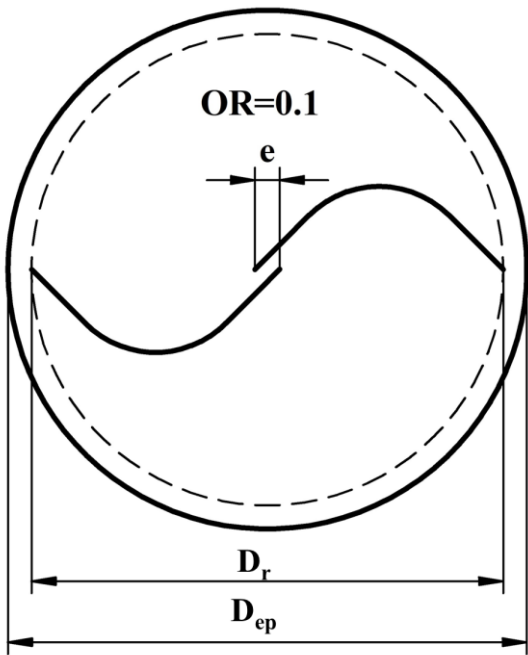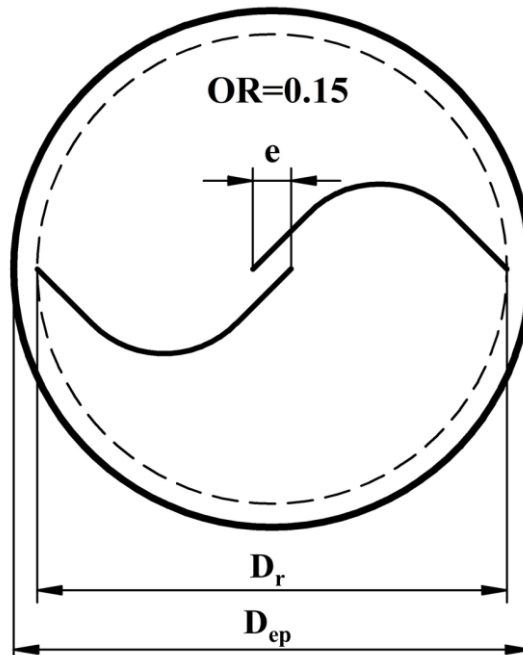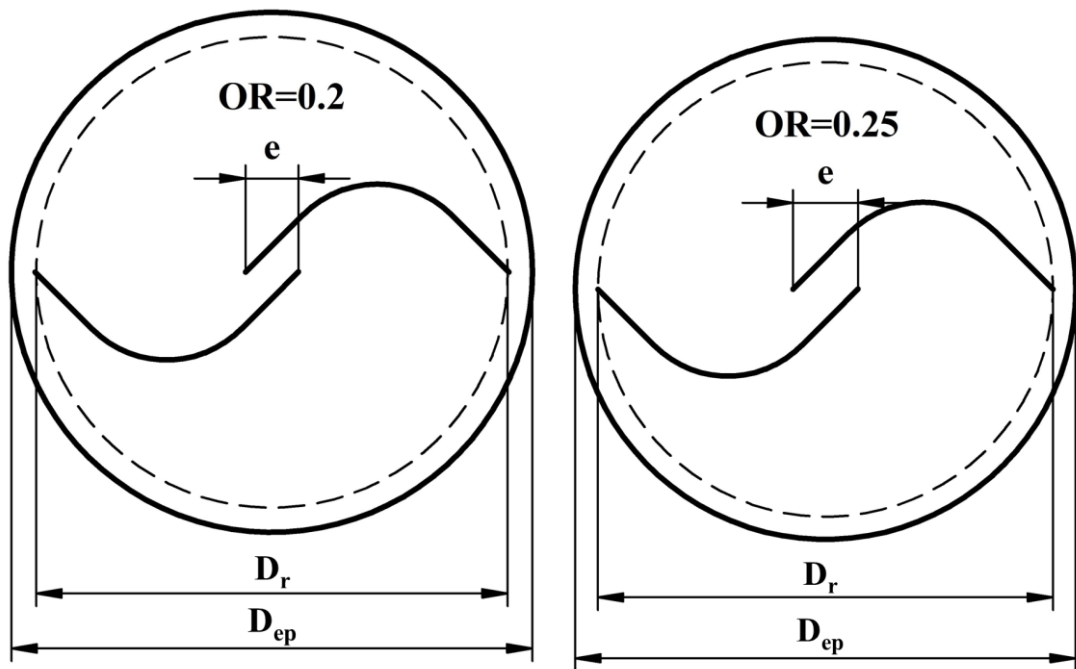
(e)

(f)
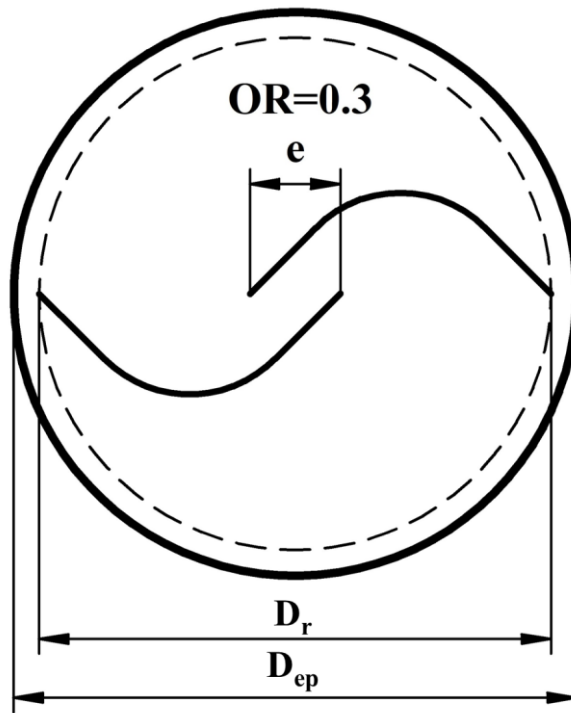
(g)

Figure 3.9 (a-g) Schematic of modified V-shaped rotor blade with different overlap

ratios (OR-0.0 to 0.3)

Table 3.4 Dimensions of the turbine blade with different overlap ratios (0.0-0.3)

Sl. No	OR (mm)	e (mm)	d (mm)	D_r (mm)	H_R (mm)
1.	0.0	0.0	36	72	50.4
2.	0.05	1.8	36	70.2	49.14
3.	0.1	3.6	36	68.4	47.88
4.	0.15	5.4	36	66.6	46.62
5.	0.2	7.2	36	64.8	45.36
6.	0.25	9	36	63	44.1
7.	0.3	10.8	36	61.5	42.1

3.5 Method of development of V-shaped rotor blade with different V-angles (θ=90° to 40°)

The final developed blade profile consists of two straight lines and one arc both in advancing and returning side of the turbine blade and the angle between the two straight lines is 90°. Figure 3.10 shows the modified V-shaped rotor blade profile with a V-angle of 90°, and all the dimensions are expressed in terms of L (where L=25.46 mm). The important geometric parameters of the modified V-shaped rotor blade are height (H_R), diameter of the rotor (D_r), and endplate diameter (D_{ep}=1.1D_r) rotor blade as shown in Figure 3.10. The V-angle of 90° rotor blade is having two edges with one arc, and the length of each edge and arc is 0.43 and 0.56 times of original length L and on both advancing and returning blades. By maintaining the same edge (L) and arc on advancing and returning blade profile, V- angle is varied from 90°- 40° with a step of 10° decrement as shown in Figures 3.11 (a-f). In order to study the effect of V-angles (θ=90°-40°) all the rotor blades are designed with a constant aspect ratio (AR) and overlap ratio (OR) of 0.7 and 0.0 based on the previous investigation (Golecha et al. 2011; Sarma, N. K. Biswas and Misra 2014). The important geometric dimensions of the rotor blade for different V-angles ranging from 90°-40° are presented in Table 3.5.

52
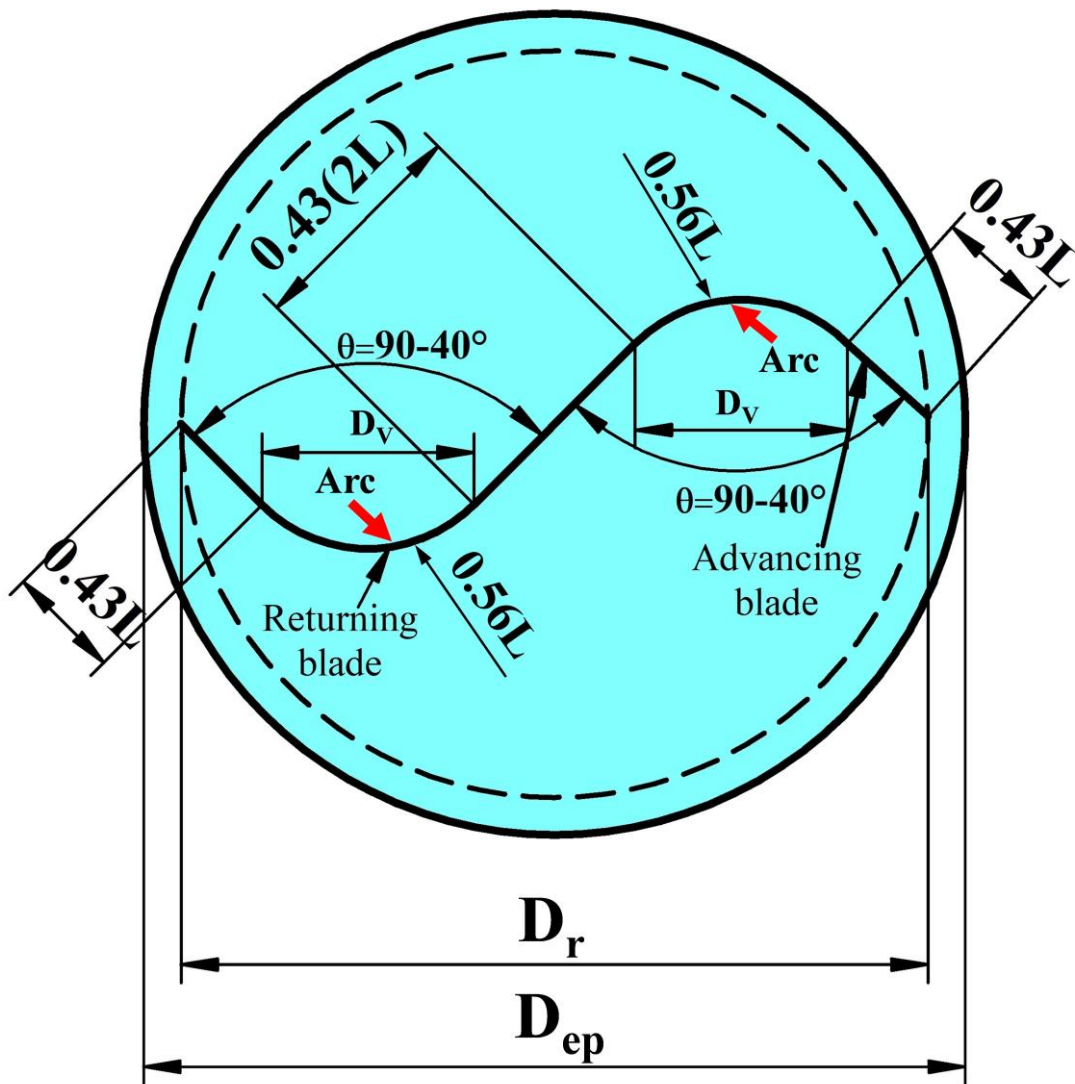
Figure 3.10 Schematic of modified V-shaped rotor blade with varying V-angles ranging from 90°-40°
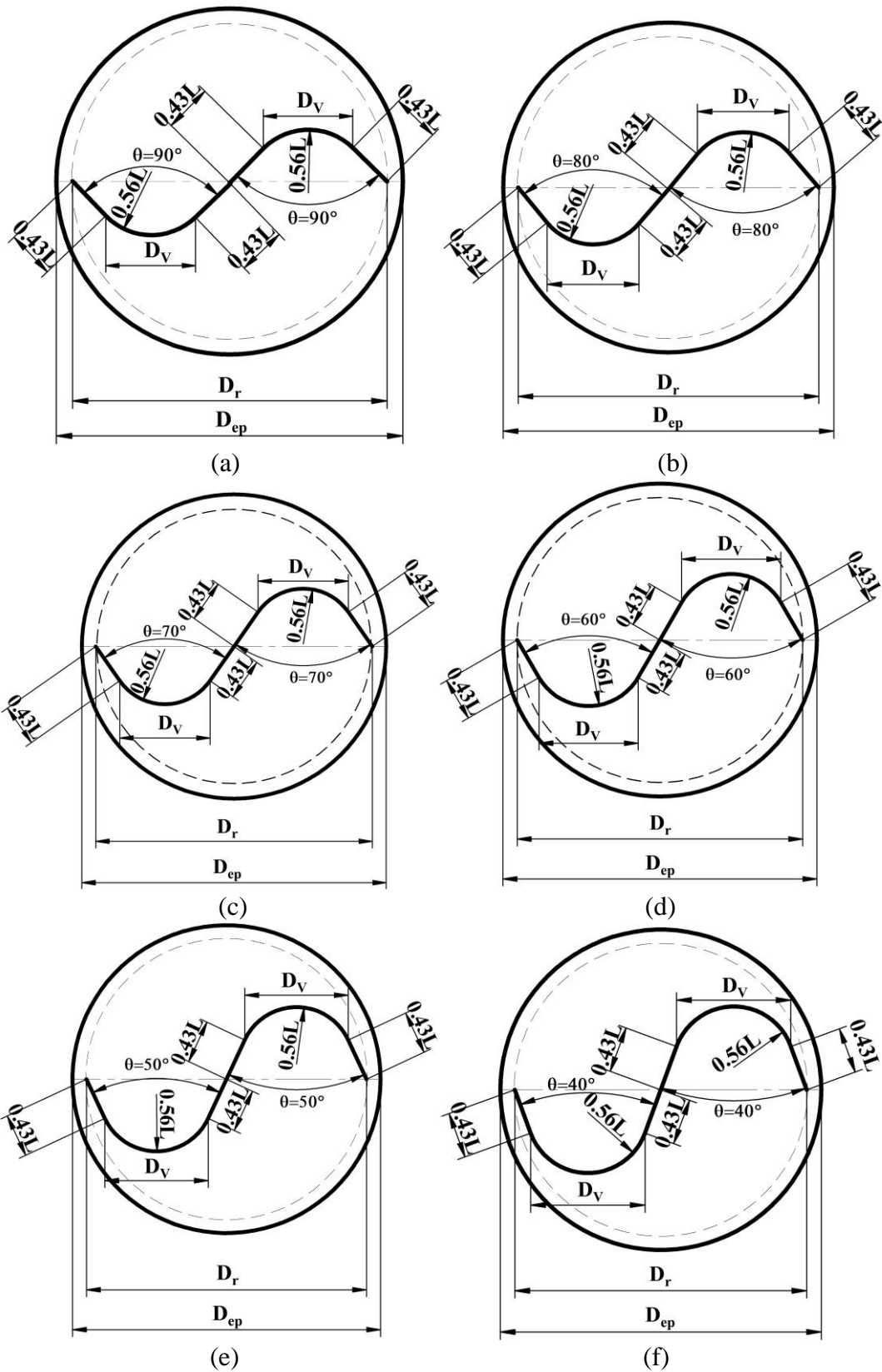
Figure 3.11 (a-f) Schematic of modified V-shaped rotor blade with different V-angles

(θ=90°-40°)

54

Table 3.5 Important geometric dimensions of the computational domain and rotor blades ($V_{90°-40°}$).

Dimensions of rotor blades and computational domain							
Sl. No	Parameter	$V_{90°}$	$V_{80°}$	$V_{70°}$	$V_{60°}$	$V_{50°}$	$V_{40°}$
1.	D_r (mm)	72	72.6	72.62	72.11	71.03	69.42
2.	H_R (mm)	50.04	50.82	50.83	50.57	49.72	48.5
3.	$D_{ep}=1.1D_r$ (mm)	79.2	79.82	79.88	79.32	78.13	76.36
4.	D_V (mm)	20.46	22.17	23.71	25.06	26.23	27.19
5.	AR (Dimensionless)	0.7					
6.	OR (Dimensionless)	0.0					
7.	t (mm)	1					
8.	L (mm)	25.46					
9.	Width of the domain (mm)	215					
10.	Depth of the domain (mm)	70					
11.	Length of the domain (mm)	612					

3.6 Experimental test rig and multipurpose tilting flume

Figure 3.12 (a and b) shows the schematic and pictorial view of the rotor test setup used in the present work. It consists of four threaded studs, which are used as pillars to mount the test rig. A mild steel plate is bolted to the threaded rods at its four ends. Flange bearing (SKF make) is fitted to the upper side of the mild steel plate with the aid of four fasteners. The scaled-down Savonius rotor with endplates is fabricated using a galvanized iron sheet of 1mm thickness (t) fitted to flange bearing by a 12 mm shaft. Rope dynamometer equipped with weighing pan, spring balance (2.5-gram accuracy), and pulley are used for applying the load to Savonius rotor shaft. Nylon string of 1 mm diameter is wound around the rotor shaft and connected to a weighing pan and spring balance by means of three pulleys attached to the structure. A digital tachometer (Pyle make) is used to measure the RPM of the shaft with the help of a reflector attached to the shaft.
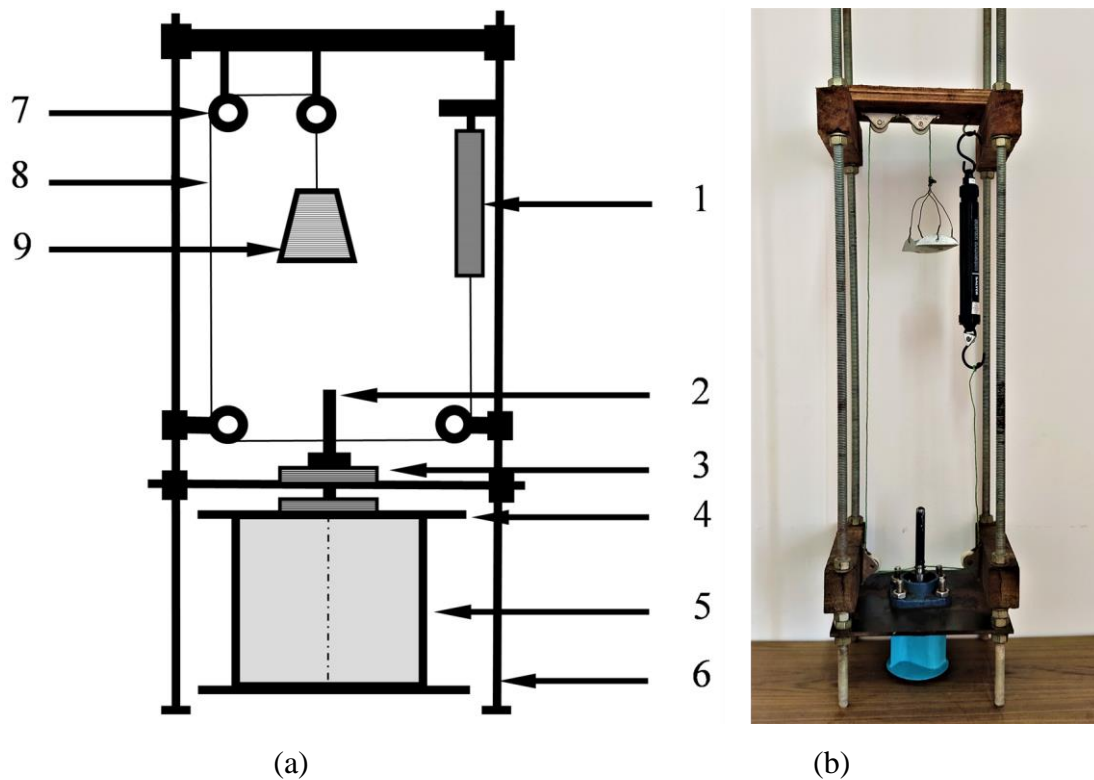
Figure 3.12 (a) Schematic of experimental setup and (b) pictorial view of experimental test rig

1. Spring balance, **2.** Shaft, **3.** Flange bearing, **4.** Endplates, **5.** V-shaped rotor blade,

6. Supporting structure, **7.** Pulley, **8.** Rope, **9.** Weighing pan.

Figures 3.13 (a and b) show the schematic and photograph of a multipurpose tilting flume having a length, width, and height of 4.75m, 0.215m, and 0.35m, respectively. The sidewalls of the tilting flume are made up of acrylic material. The flume has an inlet and outlet with a collecting tank at its extreme ends. This tilting flume is having a recirculation type of flow employing a two-monoblock pump (SHARP make) of 2.0 HP capacity with a maximum discharge capacity of 0.01544 m^3/s, fixed to the flume bottom structure, and two independent control valves provided for each pump to regulate the discharge. A pre-calibrated rectangular notch attached at the flume outlet has a coefficient of discharge (C_d) of 0.6. The lifting mechanism is employed by two screw threads placed at the inlet and outlet side of the tilting flume, which can give a slope of ±2° with an increment of 0.5. The photograph of a side view and front view of the experimental setup in a multipurpose tilting flume with height gauge are shown in Figures 3.13 (c, d, and e).
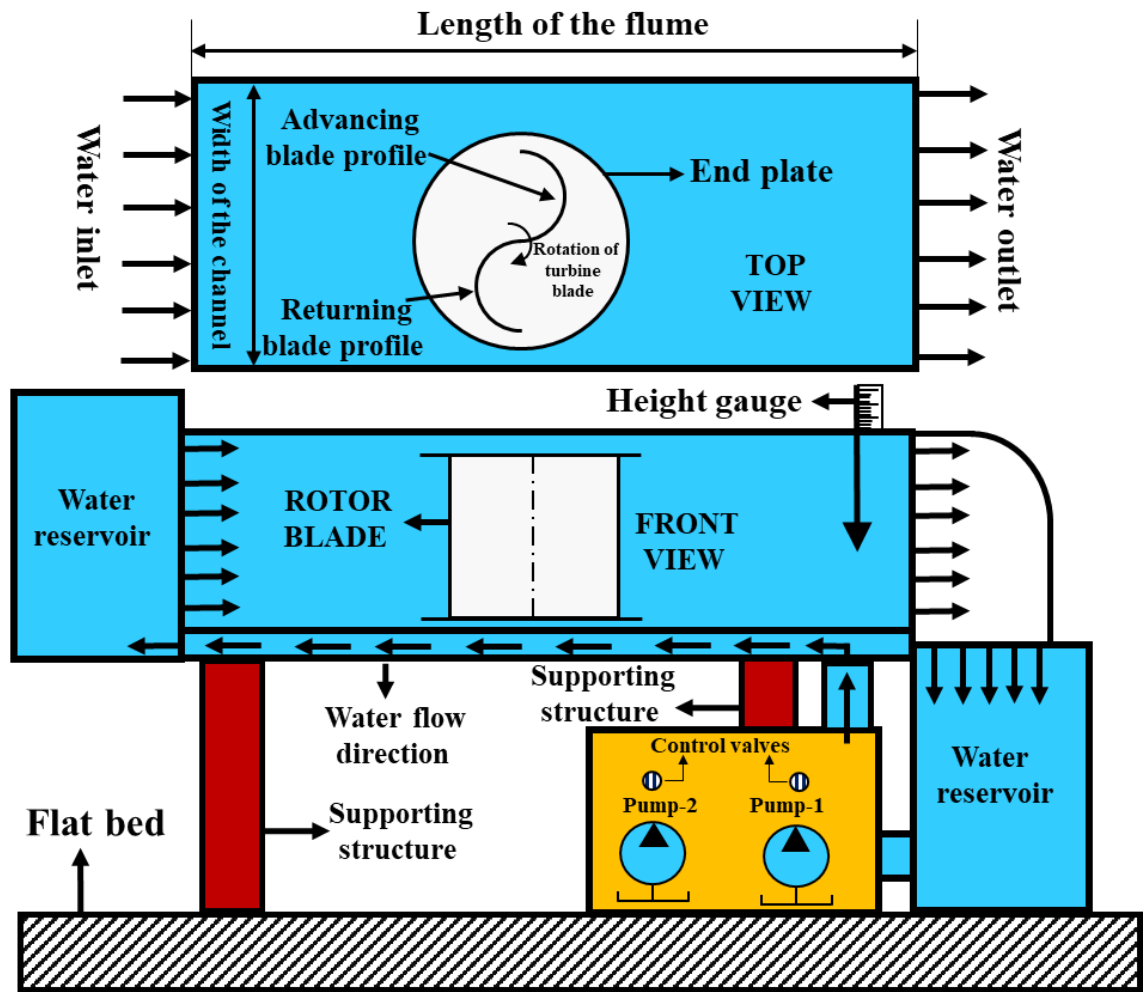
(a) Schematic of multipurpose tilting flume with rotor test rig
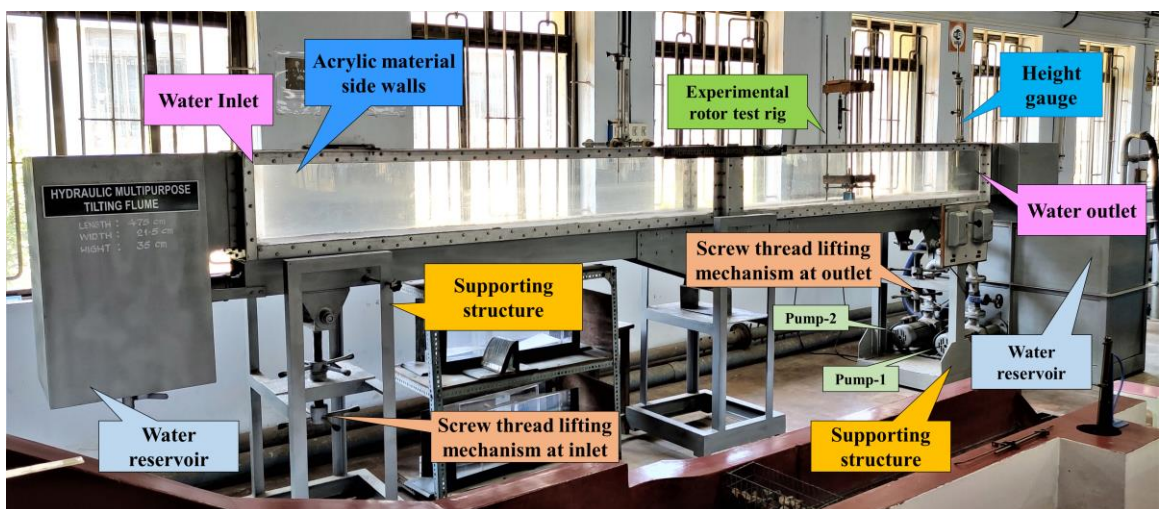
(b) Photograph of multipurpose tilting flume with rotor test rig

| (c) | (d) | (e) |

Figure 3.13 (a) Schematic and (b) photograph of multipurpose tilting flume with (c) rotor test rig in side view and (d) front view with (e) height gauge for the modified Savonius hydrokinetic turbine blade with varying bed slopes

3.7 Numerical methodology for conventional and tapered Savonius turbine blades

3.7.1 Three-dimensional computational domain and meshing for сonventional and tapered turbine blades

Figures 3.14 (a-f) shows the three-dimensional geometric model for conventional and tapered turbine blades created using ANSYS design modeler. The essential geometric parameters are diameter (D_r), height of the turbine blade (H_R), top and bottom endplates (D_{ep}) for conventional turbine blade (Figures 3.14 (a-b)) with front and side views. The tapered turbine (Figures 3.14 (c-d)) blade consists of varying diameters from the top portion to the bottom portion of the rotor blade with front and side views. The top and bottom diameters of the turbine are represented as D_{Top}, D_{Bottom}, and the two endplates are fitted at the top and bottom side of the turbine blade, and its dimension is considered as $1.1D_{Top}$ for both top and bottom endplates. Figure 3.14 (e and f) shows the isometric view of the conventional and tapered turbine blades with all essential geometric parameters.

CONVENTIONAL TURBINE BLADE

FRONT VIEW

Diameter of the turbine (D_Top)

d_T d_T

Thickness of rotor blade (t)

Returning blade   Advancing blade

d_B d_B

Diameter of the turbine (D_Bottom)

Diameter of the end plate (D_ep)

SIDE VIEW

Thickness of the plate (t)

Top and bottom end plates

Height of the turbine (H_R)

Thickness of the plate (t)

Diameter of the end plate (D_ep)

(a)   (b)

TAPERED TURBINE BLADE

FRONT VIEW

Top diameter of the turbine (D_Top)

d_T d_T

Thickness of rotor blade (t)

5°

Returning blade   Advancing blade

5°

Thickness of the plate (t)

d_B d_B

Bottom diameter of the turbine (D_Bottom)

Diameter of the end plate (D_ep)

SIDE VIEW

Thickness of the plate (t)

5°

Top and bottom end plates

Height of the turbine (H_R)

Thickness of the plate (t)

Diameter of the end plate (D_ep)

(c)   (d)

Figure 3.14 Three dimensional geometric models of conventional (a, b and e) and tapered (c, d, and f) turbine blade with different views (front, side, and isometric views)

3.7.2 Computational domain with boundary conditions

The flow field around the Savonius hydrokinetic turbine blade profile is time-dependent and complex due to flow separation and wake creation. For solving fluid flow problems around the Savonius hydrokinetic turbines, CFD analysis is a powerful tool in the present scenario (Talukdar et al. 2018). Earlier CFD simulations using 2D and 3D approaches show a significant advantage to investigate the flow behavior of blade profile, 2D simulations were preferred more in symmetrical modelling with respect to the rotational axis, which simplifies the complexity of modelling and reduces computational time. Whereas 3D simulations will increase the computational time, but it also increases the accuracy of the results by analyzing the blade profile three-dimensionally, which is more similar to the practical application (Mereu et al. 2017; Ostos et al. 2019a; b; Shaheen and Abdallah 2016; Talukdar et al. 2018; Tian et al. 2018; Zhang et al. 2017a).

Mereu et al. 2017 and Shaheen and Abdallah 2016 extended the 2D numerical analysis to study the wake generated on a series of Savonius turbines placed in a different order

in the form of a farm approach due to its simplicity the analysis. In the present investigation, conventional and tapered turbine blades were modelled and CFD analysis were carried out for both the turbines. The tapered Savonius hydrokinetic turbine is symmetrical along the rotational axis, but there was a change in the blade profile and the turbine's height. The sectional plane of advancing and returning profile enlarges as height increases, hence the axis of the centre point of curved profile changes with height of the turbine. These changes in blade profile increases the complexity of the turbine and demands 3D analysis for a reliable solution. The 3D analysis also enhances the study of drag and variation of pressure with respect to vertical direction of the turbine blade, which is not possible in 2D simulations with respect to tapered blades. ANSYS Fluent 14.5 is used for modelling and simulations of tapered and conventional turbines here.

Figures 3.15 (a and b) show the three-dimensional domain along with a turbine blade in the irrigation channel and various boundary conditions used for CFD analysis. The dimension of the computational domain is 103.6 mm (Depth of water = H_W) $\times$ 612 mm (Length of the computational domain) $\times$ 215 mm (width of the domain). The computational domain is categorized into two important regions: the rotating zone (turbine blade) and a fixed zone (irrigation channel). The turbine blade is placed precisely at the center of the domain and rotating zone created to the turbine blade, and the dimension of the rotating zone is 1.5 times the turbine blade diameter ($1.5D_r$) based on the previous investigation carried out by various researchers for similar Savonius turbine blades (Kumar and Saini 2017b; a; Saini and Saini 2018, 2020). Figure 3.15(c) shows a turbine blade in a rotating zone with all-important geometric parameters. The distance between the front and rear face of the computational domain from the turbine blade is three times the diameter of the turbine blade ($3D_r$) (Sarma, N. K. Biswas and Misra 2014). The various important dimensions of the computational domains are presented in Table 3.6.

Table 3.6 Important dimensions of the three-dimensional computational domain.

Sl. No	Parameter	Values
1.	Length of the domain (mm)	612
2.	Width of the domain (mm)	215
3.	Diameter of the rotating zone (mm)	$1.5D_r$
4.	Depth of water (H_w) (mm)	103.6
5.	The velocity of water (V_W) (m/s)	0.5
6.	Diameter of the conventional turbine blade $D_r= (D_{Top}=D_{Bottom})$ (mm)	72
7.	Effective diameter of the tapered turbine blade $D_r= (D_{Top}+D_{Bottom})/2$ ($D_{Top}= 72$ mm, $D_{Bottom}=60$ mm)	66
8.	Endplate diameter of the turbine (D_{ep}) (mm)	$1.1D_r$
9.	Position of the turbine blade from front face (Velocity inlet) (mm)	$3D_r$
10.	Position of the turbine blade from rear face (Pressure outlet) (mm)	$3D_r$
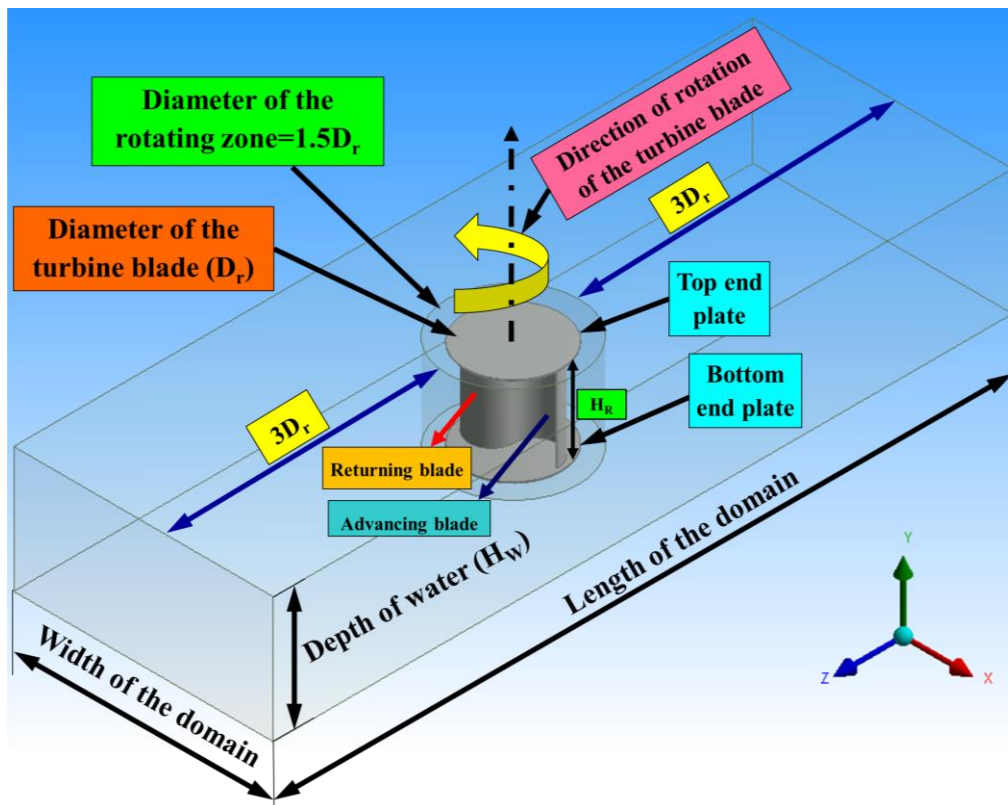
(a)
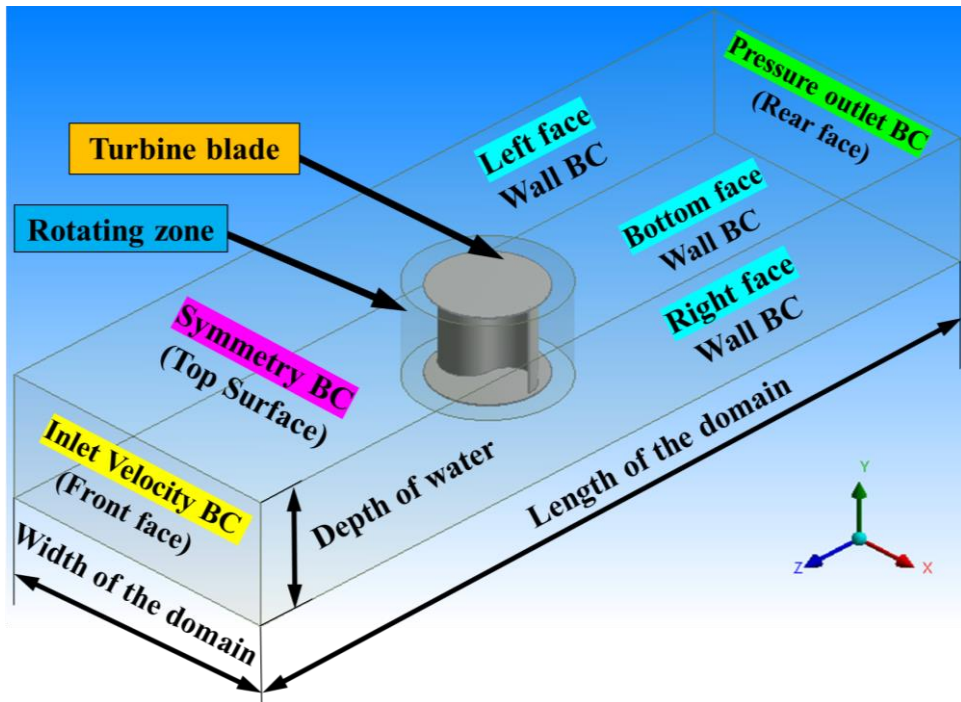
(b)
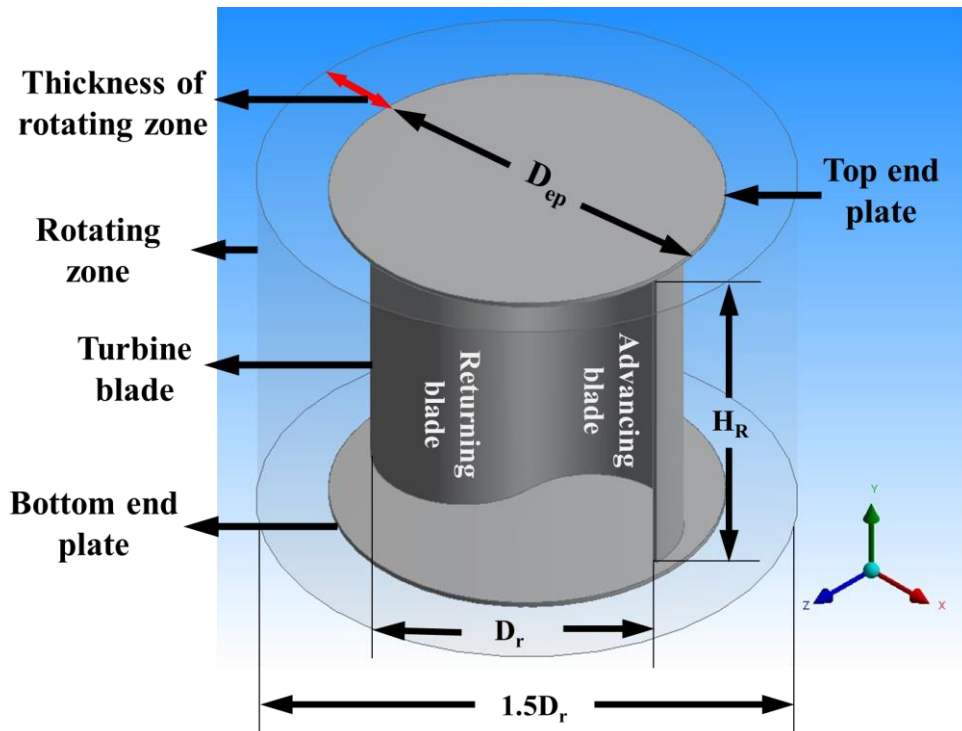
(c)

Figure 3.15 (a) Three-dimensional computational domain with various geometric dimensions, (b) computational domain with various boundary conditions, and (c) turbine blade in rotating zone

3.7.3 Meshing and boundary conditions

The computational domain created using ANSYS design modeler is imported to ANSYS workbench for the meshing of the computational domain with a turbine blade in a rotating zone. The tetrahedral mesh was created by means of patch conforming method. The fine mesh elements designated for the rotating zone to capture more physics and study the flow field around the turbine blade and coarse mesh applied for the fixed region (irrigation channel) are shown in Figures 3.16 (a and b). The inflation layer is given to the turbine blade profile to study the effect of the boundary layer with a first-layer thickness of 0.04 mm, and maximum layers of 8 with a growth rate of 1.2 is shown in Figures 3.16 (c) and non-dimensional y^+ value maintained for the present simulation is less than 1. This is important when using the SST k-ω model to simulate the high separation rates and adverse pressure gradients across the blades. Therefore, the flow is solved at the wall limits of the blades to estimate the dimensionless velocity as a linear function of y^+. Due to higher value of y^+ simulation accuracy is reduced because the specified ANSYS wall functions are unresolved by the flow of the boundary layer (Mosbahi et al. 2019, 2020a; Talukdar et al. 2018).

The various boundary conditions assigned to the computational domain for CFD analysis are velocity inlet (0.5 m/s) for the front face of the domain and pressure outlet boundary condition (Zero-gauge pressure) for the rear face of the domain. The bottom, left, and right faces of the domain are considered as a slip boundary condition (shear rate equal to zero). The top surface of the domain considered as a symmetry boundary condition based on the previous investigation carried out by various researchers for a similar Savonius hydrokinetic turbine study using water as a working medium (Elbatran et al. 2017; Kumar and Saini 2017b; a; Saini and Saini 2020; Sarma, N. K. Biswas and Misra 2014). The various boundary conditions used for the present simulation are presented in Table 3.7. For the turbine blade, the wall boundary condition applied (no-slip) and angular velocity (ω) applied to the rotating zone based on the TSR ranging from 0.7 to 1.3.
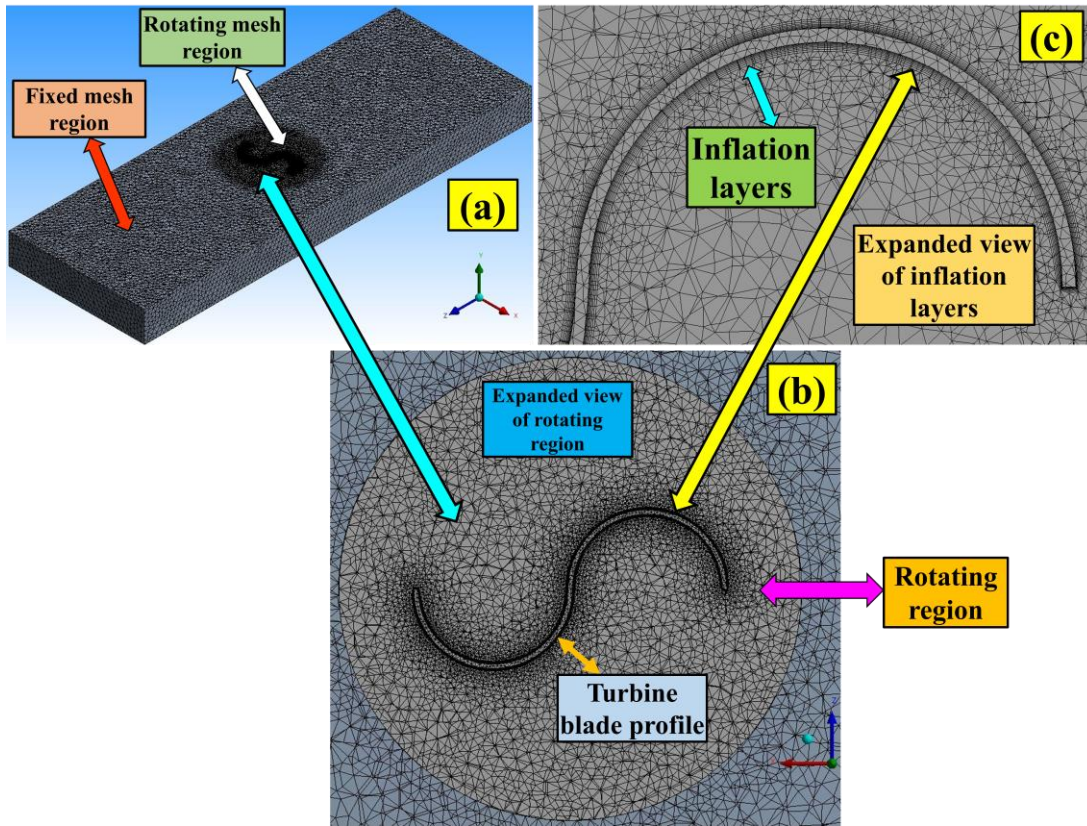
Figure 3.16 (a) Meshing of the three-dimensional computational domain, (b) turbine blade in the rotating zone, and (c) expanded view of inflation layers

Table 3.7 Various boundary conditions used in CFD simulation

Sl. No	Faces of the computational domain	Type of boundary	Boundary conditions
1.	Front face	Velocity BC	0.5 m/s
2.	Rear face	Pressure BC	Zero-gauge pressure
3.	Left face	Wall	No-Slip BC
4.	Right face	Wall	
5.	Bottom face	Wall	
6.	Top face	Symmetry	Symmetry
7.	Turbine blade	Wall BC (No-slip)	Angular velocity is given to the rotating zone base on TSR (0.7-1.3)

3.7.4 Grid and time dependency study

The CFD simulation was carried out for mesh elements 1849928, 1904296, 1987751, 2074273, and 2165798. As the number of mesh elements increases from 1849928 to 1904296, there is a change in the value of C_T with respect to TSR. Similarly, from 1904296 to 1987751, the difference in the value of C_T decreased, and with the increase in the number of mesh elements from 1987751 to 2074273 and 2165798, the change in the value of C_T is negligible. Therefore, mesh elements 1987751 are considered as a baseline and as an optimum number of mesh elements for the present simulation to reduce the computational time. The variation of C_T with respect to element size at a different angle of rotation (θ) of the turbine blade is shown in Figure 3.17 (a).

Similarly, by taking the optimum number of mesh elements of 1987751, time-dependent analysis was carried out to find out the optimum time step. Since the present CFD simulation is the unsteady case, the optimum timestep size is essential for the calculation of C_T by using the optimum number of mesh elements of 1987751. The variation of C_T with respect to the number of mesh elements and quality of the mesh is expressed in terms of orthogonality, aspect ratio, skewness, and element quality are presented in Table 3.8. Based on the Richardson extrapolation method (Boache 1994), the GCI value obtained is 0.293. The percentage deviation of the obtained value with the grid-independent value for 1987751 mesh elements is 2.36%.

To compute optimum timestep size, the three-dimensional CFD simulations were carried out using various time steps such as 10°, 5°, 2.5°,1°, and 0.5°, respectively. For the time step of 10°, 5°, and 2.5° there is a difference in the value of C_T with respect to TSR and for 1° and 0.5° there is no change in the value of C_T. Therefore, the time step of 1° is considered an optimum time step and reduces computational time. The variation of C_T with respect to time step from 10°, 5°, 2.5°,1°, and 0.5° respectively shown in Figure 3.17 (d). A similar optimum time step of 1° is considered for CFD simulation of Savonius turbines by various researchers (Elbatran et al. 2017; Eshagh et al. 2020; Mosbahi et al. 2019, 2020a; Talukdar et al. 2018; Zhang et al. 2019). The calculation of time step size with respect to TSR is explained in the TSS calculation section for 0.7 TSR, and CFD details are explained in Table 3.9. The values of time step size for

conventional and tapered turbine blades for 0.5 m/s inlet velocity of water for a TSR range of 0.7–1.3 with an increment of 0.1 are shown in Tables 3.10 and 3.11.

Table 3.8 Variation of C_T with respect to the number of mesh elements, mesh quality and percentage difference

Number of mesh elements	Quality of mesh				C_T	Percentage error (%)
	Average Orthogonality	Skewness	Aspect ratio	Element quality		
1849928	0.88113	0.21178	4.6878	0.6701	0.2993	0.066
1904296	0.88068	0.21193	4.6203	0.67399	0.2995	0.16
1987751	0.88164	0.20953	4.523	0.6767	0.3000	0.033
2074273	0.88082	0.21153	4.4528	0.67926	0.3001	0
2165798	0.88117	0.21052	4.3691	0.6826	0.3001	--
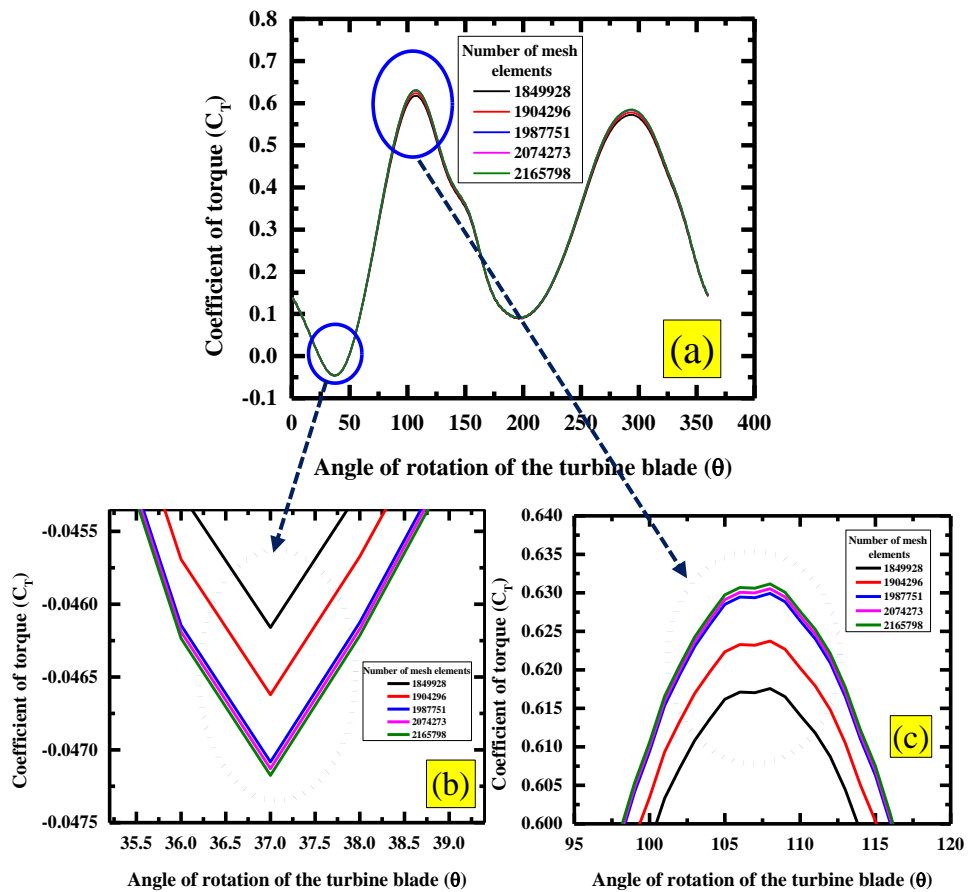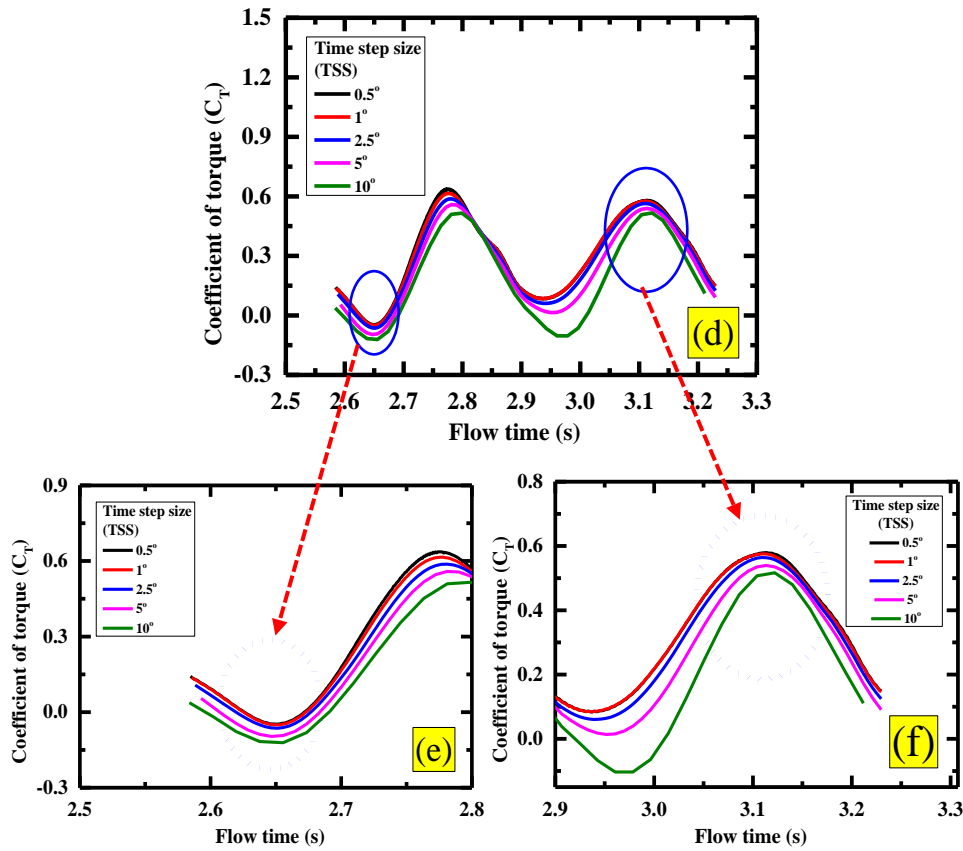
Figure 3.17 (a) Variation of C_T with respect to the number of mesh elements, (b) expanded view of $C_{T\,min}$, (c) expanded view of C_{Tmax}, (d) variation of C_T with respect to flow time for varying time steps, (e) expanded view of C_{Tmin} for varying time step (f) expanded view of C_{Tmax} for varying time steps (0.5°, 1, 2.5, 5 and 10°)

Table 3.9 Details of the CFD simulation using Sliding mesh technique

Sl. No	Performance parameter	Details
1.	The total number of revolutions have given to the turbine blade during CFD simulations	05
2.	Computation of C_T	The average value of C_T for last one complete revolution of the rotor blade
3.	Computation of C_P	TSR×C_T
4.	Total number of rotor blades	02 (Conventional and tapered turbine blades)
5.	TSR range	0.7-1.3 TSR with an increment of 0.1,

		Total 7 TSR
6.	Total number of CFD simulations	Number of rotor blades × TSR range (0.7-1.3) = 2*7= 14
7.	Optimum time step size (TSS) from time step study	1° in each time step
8.	Total number of time steps in each revolution	360-time steps
9.	Total time steps in each simulation with respect to TSR	360*5= 1800

Table 3.10 Time step values for a conventional turbine with respect to TSR (0.7-1.3)

Sl. No	Time step values for conventional turbine blade for AR=1.0, OR=0.0 and V_W=0.5 m/s			
	Velocity of water (V_W) m/s	TSR	Conventional turbine blade (Timestep size) (s)	Flow time
1.	0.5	0.7	0.001794286	3.230
2.	0.5	0.8	0.00157	2.826
3.	0.5	0.9	0.001395556	2.512
4.	0.5	1	0.001256	2.261
5.	0.5	1.1	0.001141818	2.055
6.	0.5	1.2	0.001046667	1.884
7.	0.5	1.3	0.000966154	1.739

Table 3.11 Time step values for a tapered turbine with respect to TSR (0.7-1.3)

Sl. No	Time step values for tapered turbine blade for AR=1.0, OR=0.0 and V_W=0.5 m/s			
	Velocity of water (V_W) m/s	TSR	Tapered turbine blade (Timestep size) (s)	Flow time
1.	0.5	0.7	0.001644762	2.96
2.	0.5	0.8	0.001439167	2.59
3.	0.5	0.9	0.001279259	2.30
4.	0.5	1	0.001151333	2.07
5.	0.5	1.1	0.001046667	1.88
6.	0.5	1.2	0.000959444	1.73
7.	0.5	1.3	0.000885641	1.59

3.7.5 Governing equations

The governing equations (3.1 to 3.5) for the unsteady, viscous, and incompressible turbulent flow are the Navier-Stokes equations, which can be written in the following form.

Continuity equation

$$\frac{\partial(u_i)}{\partial x_i} = 0 \tag{3.1}$$

Momentum equation

$$\rho_W \left(\frac{\partial u_i}{\partial t} + \frac{\partial(u_i u_i)}{\partial x_i} \right) = -\frac{\partial p}{\partial x_i} + \frac{\partial}{\partial x_i}\left(-\rho_W \overline{u_i' u_j'} \right) + \frac{\partial}{\partial x_i}\left[\mu_W \left(\frac{\partial u_i}{\partial x_j} + \frac{\partial u_j}{\partial x_i} \right) \right]$$

Where $\left(-\rho_W \overline{u_i' u_j'} \right) =$ **Reynolds stress term** $\tag{3.2}$

$$\left(-\rho_W \overline{u_i' u_j'} \right) = \mu_t \left(\frac{\partial u_i}{\partial x_j} + \frac{\partial u_j}{\partial x_i} \right) - \frac{2}{3}(pk)\delta_{ij} \tag{3.3}$$

The SST turbulent model expressed in the mathematical form:

$$\frac{\partial(pk)}{\partial t} + \frac{\partial}{\partial x_i}(pku_i) = \frac{\partial}{\partial x_j}\left(\Gamma_k \frac{\partial k}{\partial x_j} \right) + G_k - Y_k \tag{3.4}$$

$$\frac{\partial(p\omega)}{\partial t} + \frac{\partial}{\partial x_i}(p\omega u_i) = \frac{\partial}{\partial x_j}\left(\Gamma_k \frac{\partial \omega}{\partial x_j} \right) + G_\omega - Y_\omega + D_\omega \tag{3.5}$$

In the previous equations, $u_i = (u, v, w)$ are the velocity components in the directions of $x_i = (x, y, z)$, ρ_w is the density of water in kg/m^3, ω represents specific turbulence dissipation, μ_w represents the dynamic viscosity of water in (kg/m .s) , k is the turbulence kinetic energy. Γ_k and Γ_ω are the effective diffusivity for k and ω. G_k is the generation of turbulence kinetic energy due to mean velocity gradients, and G_ω represents the generation of ω. Y_k and Y_ω represents the dissipation of k and ω due to turbulence, while D_ω is the cross-diffusion term.

3.7.6 Selection of the turbulence model

Various turbulence models available are based on the Reynolds number (Re) and configuration of the turbine blade to simulate the flow, such as Spalart–Allmaras model (1-equation), Realizable k-ε model, RNG k-ε model, standard k-ω model (Talukdar et al. 2018), standard k-ε model and SST k-ω model can be used for the simulation of a turbine blade. The standard k-ε model is a simple turbulence model and is more appropriate for the computation of turbulent flow. This model provides better findings than Spalart–Allmaras in turbine blade simulation studies (Talukdar et al. 2018).

Furthermore, it is found that both the realizable model and the RNG k-ε model have predicted significantly better results as compared to standard k-ε and Spalart–Allmaras model (Talukdar et al. 2018). The SST k-ω turbulence model is a two-equation eddy viscosity model that integrates the benefits of both k-ε and k-ω formulation for free stream flow and rotor blade boundary layer. It is also exhibiting smaller resistance to free stream conditions as compared to other turbulence models. The SST k-ω model is utilized around the flow field because it is well suitable for simulating flow in the viscous sublayer wherever greater accuracy is required at the boundary layer. The SST k-ω model) captures an extensive flow, such as flow with adverse pressure gradients, flow over airfoils, rotating flows, and low Reynolds number (Re) flow. It has already been used extensively in similar studies by various researchers (Kacprzak et al. 2013; Mereu et al. 2017; Roy and Ducoin 2016; Shaheen et al. 2015; Talukdar et al. 2018). Hence, the unsteady SST k-ω turbulence model is used for three-dimensional CFD simulation in this study.

3.7.7 Simulation procedure

The three-dimensional meshing of the computational domain and turbine blade in the rotating zone is exported to ANSYS Fluent 14.5 software for the evaluation of various performance parameters such as C_T and C_P using unsteady sliding mesh technique, and a similar method was used for unsteady computational fluid dynamics (CFD) simulation of Savonius turbine blades by various researchers (Selection of turbulence model explained in chapter 3, section 3.13).

The working fluid taken for the present CFD simulation is water, and it is designated from the ANSYS Fluent 14.5 database. In the cell zone condition section, angular velocity (ω) is applied to the rotating zone with respect to TSR ranging from 0.7 to 1.3 and fixed zone considered an irrigation channel. The boundary conditions used in the present simulation are inlet velocity (V_w) of 0.5 m/s for the front face, pressure outlet (zero-gauge pressure) to the rear face, and left, right, and bottom face of the domain deliberated as a slip boundary condition. Similarly, the top surface of the domain is considered as a symmetry boundary condition based on previous CFD investigation performed by various researchers for similar 3D CFD simulations using Savonius hydrokinetic turbines (Ghosh et al. 2015; Kumar and Saini 2017b; a; Mosbahi et al. 2019, 2020a; Sarma, N. K. Biswas and Misra 2014).

The reference values essential for the estimation of C_T and C_P of the turbine blade are area of the turbine ($A_R = H_R D_r$), density of water (ρ_w=998 kg/m^3), the viscosity of water (μ_w) and radius of the turbine blade ($D_r/2$) are computed from velocity inlet. A SIMPLE scheme was chosen for the pressure velocity couplings (Kumar and Saini 2017b; a; Sarma, N. K. Biswas and Misra 2014; Talukdar et al. 2018), for spatial discretization, least-squares cell-based approach is applied, and 2nd order selected for pressure. The 2 nd order upwind scheme assigned for momentum, turbulent kinetic energy, specific dissipation rate (Kumar and Saini 2017a; b), and finally, 1st order implicit is given for time-dependent formulation to reduce the computational time (ANSYS FLUENT 14.5 User's Guide 2013). The value of 10^{-6} was given for the convergence criteria for the estimation of continuity, momentum, and turbulence equations (Mosbahi et al. 2020a; b; Zhao et al. 2020) . Standard initialization was taken and computed from the inlet velocity, and the absolute reference frame was specified. For the calculations of C_T and C_P, an optimal time step of 1° is given (the turbine blade rotates 1° in each time step and method to evaluate the time step size is explained in chapter 3, section 3.16), and it is evaluated based on the angular velocity (ω) of the turbine blade with respect to TSR (0.7–1.3). In the present CFD simulation, five revolutions are given to the turbine blade, and 360-time steps in each revolution and total of 1800 timesteps for five revolutions of the turbine blade, and the value of C_T was calculated by taking the average value of C_T for the last one revolution of the turbine blade. A similar procedure

was applied for all the TSR ranging from 0.7 to 1.3. In the present CFD investigation, two turbine blades were used (conventional and tapered), and 14 simulations were carried out to calculate C_T and C_P with respect to TSR (0.7–1.3).

3.8 Numerical methodology for the development of novel V-shaped blade (V_1-V_5)

3.8.1 Three-dimensional geometric modeling

Figures 3.18 (a-c) show the three-dimensional geometric models created using ANSYS design software. The various important geometric parameters such as height (H_R), diameter (D_r), thickness (t) (top plate, bottom plate, and turbine blade), and endplate diameter of the turbine (D_{ep}) (top and bottom) are also shown in the Figures 3.18 (a-c).

(a)   (b)

(c)
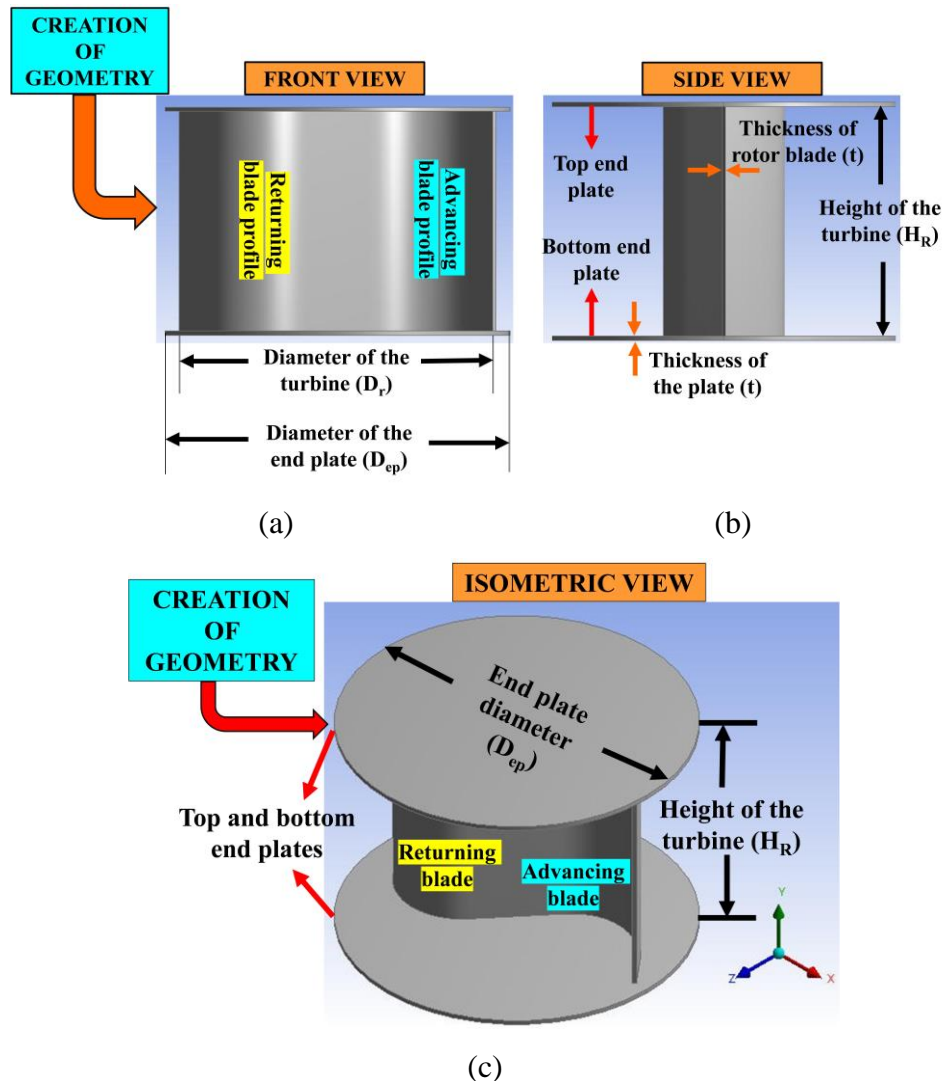
Figure 3.18 Three-dimensional rotor blade (a) front view (b) side view (c) isometric view with all-important geometric parameters

3.9 Modified V-shaped turbine blade with different overlap ratios (OR) ranging from 0.0-0.3 with an increment of 0.05 and with different V-angle (V$_{90°-40°}$)

Figures 3.19 (a-h) shows the three-dimensional geometric model created using ANSYS design modelling software. The three-dimensional modified V-shaped turbine blade in different views such as top, front, side, and isometric views for without and with overlap ratios (OR), respectively. The various geometric parameters such as diameter of the turbine (D$_T$) and endplate (D$_{ep}$), thickness of the turbine (t), and advancing and returning bucket diameter of the turbine blade (d) shown in Figures 3.19 (a-h). The aspect ratio (AR) of the turbine blade maintained in the present simulation is 0.7 for without and with an overlap ratio case based on the previous investigation carried out by various researchers using Savonius hydrokinetic turbines (Golecha et al. 2011, 2012; Kailash et al. 2012; Sarma, N. K. Biswas and Misra 2014).

(a)　　　　　　　　　　　　　　(b)

(c)　　　　　　　　　　　　　　(d)
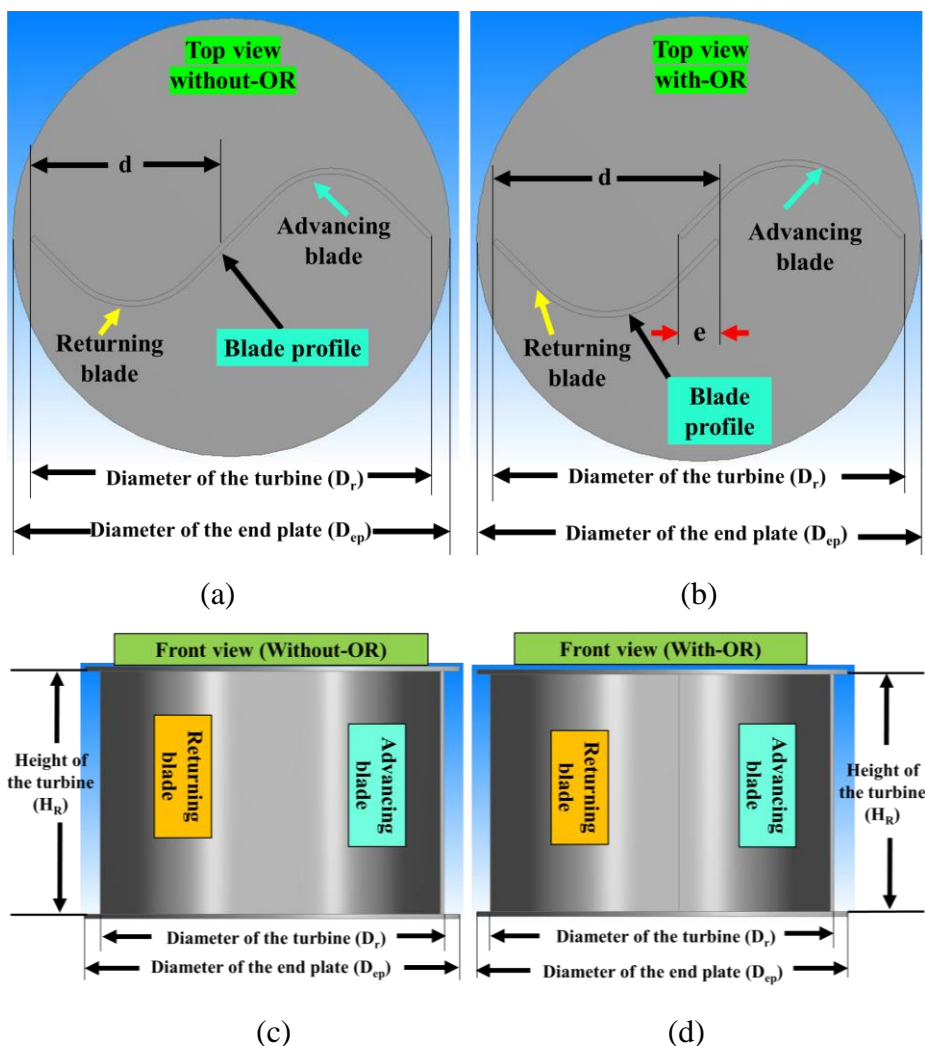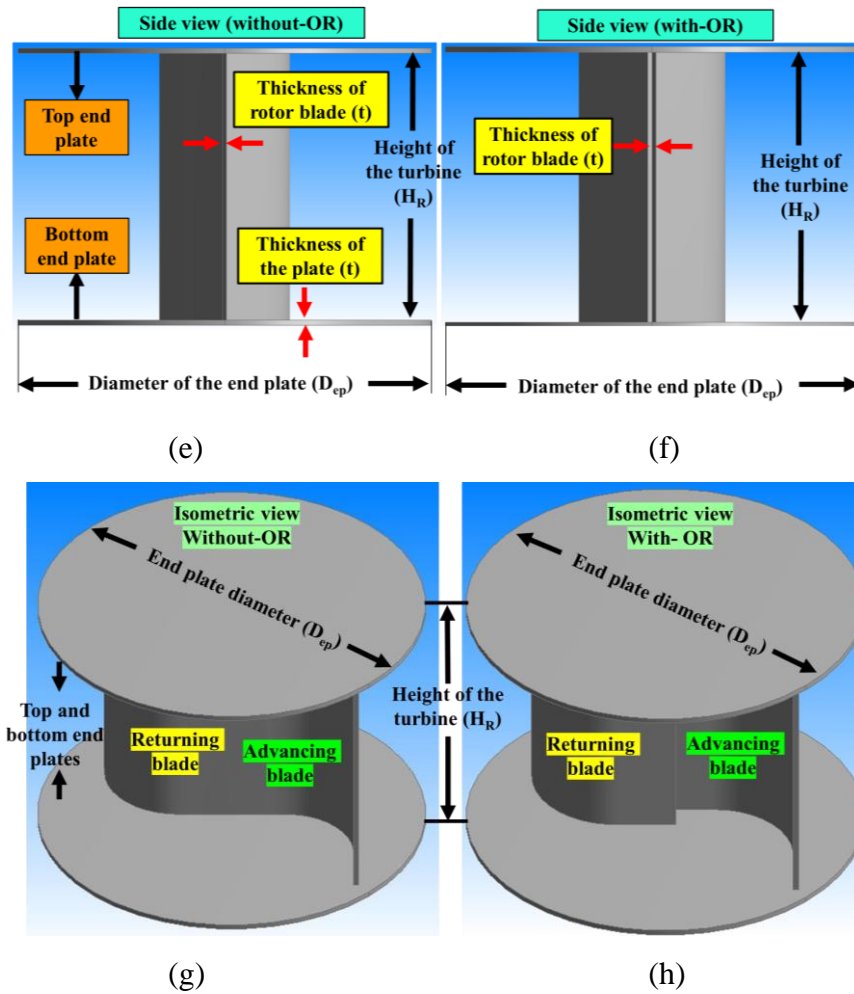
Figure 3.19 (a-h) 3-D modified V-shaped rotor blade with and without OR

Figure 3.20 (a) illustrates the three-dimensional computational domain equivalent to irrigation channel modelled using ANSYS design software. The computational domain is having two zones one is a rotating zone, and the second one is a stationary zone. The rotating zone is created by using an enclosure with a cushion radius of 14.4 mm, i.e., 1.5 times the diameter of the turbine blade (Kumar and Saini 2017a; b; Saini and Saini 2018) as shown in Figure 3.20 (b). Similarly, a stationary zone (rectangular domain) was made using the enclosure with a non-uniform cushion on the rotor blade and rotating zones. The interface created between the rotating zone and stationary zone using boolean operation. The rotor blade is placed at a distance of three times the diameter of the turbine blade from the front and rear faces of the computational domain (Sarma, N. K. Biswas and Misra 2014).
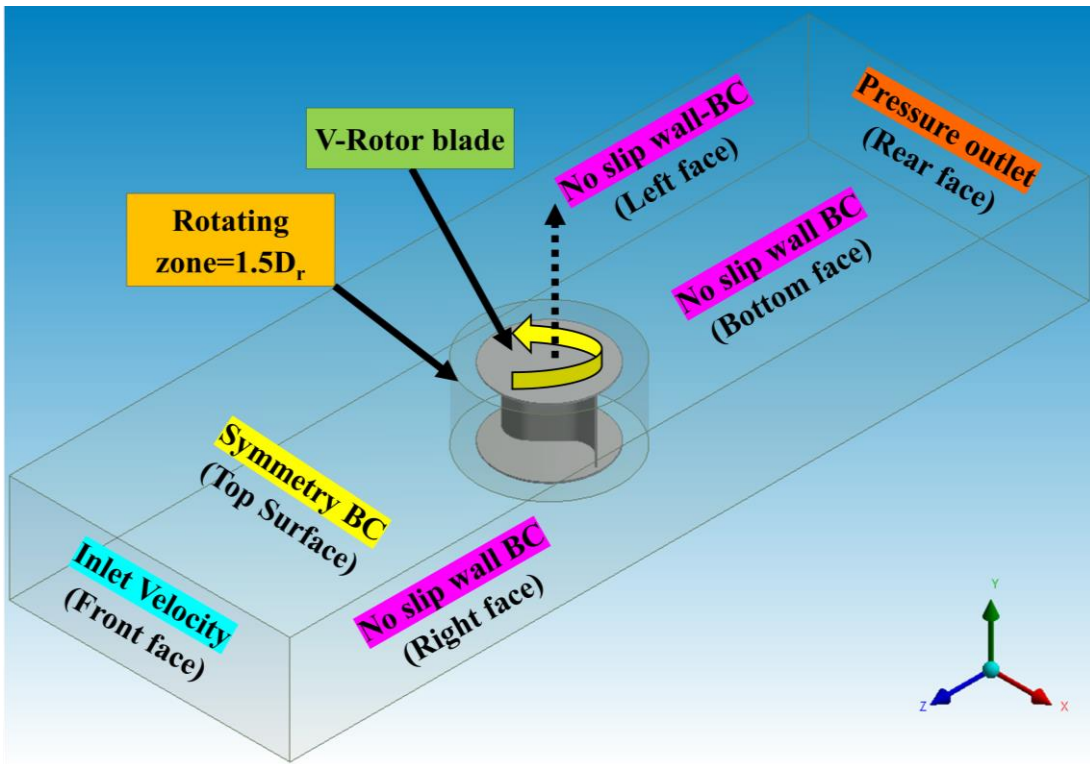
(a)
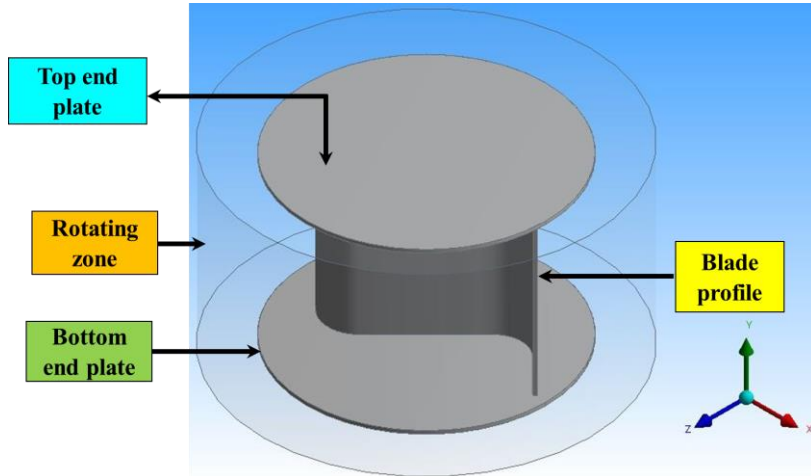
(b)

Figure 3.20 (a) Three-dimensional computational domain and (b) rotating zone

3.9.1 Meshing of computational domain and boundary conditions

The geometric model developed using ANSYS design modeling software is imported into ANSYS meshing and tetrahedral mesh is assigned using patch conforming technique. A coarse mesh is applied to the fixed zone and fine mesh to the rotating zone

to study the effect of blade profile and capture the physics during turbine blade rotation. The inflation layer is applied to a turbine blade with a first-layer thickness of 0.00004 m and a growth rate of 1.2 to study the boundary layer effect. The non-dimensional wall distance y^+ value maintained in the present simulation is less than 1. The quality of mesh, such as orthogonality, skewness, and aspect ratio are 0.87256, 0.22099, and 4.1192, respectively, which are within the acceptable and acceptable ranges (ANSYS FLUENT 14.5 User's Guide 2013; Sarma, N. K. Biswas and Misra 2014). The meshing of the outer fixed zone, inner rotating zone, and inflation layer applied to the turbine blade are shown in Figures 3.21 (a-c).

After completing meshing, the various boundary conditions applied to the respected faces of the computational domain. The significant boundary conditions given to the domain are velocity inlet (front face), pressure outlet (rear face), wall boundary conditions (right, left, and bottom face), and top face is considered as symmetry boundary conditions based on the previous investigation carried out by various researchers (Elbatran et al. 2017; Kumar and Saini 2017b; a; Mosbahi et al. 2019, 2020a; Sarma, N. K. Biswas and Misra 2014). The values of boundary conditions used in the present simulation are shown in Table 3.12.
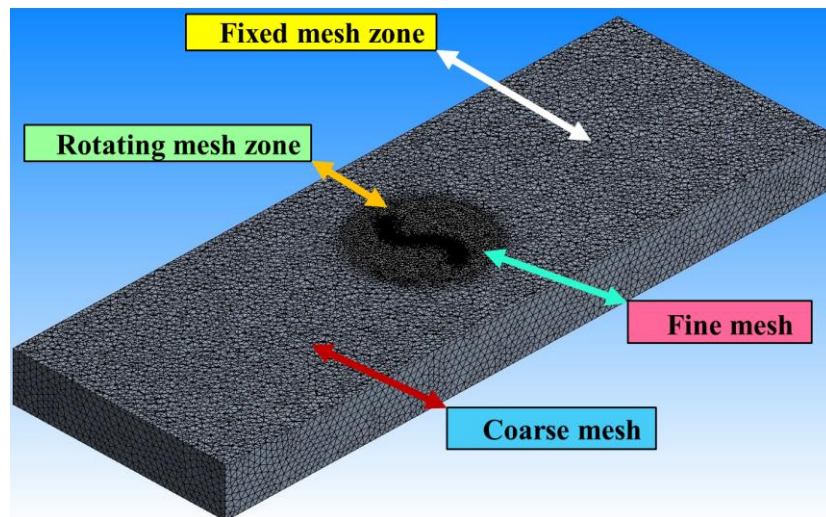
(a)
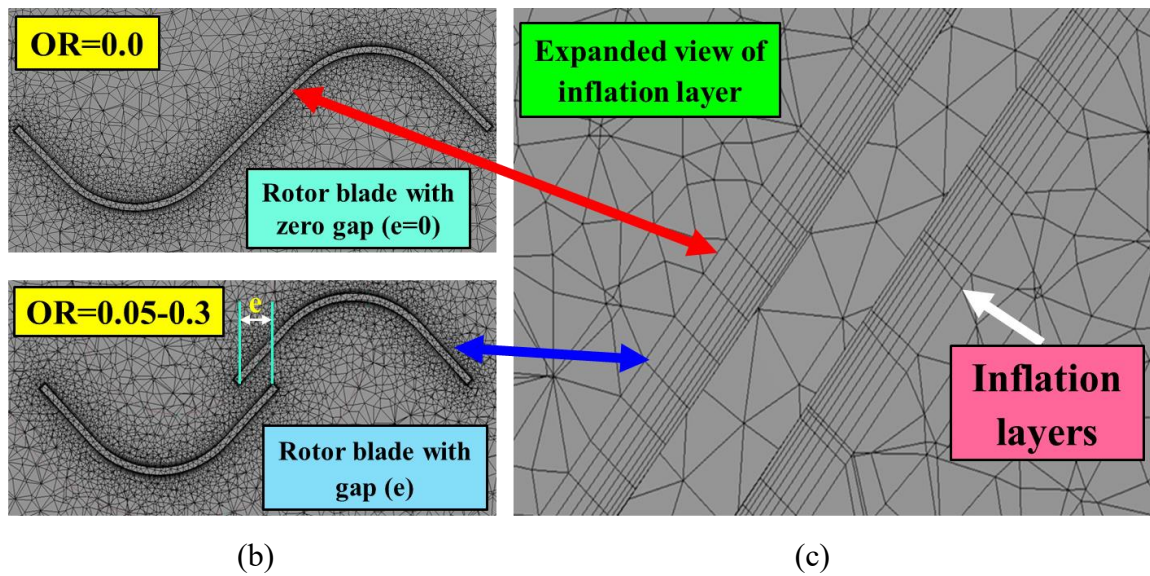
Figure 3.21 (a) Meshing of the computational domain (fixed and rotating zone), (b) turbine blade in a rotating zone, and (c) inflation layers on turbine blade

Table 3.12. Boundary conditions for various faces of the computational domain.

Sl. No	Faces	Boundary condition	Value of boundary conditions
1.	Front face	Velocity inlet BC	0.3090 m/s
2.	Rear face	Pressure outlet BC	Zero pressure gauge
3.	Left, right, and bottom face	Wall BC	No-slip wall BC
4.	Top surface	Symmetry BC	Symmetry BC
5.	Turbine blade	Wall BC (No-slip wall)	Angular velocity (ω) given to rotating zone with respect to TSR

3.9.2 Grid and time dependency study

The impact of a number of mesh elements on rotor blade performance such as, C_P and C_T with respect to TSR were studied using 3-D transient simulations for a V blade with an angle of 90°, with the different number of mesh elements such as 794124, 962432, 1159705, 1250103, 1332064, and 1462049 respectively. There is no significant difference in the value of C_T when the number of mesh elements were increased.

78

Therefore, 1159705 is considered as the ideal number of mesh elements (baseline) to minimize computational time. The variation of C_T with respect to flow time for a various number of mesh elements is shown in Figure 3.22 (a) and the magnified view of maximum $(+C_{Tmax})$ and minimum $(-C_{Tmin})$ values of C_T is shown in Figures 3.22 (b and c). When the number of mesh elements increased from 1159705 to 1462049, the change in the value of C_T is very marginal, hence the lower number of mesh elements of 1159705 is taken as a baseline for the calculation of C_T with respect to TSR with a numerical uncertainty value of 0.103806 %. The quality of mesh selected for the present investigation are under an acceptable level (ANSYS FLUENT 14.5 User's Guide 2013; Balduzzi et al. 2016; Kumar and Saini 2017a; b; Sarma, N. K. Biswas and Misra 2014). All grid dependence study simulations were conducted using a time step size of 1°. The influence of time step size for transient calculations is very significant to optimize the simulation, and a time-dependent study is essential to calculate the optimum time step size. The C_T values are shown in Table 3.13 for a various number of mesh elements.

Table 3.13. Grid independency study for a rotor blade of $V_{90°}$ at 0.7 TSR.

Sl. No	Number of mesh elements	C_T for 0.7 TSR	Numerical error %
1.	794124	0.285	1.041667
2.	962432	0.288	0.242466
3.	**1159705**	**0.2887**	**0.103806 (Base line)**
4.	1250103	0.289	0.110604
5.	1332064	0.28932	0.031098
6.	1462049	0.28941	-------

The three-dimensional transient simulation was performed for an optimum number of mesh elements with 1159705 mesh elements, and performance parameters such as C_T, C_P in relation to TSR were calculated for time steps 15°, 10°, 5°, 2°, 1° and 0.5° respectively (Figure 3.22 (d)). For the time step size of 15° and 10°, the difference in C_T values is higher, and an expanded view of maximum and minimum values of C_T is shown in Figures 3.22 (e and f); likewise, the difference value of C_T at 5° and 2° is slightly lower as presented in Figure, and the difference in the value of C_T is negligible for the time step size of 1° and 0.5° as shown in Figures 3.22 (d, e and f). Therefore, in

order to reduce the computational time, 1° time step is taken as the optimum time step for calculating C_T and C_P with respect to TSR (Elbatran et al. 2017; Tian 2016; Zhang et al. 2017b; a, 2019).
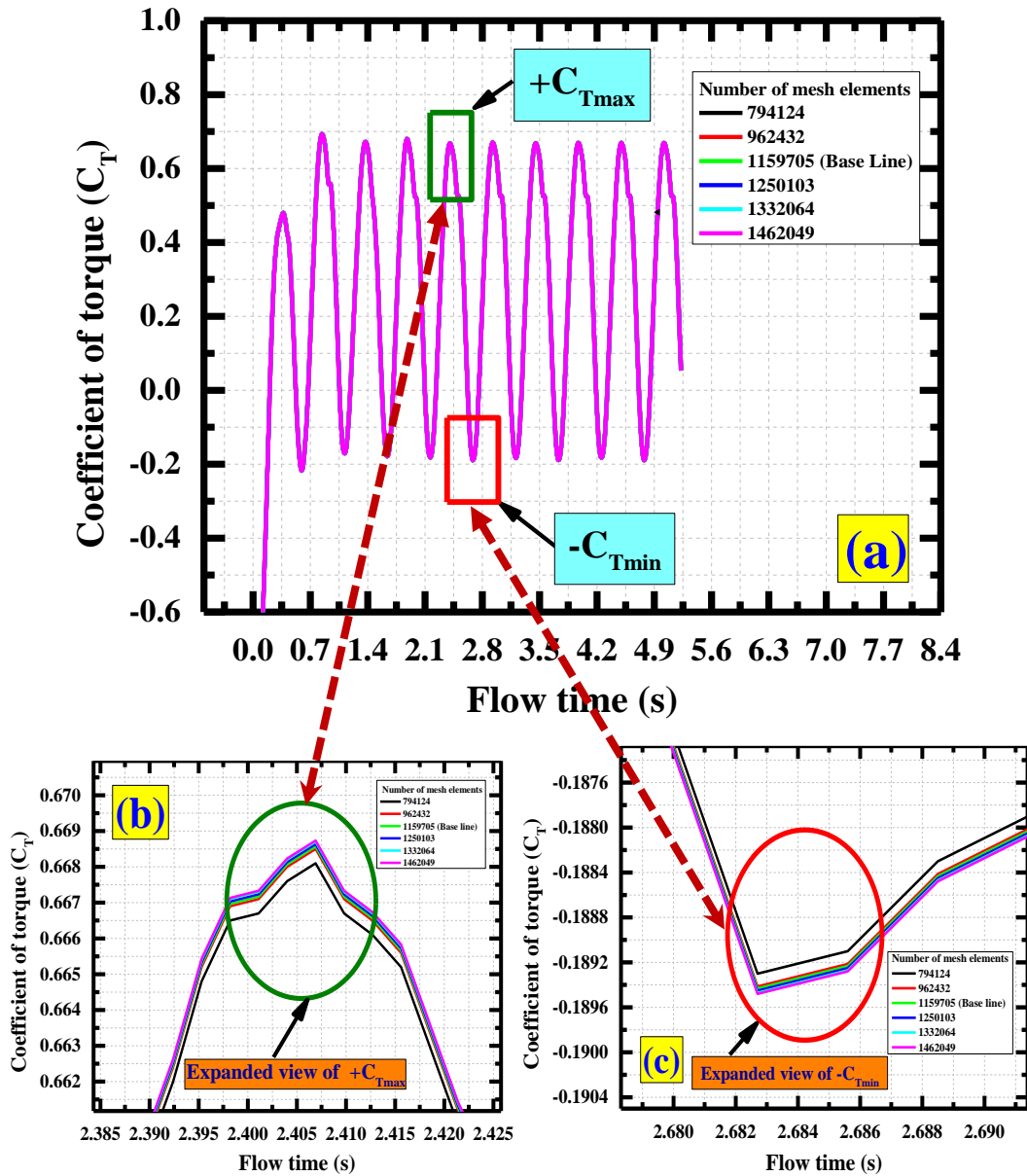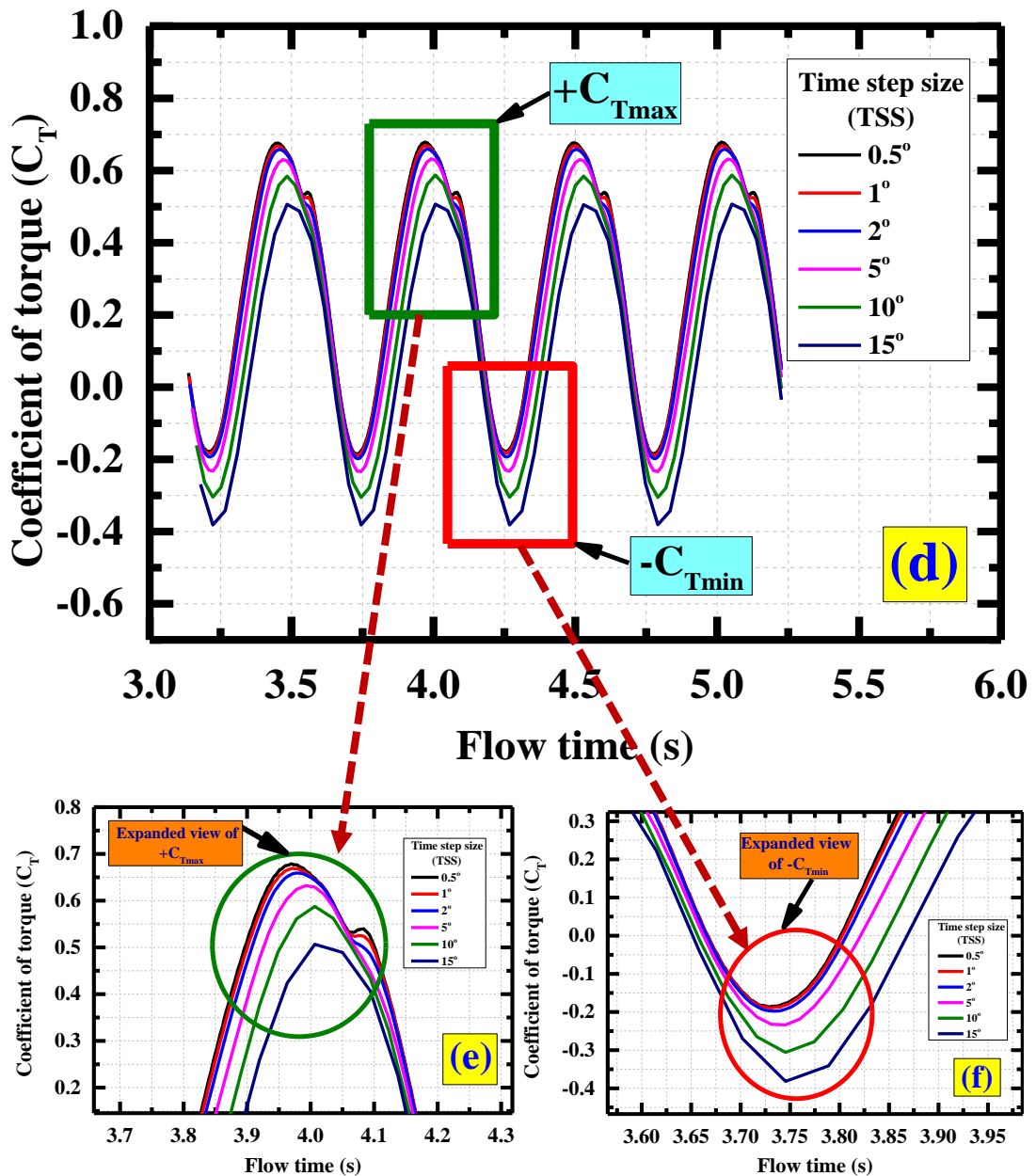
Figure 3.22 Grid and time dependency study (a) variation of C_T with respect to flow time, (b) expanded view of C_{Tmax} for C_T, (c) expanded view of C_{Tmin} for C_T at a different number of mesh elements, (d) variation of C_T with respect to flow time, (e) expanded view of C_{Tmax} for C_T and (f) expanded view of C_{Tmin} for C_T with respect to different time step sizes such as 15°, 10°, 5°, 2°, 1° and 0.5° respectively

3.9.3 Simulation method

A three-dimensional transient, pressure-based solver with absolute velocity formulation was used for the present case. It is found that the achieved dimensionless wall distance (y^+) value is less than 1. The turbulence model used is coupled two-equation SST k-ω model based on previous research carried out by other researchers to capture the high separation levels and adverse pressure gradients around the blade wall (Elbatran et al. 2017; Ferrari et al. 2017; Kacprzak et al. 2013; Mosbahi et al. 2019, 2020a; Roy 2015; Shaheen et al. 2015; Talukdar et al. 2018). Therefore, the flow is resolved at the wall boundaries of the turbine blade to approximate the dimensionless velocity as a linear function of y^+. The higher y^+ leads to decreased simulation precision, as the wall functions recommended by ANSYS will not solve the boundary layer flows problems. The density (ρ_w) and viscosity of water (μ_w) is taken as 998.2 kg/m^3 and 0.001003 kg/m-s. Stationary zone and rotating zones are constructed using cell zone conditions, and angular velocity (ω) is given to the rotating zone based on the experimental tip speed ratio (TSR) of the rotor, and axis of rotation of the rotor are Y-axis. Boundary conditions provided with an inlet velocity of 0.3090 m/s and zero-gauge pressure given to the pressure outlet.

The reference values presented in Table 3.14 are very significant to calculate the performance parameters such as C_T and C_P. The various parameters required for reference values in ANSYS Fluent are length (L) of the turbine (Radius of turbine blade = 0.5D$_r$), viscosity (μ_w), density (ρ_w) of the water, and all the calculations computed from the velocity inlet. Based on a time-dependent study conducted in the previous section and also to reduce computational time, the optimum time step size (TSS) of 1° is chosen for the CFD simulation and the values of time step size for the rotor blade with an angle of different 90° and with varying overlap ratio (OR) ranging from 0.0-0.3 with an increment of 0.05 and the turbine blade with different V-angles (V$_{90°-40°}$) presented in Table 3.15-3.17. Section 3.9.5 explains the procedure for calculating the time step size (TSS) for a TSR of 0.7 and the simulation procedure described in Table 3.18 for the C_T and C_P calculation with respect to TSR.

Table 3.14 Reference values used for three-dimensional numerical simulation

Sl. No	Parameter	Values
1.	Area ($H_R \times D_r$) m^2	0.003672
2.	Length (Radius of the rotor ($0.5D_r$)) m	0.036
3.	Velocity of water (V_w) m/s	0.3090
4.	Density of water (ρ_w) kg/m^3	998.2
5.	Viscosity of water (μ_w) kg/m-s	0.001003

In solutions, a SIMPLE scheme was selected for the pressure velocity couplings, least-square cell-based for spatial discretization, and the second-order for pressure is selected (Talukdar et al. 2018). The second-order upwind scheme selected for momentum, turbulent kinetic energy, specific dissipation rate, and lastly first-order implicit specified for transient formulation. The value of 1×10^{-6} provided for continuity, momentum, and turbulence equation convergence criteria (Mosbahi et al. 2019, 2020a; b). Standard initialization is considered and calculated from a velocity inlet with an absolute reference frame. To calculate C_T and C_P, the time step size is required, and it is calculated using angular velocity (ω) of the turbine blade. Based on a time-dependent study conducted in the previous section and also to reduce computational time, the optimum time step size (TSS) of 1° is chosen for the present simulation and the values of time step size for the rotor blade with different V-angles ($V_{90°-40°}$) presented in Table 3.15 to 3.17. Section 3.10.4 explains the procedure for calculating the time step size (TSS) for a TSR of 0.7 and the simulation procedure described in Table 3.18 for the C_T and C_P calculation with respect to TSR.

3.9.4 Method to evaluate time step size (TSS)

The time step size calculation for 0.7 TSR is described below for a rotor blade of $V_{90°}$. The TSR is determined by using equation (3.5)

$$\text{TSR } (\lambda) = \frac{\omega D_r}{2V_w} \tag{3.5}$$

Where, ω = angular velocity of the turbine blade in rad/s, D_r = diameter of the turbine

blade in mm and V_w= Velocity of water in m/s

In terms of angular velocity (ω), equation (3.5) can be expressed

$$\omega = \frac{2 \times V_W \times \lambda}{D_r} \qquad (3.6)$$

The turbine blade angular velocity (ω) can be written as

$$\omega = \frac{2\pi \times N}{60} \qquad (3.7)$$

Equating equations (3.6) and (3.7)

$$\omega = \frac{2\pi \times N}{60} = \frac{\lambda \times 2 \times V_W}{D_r} \qquad (3.8)$$

Equation (3.8) specified in RPM (N)

$$N = \frac{60 \times \lambda \times 2 \times V_W}{2\pi \times D_r} \qquad (3.9)$$

Where V_w= 0.3090 m/s, D_r=72 mm, λ=0.7

$$\boxed{N = 57.37 \text{ RPM} = \frac{57.37}{60} \text{RPS}} \qquad (3.10)$$

N=0.9562 RPS

N=1/ (0.9562) =1.0457 SPR $\qquad$ (3.11)

$$N = \frac{1.057}{360} \text{ s}$$

Where, one revolution =360° $\qquad$ (3.12)

$$\boxed{\text{Time step size } (TSS) = 0.002904 \text{ s}} \text{ for 1° time step} \qquad (3.13)$$

Flow time = Time step size (TSS)*(Total number of time steps in each simulation)

Total number of time steps in each simulation = (Number of time steps in each revolution) *(Total number of revolutions in each simulation)

Total number of time steps in each simulation= 360*5= 1800

Flow time= (0.001794286) *(1800) =5.22 s

Table 3.15 Time step size (TSS) calculations for various OR from 0.0-0.15

Sl. No	TSR	TSS=timestep size (s), Total simulation time=TST (s)							
		OR-0.0		OR-0.05		OR-0.1		OR-0.15	
		TSS (s)	TST (s)	TSS (s)	TST (s)	TSS (s)	TST (s)	TSS (s)	TST (s)
1.	0.7	0.002904	5.22	0.00283	5.094	0.00275	4.95	0.002685	4.833
2.	0.8	0.00254	4.572	0.00247	4.446	0.00241	4.338	0.002349	4.2282
3.	0.9	0.00225	4.05	0.00220	3.96	0.00214	3.852	0.002088	3.7584
4.	1.0	0.00203	3.654	0.00198	3.564	0.00193	3.474	0.001879	3.3822
5.	1.1	0.00184	3.312	0.00180	3.24	0.00175	3.15	0.001709	3.0762
6.	1.2	0.00169	3.042	0.00165	2.97	0.00160	2.88	0.001566	2.8188
7.	1.3	0.00156	2.808	0.00148	2.736	0.00148	2.664	0.001446	2.6028

Table 3.16 Time step size (TSS) calculations for various OR from 0.2-0.3

Sl. No	TSR	OR-0.2		OR-0.25		OR-0.3	
		TSS (s)	TST (s)	TSS (s)	TST (s)	TSS (s)	TST (s)
1.	0.7	0.00261	4.698	0.00254	4.572	0.00246	4.428
2.	0.8	0.00228	4.104	0.00222	3.996	0.00215	3.87
3.	0.9	0.00203	3.654	0.00197	3.546	0.00191	3.438
4.	1	0.00182	3.276	0.00177	3.186	0.00172	3.096
5.	1.1	0.00166	2.988	0.00161	2.898	0.00157	2.826
6.	1.2	0.00152	2.736	0.00148	2.664	0.00143	2.574
7.	1.3	0.00140	2.52	0.00136	2.448	0.00132	2.376

Table 3.17. Calculation of time steps for $V_{90°-40°}$ configuration of rotor blades.

Sl. No	V_w (m/s)	TSR	Time step size (TSS)					
			Turbine blade with different $V_{90°-40°}$					
			$V_{90°}$	$V_{80°}$	$V_{70°}$	$V_{60°}$	$V_{50°}$	$V_{40°}$
1.	0.3090	0.7	0.002904	0.00292	0.002928	0.0029078	0.002864	0.002799
2.	0.3090	0.8	0.002540	0.002561	0.002562	0.0025443	0.002506	0.002449
3.	0.3090	0.9	0.002258	0.002276	0.002277	0.0022616	0.002227	0.002177
4.	0.3090	1	0.002032	0.002049	0.002049	0.0020354	0.002005	0.001959
5.	0.3090	1.1	0.001847	0.001862	0.0018634	0.0018504	0.001822	0.001781
6.	0.3090	1.2	0.001693	0.001707	0.0017081	0.0016962	0.001670	0.001633
7.	0.3090	1.3	0.001563	0.001576	0.0015767	0.0015657	0.001542	0.001507

Table 3.18 Simulation details for C_T and C_P calculation

Sl. No	Parameter	Details
1.	Total number of revolutions during one complete simulation	05
2.	Total time steps in each revolution	360 (One revolution of the turbine blade)
3.	The total time step for one complete simulation	360×5=1800
4.	Calculation of C_T	Average of C_T for last one complete revolution of the rotor blade
5.	Calculation of C_P	TSR× (Average value of C_T)
6.	Number of rotor blades	06
7.	TSR range for simulation	0.7-1.3 with an increment of 0.1, Total 7 TSR
8.	Total number of simulations	Number of rotor blades (06) ×Tip speed ratio range (0.7-1.3) = 6×7= 42
9.	Time step size (TSS)	1° in each time step (optimum time step value)

3.10 Geometric model of optimum rotor blade V$_{80°}$ with a different aspect ratio (0.7-1.75) using two and three endplates

In this section, effect aspect ratio ranging from AR=0.7-1.75 on modified V-shaped rotor blade performance were studied experimentally in a multipurpose tilting flume. Figures 3.23 (a-f) shows the three-dimensional model of the modified optimum rotor blade with a V-angle of 80° with important geometric parameters such as diameter (D$_r$), height (H$_R$), endplate diameter (D$_{ep}$) (front view, side view, and isometric views) and thickness of the turbine blade (t) with different AR ranging from 0.7-1.75. In the present case, the turbine blade with a V-angle of 80° is with zero overlap ratio (OR) is taken from CFD simulation. The modified V-shaped rotor blade consists of advancing and returning blade profiles with two endplates (top and bottom (Figure 3.23 (a)) and two endplates with middle plate (top, bottom, and middle (Figure 3.23(b)) with an endplate diameter of 1.1D$_r$ and its thickness is same as that of the turbine blade (t=1 mm). The side view and isometric view of the optimum modified V-shaped rotor blade V$_{80°}$ with two endplates with middle plates are shown in Figures 3.23 (c-f), respectively.

(a)   (b)
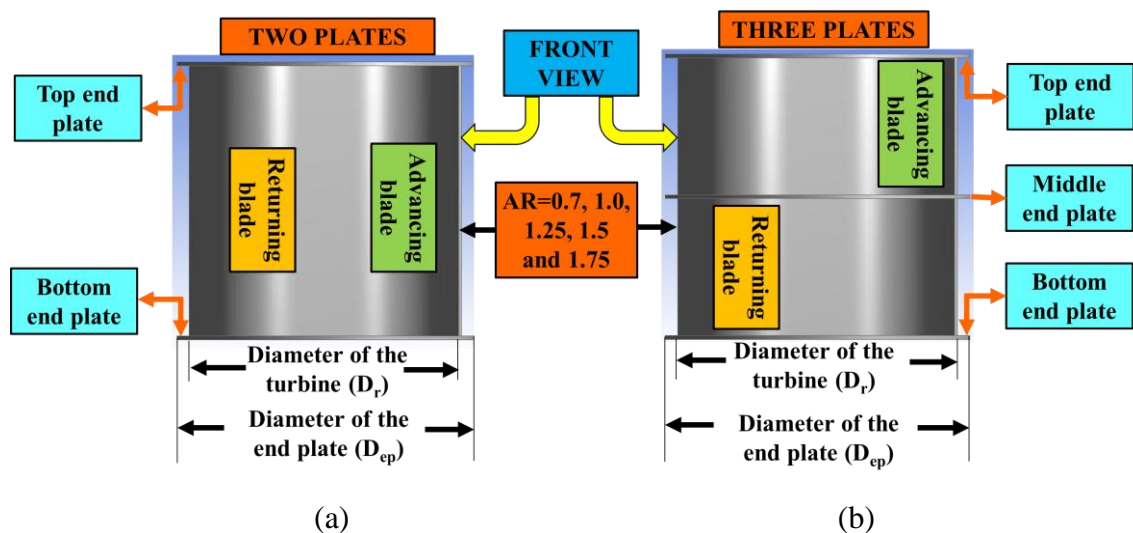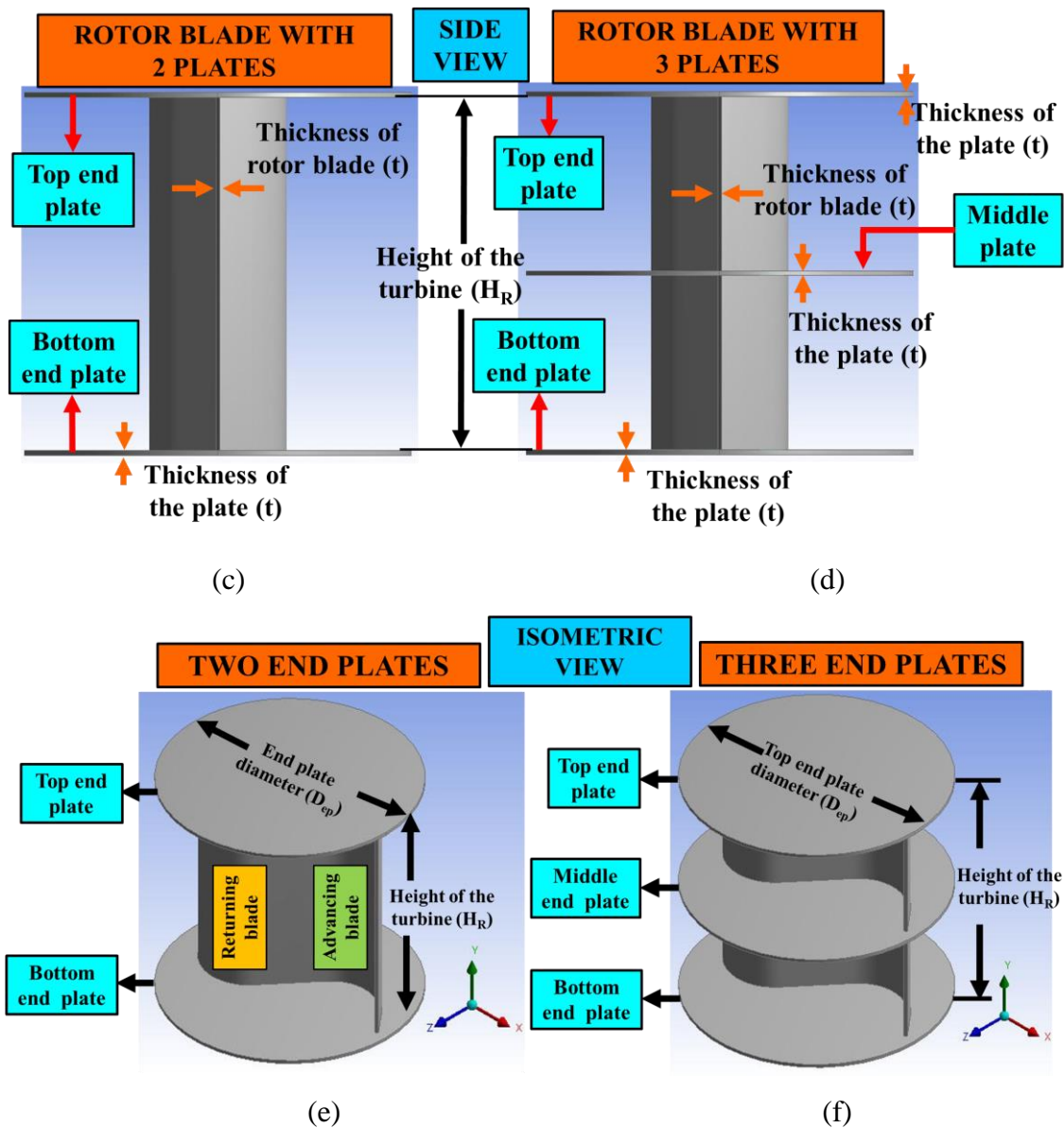
Figure 3.23 Rotor blade with different aspect ratio (AR=0.7, 1.0, 1.25, 1.5 and 1.75)

(Front view, side view and isometric view)

3.10.1 Optimum rotor blade ($V_{80°}$) with a different aspect ratio (AR) using two and three plates

In this section, the optimized rotor blade profile of 80° V-angle having an aspect ratio (AR) of 0.7 and zero overlap ratio (OR), which was obtained from the numerical simulation using a depth of water (H_w) and inlet water velocity (V_w) of 70 mm and 0.3090 m/s respectively. An experimental investigation on the fabricated rotor blade profile with V-angle 80° and the study of the influence of aspect ratio (AR) in the range

of 0.7-1.75 by using two endplates (top and bottom) and two endplates with middle plate (top, bottom, and middle) is carried out.

The depth (H_w) and velocity of water (V_w) used for the development of modified V-shaped turbine blade with an optimum V-angle of 80° using numerical simulations are 70 mm and 0.3090 m/s. Since the turbine blade should be completely immersed condition for the aspect ratio (AR) of 0.7 and turbine height is 50.82 mm, the depth of water of 70 mm is sufficient for the complete immersion of the turbine blade.

Modified V-blade with 0.7 of AR got the 50.82 mm of height, as the AR varies from 0.7 to 1.75, height of the blade also varies from 50.82 to 127.05 mm, which is presented in Table 3.19. Hence the depth of water considered for the numerical simulation (70 mm) is not sufficient for experimental studies. All the experiments were carried out at a common depth of 140 mm, hence the velocity at numerical simulation 0.3090 m/s changes to 0.513 m/s in experiments. When the numerical simulation was conducted for blade angle 80°, and AR of 0.7, the required water depth to immerse the blade was 50.82 mm optimally. The water depth was directly proportional to the velocity of the flow. To achieve a higher value of inlet flow velocity, 70 mm depth of water is considered for the numerical analysis, with a velocity of 0.3090 m/s. Simulations were restricted to a water depth of 70 mm instead of 140 mm to avoid the computational cost and time, hence the inlet velocity for simulations was considered as 0.3090 m/s and for experimental 0.513 m/s.

The diameter of the endplate (D_{ep}) used in the present case is 1.1 times the diameter of the turbine blade ($1.1D_r$) and it is selected based on the previous investigation carried out by various researchers for Savonius turbines (Akwa et al. 2012; Golecha et al. 2011; Saha et al. 2008; Patel et al. 2016; Patel et al. 2018) and 1 mm thick turbine blade and endplate is used in the present investigation. Figures 3.24 (a-e) and Figures 3.25 (a-e) shows the schematic of a modified V-shaped rotor blade with a V-angle of 80° with different AR ranging from 0.7-1.75 with two endplates (top and bottom) and two endplates with one middle plate (top, bottom, and middle) respectively.

The optimum turbine blade ($V_{80°}$) with different AR using two endplates and two endplates with one middle plate was fabricated by mild steel material with a turbine blade and endplate thickness of 1 mm and the turbine blade diameter (D_r) of 72.6 mm is shown in Figures 3.26 and 3.27. The various geometric dimensions of the turbine

blade such as height (H_R), diameter (D_r) of the rotor blade for different aspect ratios ranging from 0.7-1.75, depth of water (H_w), and velocity of water (V_w) used for the experimental investigation are presented in Table 3.19.
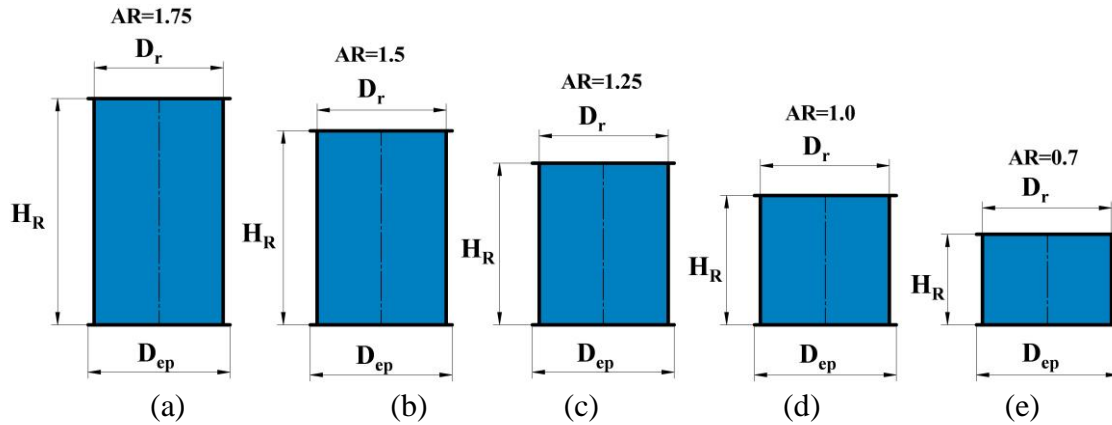
Figure 3.24 (a-e) Schematic of turbine blade with different AR (0.7-1.75) using two endplates
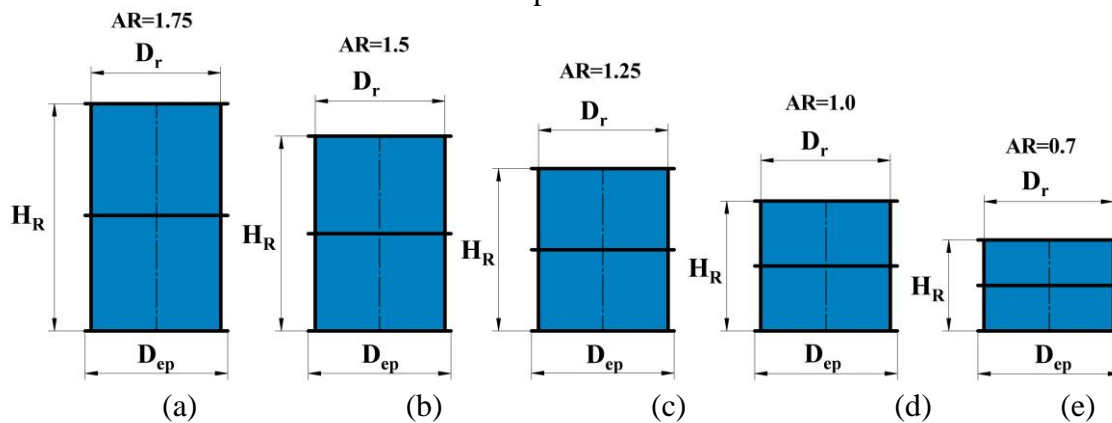
Figure 3.25 (a-e) Schematic of turbine blade with different AR (0.7-1.75) using three endplates
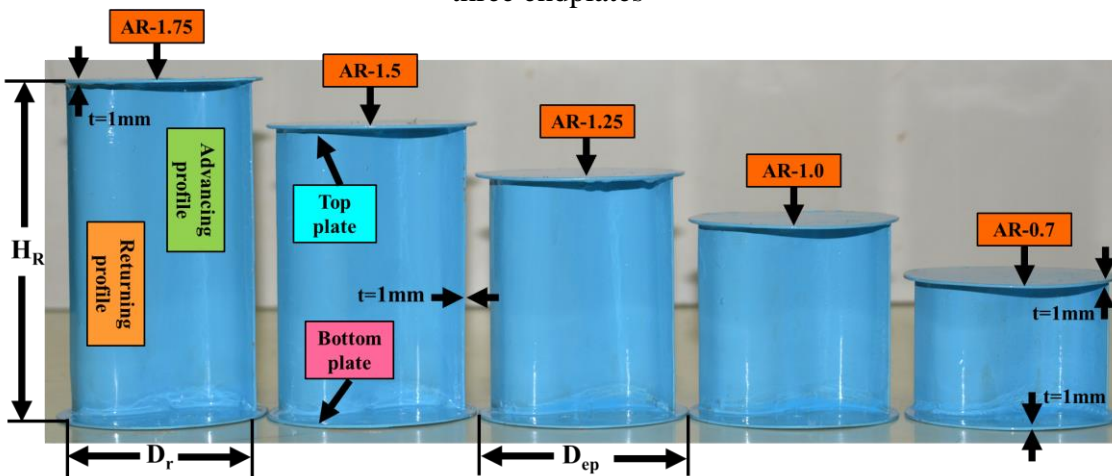
Figure 3.26 Pictorial of rotor blade with different AR (0.7-1.75) using two endplates
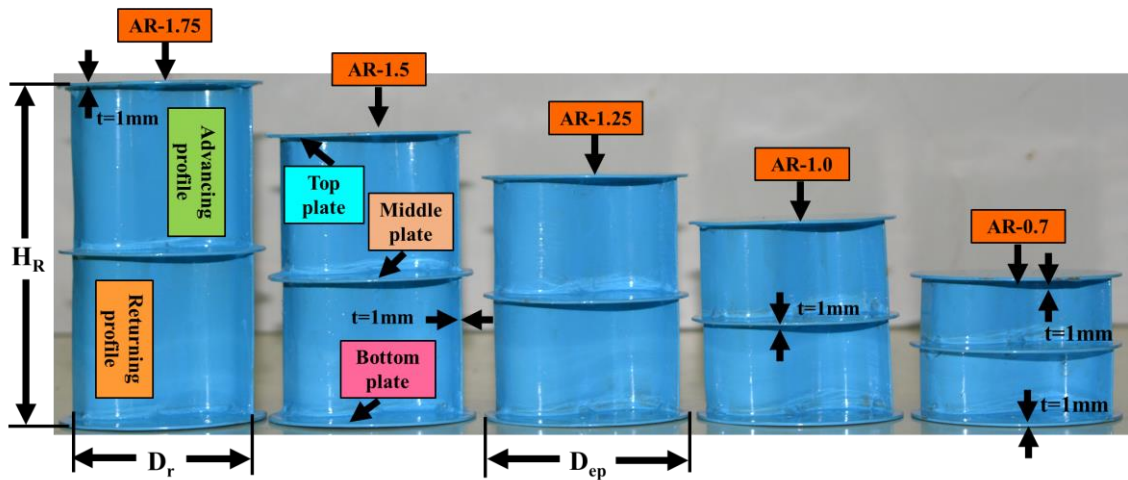
Figure 3.27 Pictorial of the rotor blade with different AR (0.7-1.75) using three
endplates

Table 3.19. Dimensions of the modified V-shaped rotor blade with a V-angle of 80°
with different AR with two (Top and bottom) and three endplates (Top, middle, and
bottom plates)

Sl.No	D_r mm	Aspect ratio (AR)	H_R (2 plates) mm	H_R (3 plates) mm	(H_w) mm	Velocity (V_w) m/s
1.	72.6	0.7	50.82	50.82	0.14	0.513
2.	72.6	1.0	72.6	72.6	0.14	0.513
3.	72.6	1.25	90.75	90.75	0.14	0.513
4.	72.6	1.5	108.9	108.9	0.14	0.513
5.	72.6	1.75	127.05	127.05	0.14	0.513

3.11 Experimental procedure for the effect of bed slope, Novel V-shaped rotor blades (V_1-V_5), and rotor blade with a different aspect ratio (AR=0.7-1.75)

The rotor test rig is placed inside the flume, and two monoblock pumps generate the
flow rate of water in the flume. The rate of water flow is measured by a rectangular
notch fixed at the outlet of the flume. The kinetic energy of the flowing water will result
in the rotation of the rotor due to energy transfer. A Rope dynamometer is used for
applying load on the rotor shaft using a weighing pan, spring balance, and pulleys. The

torque generated by the rotor found by gradually applying the load on the weighing pan until the rotor stops. The power generation from the rotor is found by measuring the RPM of the rotor shaft through a digital tachometer and the torque available. Same procedure is used for inclined cases with inclination angle of $\theta = 0°$-$2°$ with an increment of $\theta = 0.5°$. The discharge is kept constant for both horizontal and inclined cases. The velocity of water (V_w) is calculated by finding the channel's wetted area (Aw) and discharge through the rectangular notch. The measured values of torque and power is used to calculate the performance parameters such as C_T and C_P, respectively. The details of the instruments used to carry out the experiment are presented in Table 3.20.

A similar procedure is used to determine the C_P and C_T for the Novel V-shaped rotor blade profiles V_1-V_5 with a V angle of $90°$ using a depth of H_w=70 mm and velocity of water of V_w=0.3090 m/s for the aspect ratio of 0.7. The rotor blades (V_1-V_5) shown in 3.23 (f) are individually positioned inside the tilting flume (Figure 3.28 (c)). Similarly, modified V-blade ($V_{80°}$) with 0.7 of AR got 50.82 mm of height, as the AR varies from 0.7 to 1.75, the height of the blade also varies from 50.82 to 127.05 mm, which is presented in Table 3.19. All the experiments were carried out at a common depth of H_w=140 mm, hence the velocity at numerical simulation 0.3090 m/s changes to 0.513 m/s in experiments. The pictorial view of multipurpose tilting flume (Figure 3.28 (a)) along with experimental test rig (Figure 3.28 (b)) and expended view of the turbine blade with different aspect ratios using two and three plates (Figure 3.28 (c)) is shown in Figure 3.29.

Table 3.20 The instruments used to carry out the experiments in multipurpose tilting flume.

Sl. No	Instrument used	Details
1.	Multipurpose tilting flume	$W_C = 0.25$m, length of the flume =4.75m
2.	Starter	Independent starter for each pump, 1 Phase
3.	No. of control valves	2.0
4.	Pump make	SHARP
5.	Pump capacity and number of pumps	2 HP and 2.0
6.	Tachometer PLYE Make-PLT26	<u>Specifications</u> (a) RPM measurement, (b) Professional Digital Non-contact laser tachometer (c) Resolution: 2.5-1000 RPM (d) Accuracy: ±0.05%+1dgt
7.	Spring balance SALTER make	To measure net load acting on the shaft Accuracy -2.5 g accuracy
8.	Height gauge	To measure the depth of water (H_w)
9.	Scaled-down modified Savonius turbine blade	Diameter of the turbine (D_r) =72 mm Height of the turbine blade (H_R) =51 mm
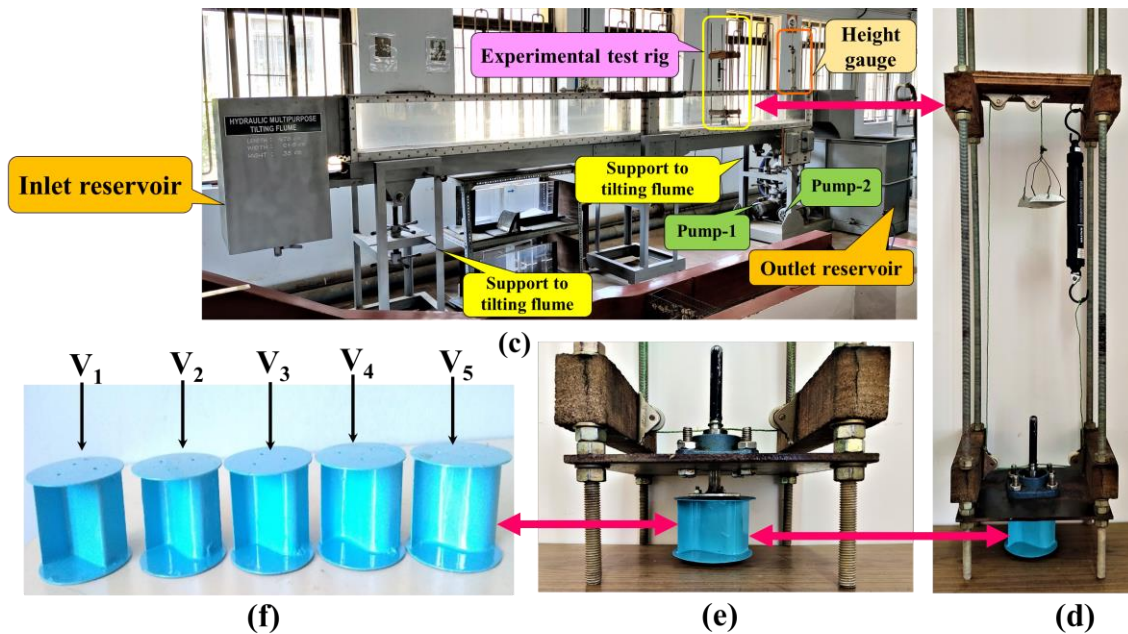
Figure 3.28 (a) Schematic of the experimental test rig, (b) pictorial of the experimental test rig, (c) pictorial of multipurpose tilting flume, (d) expanded view of experimental test rig in multipurpose tilting flume, (e) expanded view of a turbine blade in an experimental test rig and (f) pictorial of fabricated rotor blades (V_1-V_5)
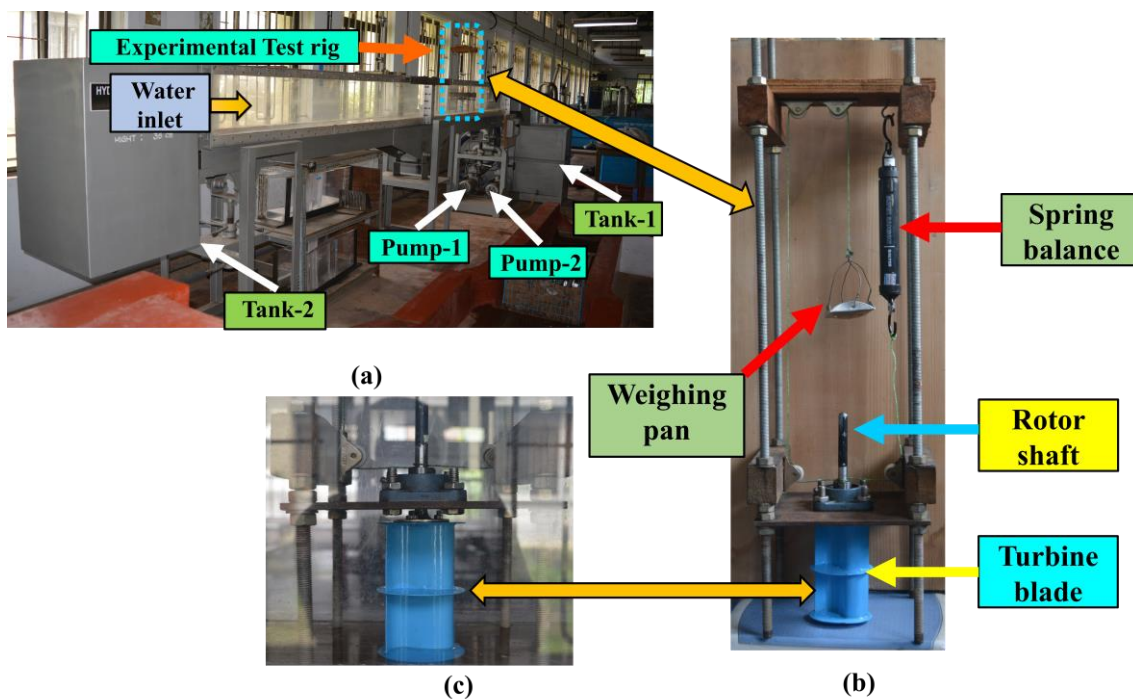
Figure 3.29 Pictorial view of multipurpose tilting flume (a) with the experimental rig (b) and (c) for the turbine blades with aspect ratio using two and three endplates.

3.12 Data reduction

The performance of Savonius water turbines expressed in terms of coefficient of power (C_P) and coefficient of torque (C_T) are given by the following equations (Golecha et al. 2011).

$$\textbf{Coefficient of torque (C}_{\textbf{T}}\textbf{)} = \frac{T_{Rotor}}{T_{Available}} = \frac{T_{Rotor}}{\left(\dfrac{1}{4}\rho_w H_R D_r^2 V_w^{\,2}\right)} \tag{3.14}$$

Where $A_R = H_R D_r$

$$\textbf{Rotor torque (T}_{\textbf{Rotor}}\textbf{)} = (W_L - S_{SB})g(R_{shaft} + R_{Rope}) \tag{3.15}$$

$$\textbf{Coefficient of power (C}_{\textbf{P}}\textbf{)} = \frac{P_{Rotor}}{P_{Available}} = \frac{\left(T_{Rotor} \times \omega\right)}{\left(\dfrac{1}{2}\rho_w \left(H_R D_r\right) V_w^3\right)} \tag{3.16}$$

$$\textbf{Tip Speed Ratio (TSR)} = \frac{\omega D_r}{2V_w} \tag{3.17}$$

$$\textbf{Reynolds number (Re)} = \frac{\rho_w V_w D_r}{\mu_w} \tag{3.18}$$

$$\textbf{Actual discharge (Q}_{\textbf{actual}}\textbf{)} = C_d \left(\frac{2}{3}\right) W_C \left(\sqrt{2g}\right)\left(H_w\right)^{3/2} \tag{3.19}$$

$$\textbf{Velocity of water (V}_{\textbf{w}}\textbf{)} = \frac{Q_{actual}}{A_W} = \frac{Q_{actual}}{\left(W_C H_w\right)} = \frac{C_d \left(\dfrac{2}{3}\right) W_C \left(\sqrt{2g}\right)\left(H_w\right)^{3/2}}{\left(W_C H_w\right)} \tag{3.20}$$

Where $A_w = W_C H_w$

$$\textbf{Blockage ratio (BR)} = \frac{W_R H_R}{W_C H_w} \tag{3.21}$$

Blockage ratio (BR), which is the ratio of the front area of the rotor to the front wetted area of the channel and is equal to 21%. From the study of Alexander and Holownia (Alexander and Holownia 1978), it is found that blockage correction is not required for the blockage ratio of less than 30%, and hence blockage correction is not included in the present work.

3.13 Experimental uncertainty

To ensure the accuracy in the validation of experimental and numerical investigation, the evaluation of errors and uncertainties obtained is very important. Error is a difference between the true value and measured value. Errors are broadly classified into random, schematic, and human error. The random and schematic errors are reduced by repeating the experiments and calibrating the instruments. The errors associated with the measurement instruments are constant, though irrespective of the high calibration performed at the end of the supplier. The experimental setup is the combination of different instruments with their own degree of variation from the true value. Therefore, error analysis also requires a consistent description to evaluate the overall degree of uncertainty. Uncertainties are calculated using equations (3.22) to (3.24). These equations obtained by the method followed by Moffat, (1988) and values for various performance parameters such as TSR, C_T, and C_P are shown below.

$$\frac{\Delta\lambda}{\lambda} = \left(\sqrt{\left(\frac{\Delta\omega}{\omega}\right)^2 + \left(\frac{\Delta D_r}{D_r}\right)^2 + \left(\frac{\Delta V_w}{V_w}\right)^2} \right) = 1.94\% \tag{3.22}$$

$$\frac{\Delta C_T}{C_T} = \left(\sqrt{\left(\frac{\Delta T_{Rotor}}{T_{Rotor}}\right)^2 + \left(\frac{\Delta T_{Available}}{T_{Available}}\right)^2} \right) = 2.6\% \tag{3.23}$$

$$\frac{\Delta C_P}{C_P} = \left(\sqrt{\left(\frac{\Delta C_T}{C_T}\right)^2 + \left(\frac{\Delta\lambda}{\lambda}\right)^2} \right) = 3.24\% \tag{3.24}$$

3.14 Closure

This chapter provided the details about experimental set-up and instruments required for smooth conduction of the experiments. This chapter also has introduced the unsteady 3-D computational fluid dynamics procedure adopted during simulation study by sliding mesh technique. The next chapter deals with results and discussion of various parametric studies using experimental and three-dimensional CFD investigation to determine the various performance parameters and to study the flow field around the turbine blades using pressure, velocity contour, and stream line plots.

Chapter 4

RESULTS AND DISCUSSIONS

This chapter provides the results and discussions of the various parametric investigations of the different blade profiles using experimental and numerical investigations to compute the various performance parameters. At first, the results are validated by comparison with the modified Savonius rotor of Golecha et al. 2011. Influence of bed slope (θ=0°-2°) on the performance of the Savonius rotor is studied experimentally and compared with the results of horizontal (θ=0°) and inclined conditions ranging from θ = 0.5°-2° with an increment of 0.5° and effect of Froude number (Fr) on the performance of the turbine with respect to different bed slope inclination (θ) of the channel. Then, CFD and experimental results of V-shaped blade profiles are compared with the CFD result of the semi-circular blade profile using a similar geometric parameter. The flow field around the modified V-shaped rotor blade with and without overlap ratio need to be studied at different angular position (θ) of the rotor blade to understand the flow field around the turbine blade. The effect of V-angle (90°-40°) on the performance of a modified V-shaped hydrokinetic turbine blade profile and develop optimum V-angle by maintaining a fixed arc radius and straight edge using ANSYS FLUENT. The flow around the modified V-shaped rotor blade profile with different V-angles (90°-40°) using pressure contour and velocity contour plots were studied. The effect of aspect ratio (AR) on the performance of the water turbine ranging from 0.7, 1.0, 1.25, 1.5, and 1.75 using two endplates (top and bottom) and two endplates with one middle plate (top, middle, and bottom) for the rotor blade with V-angle of 80° experimentally using multipurpose tilting flume.

4.1.1 Effect of bed slope (θ=0°, 0.5°, 1°, 1.5° and 2°) on the performance of modified Savonius hydrokinetic turbine

The results are validated by comparing the same for the modified Savonius rotor of (Golecha et al. 2011). Influence of bed slope (θ=0°-2°) on the performance of the Savonius rotor is studied experimentally and compared with the results of horizontal

($\theta=0°$) and inclined conditions ranging from $\theta = 0.5°-2°$ with an increment of $0.5°$. Tables 4.1 to 4.3 shows the comparison of the modified Savonius rotor (Golecha et al. 2011) with a scaled-down Savonius rotor.

4.1.2 Validation of the experimental procedure for the effect of bed slope on the performance of modified Savonius hydrokinetic turbine

Figures 4.1 (and b) show the comparison of variation of C_P and C_T concerning TSR for scaled-down rotor (present study) with modified Savonius rotor (Golecha et al. 2011) for $\theta = 0°$ bed slope. The present study's experimental results follow a similar trend with the experimental results reported by Golecha et al. 2011. It is found that $C_{Pmax} = 0.1515$ and $C_{Tmax} = 0.2179$ at a TSR of 0.7. Table 4.1 shows performance parameters such as C_{Pmax} and C_{Tmax} of Golecha et al. 2011 and the present study and the percentage increase of C_{Pmax} and C_{Tmax}. This variation in the present study is mainly because of the change in the turbine blade's dimensions, top and bottom endplates. In the present study, galvanized iron with 1 mm thickness was used, whereas, in the study proposed by Golecha et al. 2011, an acrylic sheet with a 10 mm thickness is used.

Table 4.1 Important dimensions and values of C_{Tmax} and C_{Pmax}

Sl. No	Performance parameters	Golecha et al. 2011	Present Study	Percentage increase
1.	C_{Pmax}	0.14	0.1515	8.21%
2.	C_{Tmax}	0.2	0.2179	6.7%
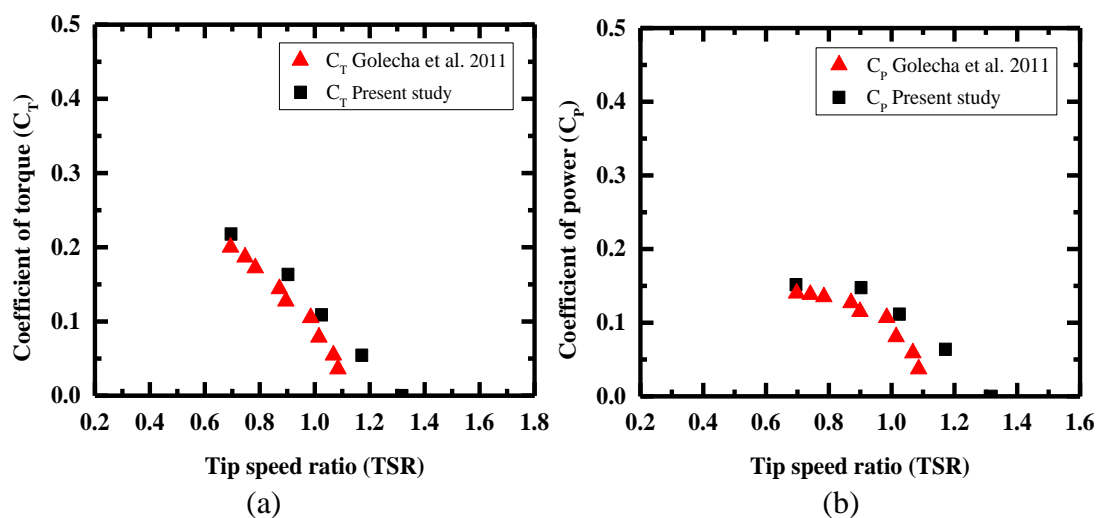
Figure 4.1 Validation of C_T and C_P with respect to TSR for the bed slope $\theta= 0°$

Figures 4.2 (a and b) shows the variation of C_T and C_P with respect to tip speed ratio (TSR) while varying bed slopes from $\theta = 0°$ to $2°$ with an increment of 0.5 for a scaled-down modified Savonius turbine blade used in the present study. The scaled-down turbine model was tested in a multipurpose tilting flume by maintaining a 70 mm depth of the water with an inlet velocity (V_w) of 0.3088 m/s for $\theta = 0°$ bed slope under complete immersion condition. The value of C_{Pmax} and C_{Tmax} with respect to TSR was found to be 0.1515 and 0.2179 at a TSR of 0.7.

Talukdar et al. 2018 obtained higher C_{Pmax} and C_{Tmax} values with respect to TSR while conducting experiments using a Savonius rotor at a fully submerged condition with an inlet velocity of 0.8 m/s. The high-pressure region on the concave side and the low-pressure region at the convex side of the advancing blade profile aids in producing a pressure drop that results in turbine rotation. This higher pressure at the concave side of the advancing blade contributes to a more significant drag coefficient, which in turn improves overall efficiency.

In the present study, the value of C_{Pmax} and C_{Tmax} with respect to TSR were found to be higher than the experimental studies carried out by Golecha et al. 2011 using a modified Savonius rotor at a fully submerged condition with an inlet velocity of 0.45 m/s. For the bed slope (θ) of 0.5°, the depth of water (H_w) was reduced to 67 mm (4.3% reduction), and the turbine blade is in a fully submerged state. The value of C_{Tmax} and C_{Pmax} are found to be 0.2296 and 0.2119 at a TSR equals to 0.9227. This observation is due to the increase in inlet velocity. As the inlet velocity of water increases, the performance of the Savonius turbine increases. Similar results were reported by Kumar and Saini 2017a while conducting three-dimensional transient CFD simulations using twisted blades by varying the twist angle with different water velocities when the turbine blade is fully submerged condition. The high-pressure zone at the concave side of the advancing blade and the low-pressure zone at the convex side of the advancing blade profile aids in producing a pressure drop, which results in turbine rotation. Furthermore, Birjandi et al. 2013 also reported that the maximum C_P might be obtained when the turbine is under fully submerged conditions while conducting experiments on a squirrel-cage hydrokinetic turbine model with two blades. The increase in the C_P is due to a reduction in the positive clearance coefficient and water level above the turbine

blade. The C_P developed by the turbine blade is increased under a fully submerged condition.

For the other bed slopes, $\theta=1°$, $1.5°$, and $2°$, the turbine's immersion level decreases to 73%, 33%, and 31% of the original height, respectively. As the depth of water (H_w) decreases with respect to bed slope (θ), the velocity of water (V_w) increases, which results in a decrease in tip speed ratio (TSR). The values C_{Tmax} and C_{Pmax} decrease due to an increase in power available ($P_{Available}$) in the flume with respect to bed slope ($\theta=1°$, $1.5°$, and $2°$), as shown in Figures 4.3 (a and b). When the turbine is partially submerged, the portion of the blade is exposed to air on the advancing side, leading to a decrease in the C_P and C_T (Birjandi et al. 2013; Talukdar et al. 2018).

The performance of a turbine increases with respect to the TSR when the turbine is in a fully submerged condition ($\theta=0.5°$), as shown in Figure 4.3 (a and b) and a submerged cross-sectional area of the turbine is 0.0037 m^2 (4.3% reduction in immersion level) with respect to bed slope $\theta=0.5°$. As the turbine is in the fully submerged condition, the entire turbine blade surface is in contact with water, and higher extraction of kinetic energy is possible ($C_{Pmax}= 0.2119$) when compared to the turbine blade, which is in partially submerged condition, and submerged cross-sectional area of the turbine blade is 0.0037, 0.0016 and 0.0012 m^2 (immersion level of turbine decreased to 73%, 33% and 31% of the original height respectively) with respect to bed slope $\theta=1°$, $1.5°$ and $2°$ ($C_{Pmax}= 0.1208$, 0.0278 and 0.0205). Under the partially submerged condition, the turbine rotor is suspended above the water surface, and only a lower portion of the blades are submerged. The water movement causes the rotor to rotate; however, the surface area of the turbine rotor on which the water impacts is reduced. When the turbine blade is exposed to air, the turbine blade hydrodynamics will be disturbed due to the density difference between air and water (density of water 850 times more massive than air) (Khan et al. 2009b). The air entrainment decreases the density of water, which is in contact with the turbine blade surface and leads to a reduction in the drag forces created in this area which, in turn, reduces the turbine performance (Birjandi et al. 2013; Runge et al. 2018).

The Savonius rotor is a unique fluid mechanical device that works on the drag effect mechanism rather than a lift mechanism. The drag coefficient of the concave surface (advancing blade) is larger than the convex surface (returning blade), forcing the rotor to rotate. This reduction in the drag coefficient of the concave and convex surface forces the rotor to rotate at a reduced C_T, which affects the turbine efficiency.

The present study reveals that the turbine rotor submergence is found to be a critical parameter that significantly affects the turbine efficiency. The turbine performance parameters obtained for bed slope of $\theta=0°$ and $0.5°$ recommend that the turbine be submerged to a depth that provides a subcritical Froude number (Fr). Due to the limitation in the current experimental setup, it was not possible to carry out the experiments under the fully submerged condition at bed slopes $\theta=1°$, $1.5°$ and $2°$ (immersion level of turbine decreased to 73%, 33% and 31% of the original height). Further studies need to be carried out at different bed slopes when the turbine rotor surface area is in complete contact with the water to obtain increased turbine performance.

Table 4.2 show a comparison of the performance parameters of the turbine under various bed slope conditions. Figures 4.2 (a and b) shows the comparison of C_T and C_P with respect to TSR for $\theta=0°$ and $0.5°$ of inclination of the channel with the literature (Golecha et al. 2011; Talukdar et al. 2018) under the fully submerged condition. Figures 4.2 (a and b) show change in C_T and C_P for the bed slope of $\theta=0°$ and $0.5°$ under the fully submerged condition of the turbine blade and it is compared to the case when the immersion level of the turbine blade is 100%. The variation of C_T and C_P with respect to TSR for the bed slope ranging from $\theta=0°-2°$ is presented in Figures 4.3 (a) and (b), respectively.

Table 4.2 Comparison of performance parameters of the turbine under various conditions.

Researcher	Type of turbine	Bed slope (θ) degree	Immersion level (%)	V_W (m/s)	C_{Pmax}	C_{Tmax}	TSR
(Talukdar et al. 2018)	Two bladed Savonius	0°	100	0.8	0.28	0.31	0.89
			80		0.10	0.17	0.61
			60		0.07	0.10	0.57
(Golecha et al. 2011)	Modified two-bladed Savonius rotor	0°	100	0.45	0.14	0.20	0.70
Present Study	Modified two-bladed Savonius rotor (Scaled-down)	0°	100	0.3088	0.15	0.22	0.70
		0.5°	**100**	**0.3266**	**0.21**	**0.23**	**0.92**
		1°	73	0.4239	0.12	0.14	0.84
		1.5°	33	0.9827	0.03	0.08	0.33
		2°	31	1.3511	0.02	0.06	0.32

The values of C_{Pmax} and C_{Tmax} with tip speed ratio (TSR) for different bed slope (θ) is presented in Table 4.3.

Table 4.3 Maximum values of C_P and C_T with respect to TSR for different bed slopes.

Sl. No	θ	H_W	V_W	C_{Pmax}	C_{Tmax}	TSR
1.	0°	70	0.3088	0.1515	0.2179	0.6955
2.	**0.5°**	**67**	**0.3266**	**0.2119**	**0.2296**	**0.9227**
3.	1°	51	0.4239	0.1208	0.1446	0.8356
4.	1.5°	22	0.9827	0.0278	0.0842	0.3298
5.	2°	16	1.3511	0.0205	0.0635	0.3235
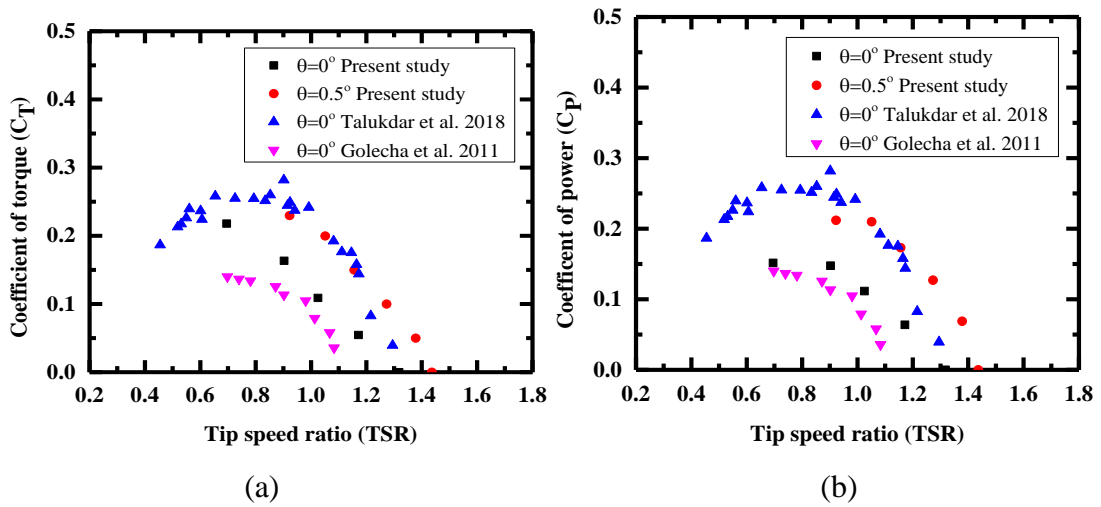
Figure 4.2 Comparison of (a) C_T and (b) C_P with respect to TSR for $\theta=0^o$ and 0.5° of inclination of the channel with the literature (Golecha et al. 2011; Talukdar et al. 2018) under the fully submerged condition

Figure 4.3 Variation of C_T and C_P with respect to TSR for $\theta=0^o$-2° of inclination of channel

4.1.3 Limitation of the present study (effect of bed slope)

In the present study, experiments are performed in a laboratory-scale water re-circulating multipurpose tilting flume with a flatbed. The available flume was designed to vary from 0° to maximum up to 2° with a maximum discharge. Due to this limitation, the laboratory experiments were carried out with a maximum bed slope up to 2 degrees with the maximum available discharge Q_{Actual} 0.01544 m^3/s. In order to maintain the same depth of water (H_w) in all the bed slopes (θ), the supply of water from the pump

should be high, i.e., more discharge (Q_{Actual}) is required from the pump. The variation of water velocity and discharge with respect to bed slope for constant depth of water (H_w) is presented in Figure 4.4.
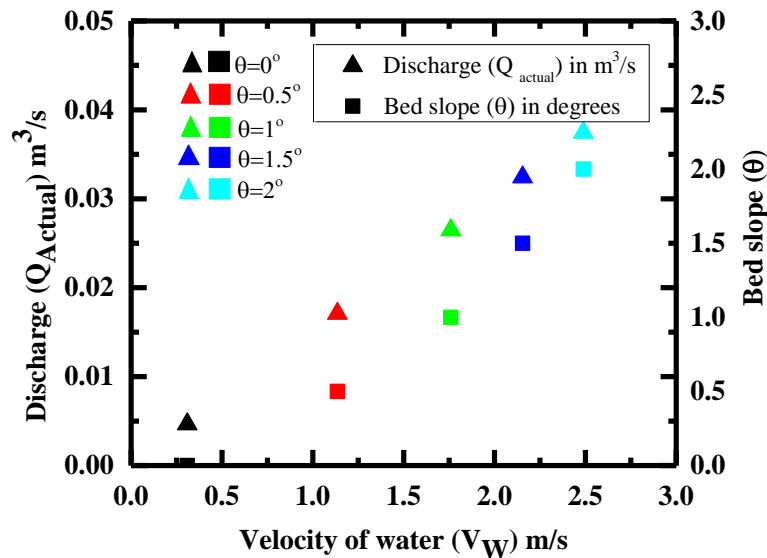
Figure 4.4 Variation of the velocity of water and discharge with respect to bed slope (θ) for a constant depth of water (H_w)

4.1.4 Effect of Froude number (Fr)

Froude number is a ratio of the inertia force to the gravitational force of the fluid (Batten and Müller 2011; Cleynen et al. 2017; Patel et al. 2017, 2019; Quaranta 2018). The value of Froude number (Fr) depends on the depth (H_W) and velocity (V_w) of water in the channel, and it can be written as

$$Fr = \frac{\text{Inertia force}}{\text{Gravitational force}} = \frac{V_w}{\sqrt{gH_w}}$$

Where,

Fr=1-Flow is critical (Inertia force = gravitational force)

Fr<1-Flow is subcritical (Inertia force < gravitational force, i.e., gravitational forces dominate over inertia force).

Fr>1-Flow is supercritical (Inertia force > gravitational force, i.e., inertia forces dominate over gravitational force)

Different types of flow occur in the irrigation channel, such as critical flow (Fr=1), subcritical flow (Fr<1), and supercritical flow (Fr>1), which depends mainly on the velocity of water (V_w) and bed slope (θ). As the bed slope increases, the velocity of the water (V_w) in the channel increases, the depth of water (H_w) decreases, and the Froude number (Fr) value increases. As the Froude number increases the magnitude of force due to gravity reduces, and inertial force increases simultaneously. On the other hand, an increase of bed slope leads to Froude number (Fr) increase, thereby the load-carrying capacity of the turbine blade increases. Whereas an increase in velocity of water (V_W) with respect to bed slope (θ), raises the torque and power values developed by the turbine blade to the maximum for $\theta=$ 2° and minimum for $\theta= 0°$. The values of maximum torque and power developed by the turbine with respect to Froude number (Fr) for different values of the velocity of the water (V_w), depth of water (H_w), and bed slopes (θ) are illustrated in Table 4.4.

Table 4.4 Typical values of Froude number (F_r) for different bed slopes.

Sl. No	Bed slope θ	Depth of water H_W (mm)	V_w (m/s)	Froude number (F_r)	Maximum $T_{Developed}$	Maximum $P_{Developed}$
1.	0º	70	0.3088	0.372	0.0063	0.0082
2.	0.5º	67	0.3226	0.397	0.0069	0.0616
3.	1º	51	0.42389	0.599	0.0119	0.0169
4.	1.5º	22	0.98265	2.11	0.0245	0.0185
5.	**2º**	**16**	**1.35115**	**3.41**	**0.0378**	**0.0292**

As the Froude number (Fr) increases from 0.372 to 0.397, the tip speed ratio (TSR) of the rotor blade increases due to an increase in velocity of water (V_W) for the bed slope ranging from $\theta=0°-0.5°$ shown in Figure 4.3 (a and b). The type of flow is subcritical flow (Fr<1). Cleynen et al. 2017 reported that a similar improvement in tip speed ratio with the increase in Froude number had been observed for free stream water wheels. Similarly, for the other bed slopes, the tip speed ratio (TSR) of the turbine blade

decreases due to an increase in water velocity, and the value of C_P and C_T decreases. For Froude number >1, the type of flow is Super critical. There is a loss of power exhibited by the turbine blade due to the high flow velocity of water, and a similar observation was reported by Quaranta 2018.

As per the torque and power values compared in Table 4.4, it is evident that bed slope of $\theta=2^\text{o}$ generates maximum value when compared to other bed slope inclinations ($\theta=0^\text{o}$, 0.5^o, $1^\text{o,}$ and 1.5^o). Hence, the Froude number (Fr) reaches the supercritical flow condition, indicating that inertia force is dominant and the maximum energy available at the bed slope of $\theta=2^\text{o}$.
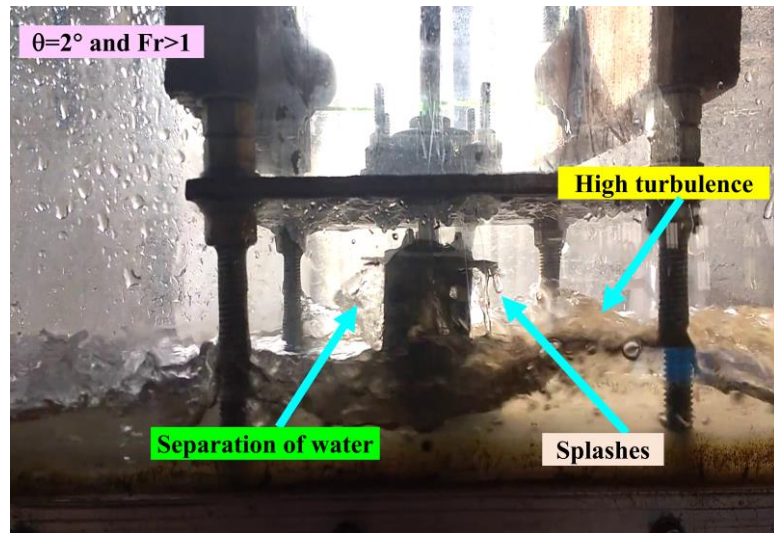
Figure 4.5 (a and b) shows the pictorial view of turbulence, splashes, and separation of water, which is developed around the turbine blade for the higher Froude number (Fr>1) at super critical flows for bed slopes of $\theta=1.5°$ and $2°$. It is observed that with the increase in the Froude number (Fr) from subcritical to critical and then to supercritical, C_T and C_P of the turbine blade decreases. This may be owing to the fact that as the Froude number (Fr) increases, Reynolds number (Re) is also increased during the interaction of turbine blade with water. Therefore, more turbulence is created around the turbine blade as shown in Figure 4.5 (a and b). This in turn increases the flow departure possibility across the turbine rotor neighborhood and results in lower C_T and C_P (Hashemi et al. 2020; Saini and Saini 2020). The turbine blade experiences more turbulence which results in local velocity spikes or drops at higher Froude number (Fr>1) and separation of water starts around the leading edge of the turbine blade as shown in Figure 4.5 (a and b) (Runge et al. 2018; Saini and Saini 2020). This causes the substantial splashing which is developed around the turbine blade (Figure 4.5 (a and b)) at supercritical flow (Fr>1) for a bed slope of $\theta=1.5°$ and $2°$ and increases drag torque on the rotor shaft, which lowers the C_T and C_P turbine (Runge et al. 2018).
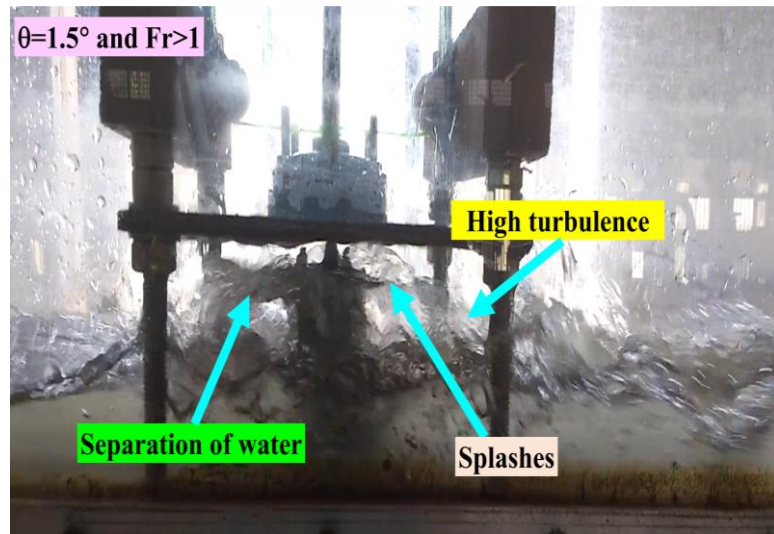
(a)

(b)

Figure 4.5 Pictorial view of turbulence, separation of water and splashes developed around the turbine blade for the supercritical flow (Fr>1) for a bed slope of θ=1.5° (a) and 2° (b).

The variation of Froude number (Fr) with respect to the depth of water (H_w) for different bed slopes (θ=0°-2°) and velocity of water (V_w) in the flume is shown in Figure 4.6. The variation of torque available ($T_{Available}$), maximum torque developed, power available ($P_{Available}$), and maximum power developed with respect to Froude number (Fr) for different bed slopes (θ=0°-2°) of the flume is presented in Figures 4.7 and 4.8.
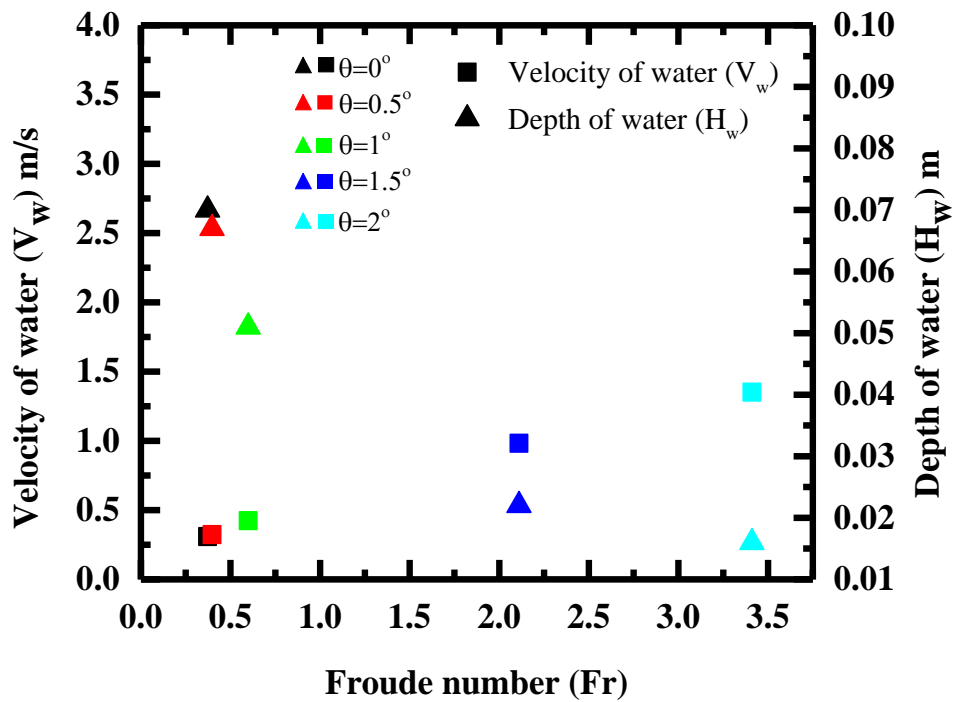
Figure 4.6 Variation of Froude number (Fr) with respect to the velocity of water (V_w) and depth of water (Hw) for different bed slope ($\theta=0°$-$2°$) inclinations of the channel
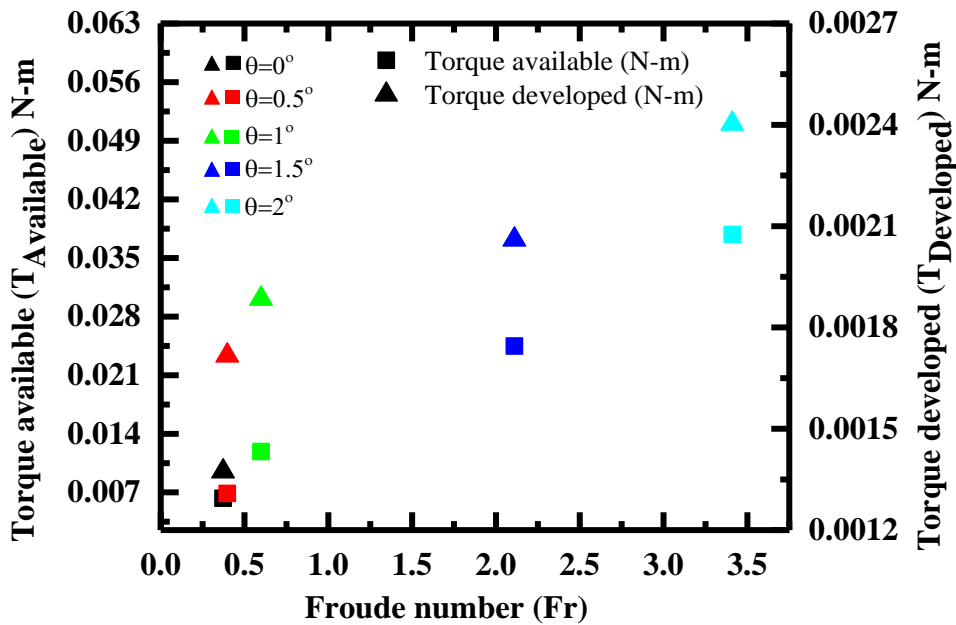
Figure 4.7 Variation of torque available and developed with respect to Froude number (Fr) for different bed slope ($\theta=0°$-$2°$) inclinations of the channel

108
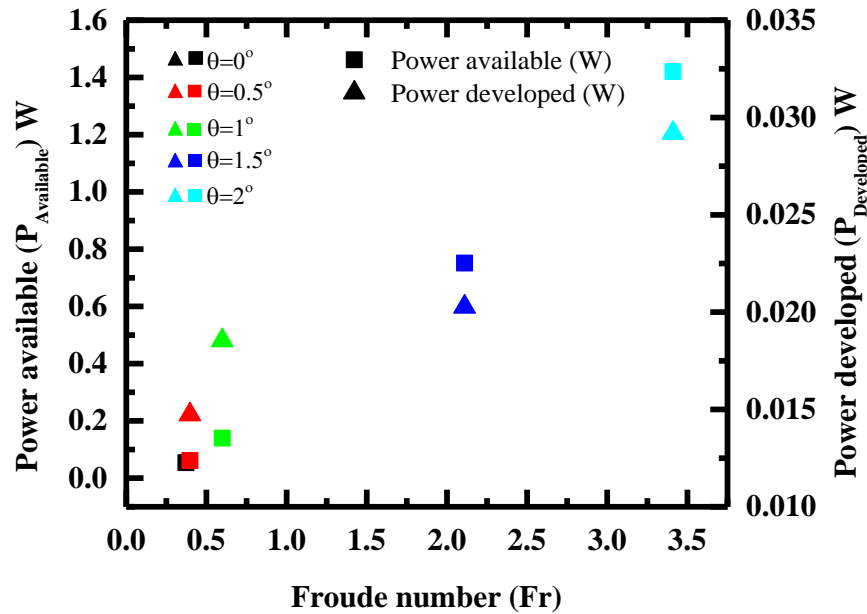
Figure 4.8 Variation of maximum power available and developed by the turbine with respect to Froude number (Fr) for different bed slope (θ=0°-2°) inclinations of the channel.

When the bed slope increases (θ =0°-2°), the depth of water (H_w) in the flume reduces, and the velocity of water (V_w) along with the available power (kinetic energy) increases as well. In order to develop the relationship between the velocity of water (V_w), depth of water (H_w), and power (P) available in the flume with respect to bed slope (θ), were plotted using second-order polynomial fit as shown in Figures 4.9 (a to c).

(a)

(b)
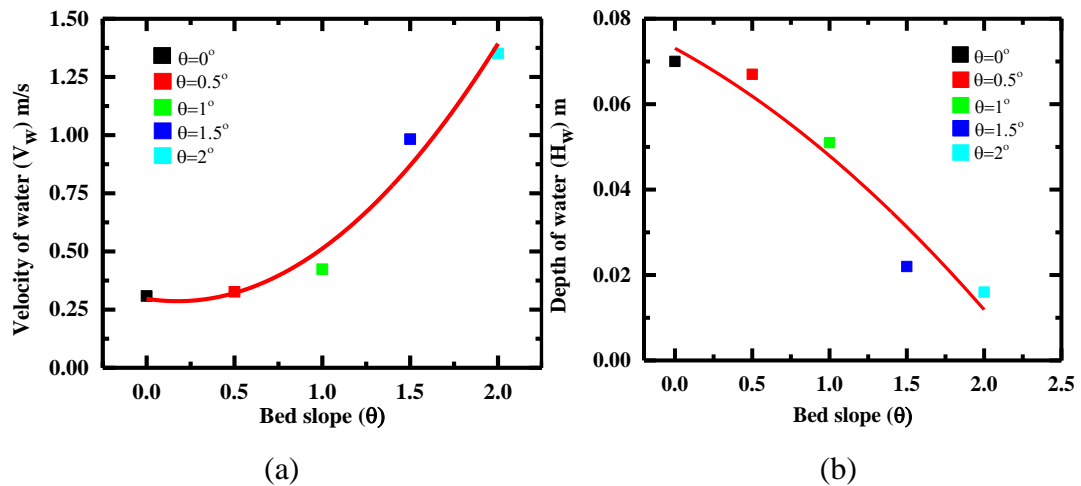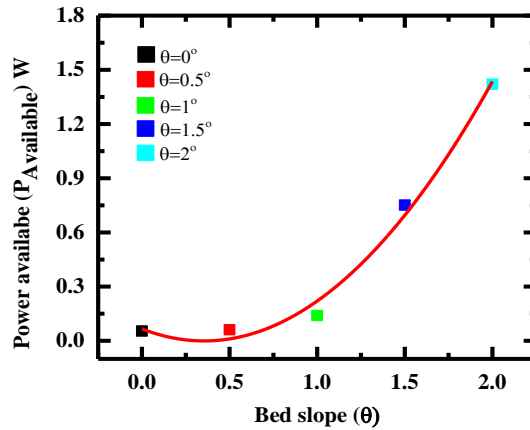
(c)

Figure 4.9 Variation of the (a) velocity of water (V_W), (b) depth of water (H_W) and (c) power available ($P_{Available}$) with respect to bed slope ($\theta=0°-2°$)

The relationship between the velocity of water (V_w), depth of water (H_w) and power available ($P_{Available}$) with respect to bed slope (θ) is expressed by the following equations. (4.1- 4.3)

$$V_w=0.332(\theta)^2-0.1163(\theta)+0.2966 \qquad (4.1)$$

$$H_w=-0.00543(\theta)^2-0.01974(\theta)+0.07309 \qquad (4.2)$$

$$P_{Available}=0.5347(\theta)^2-0.37634(\theta)+0.06618 \qquad (4.3)$$

The average discrepancy values between the results obtained by using equations 4.1-4.3 (2nd order polynomial fit) and the experimental values are listed in Table 4.5 below. Table 4.5 shows the values of the velocity of water in the channel (V_w), Reynolds number (Re), and tip speed ratio (No load condition) for different bed slope inclinations ($\theta=0°-2°$) of the channels with an increment of 0.5°. It is observed that the increase in bed slope (θ) inclination increases the velocity of the water (V_w), however, it decreases the TSR.

Table 4.5 Typical Vw, Re, and TSR values at the various bed slopes (θ) of the channel.

Sl. No	Bed slope inclination of the channel (θ)	Velocity of the water in the channel (Vw) in m/s	Reynolds number $\left(Re = \dfrac{\rho_W V_W D_R}{\mu_W} \right)$	Tip speed ratio (TSR) at No load $\left(\dfrac{\omega D_R}{2V_W} \right)$
1.	0°	0.3088	2.95×10^4	1.3177
2.	0.5°	0.3266	2.99×10^4	1.4367
3.	1°	0.4239	3.65×10^4	1.1556
4.	1.5°	0.9827	9.13×10^4	0.5215
5.	2°	1.3511	1.25×10^5	0.4853

4.2 Performance parameters (C_T and C_P) of conventional and tapered Savonius hydrokinetic turbine blades

The three-dimensional time-dependent CFD simulations were carried out for conventional and tapered Savoinius hydrokinetic turbines using ANSYS Fluent 14.5 to estimate the performance parameters such as C_T and C_P with respect to TSR ranging from 0.7–1.3 by sliding mesh technique (SMT). The aspect ratio (AR) and overlap ratio (OR) maintained in the present CFD simulation are 1.0 and 0.0 for both conventional and tapered turbine blades. The inlet velocity of water (V_w) used for the present CFD simulation is 0.5 m/s, zero bed slope and angular velocity (ω) given to the rotating zone based on the TSR ranging from 0.7 to 1.3 and five revolutions are given to the rotating zone during CFD simulation and calculated the average value of C_T for last one revolution of the turbine blade.

4.2.1 Variation of C_T and C_P with respect to TSR

Figures 4.10 (a-b) show the variation of C_T and C_P with respect to TSR for the present study with previous investigation carried out by various researchers and show similar trends when compared with literature (Golecha et al. 2011; Kerikous and Thévenin 2019a; b; Patel et al. 2016). Figures 4.11 (a and b) show the variation of C_T and C_P with

respect to TSR ranging from 0.7 to 1.3 with an increment of 0.1 for a conventional and tapered turbine blade with a taper angle of 95°. The results show that C_{Tmax} and C_{Pmax} for the conventional turbine were found to be 0.3 and 0.21 at a TSR value of 0.7 and 0.9, respectively. The C_{Tmax} and C_{Pmax} of conventional Savonius hydrokinetic turbine blade are higher than the tapered turbine blade with a taper angle of 95°. The values of C_{Tmax} and C_{Pmax} of the conventional and tapered turbine are presented in Table 4.6.

The Savonius hydrokinetic turbine blade is a drag-type device, and the effective cross-sectional area of the conventional and tapered Savonius hydrokinetic turbine is 0.005184 m^2 and 0.004752 m^2. The effective cross-sectional area of the turbine blade is reduced for the case of a tapered turbine; therefore, an exposed area of the turbine blade in the water is less for a tapered turbine blade than the conventional turbine blade. The C_{Tmax} and C_{Pmax} of the tapered turbine blade are lower when compare to conventional Savonius hydrokinetic turbines.
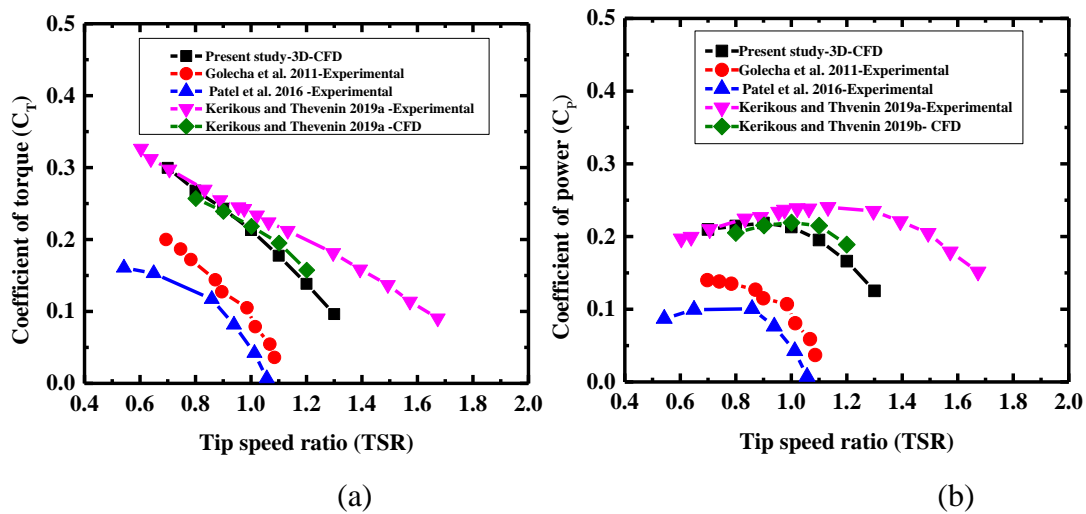

Figure 4.10 Variation of C_T and C_P with respect to TSR and comparison with the previous experimental and CFD investigation carried out by various researchers
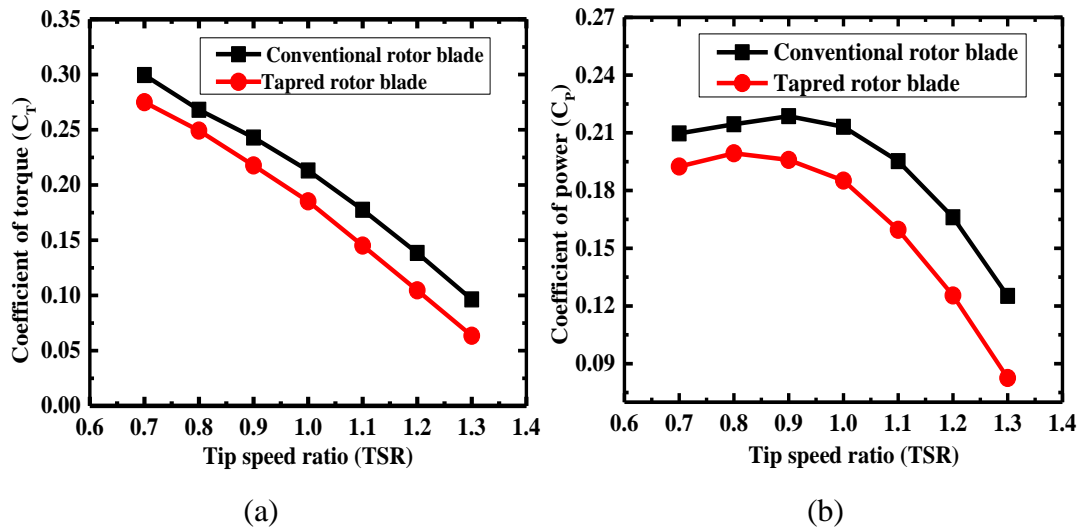
Figure 4.11 Variation of (a) C_T and (b) C_P with respect to TSR for conventional and tapered turbine blades

Table 4.6 C_{Tmax} and C_{Pmax} values of conventional and tapered turbine blade

Sl. No	Conventional turbine blade (Inside angle between H_R and D_{Bottom} is 90°)				Tapered turbine blade (taper angle of 95°) (Inside angle between H_R and D_{Bottom} is 95°)			
1.	C_{Tmax}	TSR	C_{Pmax}	TSR	C_{Tmax}	TSR	C_{Pmax}	TSR
2.	0.3	0.7	0.21	0.9	0.28	0.7	0.2	0.8

4.2.2 Variation of C_T with respect to the angle of rotation (θ) of the turbine blade

Figure 4.12 (a) shows the variation of C_T with respect to the angle of rotation (θ) of the turbine blade for the TSR ranging from 0.7 to 1.3 for conventional and tapered turbine blades. The minimum and maximum values of positive and negative coefficient of torque are represented by $+C_{Tmin}$, $+C_{Tmax}$, and $-C_{Tmin}$. During the rotation of the turbine blade, at some angle of rotations, the turbine blade develops positive torque ($+C_T$) and maximum torque ($+C_{Tmax}$), similarly at some other angle of rotations turbine blade develops negative torque ($-C_T$) and also minimum torque (C_{Tmin}). The value of C_T of the turbine blade decreases when the angle of rotation changing from 0° to 23°, i.e., positive ($+C_T$) to negative ($-C_T$) value, and the turbine experiences the negative torque completely at the angle of the rotation ranging from 24°- 49° at a TSR of 0.7 and similar

113

variation observed for other TSR ranging from 0.8 to 1.3 for conventional turbine blade. For the conventional turbine, the value of C_T is positive ($+C_T$) and increases from 50° till it reaches 107°.

The turbine blade develops the maximum coefficient of torque ($+C_{Tmax}$) at an angle of rotation (θ) of 108° and 292°. A similar variation was observed for a tapered turbine blade with a TSR ranging from 0.7 to 1.3 with respect to the angle of rotation (θ) of the turbine blade as shown in Figure 4.12 (b). It is observed from Figures 4.12 (a and b) the higher C_{Tmax} and lower $-C_{Tmin}$ developed for conventional turbine blade and lower $+C_{Tmax}$ and slightly higher $-C_{Tmin}$ developed for a tapered turbine blade. It is observed that the average value of C_{Tmax} is higher for the conventional turbine blade compared to the tapered turbine blade. Therefore, the performance of the conventional turbine blade is higher than the tapered turbine blade. A similar variation also presented using polar plots for conventional and tapered turbine blades, as shown in Figures 4.13 (a and b).
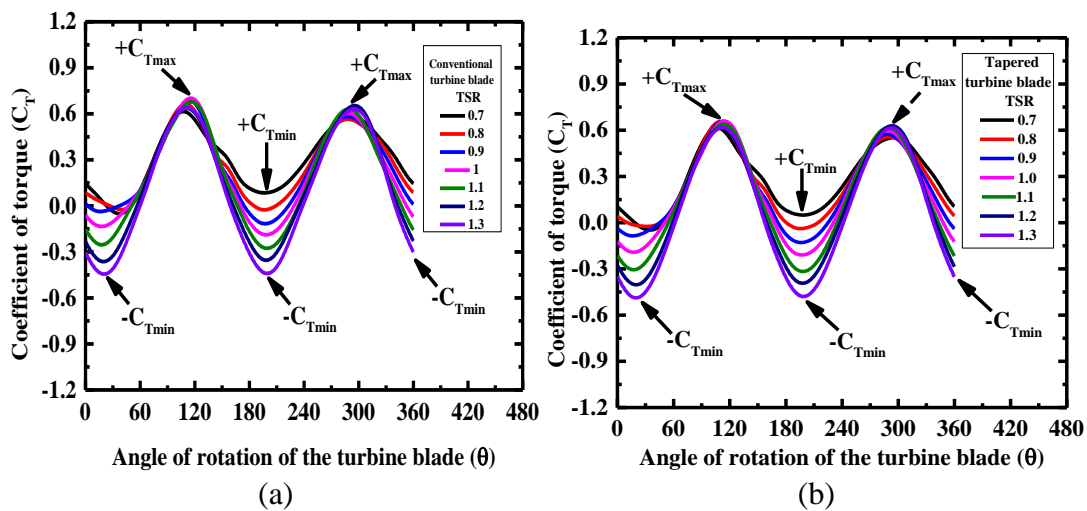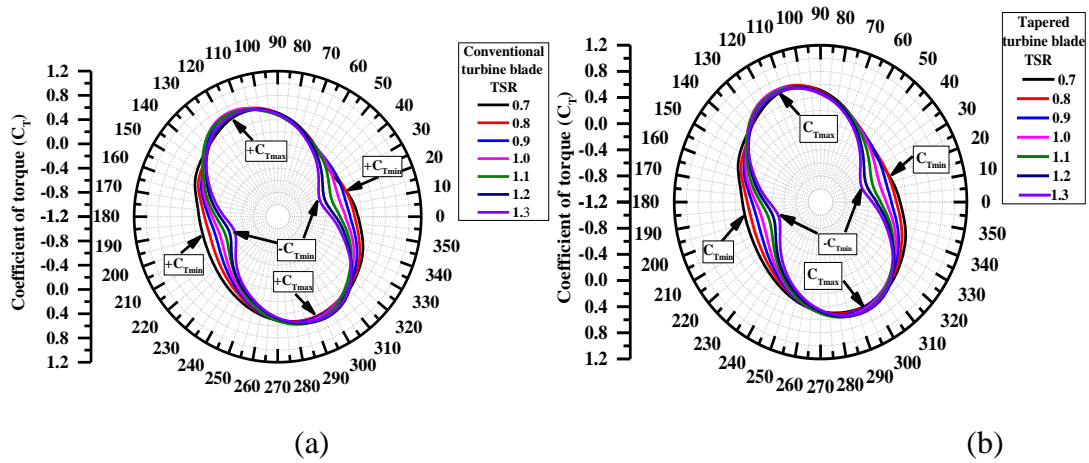

Figure 4.12 Variation of C_T with respect to the angle of rotation of the turbine blade with a TSR ranging from 0.7-1.3 for (a) conventional and (b) tapered turbine blade.

Figure 4.13 Variation of C_T with respect to the angle of rotation (θ) of the turbine blade with a TSR ranging from 0.7 to 1.3 using polar plots for (a) conventional and (b) tapered turbine blades

4.2.3 Numerical analysis using pressure contour, velocity contour, and streamline plots

4.2.3.1 Pressure contour plots

The three-dimensional unsteady CFD simulations were carried out to study the flow field at different angular positions such as $\theta = 0°$, 60°, and 120° by CFD post-processing. To analyze the flow filed around conventional and tapered turbine blades, pressure contours were plotted at different angular positions of the turbine blades with three different views such as top, front, and side views, respectively. Figures 4.14 (a-c) and Figures 4.15 (d-f) show the pressure contour plots for conventional and tapered turbine blades at three angular positions such as 0°, 60°, and 120°, respectively. The values of maximum and minimum pressure are represented by red and blue colours. The direction of the fluid flow is from left side to right side, and the direction of rotation of the turbine blade is in an anticlockwise direction, as shown in Figures 4.14 (a-c) and Figures 4.15 (d-f). The three different views are shown in pressure contour plots (Figures 4.14 (a-c) and Figures 4.15 (d-f)) such as top view (ZX plane), side view (YZ plane), and front view (XY plane).

The various significant zones developed during the rotation of the turbine blades are high-pressure zone, low-pressure zone, and very low-pressure zone. The regions formed in the present numerical simulation (pressure contour plots) follows similar trends as reported by various researchers (Elbatran et al. 2017; Kerikous and Thévenin 2019b; a; Kumar and Saini 2017a; b; Mosbahi et al. 2019, 2020a; Ramadan et al. 2020; Sarma, N. K. Biswas and Misra 2014; Talukdar et al. 2018; Zhang et al. 2019)

It can be seen that there is a drop-in pressure across the rotor from upstream to downstream, as shown in pressure contour plots (Figure 4.15). The pressure is found to be uniform at the inlet of the channel, and higher pressure values are found on the concave side of the advancing blade profile. The lower pressure zone is built on the convex side of the advancing blade profile and the concave side of the returning blade profile.

Therefore, two pressure areas, i.e., higher and lower, are located near the blades inside the flow area, which induces a drop-in pressure. The turbine blades are beginning to rotate due to this pressure drop around the rotor, which allows the Savonius hydrokinetic turbine to draw power from the moving water in the channel. For the conventional Savonius turbine blade, the pressure is found as 285 Pa at the concave surface of the advancing blade profile and negative pressure of 1193.2 Pa at the convex side of the returning blade profile. As a result of this pressure difference, the Savonius hydrokinetic turbine is beginning to rotate. The pattern of pressure contours obtained in the present study for the conventional Savonius hydrokinetic turbine is similar to pressure contours obtained in the previous studies (Kumar and Saini 2017a; b; Wahyudi, B., Soeparman, S., Wahyudi and Denny 2013; Zhang et al. 2017b).

Likewise, for the tapered turbine blade, a similar variation of pressure was observed across the rotor blade developed from upstream to downstream, as shown in pressure contour plots (Figure 4.15). The pressure is found to be uniform at the inlet of the channel, and higher-pressure values are found on the concave side of the advancing blade profile as shown in Figure 4.15. A lower pressure zone is built on the convex side

of the advancing blade profile and the concave side of the returning blade profile (Ostos et al. 2019a; Talukdar et al. 2018).

Therefore, two pressure zones, i.e., higher and lower, are located near the blades inside the flow area, inducing drop-in pressure (Talukdar et al. 2018). Due to this pressure drop around the rotor, turbine blade rotates and draws energy from the water flowing in the irrigation channel (Kumar and Saini 2017a; b). The trend of pressure contours found in the present study for tapered turbine blade is similar to pressure contours as reported in the previous studies (Kumar and Saini 2017a; b; Wahyudi, B., Soeparman, S., Wahyudi and Denny 2013; Zhang et al. 2017b).

For the tapered turbine blade, the pressure is found as 290.5 Pa at the concave surface of advancing blade profile and negative pressure of 1251.1 Pa at the convex side of the returning blade profile. Therefore, from Figures 4.14 (c) and 4.15 (f), the difference in pressure between the advancing and returning blade is maximum for the conventional turbine blade (Figure 4.14 (c)) as compared to the tapered turbine blade (Figure 4.15 (f)) at an angle of rotation of 120°, the value of C_T and C_P slightly higher for conventional turbine as compared to tapered turbine blade with a taper angle of 95°. Since the Savonius hydrokinetic turbine blade is a drag-type device, which works due to drag force between the advancing and returning blade profiles, the efficiency of energy generation depends on the cross-sectional area exposed to water (Elbatran et al. 2017; Kumar and Saini 2017b; a). For the taper turbine blade, the effective cross-sectional area exposed to water in a vertical direction is lesser than the conventional hydrokinetic turbine type. The net value of C_T and C_P is lower for tapered turbine blade compared to conventional turbine blade.
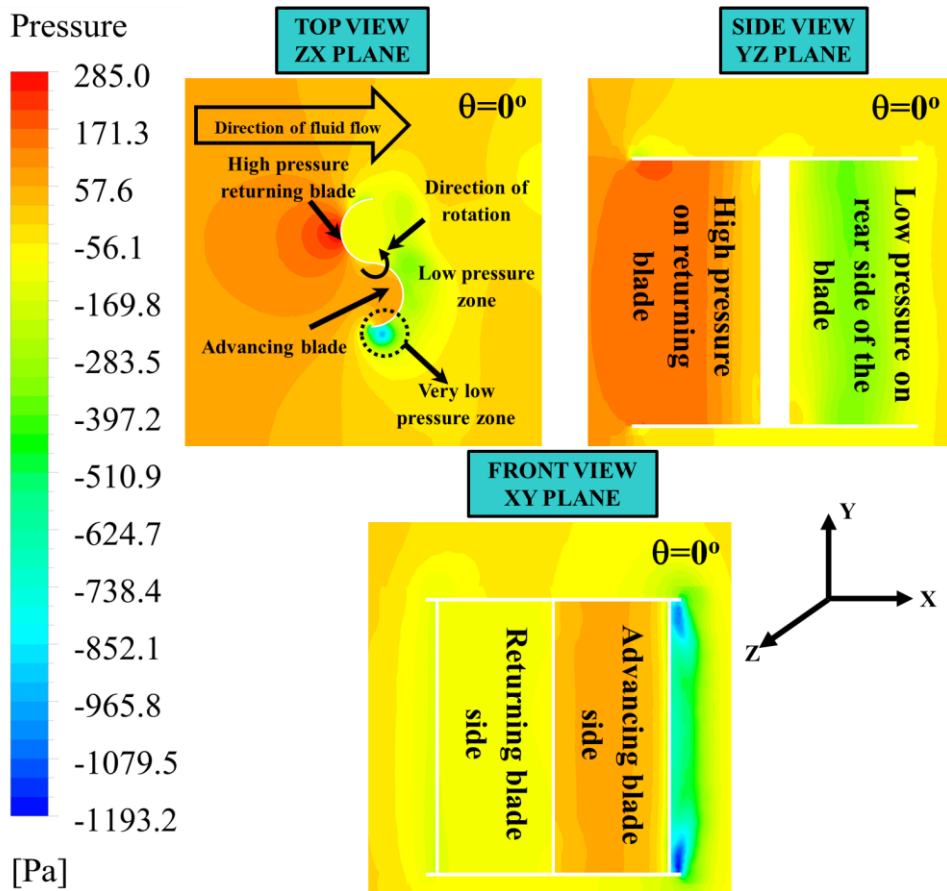
(a)
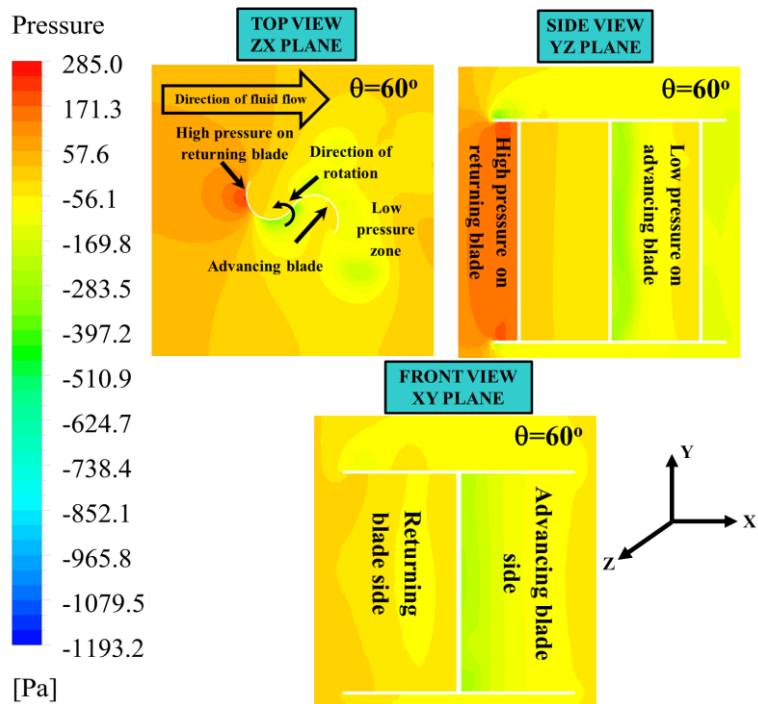
(b)
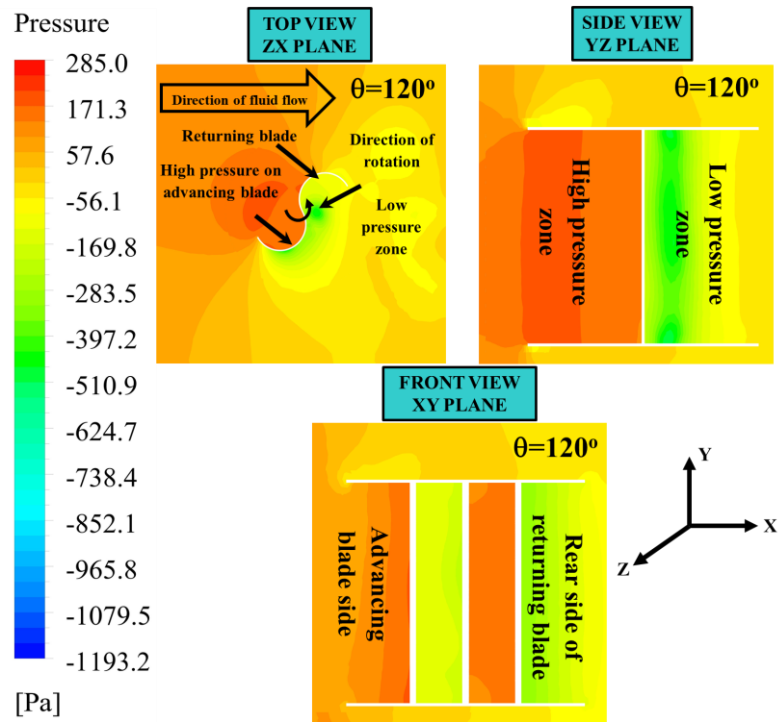
(c)

Figure 4.14 Pressure contour plots for conventional turbine blade at different angular positions θ=0° (a), 60° (b) and 120° (c)

(d)

(e)

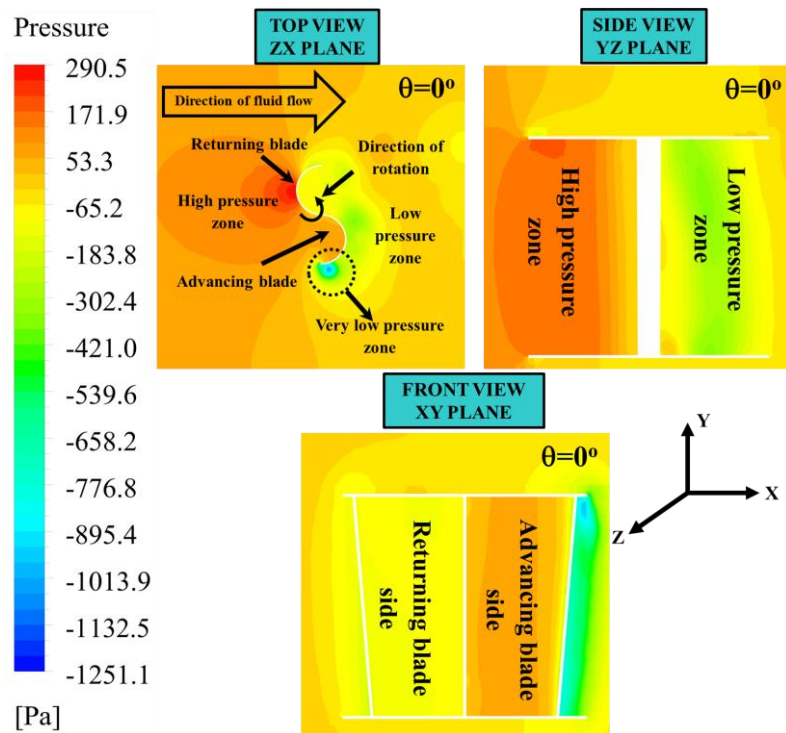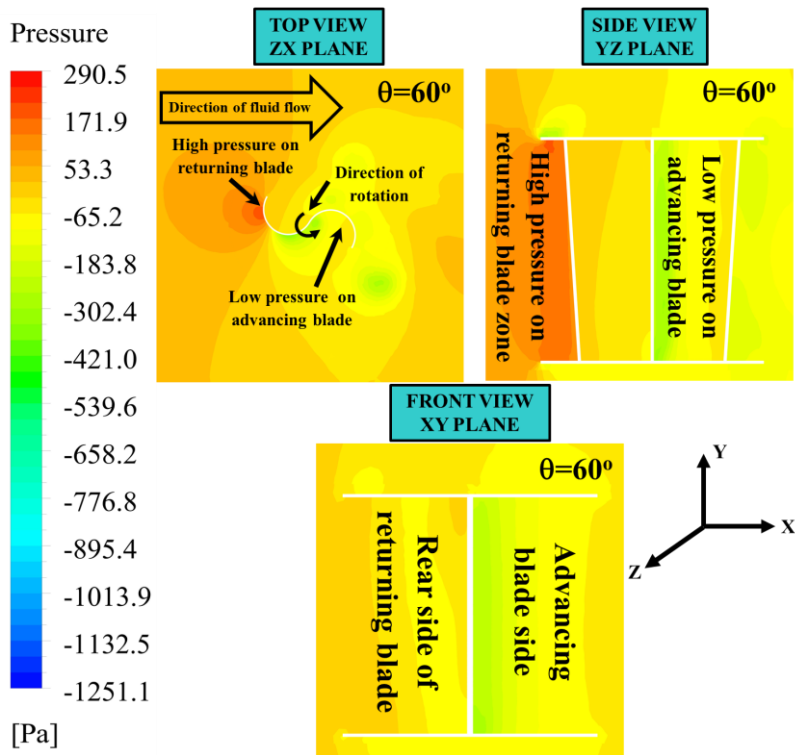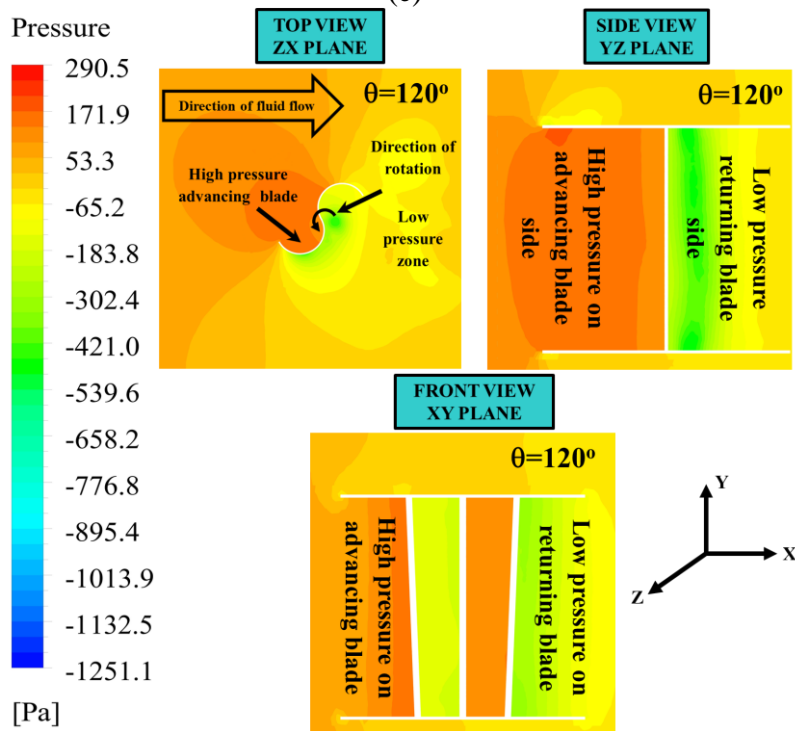

(f)

Figure 4.15 Pressure contour plots for tapered turbine blade at different angular positions θ=0° (d), 60° (e) and 120°(f)

4.2.3.2 Velocity contour and streamline plots

Velocity contour plots predict the velocity variation in different regions near the blade profiles inside the flow domain. Figures 4.16 (g-i) and Figures 4.17 (j-l) shows the velocity contour plots for conventional and tapered Savonius hydrokinetic turbine blades at three different angular positions such as θ=0°, 60° and 120° with an inlet velocity of 0.5 m/s for TSR of 0.7. All the angular positions of velocity contour plots are presented in three different views, front view (XY plane), side view (YZ plane), and top view (ZX plane), respectively. The direction of rotation of the turbine blade (anticlockwise) and fluid flow direction are shown in velocity contour plots (Figures 4.16 (g-i) and Figures 4.17 (j-l)). The maximum and minimum values of velocities are represented by red and blue colours at the left side of the velocity contour plots. The velocity of the incoming water is constant up to the turbine rotating zone. When the turbine rotates, two important zones are developed such as the high-velocity zone and wake zone. The high-velocity zone developed at the tip of the advancing blade side for the conventional and tapered turbine blades. Similarly, the wake zone is developed at the downstream side of the turbine blade for conventional and tapered turbine blades, at all the angular positions θ=0°, 60°, and 120° as shown in Figures 4.16 (g-i) and Figures 4.17 (j-l). The trend obtained in the present CFD simulations is similar to the previous investigations carried out by various researchers (Akwa et al. 2012a; Al-Ghriybaha and, Mohd Fadhli Zulkafli, Djamal Hissein Didane 2019; Kacprzak et al. 2013; Kerikous and Thévenin 2019b; Kumar and Saini 2017a; b; Mosbahi et al. 2019; Ramadan et al. 2020; Sarma, N. K. Biswas and Misra 2014).

For the conventional and tapered Savonius hydrokinetic turbine blades, the maximum velocity obtained at the tip of the advancing blade is 1.4 and 1.42 m/s at an angle of θ=0° (Alom and Saha 2018, 2019; Talukdar et al. 2018) as shown in Figures 4.16 (g) and 4.17 (j). Similarly, at an angle of 120°, the high-velocity zone developed at the rear side of the advancing blade profile, as shown in Figures 4.16 (h) and 17 (i). At an angle of rotation of 60° for the case of tapered Savonius hydrokinetic turbine, the extremely intensified piercing flow of velocity vectors moves away from the edge of the advancing blade, which in-turn decays the performance of the turbine (Sarma, N. K.

Biswas and Misra 2014; Talukdar et al. 2018). The velocity contour plots at an angular position of 60° for conventional and tapered Savonius hydrokinetic turbine blades are shown in Figure 4.16 (h) and Figure 4.17 (k). In the case of a tapered turbine blade, it is observed that the high-velocity zone is developed at the exit side of the advancing turbine blade (Figure 4.17 (k), top view ZX plane) and such a high-velocity zone is very less in conventional Savonius hydrokinetic turbine (Figure 4.16 (h)) (Talukdar et al. 2018). It is expected that these streamline patterns would have less momentum exchange between the water stream and the turbine rotor (Talukdar et al. 2018).

Such performance degradation is also reported by Sarma et al. 2014 and Talukdar et al. 2018 due to sharp velocity vectors. Therefore, there is a reduction in C_T and C_P values for the tapered turbine blade compared to the conventional turbine blade. In order to study the complete flow profile around the conventional and tapered Savonius hydrokinetic turbine, streamline plots were plotted at three different angular positions such as θ=0°, 60°, and 120° as shown in Figures 4.18 (m-r). It is evident from these figures that there is a high degree of randomness in the flow behind the conventional and tapered Savonius hydrokinetic turbine, which induces turbulence in the flow. It is observed that high turbulence zone developed at the rear side of the conventional and tapered Savonius hydrokinetic turbine (Kumar and Saini 2017a; b). The high-velocity zone developed at the tip of the advancing blade for the case of conventional and tapered turbine blades, as shown in Figures 4.18 (m) and (p) (Kumar and Saini 2017b; a). Similarly, the high-velocity zone developed at the exit side of the tapered turbine, as shown in Figure 4.18 (q) at an angle of rotation of θ=60° (Sarma, N. K. Biswas and Misra 2014; Talukdar et al. 2018).
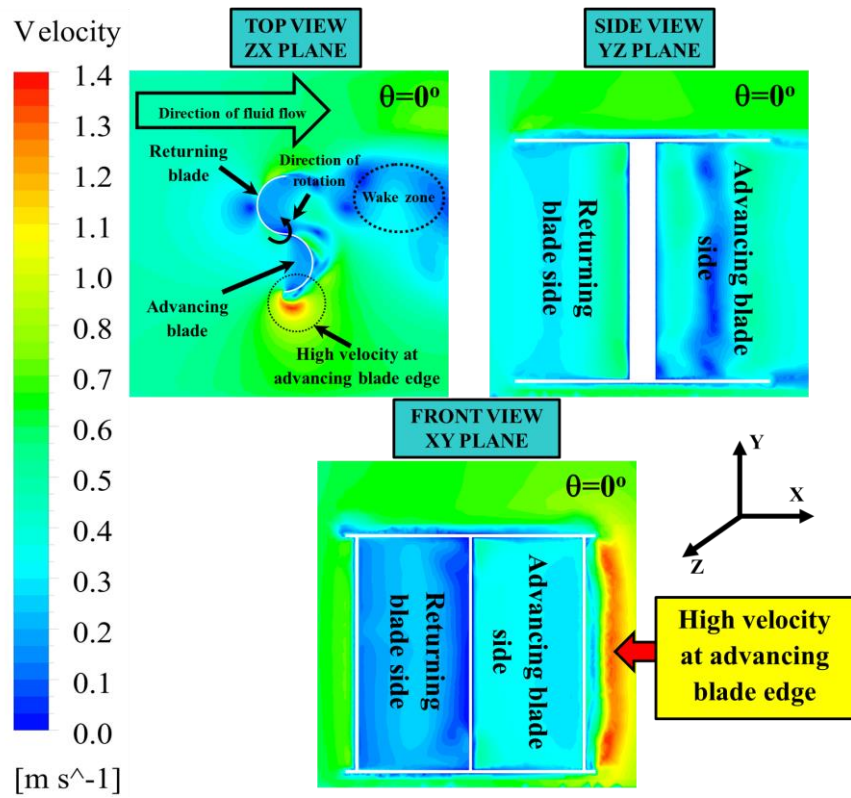
(g)
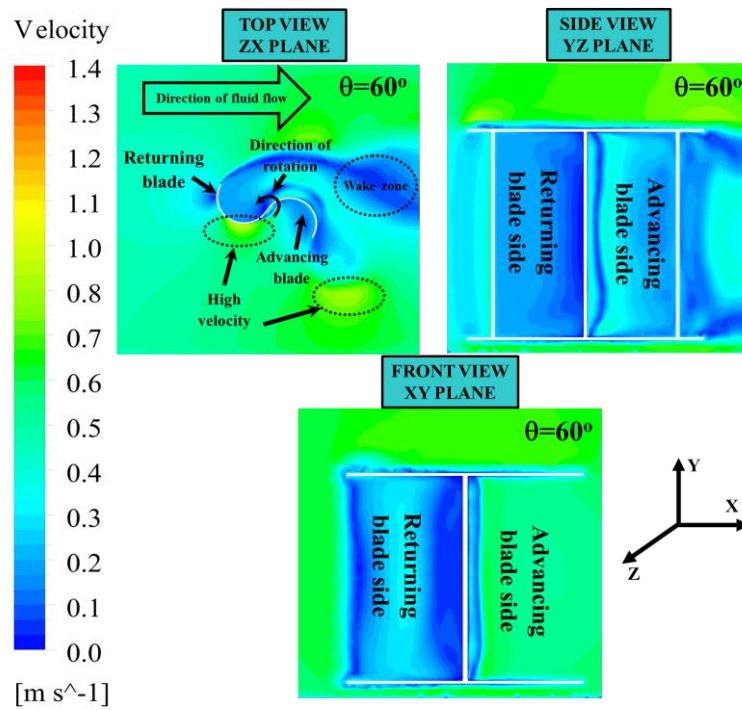
(h)
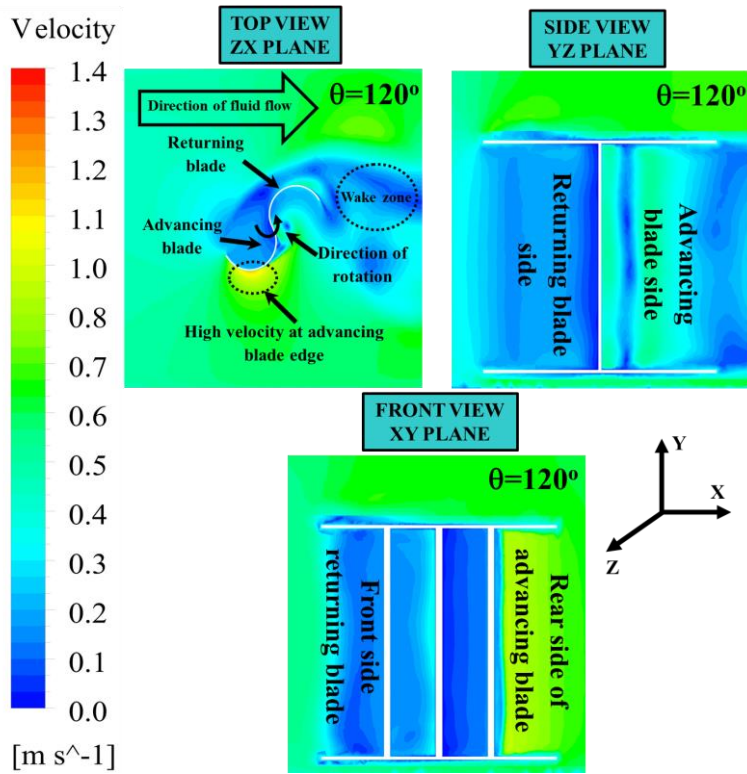
(i)

Figure 4.16 Velocity contour plots for conventional turbine blade at different angular

positions from 0° (g), 60° (h) and 120° (i)

(j)

(k)

(l)

Figure 4.17 Velocity contour plots for tapered rotor blade at different angular

positions from 0° (j), 60° (k) and 120° (l)

125

(m)

(n)

(o)

126
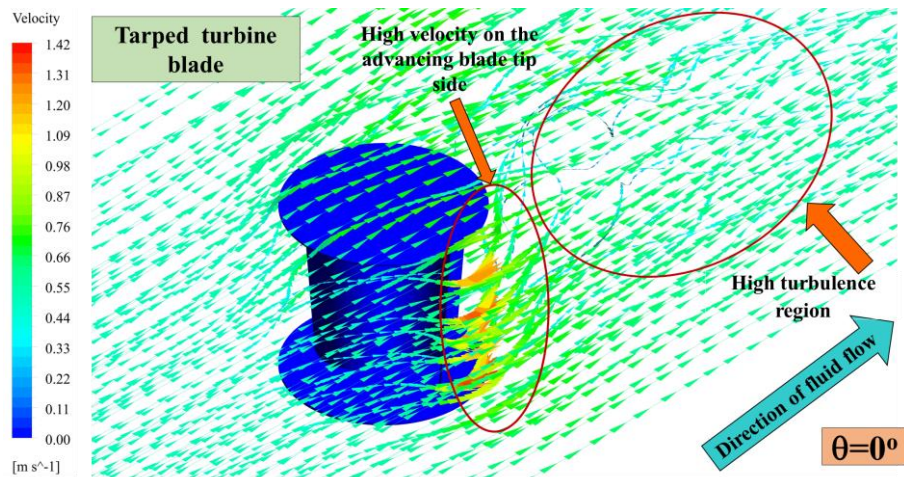
(p)
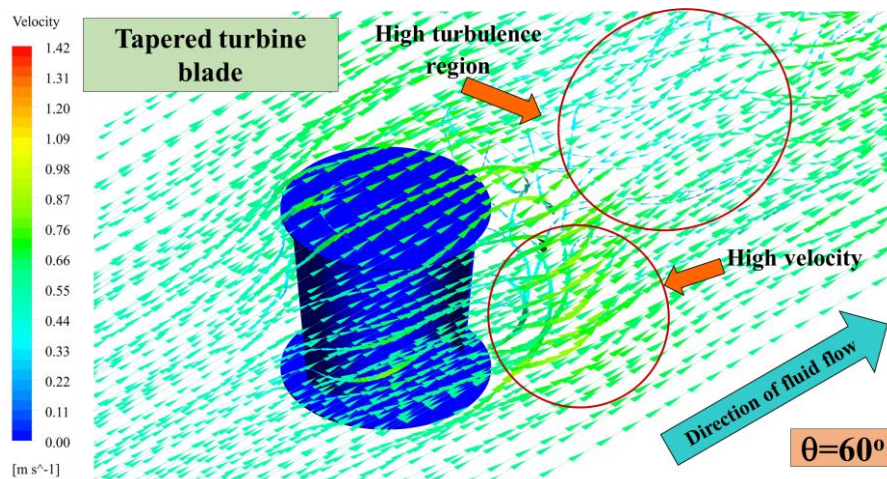
(q)
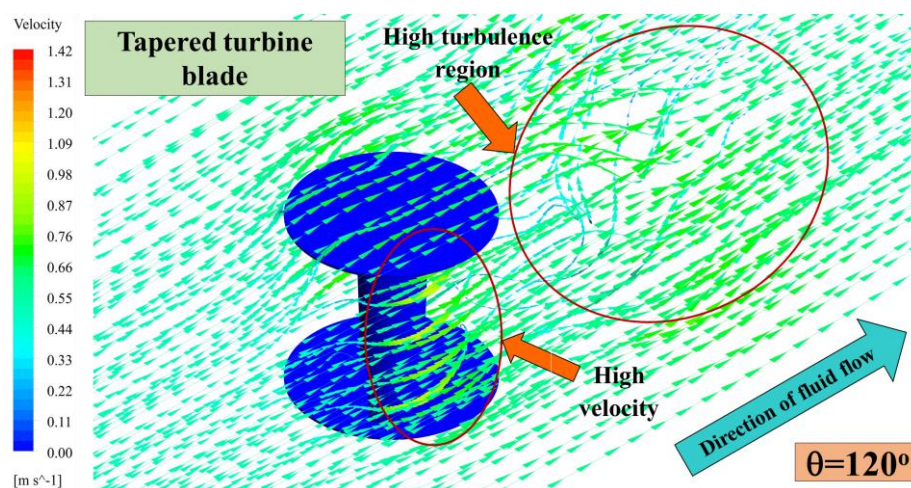
(r)

Figure 4.18 Streamline plots for (m, n and o) conventional and tapered (p, q and r)

rotor blade at different angular positions from 0°, 60° and 120°

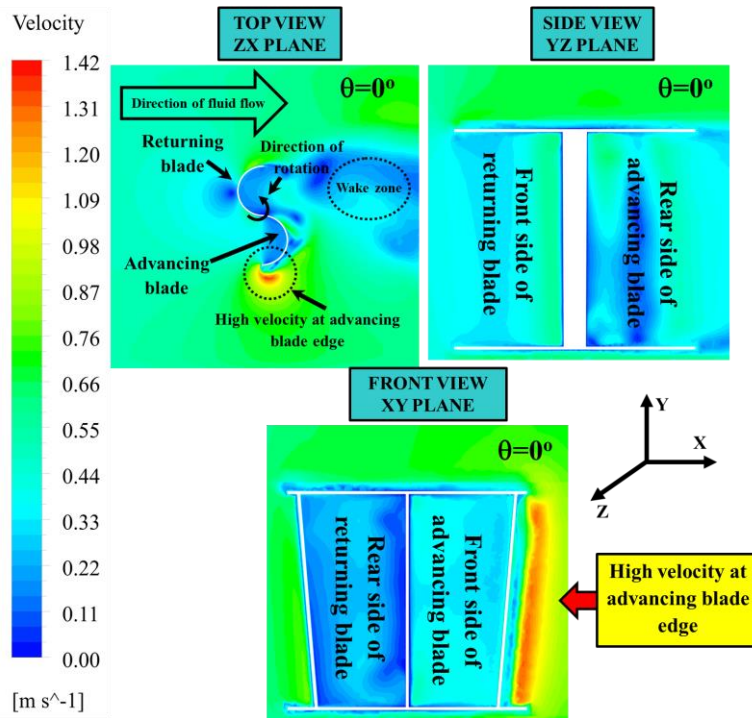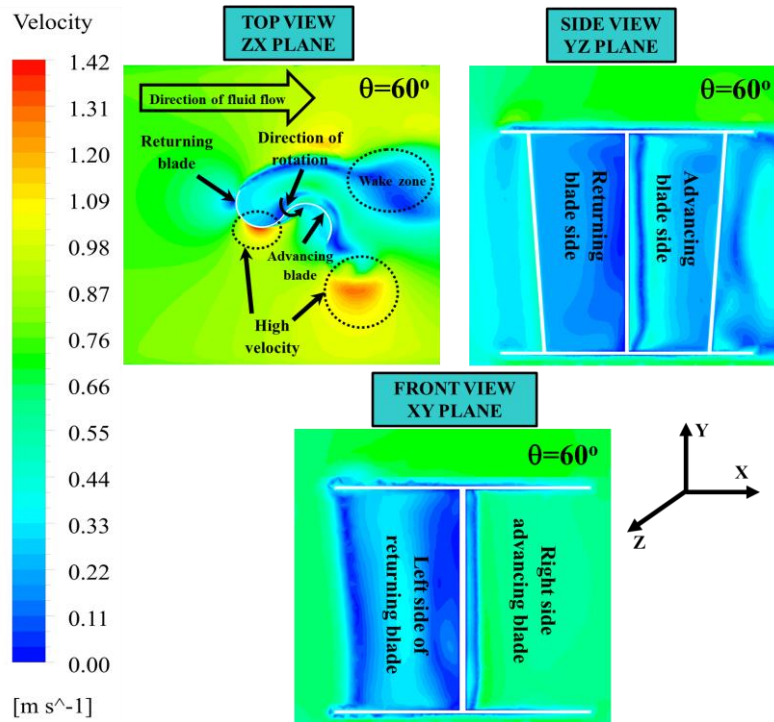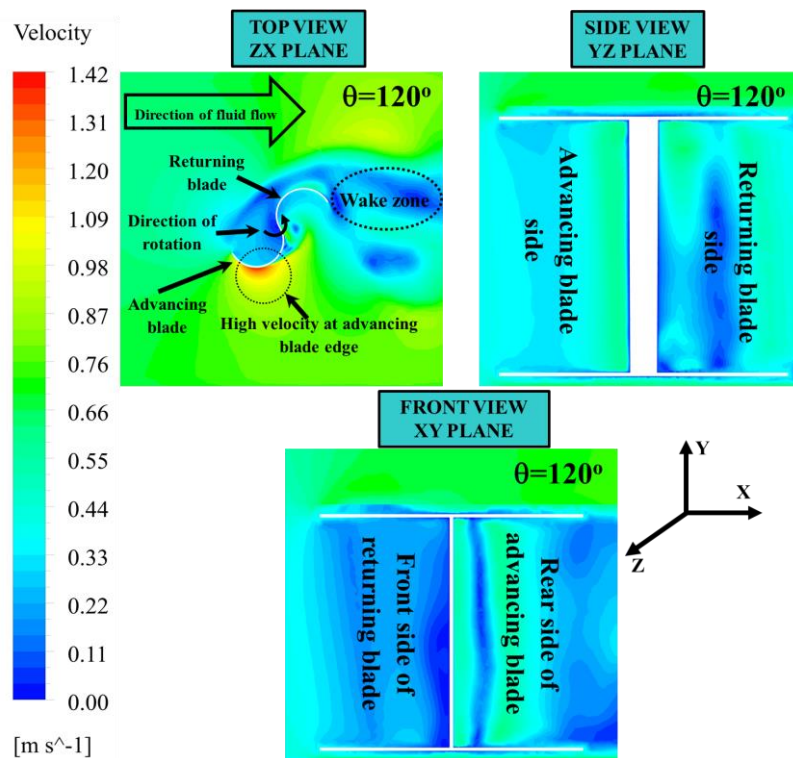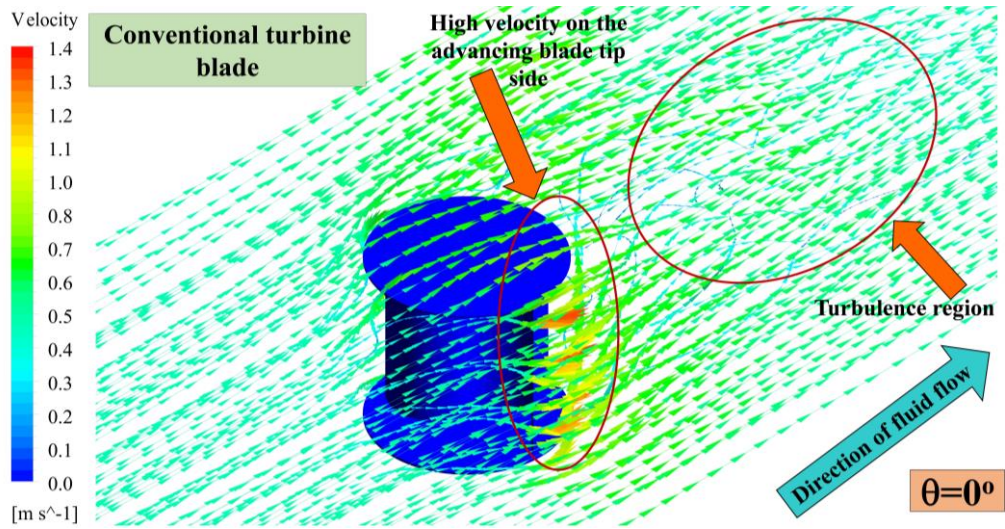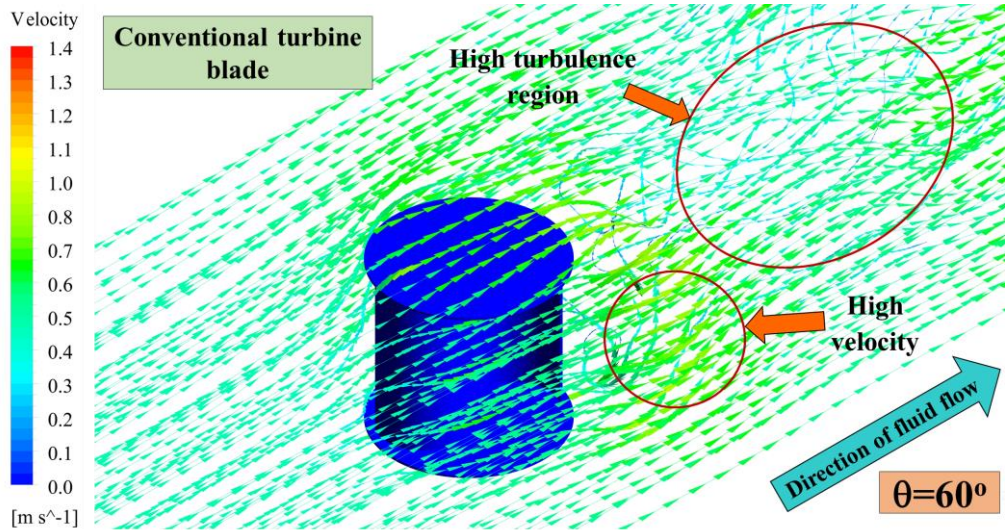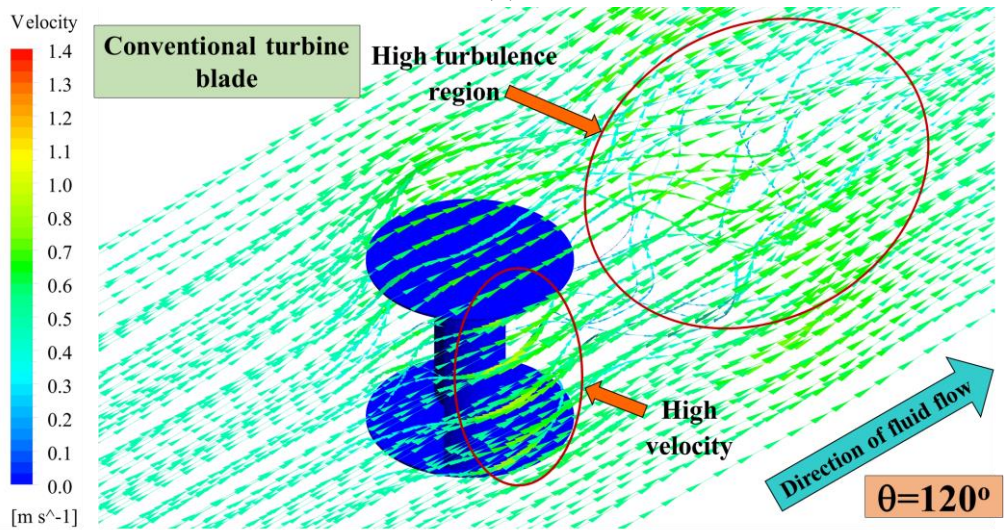### 4.2.3.3 Performance parameters

The various performance parameters, such as the C_T and C_P with respect to tip speed ratio (TSR) are calculated by using the equations 3.14 to 3.17. In the present investigation, the range of tip speed ratios used for the evaluation of C_T and C_P are 0.7–1.3 for both conventional and tapered turbine blades. From the numerical plots found from the unsteady CFD simulation results, it is seen that the value of C_T of turbine blades decreases from 0° to 23°, and it is negative at the angle of the rotation ranging from 24°- 49° at a TSR of 0.7 for the conventional turbine.

The $-C_{Tmin}$ is higher for a tapered turbine compared to a conventional turbine. For the conventional turbine, $+C_T$ is enhancing from 50° until it reaches 107° the turbine blade develops the $+C_{Tmax}$ at an angle of rotation (θ) of 108°and 292°. The $+C_{Tmax}$ is lower for a tapered turbine blade compared to a conventional turbine. From Figures 4.12 (a-b) the value of $+C_{Tmax}$ is higher and lower $-C_{Tmin}$ developed for conventional turbine and lower $+C_{Tmax}$ and higher $-C_{Tmin}$ developed for a tapered turbine blade. It is noted that the average value of C_{Tmax} is higher for the conventional turbine as compared to the tapered turbine. Therefore, the C_T and C_P of the conventional turbine blades are higher than the tapered turbine with respect to tip speed ratio (TSR) ranging from 0.7 to 1.3.

The values of C_{Pmax} with respect to TSR using experimental and CFD investigation carried out using semi-circular blade profiles and the present investigation are shown in Table 4.7. The value of C_{Pmax} for the conventional Savonius hydrokinetic turbine used in the present investigation is slightly lower than the C_{Pmax} value of the Semi-circular blade profiles. All the previous studies were carried out using the turbine blade's equal top side and bottom side diameter (without taper). In the present CFD investigation, the main aim was to study the effect of taper on the performance of the Savonius hydrokinetic turbine blade. Since overlap ratio is not considered for the present investigation C_{Pmax} is lower than the other semi-circular blade profiles. The value of C_{Pmax} for the tapered turbine with a taper angle of 95° (inside angle between H_R and D_{Bottom}) is lower compared to without taper case (conventional turbine case).

Table 4.7 Comparison of performance parameter (C_{Pmax}) with previous investigators.

Researchers	Investigation	Blade profile	Parameters	C_{Pmax}	TSR
Talukdar et al. 2018 (Without taper)	Experimental	Semi circular	AR=1.0, OR=0.15	0.28	0.89
Miyoshi Nakajima 2008 (Without taper)	Experimental	Semi circular	OR=0.36	0.25	1.1
Ferrari et al. 2017 (Without taper)	CFD	Semi circular	AR=1.1, OR=0.2	0.202	0.81
Tian et al. 2018 (Without taper)	CFD	Semi circular	AR=1.1, OR=0.182	0.2471	1.0
D'Alessandro et al. 2010 (Without taper)	Numerical	Semi circular	H_R=1 m, D_r=0.4 m	0.237	1.0
Present study (Without taper)	**CFD**	**Semi circular**	**AR=1.0, OR=0.0**	**0.21**	**0.9**
Present study (With taper- taper angle of 95°) (Inside angle between H_R and D_{Bottom} is 95°)	**CFD**	**Semi-circular**	**AR=1.0, OR=0.0**	**0.2**	**0.8**

4.3 Study for the development of Novel V-shaped rotor blade

The five different V-shaped rotor blade configurations (V_1-V_5) of 72 mm diameter (D_r) and an aspect ratio (AR) of 0.7 were tested in a multipurpose tilting water flume with an inlet water velocity (V_w) of 0.3090 m/s, zero bed slope, and without taper case to compare the present results with the literature. The performance parameters such as C_P and C_T with respect to TSR are calculated experimentally using rope type dynamometer test rig. The semi-circular and five different V-shaped rotor blade geometries used in the present investigation is modeled using ANSYS design modeller, meshing is done using ANSYS workbench, and unsteady three-dimensional numerical simulations is carried out using a sliding mesh technique (SMT).

The comparative study of experimental and numerical investigation based on performance parameters with respect to TSR of different V-shaped (V_1-V_5) and semi-circular blade profiles is presented in Figures 4.19 (a and b). The curve for numerical simulation is matched with experimental results of all the five V-shaped rotor blade configurations and compared with the numerical results of the semi-circular blade profile. The C_T of the semi-circular and V-shaped turbine blades (V_1-V_5) decreases linearly with an increase in TSR as shown in Figures 4.19 (a).

The results of the present investigation are comparable with the previously published data (Alizadeh et al. 2020; Golecha et al. 2011; Ramadan et al. 2020; Talukdar et al. 2018). The C_{Pmax} values of V-shaped rotor blades with respect to tip speed ratio (TSR) for experimental and numerical results of V-shaped and semi-circular blade profiles are listed in Table 4.8. The experimental results of C_{Tmax} and C_{Pmax} of the turbine blade V_4 is 0.25 and 0.22 at a TSR value of 0.87 are shown in Figures 4.19 (a and b). The results show that C_{Tmax} and C_{Pmax} of the turbine blade V_4 are higher than V_1, V_2, V_3, V_5 and semi-circular blade profiles as shown in Figures 4.19 (a and b). The C_{Pmax} value of the turbine blade V_4 is 19.3 % higher than the C_{Pmax} value of the semi-circular blade profile. The relative error between experimental and numerical results for the rotor blades V_1-V_5 are presented in Table 4.8. The relative error is slightly low due to the accuracy of measuring instruments used for the experimental investigations and the time step size of 1° used for the present numerical study (Elbatran et al. 2017; Talukdar et al. 2018).

Higher the time step sizes such as 2.5°, 5°, 10° and 15° increases the error between the experimental and numerical results. Therefore, 1° time step value is the optimum time step value, and the error between the numerical and experimental results is also reduced (Mosbahi et al. 2019, 2020a). The average error between the experimental and numerical for C_{Pmax} is 1.82%. Therefore, the considered numerical models seem to predict the effect on the performance of the V-shaped blade profiles and the fluid flow features around the turbine of the various V-shaped configurations. The flow field around the V-shaped (V_1-V_5) and semi-circular blade profiles is explained by using pressure and velocity contour plots at different angular positions such as θ=0°, 60° and 120° in the numerical analysis section.

130
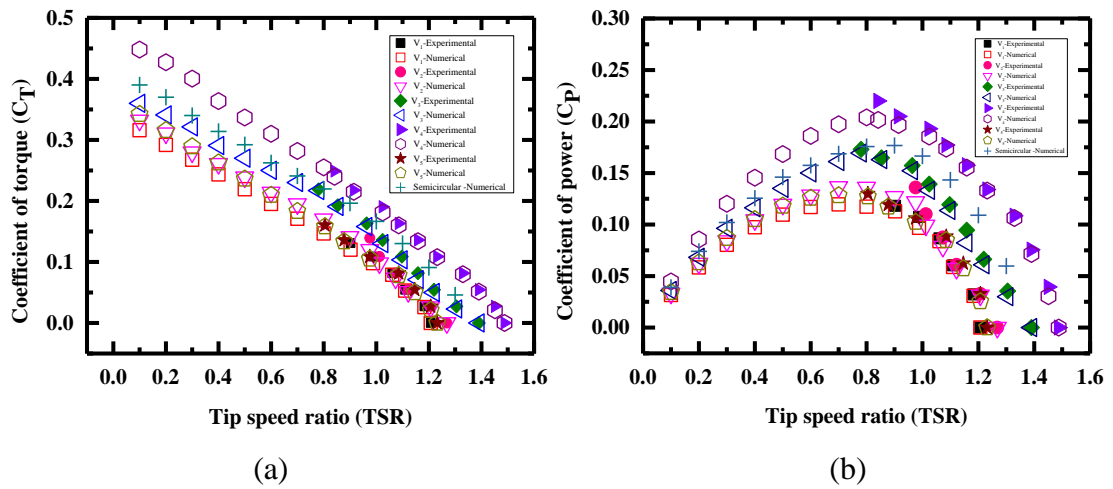
Figure 4.19 Variation of C_T and C_P with respect to TSR for semi-circular and V_1-V_5 rotor blades (Experimental and numerical).

4.4 Variation of C_T with respect to the angle of rotation (θ) of the turbine blades ((V_1-V_5) and semi-circular)

Figure 4.20 (a) shows the variation of C_T with respect to angle of rotation (θ) of the rotor blade by considering the last revolution of the semi-circular and V-shaped rotor blade profiles (V_1-V_5) for the case of C_{Pmax} with respect to experimental TSR. During the rotation, turbine blade experiences positive torque ($+C_T$) at some angle of rotation and negative torque ($-C_T$) at some other rotation angle. The rotor blade V_4 is having a positive coefficient of torque for the angle of rotation (θ) in the range of θ=65°- 170°, similarly negative coefficient of torque in the range of θ=170° to 240° at a TSR of 0.87. The semi-circular, V_3, and V_4 rotor blade profiles exhibit maximum ($+C_{Tmax}$) and minimum ($-C_{Tmin}$) peak C_T at a TSR of 0.9, 0.79 and 0.87 as compared to other blade profiles (V_1, V_2, and V_5).

The value of $+C_{Tmax}$ is higher and $-C_{Tmin}$ is lower for V_4 compared to other blade profiles (semi-circular, V_1, V_2, V_3, and V_5). The average value of C_T for the last revolution of the turbine blade V_4 is higher compare to other blade profiles (semi-circular, V_1, V_2, V_3, and V_5). Figure 4.20 (b) shows the polar plot for semi-circular and V-shaped rotor blade profiles with respect to blade rotation (θ) for the case of C_{Pmax} with respect to experimental TSR. The rotor blade V_4 is having a maximum value of C_T at θ=120°,

131

θ=300° and minimum -C_T at θ=30° and θ=210° (Ostos et al. 2019a). The flow field around the semi-circular and V-shaped blade profiles (V₁-V₅) at different angular positions such as θ=0°, 60° and 120° is explained using pressure and velocity contour plots.

(a)

(b)
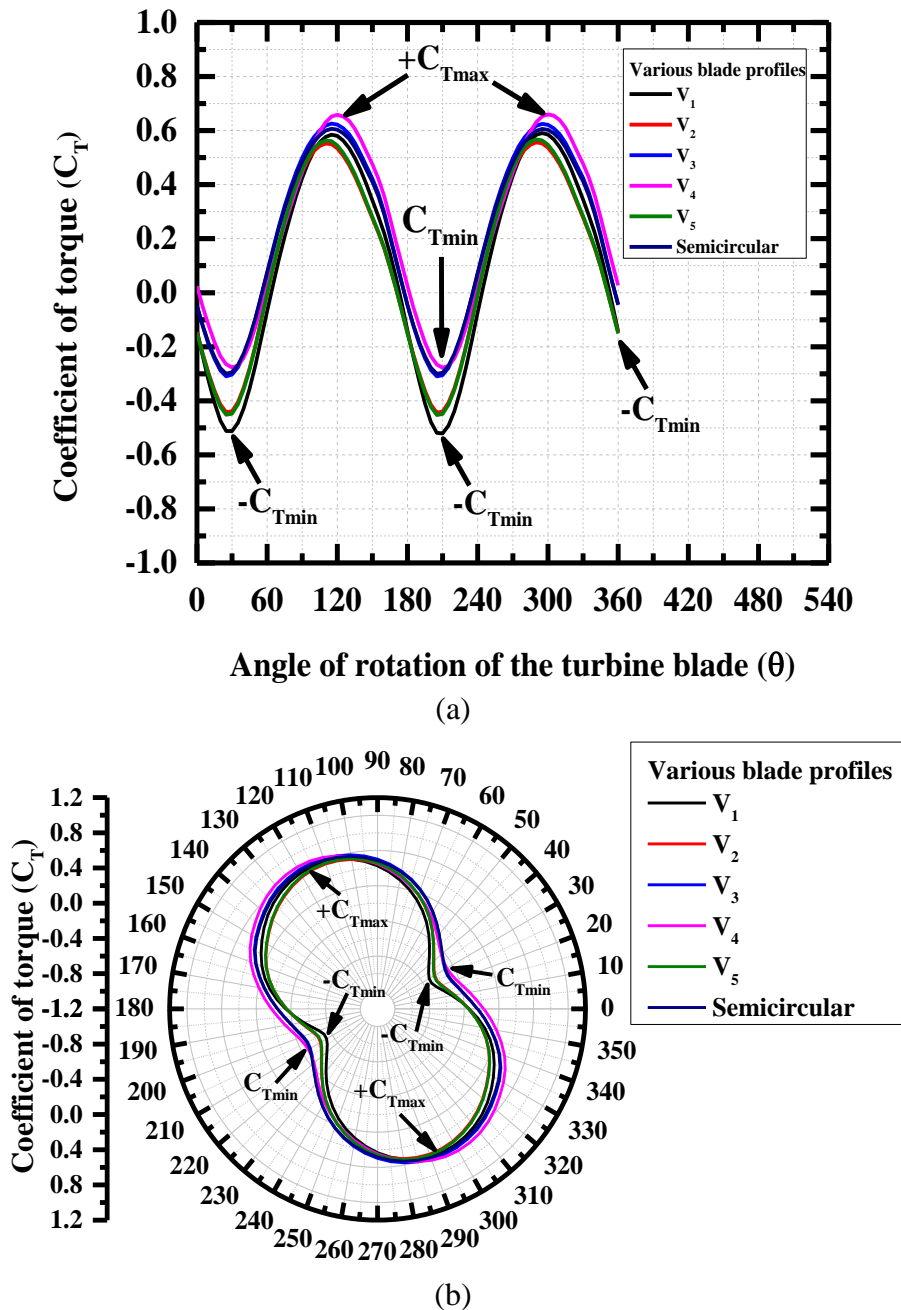
Figure 4.20 (a) Variation of C_T with respect to rotor blade rotation (θ) and (b) variation of C_T with respect to rotor blade rotation (θ) using the polar plot for semi-circular and V₁-V₅ blade profiles

132

Table 4.8 Experimental and numerical comparison of semi-circular and V-shaped blade profiles

Sl. No	Blade profile	Experimental/ CFD	C_{Pmax}	TSR	Relative error %
1.	V_1	Experimental	0.118	0.91	1.6
		CFD	0.12	0.7	
2.	V_2	Experimental	0.136	0.98	0.72
		CFD	0.137	0.7	
3.	V_3	Experimental	0.173	0.79	1.16
		CFD	0.171	0.79	
4.	V_4	Experimental	0.22	0.87	4.7
		CFD	0.21	0.87	
5.	V_5	Experimental	0.13	0.81	0.7
		CFD	0.129	0.7	
6.	Semi-circular	CFD	0.176	0.9	------

4.4.1 Numerical analysis

In this section, numerical analysis of semi-circular and V-shaped rotor blade profiles (V_1–V_5) is carried out using the sliding mesh technique (SMT). The simulation results for semi-circular and V-shaped blade profiles (V_1–V_5) are extracted with respect to the distribution of flow around the semi-circular and V-blades, and maximum values of C_P obtained for respective experimental values of TSR =0.91 (V_1), 0.98 (V_2), 0.79 (V_3), 0.87 (V_4), 0.81 (V_5) and 0.9 (semi-circular) with an inlet water velocity of Vw = 0.3090 m/s.

4.4.2 Pressure contour plots

Figures 4.21 (a-r) shows the pressure contour plots for semi-circular and V-shaped rotor blade configurations (V_1-V_5) with different angular positions θ=0°, 60° and 120° with respect to experimental C_{Pmax}. The maximum and minimum pressure values are shown on the legend with red and blue colours. Figures 4.21 (a-r) shows that pressure drop

across the rotor blade from upstream to the downstream side of the computational domain. The pressure found at the computational domain inlet is uniform, whereas the pressure values are found to be higher on the upstream side of the turbine blade and lower pressure on the downstream side. The contour plots obtained from numerical studies illustrate fluid flow direction, the direction of rotor blade motion, and several significant zones formed during rotor blade rotation. The pressure distribution patterns obtained in the present investigation for semi-circular blade profile is similar to the contours obtained in the previous studies (Fujisawa and Gotoh 1992; Kumar and Saini 2017b; a; Layeghmand et al. 2020; Ramadan et al. 2020; Sarma, N. K. Biswas and Misra 2014; Shaheen et al. 2015; Talukdar et al. 2018).

The turbine blade extracts power from the flowing water in the channel due to high-pressure zone at the front side of the advancing blade side and low-pressure zone at the rear side of the advancing blade side helps in creating the pressure drop which affects the rotation of the turbine blade (Elbatran et al. 2017; Mosbahi et al. 2020a; Talukdar et al. 2018). Figures 4.21 (a-r) demonstrates that the pressure at the upstream side of the flow near the blade area is highest, while the downstream side has a lower pressure area (Talukdar et al. 2018). The rotation of blade is created due to difference in values of these two pressure areas. The pressure distributions around semi-circular and V-shaped blade profiles (V_1-V_5) at the different angular position of θ= 0°, 60° and 120° are shown in Figures 4.21 (a-r).

At the blade rotation angle, θ=0° high-pressure zone is observed at the returning blade side and low-pressure zone is developed at the downstream side of the advancing blade for semi-circular and V_1-V_5 rotor blade profiles used for the simulation (Ostos et al. 2019a) as shown in Figures 4.21 (a, d, g, j, m and p). At rotation angle of θ=60° the distribution of pressure is similar to θ=0° shown in Figures 4.21 (b, e, h, k, n, and q). For the rotation angle of θ=120°the high-pressure zone is developed at the advancing blade side, and the low-pressure zone is developed at the returning blade side (Ostos et al. 2019a) as shown in Figures 4.21 (c, f, i, l, o and r).

During the rotor blades V_1 and V_2 rotation, at an angle of rotation of $\theta=60°$ the pressure acting on the returning blade profile side is higher due to the higher straight edge profile on the returning blade side as shown in Figures 4.21 (e and h). It is observed that high pressure acting on the returning blade profile develops more drag and tends to produce greater negative torque ($-C_{Tmin}$) due to two complete straight edges (100%) of blade profile V_1 and V_2 is having 81% of the straight edge with a very small arc radius of 0.18L at the returning blade profile side (Figures 4.21 (b and c)). Hence at an angle of rotation of $\theta=60°$, the performance of rotor blades V_1 and V_2 is reduced due to greater production of $-C_{Tmin}$. The value of $-C_{Tmin}$ for the turbine blade V_2 is slightly lower than V_1. The net C_P developed by the turbine blade V_1 is lower than V_2.

For the rotor blades V_3 and V_4 at an angle of rotation of $\theta=60°$, the straight edge length on the returning side of blade profile V_3 and V_4 decreases by 0.62L, 0.43L respectively and the arc radius of blade profile 0.37L and 0.56L slightly increase V3 and V4. Since the turbine blade V_3 is having a higher straight edge on the returning blade profile than V_4, it is observed that pressure acting on the returning blade profile for the turbine blade V_3 is higher than V_4. Because of this, slightly higher drag and more negative torque is developed by the turbine blade V_3 than the turbine blade V_4. Therefore, the net performance of the turbine blade V_3 is lower than the turbine blade V_4.

The rotor blade V_5 has a bigger arc radius of 0.75L and the least straight edge length of 0.24L compared to the rest of the profiles. The arc radius of the V_5 turbine blade is 4.2, 2.02, and 1.4 times V_2, V_3 and V_4 blade profiles. At $\theta=0°$, the normal frontal area and curvature of the returning blade profile V_5) has a slightly flatter surface that is more exposed to a high-pressure zone when compared to V_2, V_3 and V_4. The width of arc at the returning blade surface is also higher than V_2, V_3, and V_4 blade profiles. Therefore, effective negative torque developed by the returning blade profile for the turbine blade V_5 is greater as compared to V_2, V_3, and V_4. Similarly, the positive torque developed is also lower due to the greater arc radius and slightly flatter surface at the advancing blade profile. There is a drastic reduction of the turbine blade's water retention capability during rotation due to a slightly flatter surface at the advancing blade. Therefore, the turbine blade V_5 will not receive a sufficient load, and stops at the

threshold load. This results in a reduction of net power developed by the turbine blade V_5.

It is observed from Figure 4.21 (o) that the difference in pressure acting on the advancing and returning blade is maximum for the turbine blade V_4, and it is minimum for the turbine blade V_1 (Figure 4.21 (d)), when the angle of rotation of the turbine blade is at $\theta=120^o$. A similar trend of higher pressure differences between advancing and returning blade profiles is observed in the research work carried out for the enhancement of C_P as reported by Kumar and Saini, 2017a; Mosbahi et al., 2019; Ramadan et al., 2020; Wahyudi et al., 2015, 2013; Zhang et al., 2017b.

The maximum power extraction is obtained for the blade profile V_4, when the angle of rotation of the turbine blade is at $\theta=120^o$ as shown in Figure 4.21 (o). The least power extraction occurs for the case of rotor blade V1 (Figure 4.21 (f)) compared to the remaining blade profiles. The arc angle of returning blade side of a semi-circular blade profile (Figure 4.21 (a)) is higher than the V_4 blade profile (Figure 4.21 (m)). Due to more arc in returning blade side of semi-circular blade profile, high-pressure zone exposed to the region with more arc is higher and high-pressure region adversely affects the returning blade side, which reduces C_P (Ramadan et al. 2020) as compared to V_4 blade profile.

A greater negative pressure zone is formed near the tip of the advanced blade profile for the rotor blade V_4 at an angle of rotation of $\theta=0°$ as shown in Figures 4.21 (m) and behind the advanced blade, a wide low-pressure zone is developed for the rotor blade V_4 (Figure 4.21) as compared to semi-circular, V_1, V_2 and V_3 blade profiles as shown in Figures 4.21 (a, d, g, j and p), which helps in increasing the driving torque of the rotor blade V_4 (Ramadan et al. 2020; Saad El-Deen et al. 2020). Due to lower arc at the returning blade profile for the rotor blade V_4 as compared to the semi-circular blade, there is a reduction of drag force and therefore negative torque developed by the V_4 blade profile is lower than the semi-circular blade profile. The average torque generated by the turbine blade V_4 thus obviously increases, as illustrated in Figures 4.20 (a and

b). Therefore, the rotor blade V_4 captures more power and net power developed by the turbine V_4 increases.

At $\theta=0°$, the stagnation point on the returning side of the rotor blade V_4 (Figure 4.21 (m)) is nearer to the tip of the blade as compared to the semi-circular blade profile (Figure 4.21 (a)) leads to lower negative torque (Tian et al. 2018). Because of the greater blade curvature in the semi-circular profile, it is assumed that flow separation occurs earlier than the V_4 blade profile (Alom and Saha 2019; Shaheen et al. 2015).

In addition, at $\theta=120°$, the area of high-pressure zone generated at the advancing side of the blade profile V_4 (Figure 4.12 (o)) is more compared to the semi-circular blade profile (Figure 4.21 (c)). These differences in the area of pressure zones are the main feature of improving the power produced between the semi-circular (Figure 4.21 (c)) and V-shaped blade design (V_4) (Figure 4.21 (o)). The rotor blade profile V_4 helps to guide more fluid into the rotor's advancing blade side to enhance the positive torque generated on it as compared to the semi-circular blade profile. In this technique, the V-shaped blade profile plays a vital role in improving the turbine's performance and the novelty of the blade profile V_4.

Also, the V_4 advanced blade profile has two low-pressure zones ($\theta=0°$), and the semi-circular blade profile has one low-pressure zone, as shown in Figures 4.21 (a and m). These two low-pressure zones permit V_4 blade profile to capture more power than the semi-circular blade profile (Ramadan et al. 2020). Therefore, C_P of the V_4 blade profile is increased up to 19.3% as compared to the conventional semi-circular blade profile.

(a)   (b)   (c)

(d)   (e)   (f)

(g)   (h)   (i)

138
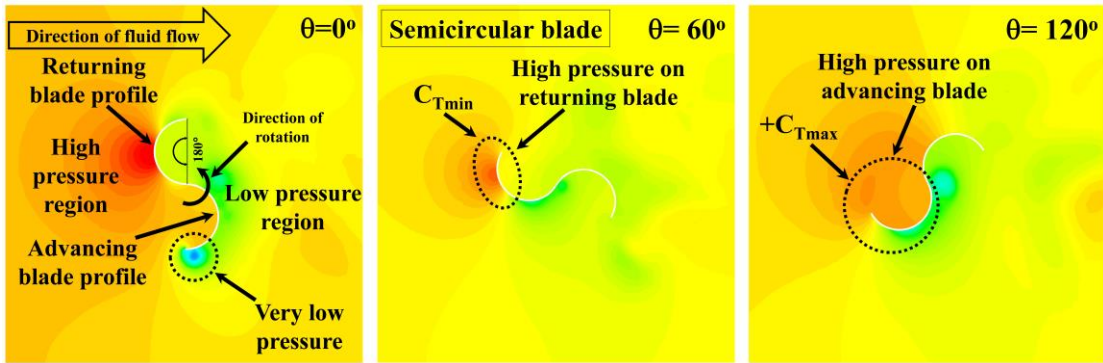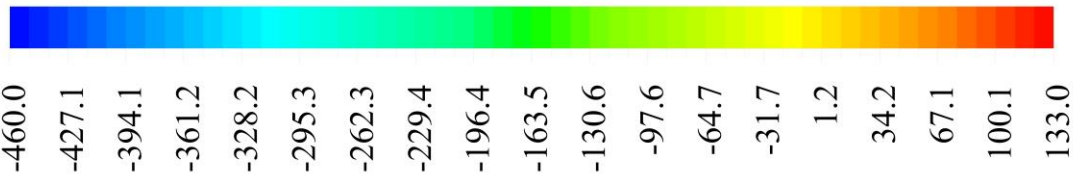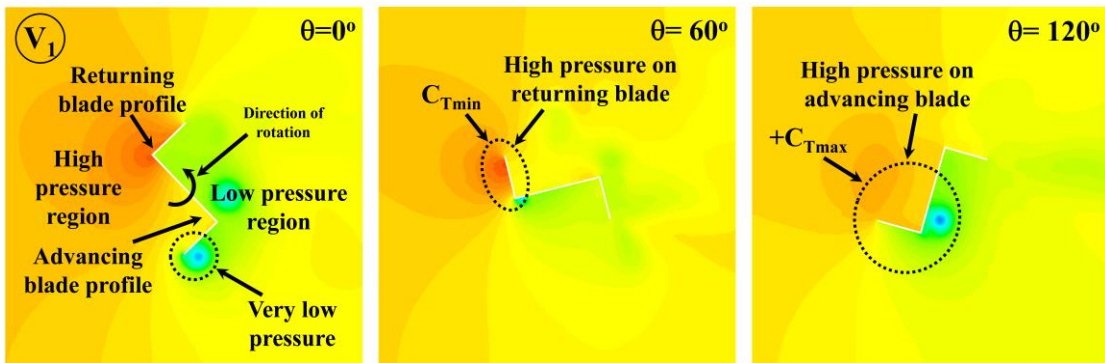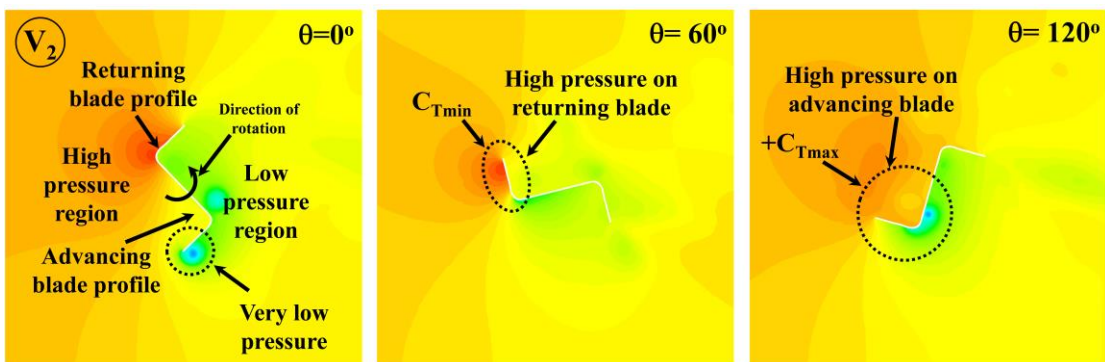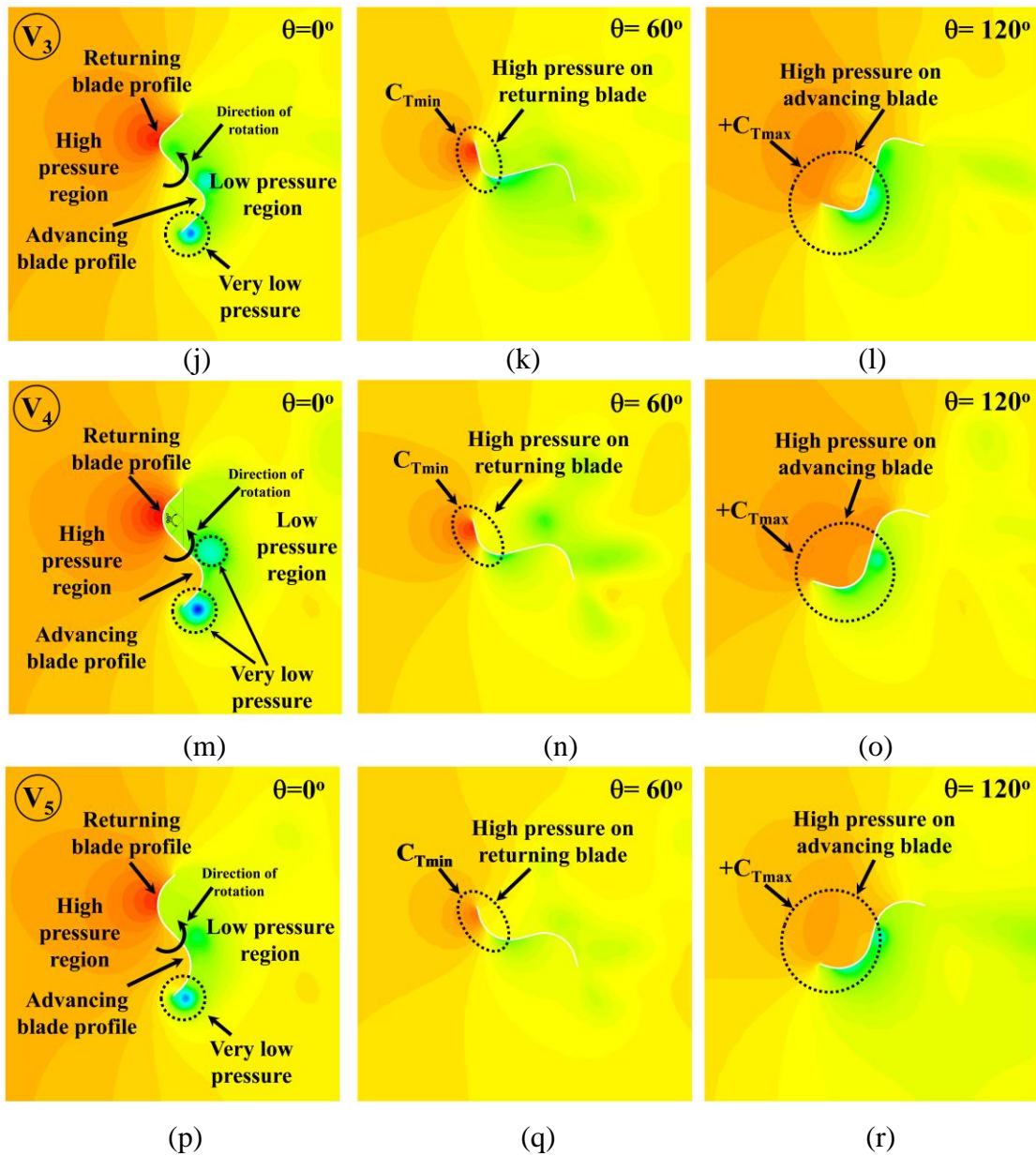
Figure 4.21 Pressure contour plots (θ= 0°, 60° and 120°) for semi-circular, V_1, V_2, V_3, V_4 and V_5 rotor blade profiles.

4.4.3 Velocity contour and Streamline plots

The velocity contour plots around the semi-circular and V-shaped rotor blade profiles (V_1-V_5) are shown in Figures 4.22 (a-r). The water velocity is constant at the upstream side till it reaches the rotating zone. When the turbine starts to rotate, various important zones are developed, i.e, high-velocity zone and wake zone. From these plots, it is observed that a high-velocity zone is developed at the tip of the advancing side of semi-

circular and V-shaped blade profiles (V_1-V_5). The wake zone is seen at the downstream side of the turbine blade and flow separation occurs at the tip of the returning blade (Fujisawa and Gotoh 1992; Layeghmand et al. 2020; Ramadan et al. 2020; Shaheen et al. 2015; Talukdar et al. 2018; Tian et al. 2018). The zonal velocity distribution observed in the present case matches with the study cases documented by the previous researchers in their respective articles (Kumar and Saini 2017b; a; Ramadan et al. 2020; Sarma, N. K. Biswas and Misra 2014; Talukdar et al. 2018; Zhang et al. 2017a).

There is a very low-velocity zone along with high-pressure zone, where the flow is semi-stagnant and acts as a brake (Ramadan et al. 2020) as shown in Figures 4.22 (a, d, g, j, m, and p). It is noticed that when water reaches the turbine blade, the velocity of water decreases at the leading edge of blade and wake zone is developed towards the downstream at different rotor angles (Fujisawa and Gotoh 1992; Shaheen et al. 2015). The angle of rotation of semi-circular and five different blade configurations are shown in velocity contour plots at θ=0°, 60° and 120° respectively corresponding to C_{Pmax}.

The rotor blade V_4 (TSR=0.87) has a greater velocity at the tip (tip vortices) of the advancing blade profile (Layeghmand et al. 2020), which results in reduced pressure at the advancing blade tip as compared to semi-circular, V_1, V_2, V_3 and V_5 rotor blade profiles. This is because the advancing side of the rotor blade profile V_4 has two straighter edges and a small arc, making it easier for the fluid flow from advancing blade tip (Tian et al. 2018). Similarly, due to small arc and two straight edges at the returning blade profile V_4, which reduces the pressure on the returning blade profile which results in lower negative torque and higher positive torque compared to semi-circular, V_1, V_2, V_3 and V_5 rotor blade profiles. The separation of fluid in semi-circular blade profile is higher (Figure 4.22 (b)) (Ramadan et al. 2018) as compared to the rotor blade V_4 (Figure 4.22 (n)) which results in higher performance for the rotor blade V_4 .

The wake formation on the concave side of the semi-circular returning blade profile is found to be larger than the V_4 blade profile (Alom and Saha 2019). There is a smaller velocity zone on the V_4 blade profile's returning side (Figure 4.22 (m)), indicating its lower negative torque as compared to the semi-circular blade profile (Figure 4.22 (a)).

This represents that the V_4 blade profile is having higher C_P as compared to semi-circular blade profile.

Due to the higher arc radius at the returning side of the semi-circular blade profile (Figures 4.22 (a)), it acts as the shield in front of the incoming fluid flow which results in a deeper stagnant zone (Eshagh et al. 2020; Tian et al. 2018). The stagnation point for the semi-circular blade profile case is at the midpoint of returning blade side (Figures 4.22 (a)) and not nearer to the tip of the blade as compared to the rotor blade V_4 (Figures 4.22 (m)) (Tian et al. 2018). This increases the pressure on the returning blade profile resulting in greater negative torque for the semi-circular blade case than the V_4 rotor blade.
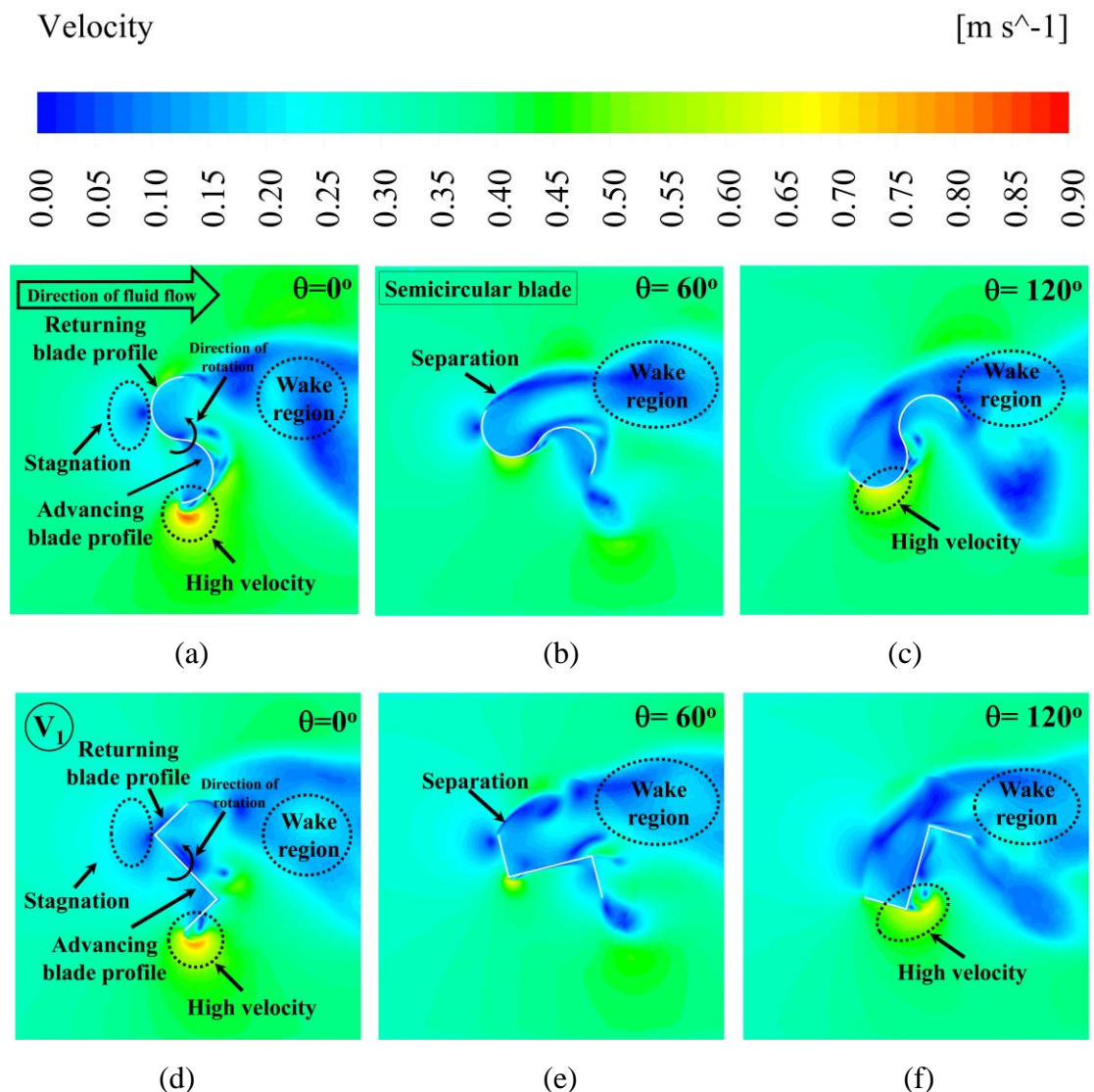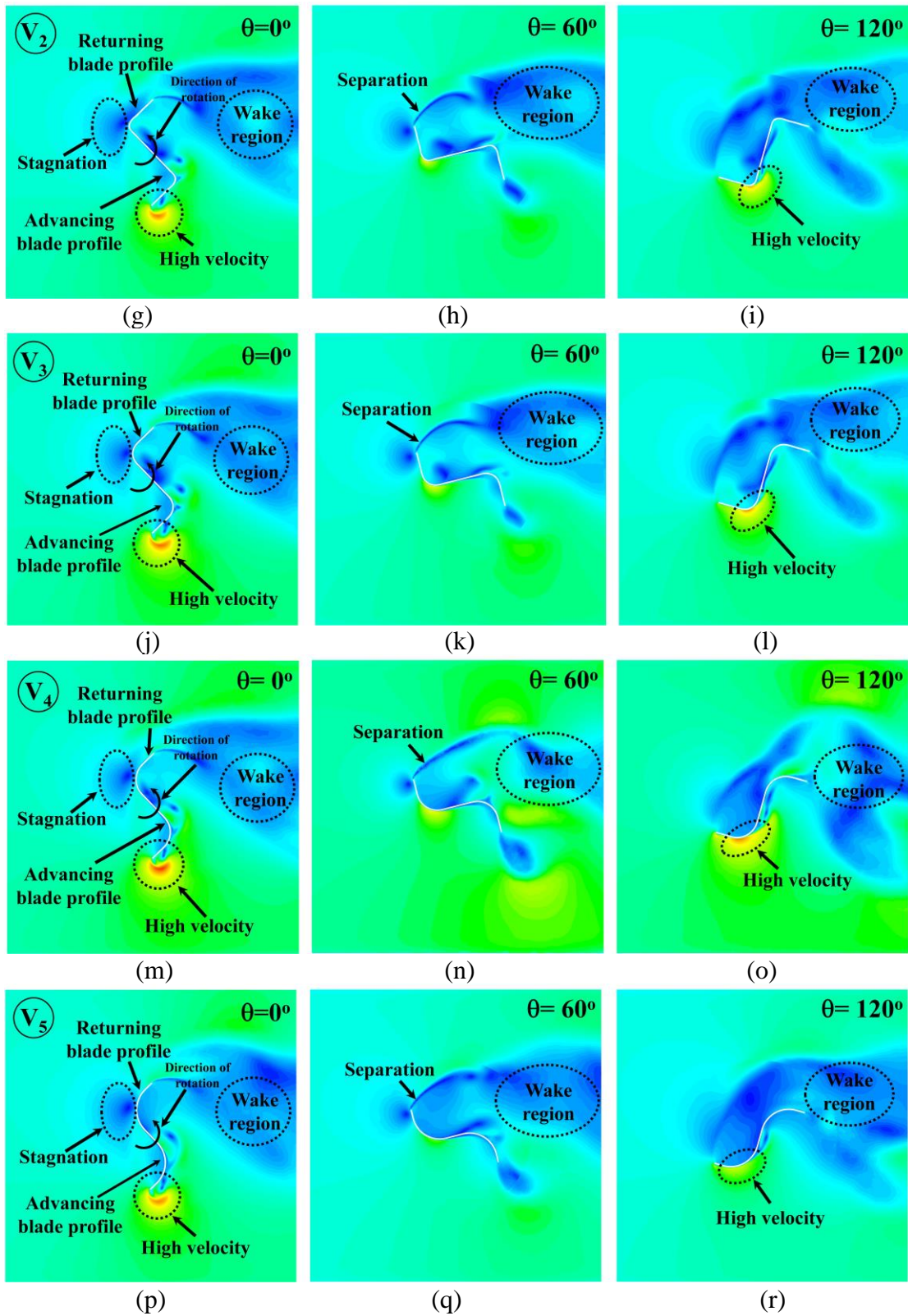
Figure 4.22 Velocity contour plots (θ= 0°, 60° and 120°) for semi-circular, V_1, V_2, V_3, V_4, and V_5 rotor blade profiles

4.4.4 Performance parameters of the semi-circular and V-shaped turbine blades (V_1-V_5)

The semi-circular and V-shaped rotor blade configurations (V_1-V_5) are designed and performance analysis is carried out using three-dimensional transient simulations using a sliding mesh technique (SMT). From the numerical plots obtained from the CFD simulation, turbine blade torque increases for the rotor blade angle ranging between $\theta=60^o$ to 170° and the further increase in blade angle ranging from $\theta=170^o$ to 240° decreases the blade torque. The positive C_T obtained when the rotor blade is at an angular position range of $\theta=60^o$ to 170° is shown in pressure contour plots (Figures 4.21 (a-r)) and polar plots (Figure 4.20 (b)).

The C_T increases due to the increase in pressure difference between the advancing and returning side of the turbine blade at an angular position from 60°-170°. Similarly, the negative torque is attained when the turbine blades are at an angular position range of $\theta=0^o$ to 60° and $\theta=170^o$ to 240°. The maximum value of C_T is reached when the turbine blade is at an angular position of 120° and the minimum at an angular position of $\theta=30^o$. Among the blade profiles, semi-circular and V_1-V_5 the C_{Tmax} and C_{Pmax} is observed for V_4 and the minimum value is for the rotor blade V_1.

4.5 Effect of overlap ratio (OR) for the modified V-shaped rotor blade V_4
4.5.1 Variation of C_T and C_P with respect to TSR for the rotor blade V_4 with OR=0.0-0.3

In this section, the three-dimensional transient CFD simulations were carried out using optimum blade profile taken from the previous study (V_4) to compute the effect of OR with zero bed slope and without taper case to compare the present results with previous literature. The turbine blades with different OR ranging from 0.0 to 0.3 were studied with an aspect ratio (AR) of 0.7 using CFD simulations and inlet velocity of water (V_W) maintained is 0.3090 m/s to evaluate C_T and C_P with respect to TSR (0.7-1.3).

The performance parameter such as C_T and C_P, calculated with respect to TSR ranging from 0.7 to 1.3. The turbine blade with an OR of 0.0 is compared with a varying OR ranging from 0.05-0.3, as shown in Figures 4.23 (a-l). The values of C_{Tmax} and C_{Pmax} with respect to TSR for different overlap ratios (0.0 to 0.3) presented in Table 4.9. Table 4.9 shows that the turbine blade with an OR of 0.0 has C_{Tmax} and C_{Pmax} of 0.29 and 0.22 at a TSR of 0.7 and 0.9 respectively. As OR increases from 0.05-0.3 with an increment of 0.05, the performance of the turbine blade is decreased. It was observed that the turbine blade without overlap ratio (OR=0.0) gives a superior performance as compared to a turbine blade with OR ranging from 0.05-0.3. Figures 4.24 (a and b) show the variation of C_T and C_P for all the overlap ratios from 0.0-0.3 with respect to TSR (0.7-1.3). To understand the flow field around the turbine blade without (OR=0.0) and with overlap ratio (OR=0.05-0.3) and their effect on the performance of the modified V-shaped turbine blade is explained using pressure contour plots, velocity contour plots and streamline plots using ANSYS post-processing module.

Table 4.9 Values of C_{Tmax} and C_{Pmax} with respect to overlap ratio (OR=0.0-0.3)

Sl.No	OR	C_{Tmax}	TSR	C_{Pmax}	TSR
1.	0	0.29	0.7	0.22	0.9
2.	0.05	0.27	0.7	0.20	0.9
3.	0.1	0.25	0.7	0.18	0.8
4.	0.15	0.24	0.7	0.17	0.8
5.	0.2	0.23	0.7	0.16	0.8
6.	0.25	0.21	0.7	0.15	0.8
7.	0.3	0.19	0.7	0.14	0.8
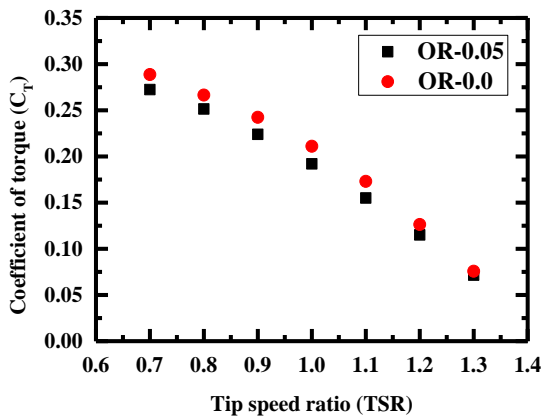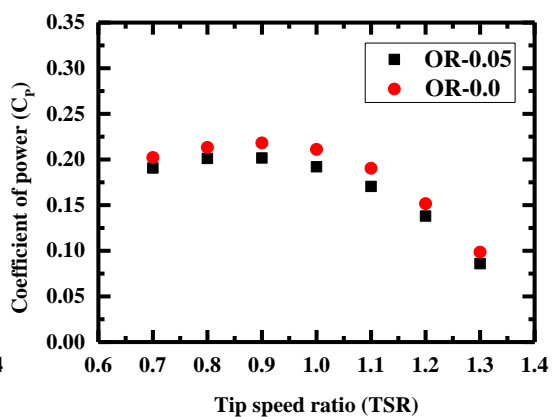
(a)　　　　　　　　　　　　　　　(b)
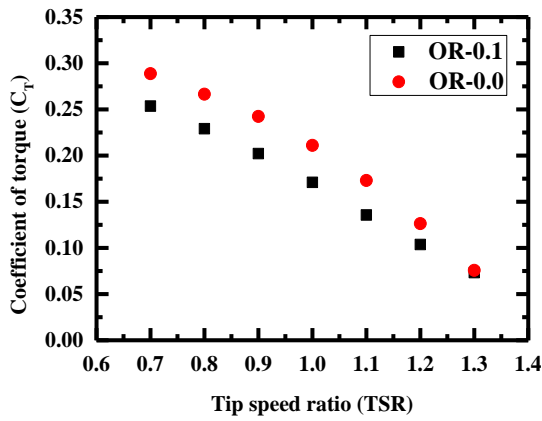
(c)
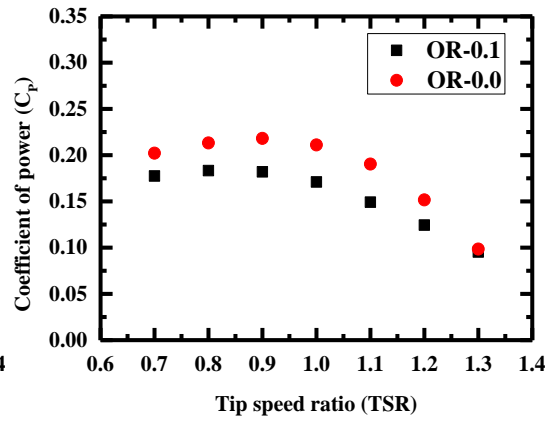
(d)
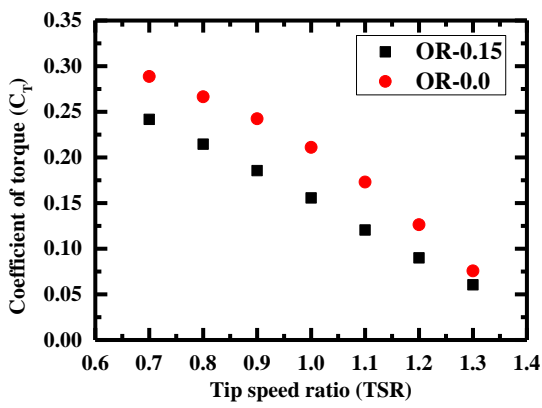
(e)
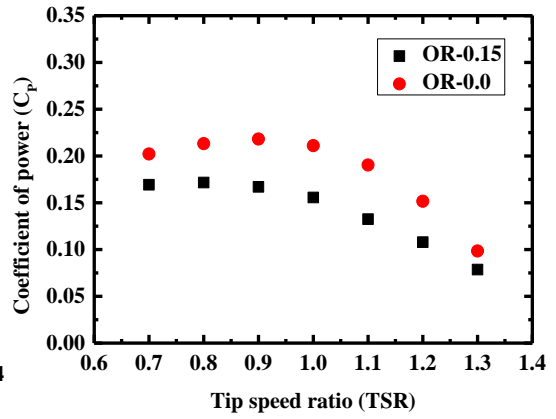
(f)
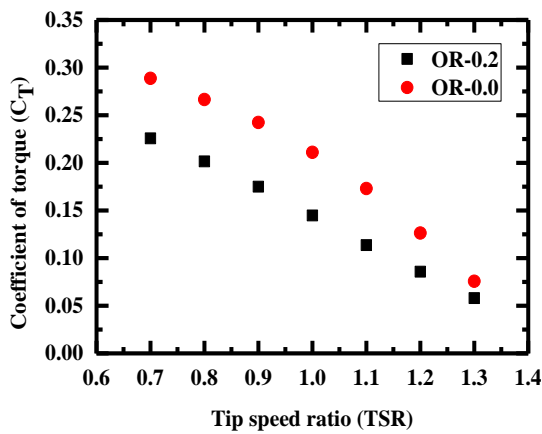
(g)
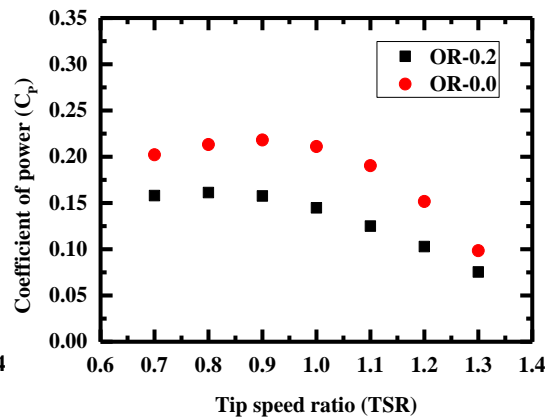
(h)
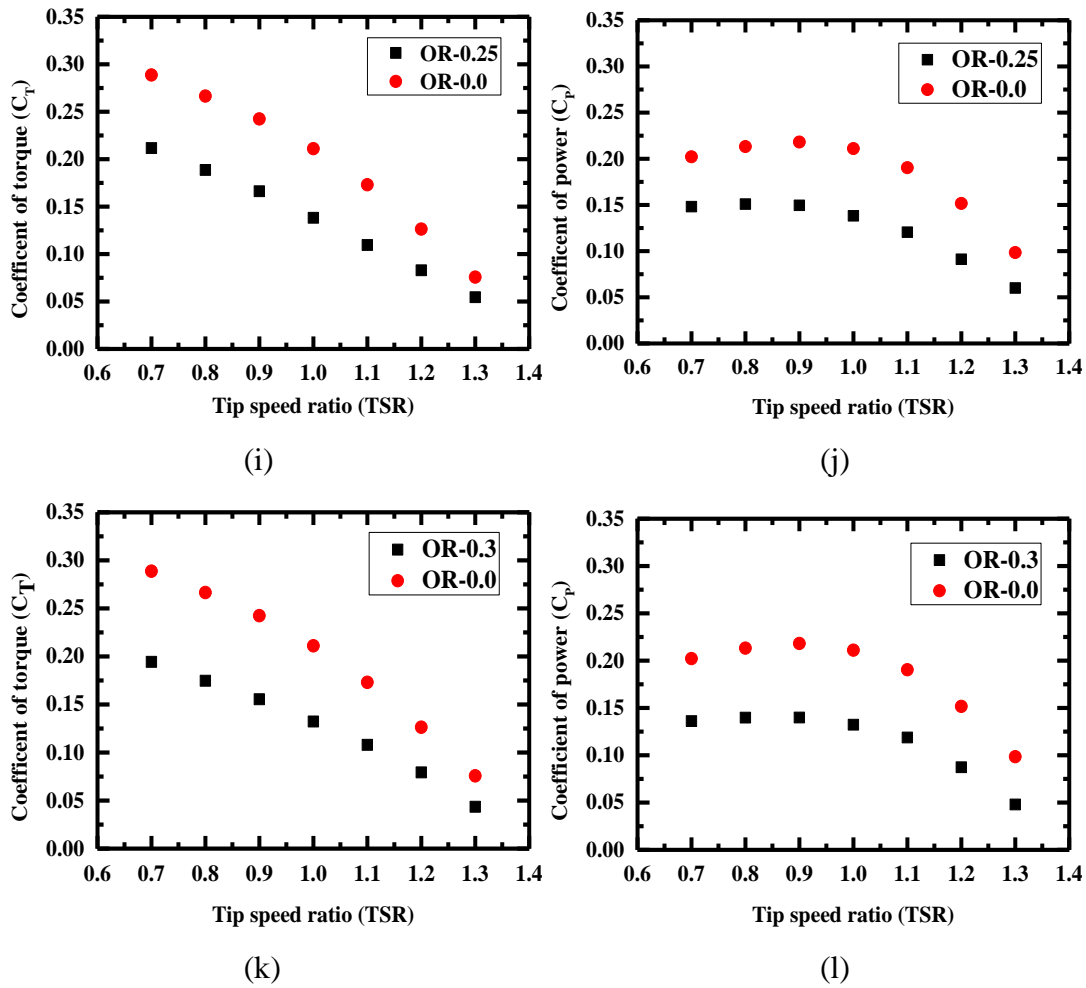
Figure 4.23 (a-l) Variation of C_T and C_P versus TSR for modified V-shaped rotor

blade with OR=0.0 and (b-l) OR=0.05-0.3
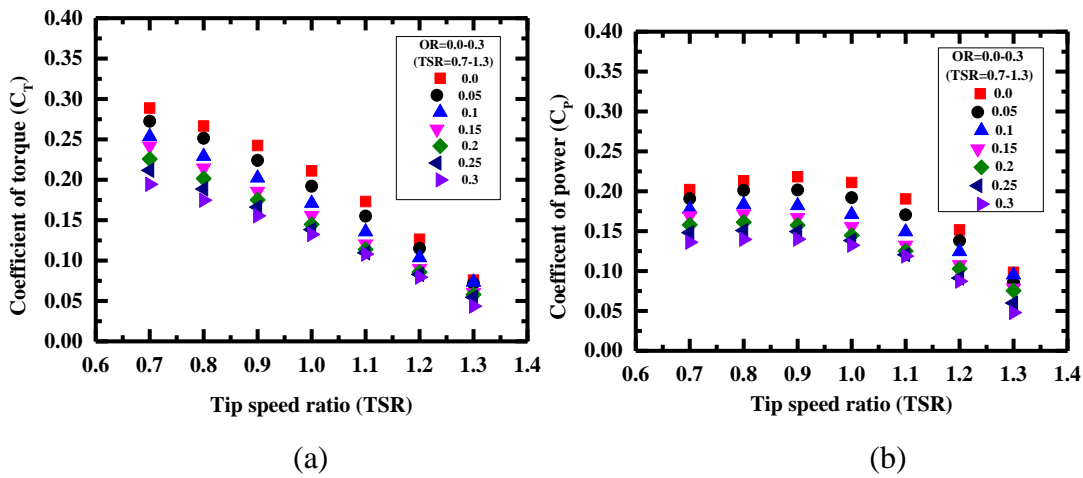
Figure 4.24 Variation of (a) C_T and (b) C_P with respect to TSR with an OR of 0.0-0.3

4.5.2 Variation of C_T with respect to the angle of rotation (θ) of a turbine blade with an OR ranging from 0.0-0.3 and polar plots

Figures 4.25 (a-g) shows the variation of C_T with respect to the angle of rotation (θ) for the last two revolutions (θ=0°-720°) of the turbine blade with an OR ranging from 0.0-0.3 with varying TSR (0.7-1.3). The rotor blade with an OR of 0.0 is having higher positive C_{Tmax} and lesser negative C_{Tmin} at a TSR of 0.7, as shown in Figure 4.25 (a). The values of C_{Tmax} for the turbine blade with a TSR of 0.7 and 0.0 OR found at a different angle of rotations such as θ=109°, 288°, 469° and 649°. Similarly, the values of C_{Tmin} were obtained at an angle of rotations such as θ= 26°, 205°, 386° and 565°.

A similar trend was obtained for the remaining overlap ratios (0.05-0.3) with a TSR range of 0.7-1.3. But the value of C_{Tmax} decreases with respect to overlap ratio (0.05-0.3), and the average C_T decreases. The value of the average C_{Tmax} is higher for the turbine blade with 0.0 OR compared to the turbine blade with OR ranging from 0.05-0.3 with respect to TSR (0.7-1.3). The peak positive C_{Tmax} decreases with the increase in OR from 0.05 to 0.3 is shown in Figure 4.25 (h) for the rotor blade with an OR ranging from 0.0-0.3 with respect to the angle of rotation (θ) of the turbine blade.

With the increase in overlap ratio from 0.05-0.3, the peak C_T decreases, and a negative C_T increases with respect to the angle of rotation (θ) of the rotor blade. The variation of C_T with respect to θ also be presented using polar plots, as shown in Figures 4.26 (a-g). The variation of C_T with respect to θ with an OR ranging from 0.0-0.3 for a TSR of 0.8 is shown in Figure 4.26 (h). The value of C_T decreases with respect to OR the distance between the C_{Tmax} decreases, as shown in Figures 4.26 (a-g).

(a)

(b)

(c)

(d)

(e)

(f)

148
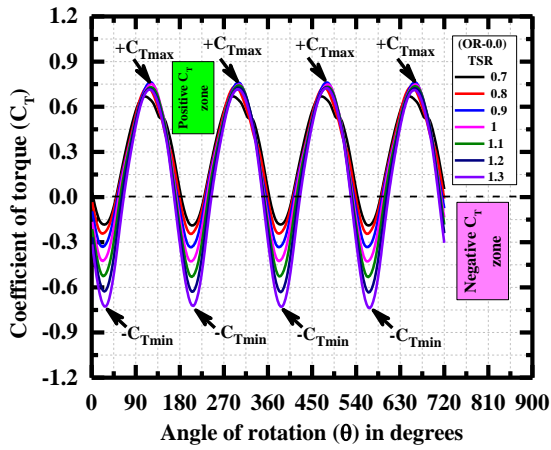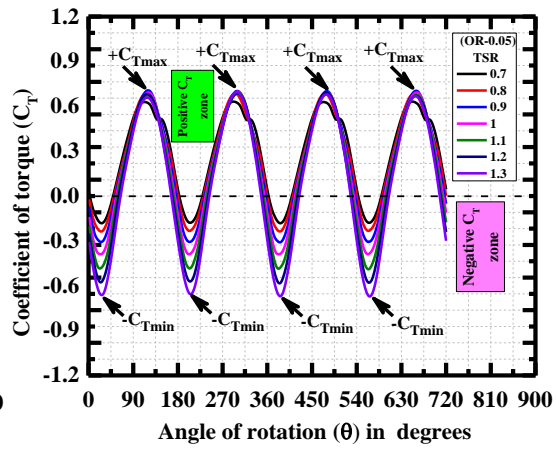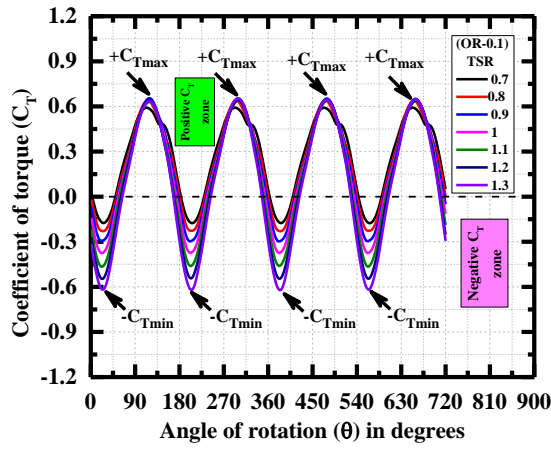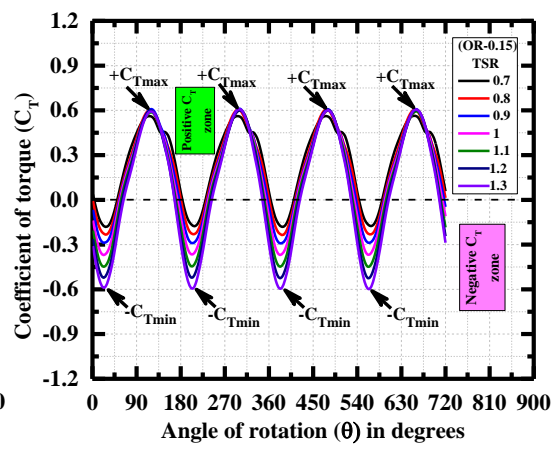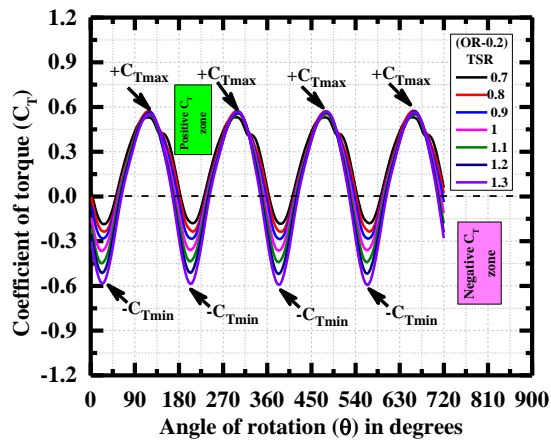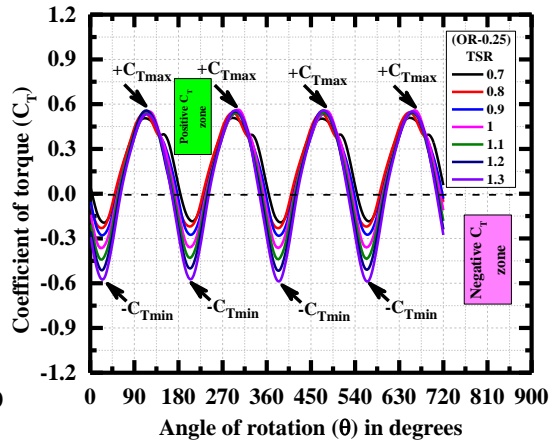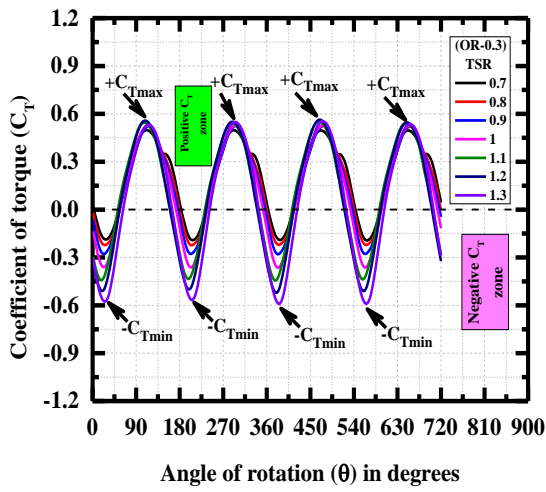
(g)
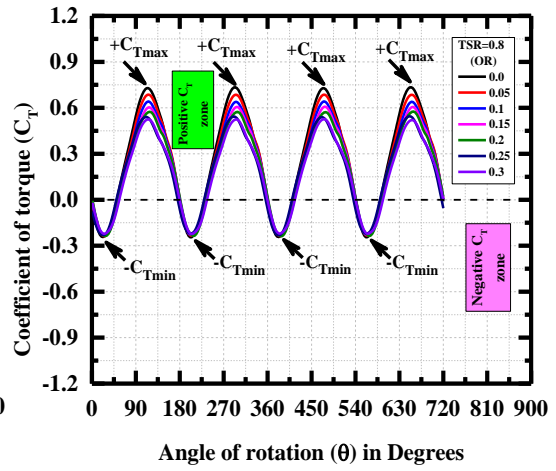
(h)

Figure 4.25 (a-g) Variation of C_T versus angle of rotation (θ) of the rotor blade with respect to TSR (0.7-1.3) for varying OR (0.0-0.3) and (h) turbine blade with different OR (0.0-0.3) for a TSR of 0.8
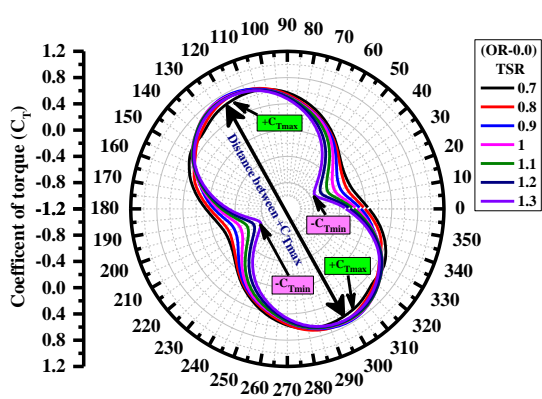
(a)
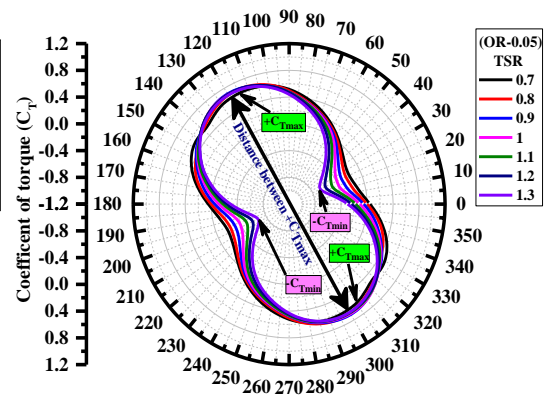
(b)
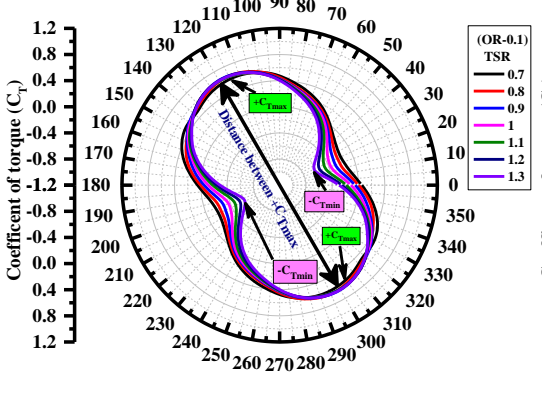
(c)
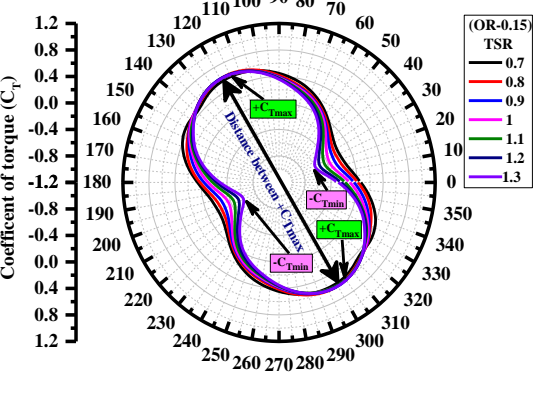
(d)
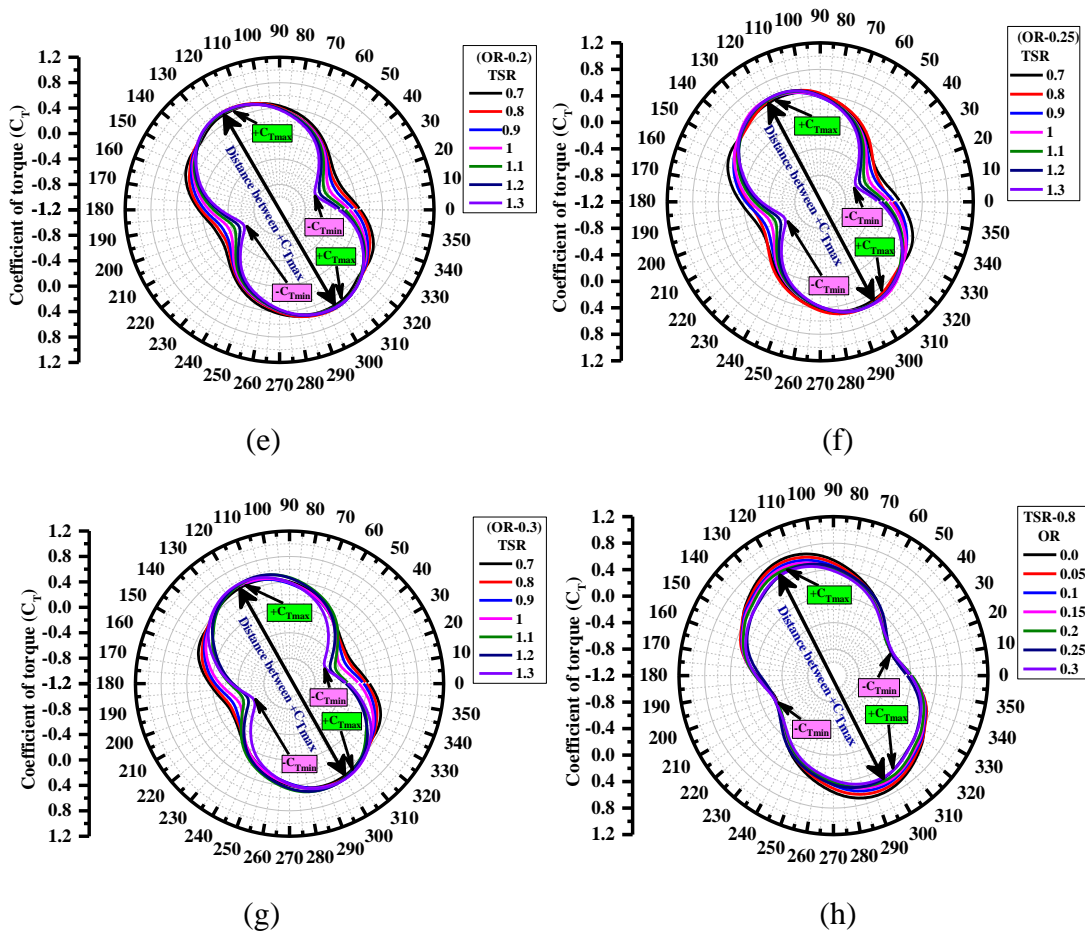
Figure 4.26 (a-g) Variation of C_T versus angle of rotation of the turbine blade with different OR (0.0-0.3) using polar plot with varying TSR (0.7-1.3) and turbine blade with different OR and TSR of 0.8 using (h)

4.6 Numerical analysis

4.6.1 Pressure contour plots

In this section, the flow field around the modified V-shaped rotor blade such as pressure, velocity contour, and streamline plots were studied using ANSYS postprocessing for the turbine blade with an overlap ratio ranging from 0.0-0.3. Figures 4.27 (a-g) show the pressure contour plots for modified V-shaped turbine blades with different OR ranging from 0.0-0.3 with a TSR of 0.7. The direction of fluid flow and direction of rotation of the turbine blade are shown in Figures 4.27 (a-g).

During the rotation of turbine blades, various significant zones developed during the CFD simulation, such as a high-pressure zone, low-pressure zone, and very low-pressure zones, represented in red and blue colors on the left side of the legend. The turbine blade rotates in the anticlockwise direction due to the pressure difference between advancing and returning blade profiles, as shown in Figures 4.27 (a-g).

The important critical zones developed in the present CFD simulation are similar to CFD simulations carried out by previously published data. The variation of pressure around the modified V-shaped turbine blades validated with the CFD results of the previous study carried out by various researchers with similar boundary conditions (Kerikous and Thévenin 2019b; a; Kumar and Saini 2017b; a; Ramadan et al. 2020; Sarma, N. K. Biswas and Misra 2014; Talukdar et al. 2018; Zhang et al. 2017a).

Figures 4.27 (a-g) shows the variation of pressure for the turbine blade with different OR ranging from 0.0-0.3. The pressure variation was demonstrated in three different angular positions, such as $\theta=0°$, 60° and 120), to study the variation of pressure acting on the advancing and returning blade profiles. The pressure difference between the advancing and returning blade profiles is maximum when the turbine blade is at an angular position of $\theta=120°$ for the turbine blade with an OR of 0.0 compared to the turbine blade with an OR ranging from 0.05-0.3 as shown in Figures 4.27 (a-g). At an angular position of $\theta=120°$ the turbine blade with an overlap ratio of 0.0 extracts, maximum power compared to turbine blade with other overlap ratios (0.05-0.3). With the increase in OR from 0.05-0.3, the pressure acting of the returning blade increases. This will reduce the net power developed by the turbine blade, as shown in Figures 4.27 (b-g).
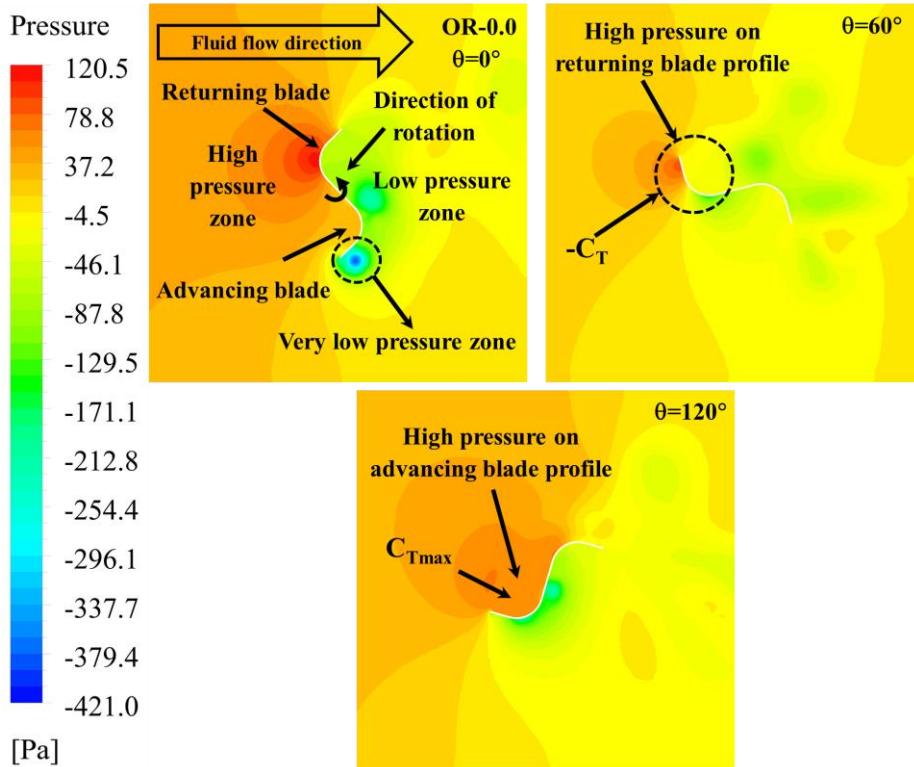
(a)
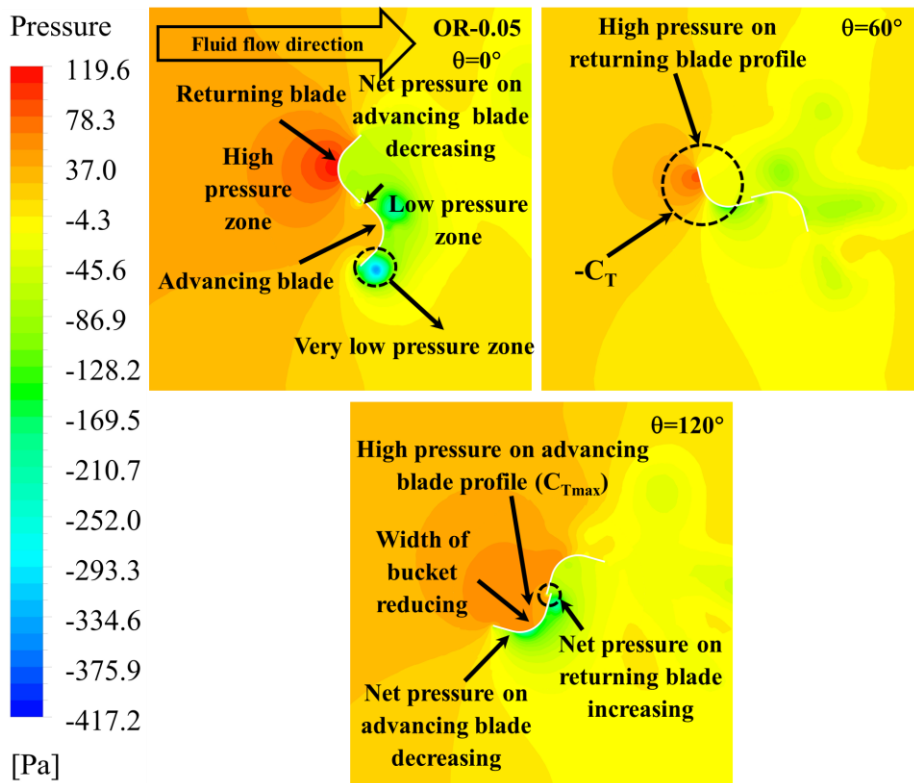
(b)
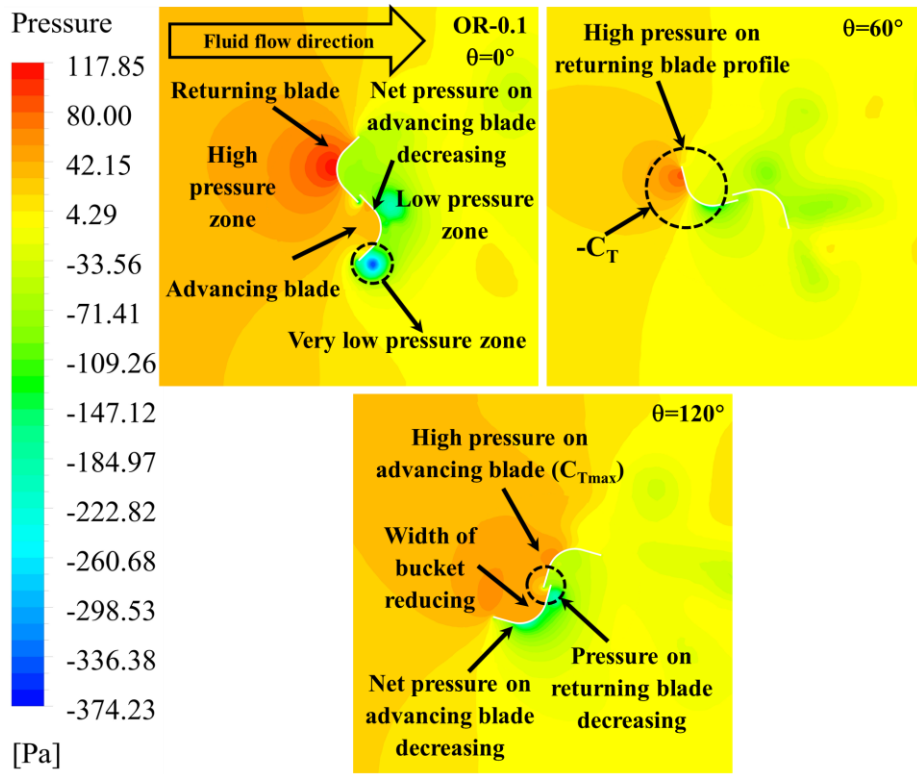
(c)

(d)

(e)
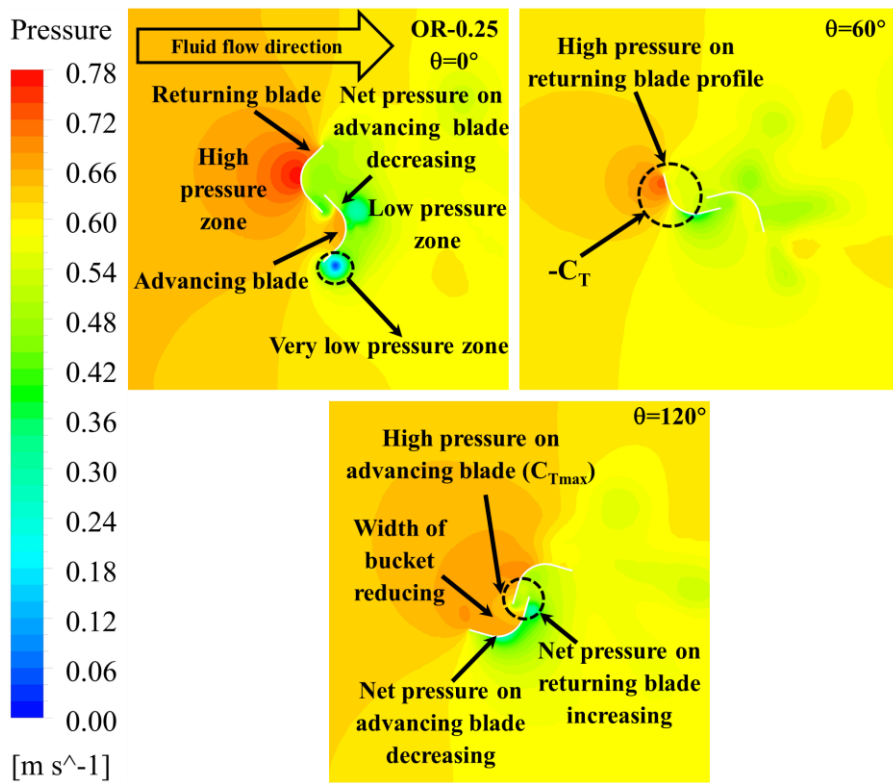
(f)
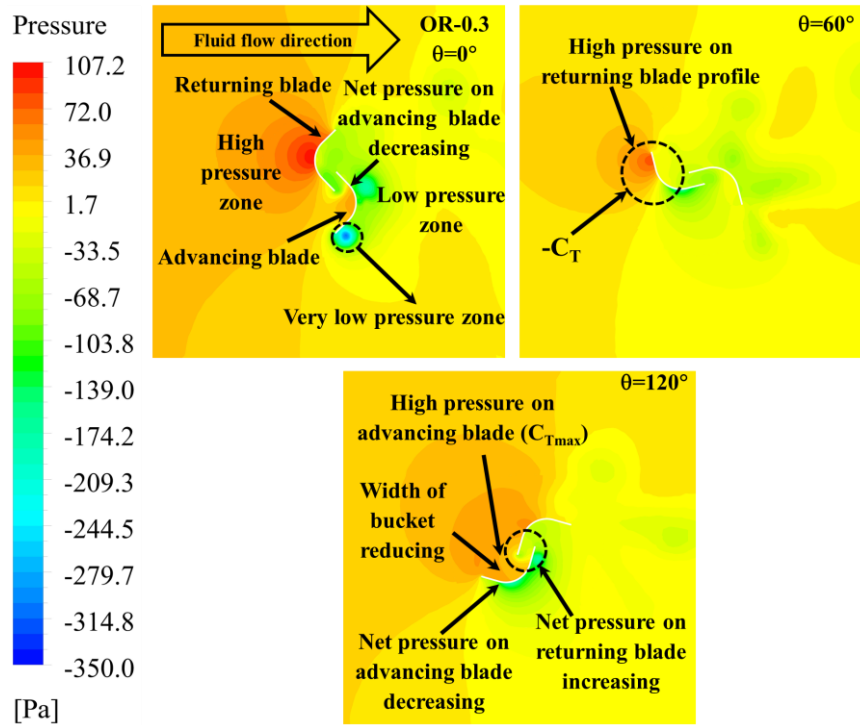
(g)

Figure 4.27 (a-g) Pressure contour plots of the turbine blades with different OR ranging from 0.0-0.3 at angular positions of θ=0°,60° and 120°

4.6.2 Velocity contour and streamline plots

Figures 4.28 (a-g) show the turbine blades' velocity contour plots with different OR ranging from 0.0 to 0.3 with a TSR of 0.7. The various important zones developed during the turbine blade rotation for the case velocity contour plots are the high-speed vorticity zone and wake zone. The high-speed vorticity zone developed at the tip of the advancing blade profile, and the wake zone developed at the downstream side of the turbine blade (Kumar and Saini 2017b; a; Talukdar et al. 2018; Zhang et al. 2017a) with an OR of 0.0-0.3 during the rotation of the turbine blade at different angular positions (θ=0°, 60° and 120°).

The turbine blade with an OR ranging from 0.05-0.3, another significant zone developed known as overlap jet zone (Kacprzak et al. 2013) between the gap (e) of advancing and returning blades as shown in Figures 4.28 (b-g).

The velocity contours plots obtained in the present study exhibits that similar trends (high-speed vorticity zone and wake zone) and validated with previously published results using the Savonius hydrokinetic turbines (Kerikous and Thévenin 2019b; a; Kumar and Saini 2017b; a; Sarma, N. K. Biswas and Misra 2014; Talukdar et al. 2018). The new zone known as overlap jet zone developed for the turbine blade with an OR ranging from 0.05-0.3 validated with the previously published result for the case of a turbine blade with an overlap ratio (Kacprzak et al. 2013).

The maximum velocity observed at the tip of the advancing blades for all the turbine blades (OR 0.0-0.3) is represented by red color, as shown in Figures 4.28 (a-g). The OR (0.05-0.3) effect in a modified V-shaped turbine blade increases the negative torque, and the average C_P decreases due to an increase in vorticity loss and similar observation reported by (Kamoji et al. 2009b). In the present work, for the case of a modified V-shaped turbine blade, the development of overlap jet in the present velocity contour, which is parallel to the turbine blade straight edges between the advancing and returning blades of the turbine.

The effect of overlap jet on the returning turbine blade is acting in a parallel direction for the case of a turbine blade with different OR (0.05-0.3). If the overlap jet is parallel to advancing and returning blades gaps (e), therefore the impact of overlap jet developed in between the blade straight edges is not acting on the rear side of the returning blade profile and loss of vorticity is increasing leads to reduction of C_T and C_P for the case of a turbine blade with overlap ratio (0.0-0.3). With the growth in overlap ratios (OR) from 0.05 to 0.3, the performance parameters such as C_T and C_P reduced with respect to TSR.

In Figures 4.28 (b-g), for the turbine blade with an OR of 0.5-0.3 at an angular position of $\theta=60^o$ sharp, a highly intensified velocity stream is separated from the tip of the advancing blade, thereby degrading turbine efficiency. This pattern is considered to be less efficient between the water stream and the turbine rotor.

The deterioration of performance due to sharp velocity observed after the tip of the advancing blade, which was reported by Sarma, N. K. Biswas and Misra 2014 and Talukdar et al. 2018.

Figures 4.29 (a-g) shows the streamline plots for the turbine blades with an OR ranging for 0.0-0.3 for a TSR of 0.7 to study the flow of fluid around the turbine blades. The direction of fluid flow is shown in Figures 4.29 (a-g) turbine blade is rotating in the anticlockwise direction and the maximum velocity is developed at the tip of the advancing side of the turbine blades for all the cases of the turbine blades (OR 0.0-0.3).
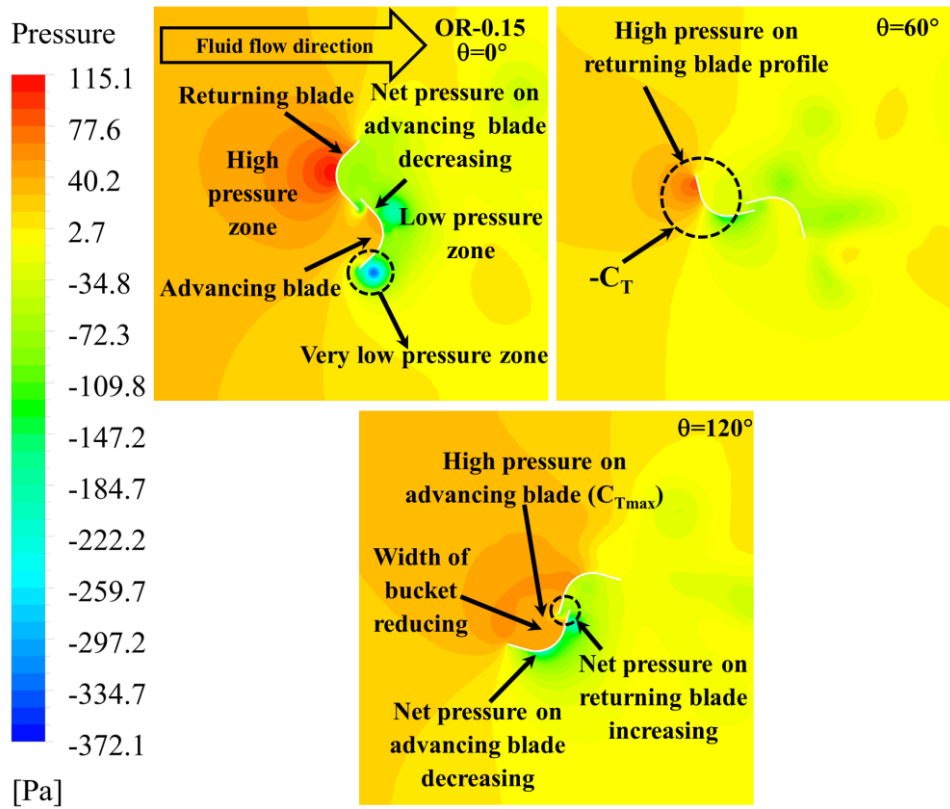

(a)
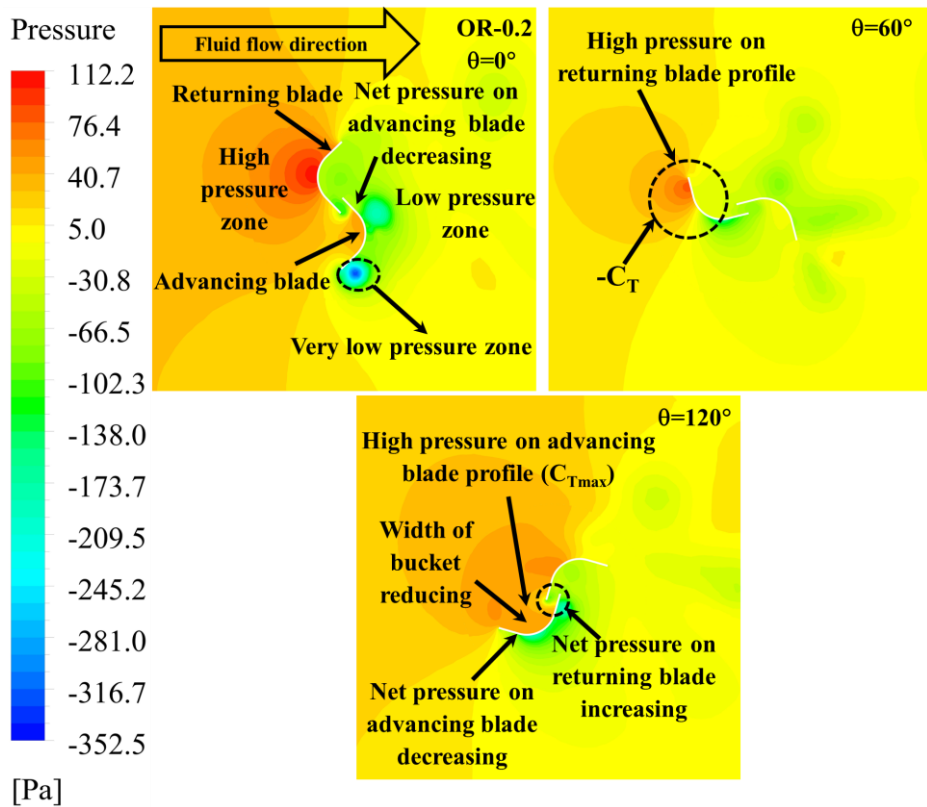
(b)

(c)

(d)

(e)

159
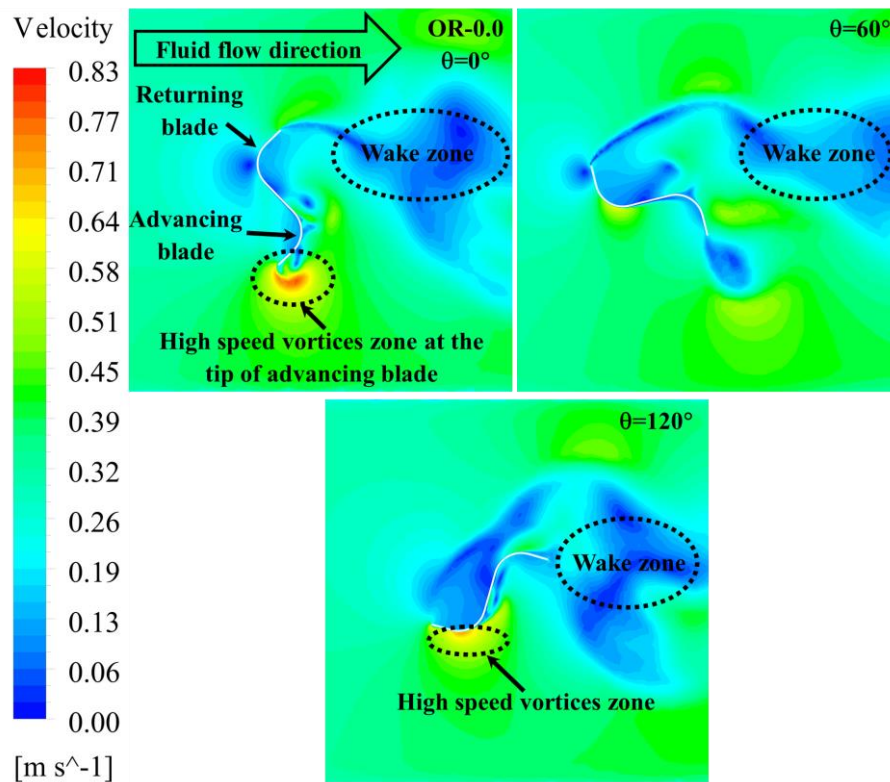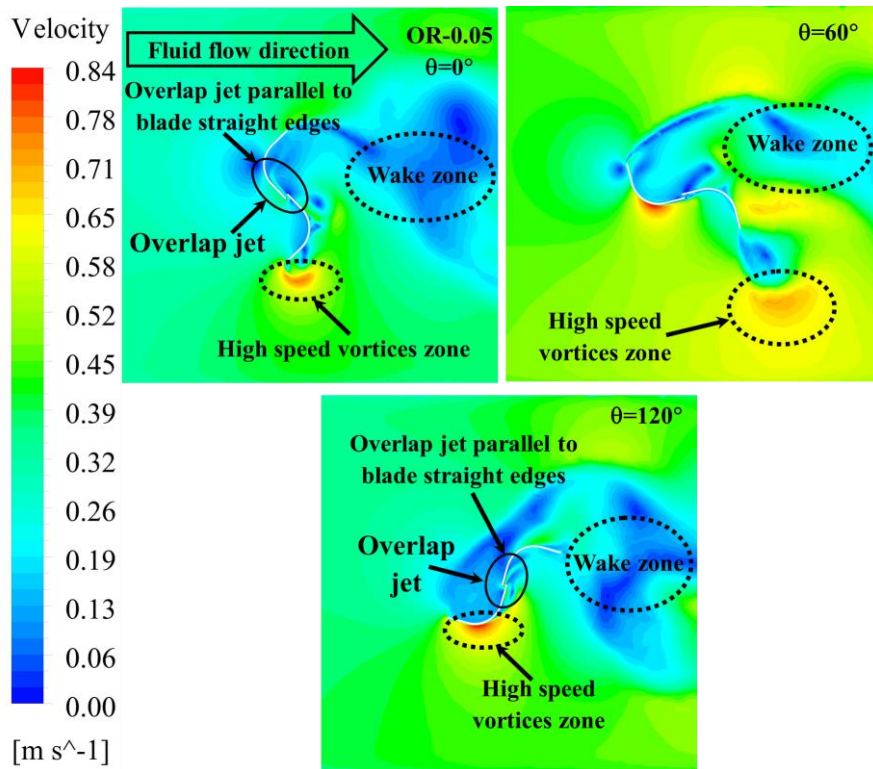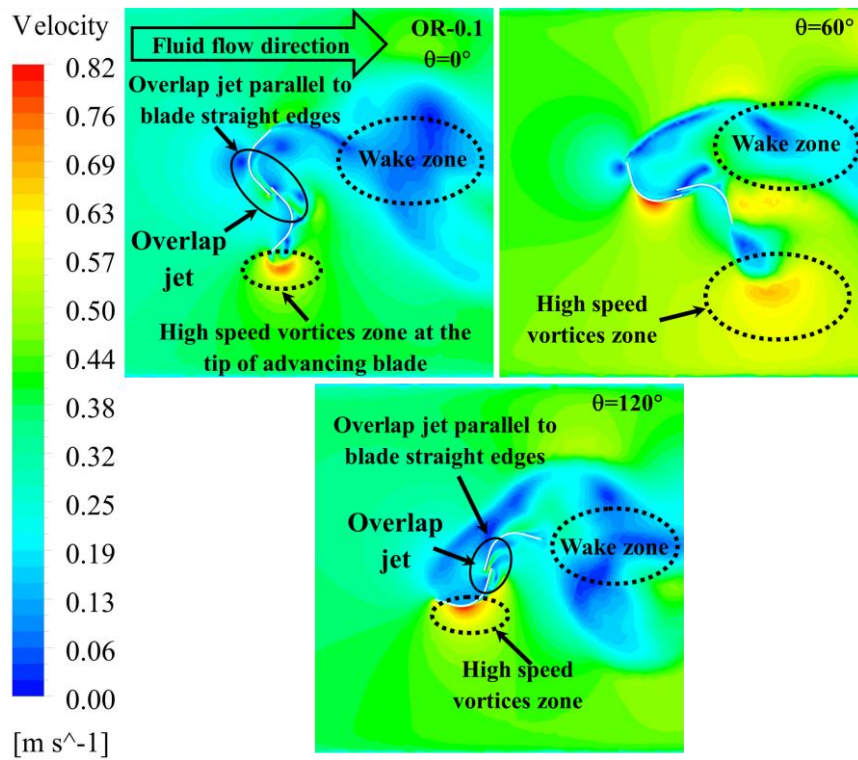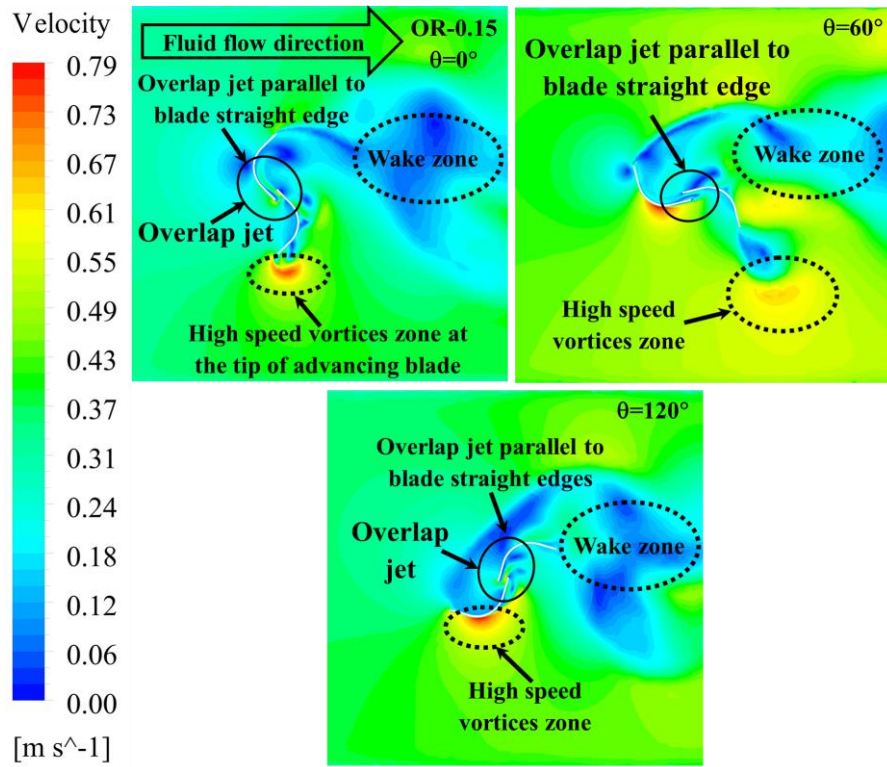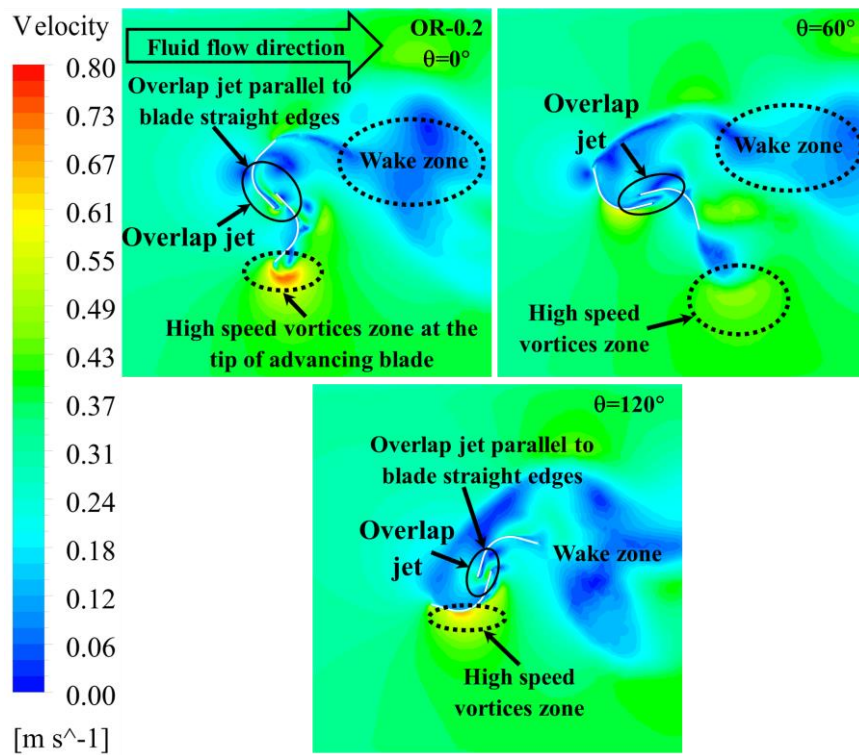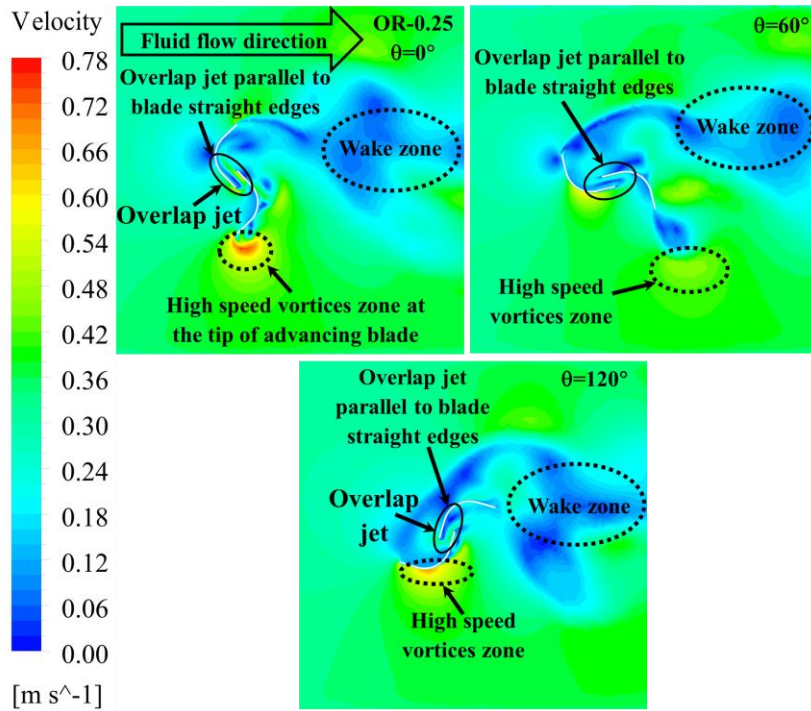
(f)
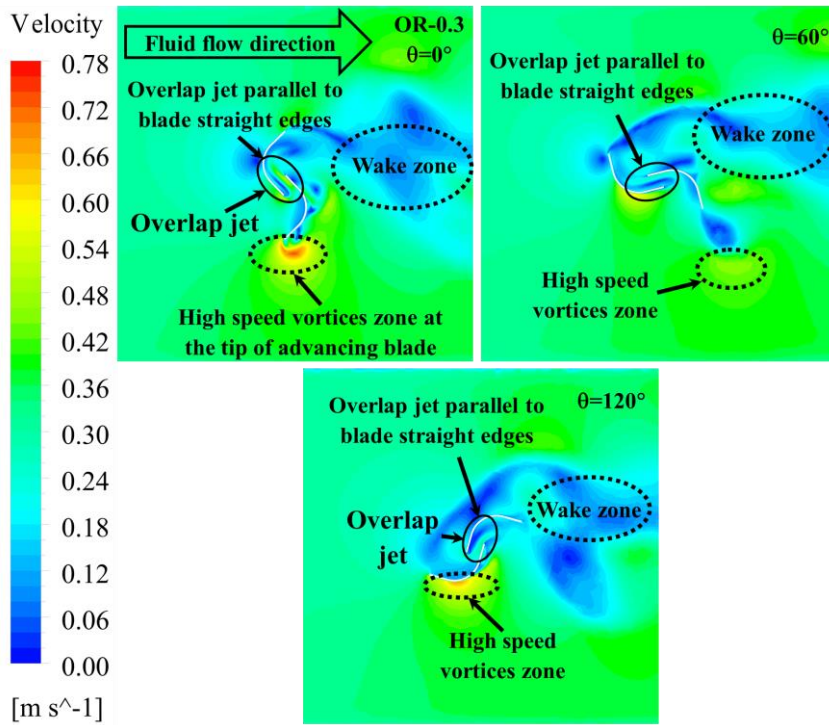
(g)

Figure 4.28 (a-g) Velocity contour plots of the turbine blades with different OR at angular positions of θ=0°, 60° and 120°

(a)

(b)

(c)

(d)

162

(e)

(f)

163
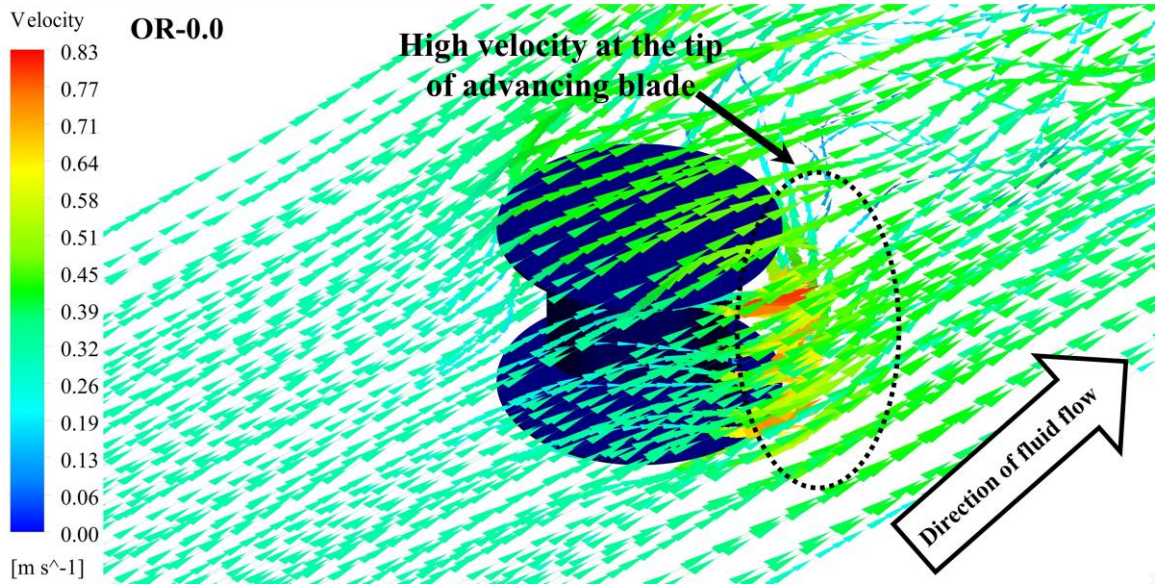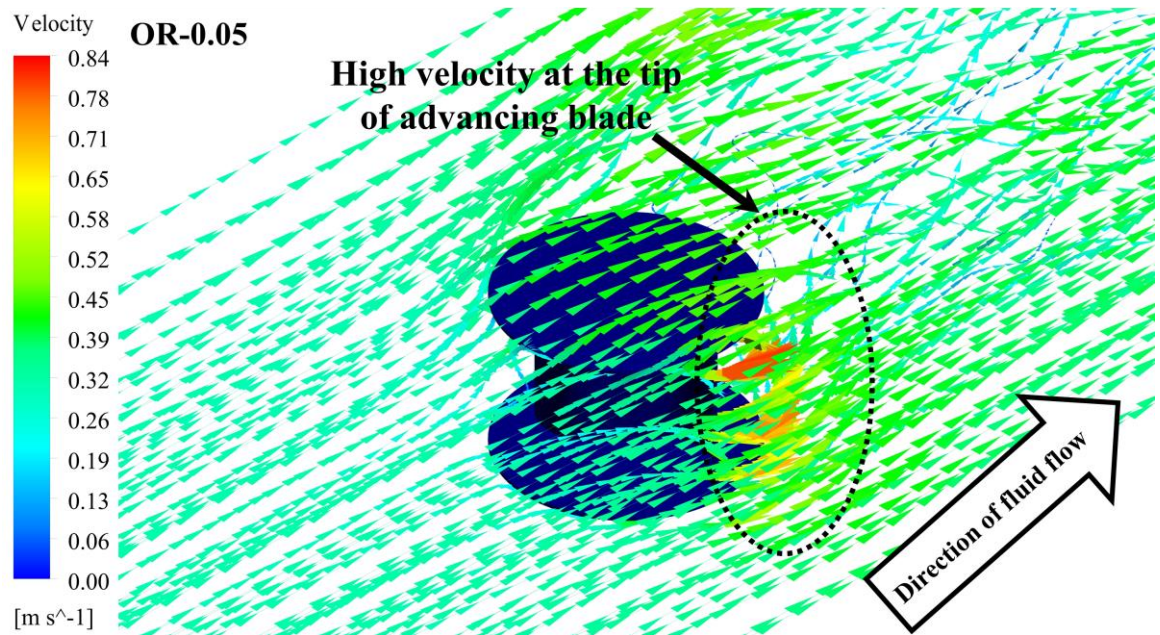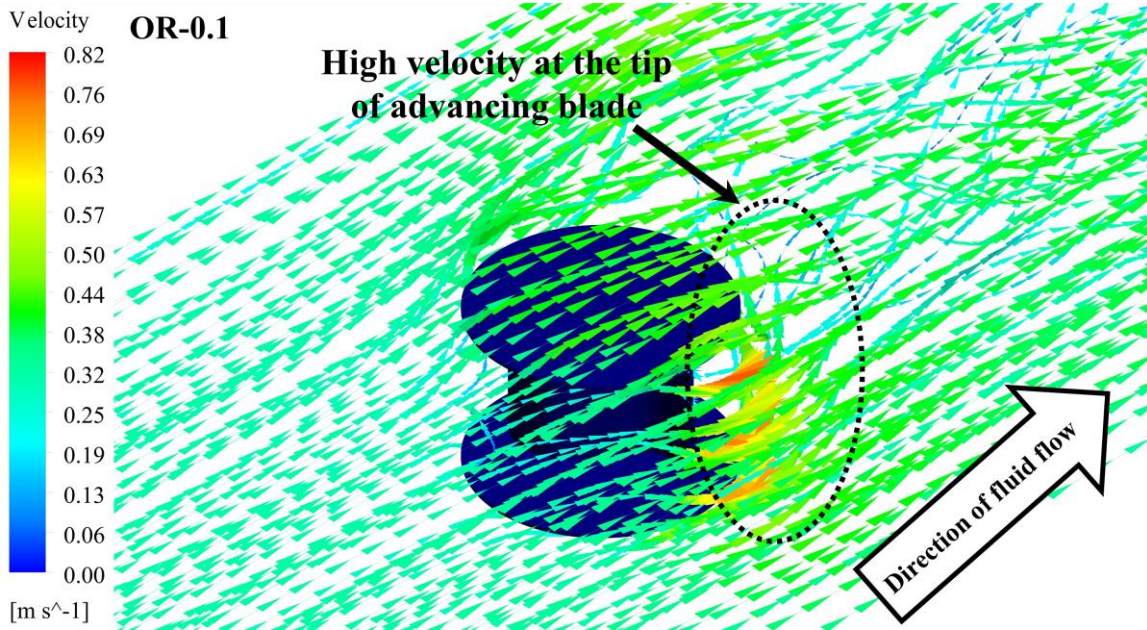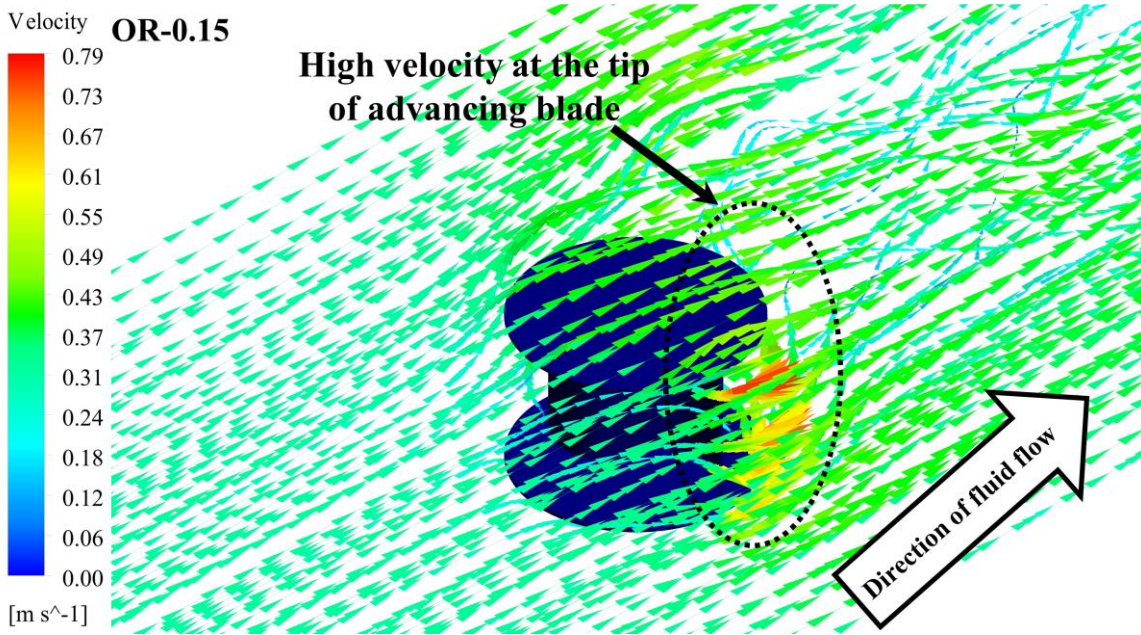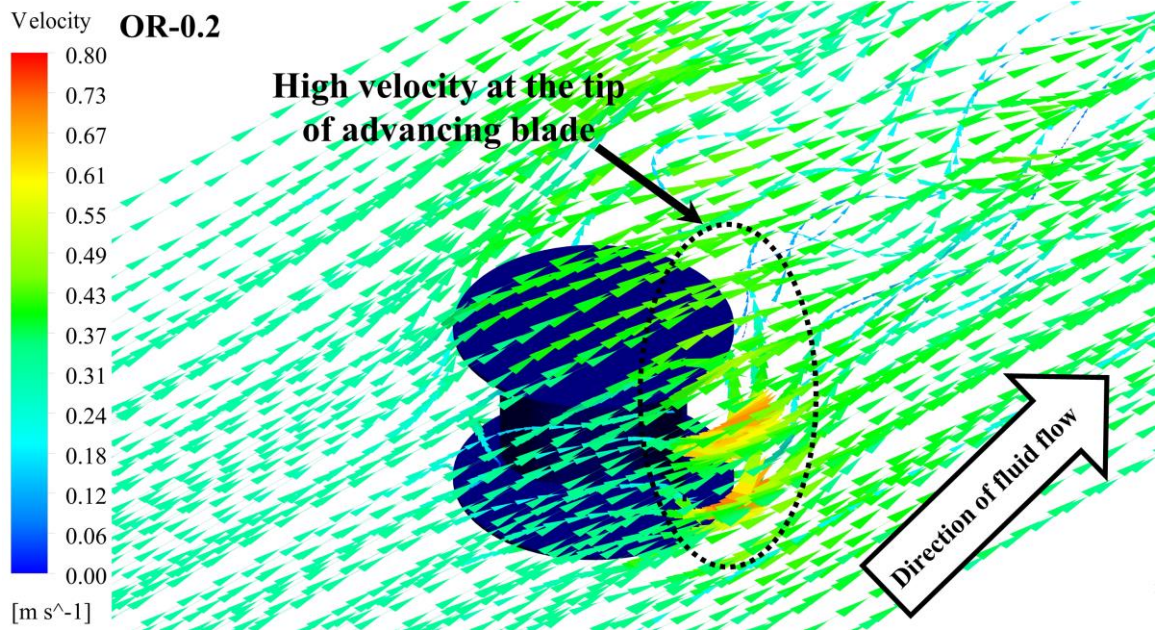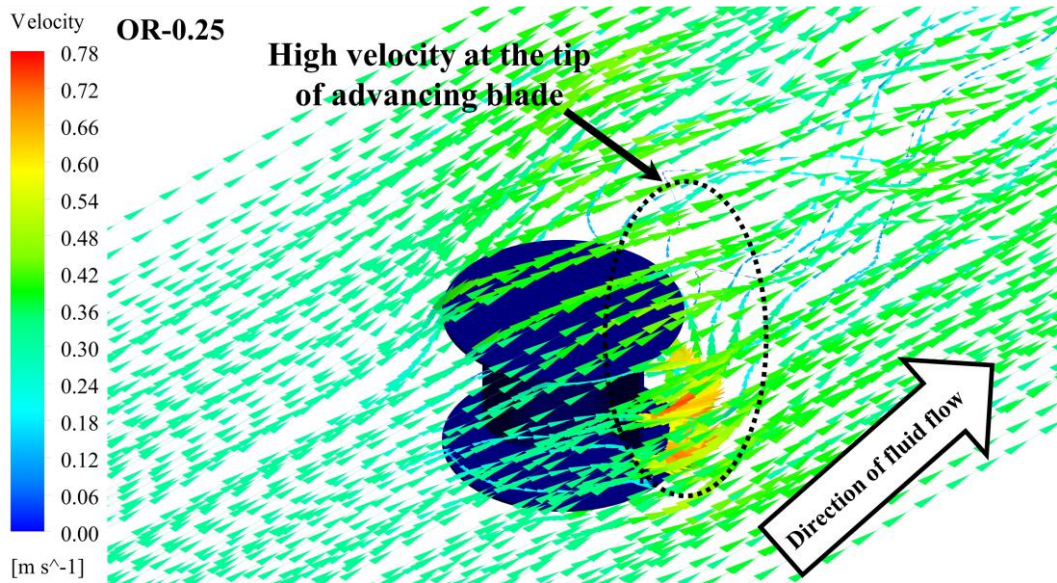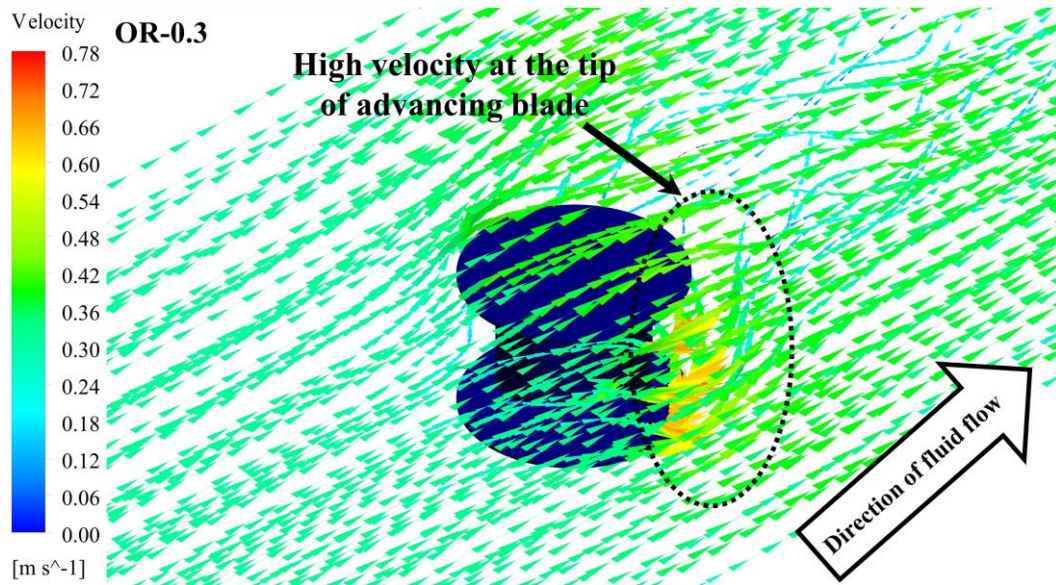
(g)

Figure 4.29 (a-g) Stream line plots of the turbine blades with different overlap ratios (0.0-0.3) at an angular position of θ=0°

4.7 CFD analysis for the effect of V-angle ($V_{90°-40°}$) on the performance of modified V-shaped rotor blade

4.7.1 Variation of C_T and C_P with respect to TSR for the performance of modified V-shaped rotor blade by varying the V-angles

In this section 3D numerical investigation is carried out using the optimum rotor blade V_4 to study the effect of V-angle ranging from $V_{90°}$-$V_{40°}$ to compute C_P and C_T with respect to TSR with zero bed slope and without taper case to compare the present results with the literature. A three-dimensional transient simulation was carried out on a 90° V-angle rotor blade profile with an inlet water velocity of 0.3090 m/s, and angular velocity (ω) is given to the rotating zone based on the TSR (0.7-1.3).

Figure 4.30 (a and b) shows the results of rotor blades such as $V_{90°-40°}$, the variation of C_T and C_P is recorded with respect to TSR. It was found that the turbine blade with an angle of $V_{80°}$ is giving a maximum C_T and C_P of 0.2940 and 0.2279 at a TSR of 0.7 and 0.9 respectively as compared to other V-angles in between 40° to 90°. The results are tabulated in Table 4.10 for more insight with a maximum value of C_P and C_T with

164

respect to TSR. The flow field around the various V- blades with different V-angles ranging from 90°-40° and the effect of V-angle on the performance of the turbine blade is explained using variation of C_T with respect to angle of rotation (θ) in Figures 4.31 and 32 (a-g) and pressure contour plots in Figures 4.33 (a-f).

(a)   (b)
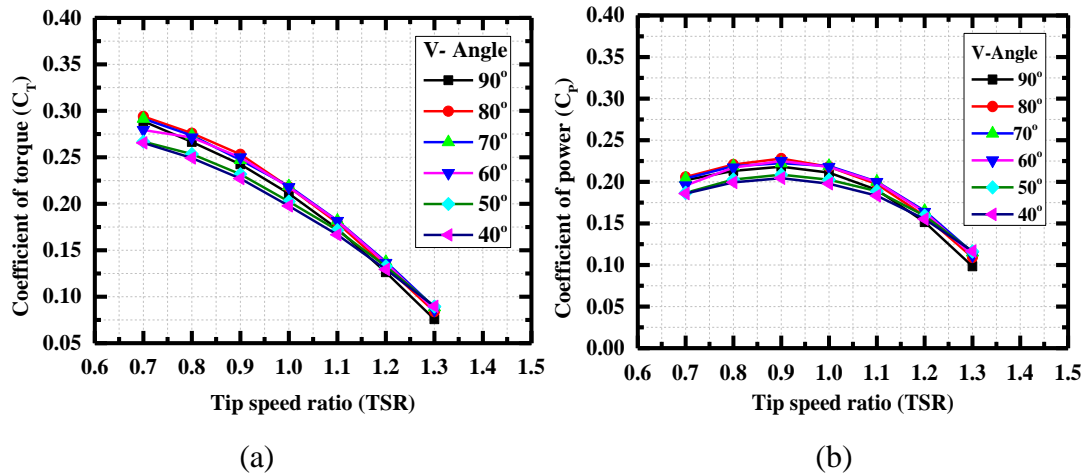
Figure 4.30 (a and b) Variation of C_T and C_P with respect to TSR for the rotor blades $V_{90°-40°}$

Table 4.10 C_{Tmax} and C_{Pmax} values for different V-blades with respect to TSR

Sl. No	V-angles	C_{Tmax}	TSR for C_{Tmax}	C_{Pmax}	TSR for C_{Pmax}
1.	90°	0.2887	0.7	0.2182	0.9
2.	80°	0.2940	0.7	0.2279	0.9
3.	70°	0.2915	0.7	0.2224	0.9
4.	60°	0.2794	0.7	0.2250	0.9
5.	50°	0.2668	0.7	0.2086	0.9
6.	40°	0.2655	0.7	0.2044	0.9

4.7.2 Variation of C_T with respect to angle of rotation (θ) for different rotor blades ($V_{90°-40°}$) and polar plots

Figure 4.31 (a) represents the C_T profile of modified V-blade at an angle of 90°, for different TSR values, with different V-angles Figures 4.31 (a-g), with respect to angle of rotation (θ). As the blade is exposed to the water stream, the kinetic energy in water flow initiates the accumulation of pressure on the blade profile (Figure 4.33 (a)). The

165

blade profile includes advancing (concave) and returning (convex) profile (geometry) to absorb the energy from the stream of water. At reference point θ = 0°, whole blade profile is exposed to the pressure created by the stream of water, but the maximum pressure point was observed nearer to returning profile as it creates more drag for the rotation (anti-clockwise) of the blade, and there was some pressure accumulated at advancing profile too. Because of positive pressure accumulation at the inlet side and movement of the blade along the rotational axis, negative pressure was also identified at the backside of the advancing blade profile.

These combined effects of energy transfer from water stream to blade cause the rotation of blade along its axis. As the blade advances to 26° (Figure 4.33 (a)), the exposure of advancing the profile to inlet water stream became minimum. Hence, the energy transfer to the blade is also minimum, and drag created by the returning blade also increases, but less negative pressure points are observed. Hence C_{Tmin} was observed at 26° in Figure 4.33 (a). Further rotation of the blade to an angular position of 109°, the returning blade is replaced as advancing blade and vice-versa) receives maximum energy from the water stream. At this angle, concave part of the blade extracts the maximum energy, the part of pressure accumulated on returning blade also causes the positive net effect on the rotation of the blade (Figure 4.33 (a)). Hence maximum C_T value obtained at θ=109° for 0.7 TSR (Ostos et al. 2019b). The numerical results of C_T are tabulated in Table 4.11 for standard values of θ.

The simulations were carried out for different TSR's of 0.8, 0.9, 1.0, 1.1, 1.2, and 1.3, and results were shown in Figures 4.31. It is observed that very small increase in C_T is observed till the TSR value of 0.9, as the TSR value increases to 1.3, there is a decrease in C_T at θ=26°an angular position which results in highest negative torque. The position of C_{Tmax} advances in very small steps when the TSR value increases to 1.3 (Zhang et al. 2017b). Similarly, Figures 4.31 (b-f) shows the plot of C_T with respect to the angle of rotation for modified V blade with V angle of 80°, 70°, 60°, 50° and 40° respectively. The same plots are also represented in polar form at Figures 4.32 (a-g).

Table 4.11 shows the values of C_T at a different angle of rotation for modified V blade at different V-angles. The maximum C_T was observed for $V_{90°}$ ($C_T = 0.647$, at $\theta = 120°$ (Table 4.11)), and for the relative negative C_T at 210° is -0.1894. Similarly, for $V_{80°}$, maximum and minimum C_T is 0.6303 and -0.1149 at 120° and 210° of rotation. The highest cumulative effect of C_T was observed at $V_{80°}$. Hence modified V-blade at angle of 80° shows the highest C_T compared to other V-angles. The effect of V-angles on C_T regarding angle of rotation is shown in Figures 4.31 (g) and 4.32 (g).

Table 4.11 Positive and negative values of C_T for different angular positions.

Angle of rotation (θ)	$\pm C_T$	$V_{90°}$	$V_{80°}$	$V_{70°}$	$V_{60°}$	$V_{50°}$	$V_{40°}$
0°	$+C_T$	0.04918	0.05571	0.0661	0.0604	0.0637	0.0423
30°	$-C_T$	-0.17767	-0.12243	-0.1081	-0.1156	-0.1054	-0.1111
60°	$+C_T$	0.15794	0.18082	0.1743	0.1376	0.1186	0.1503
90°	$+C_T$	0.57095	0.54737	0.5296	0.5276	0.5428	0.5815
120°	$+C_T$	0.64763	0.63037	0.6434	0.6368	0.5876	0.5591
150°	$+C_T$	0.5086	0.45405	0.4427	0.4196	0.3403	0.2968
180°	$+C_T$	0.04986	0.05937	0.0641	0.0586	0.0650	0.0442
210°	$-C_T$	-0.18194	-0.11479	-0.1072	-0.1091	-0.0603	-0.0276
240°	$+C_T$	0.15961	0.18458	0.1775	0.1541	0.2016	0.2396
270°	$+C_T$	0.57072	0.55271	0.5288	0.5323	0.5201	0.5251
300°	$+C_T$	0.64571	0.62789	0.6471	0.6368	0.5615	0.5412
330°	$+C_T$	0.51143	0.45186	0.4430	0.4235	0.3764	0.3507
360°	$+C_T$	0.05296	0.05856	0.0683	0.0625	0.0661	0.0441
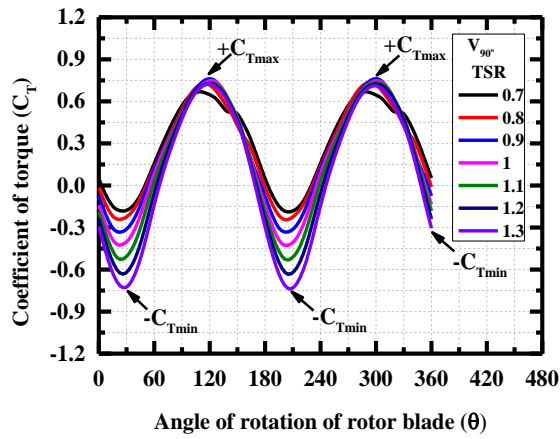
(a)
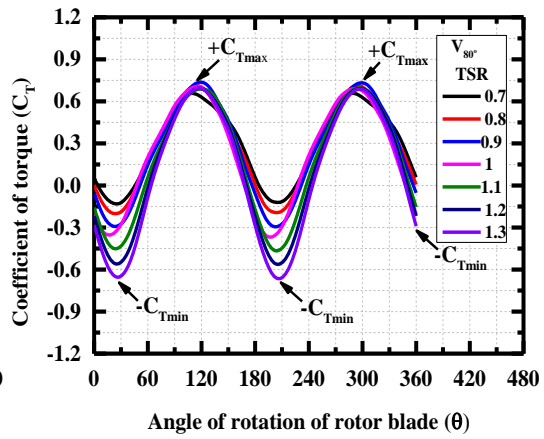
(b)
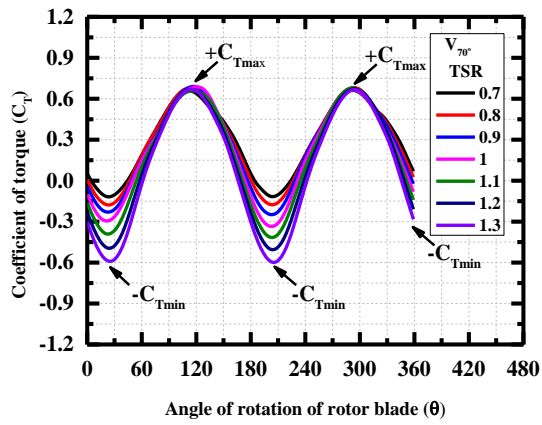
(c)
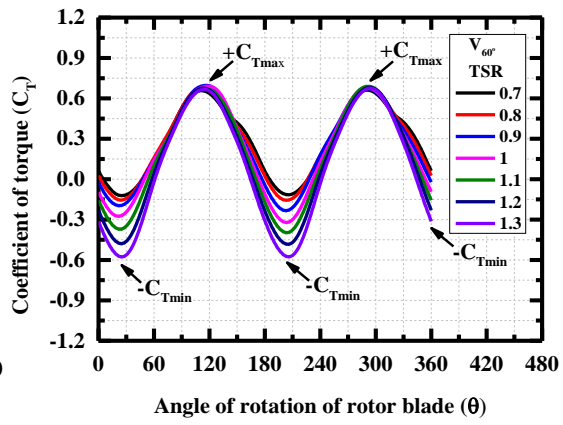
(d)
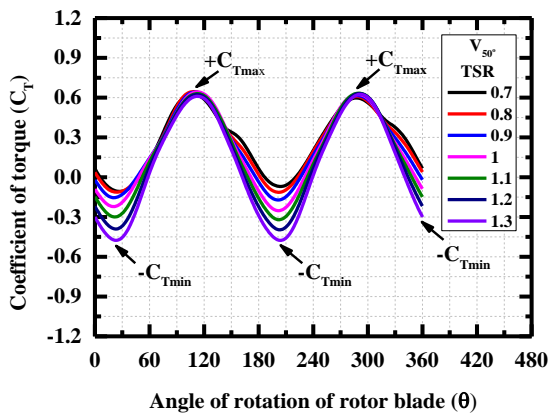
(e)
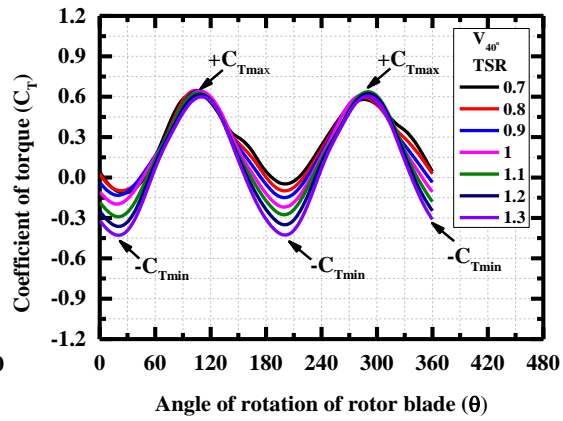
(f)
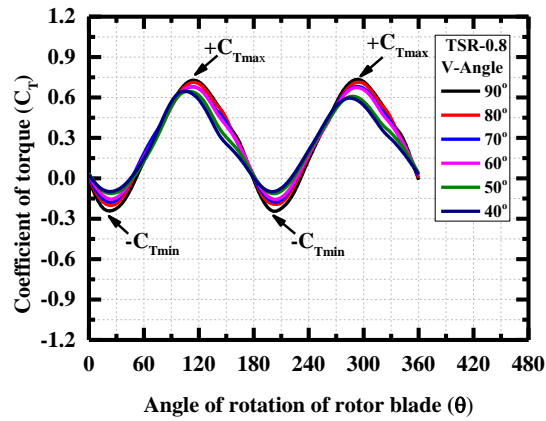
(g)

Figure 4.31 Variation of C_T with respect to rotor blade rotation (θ)

(a)

(b)

(c)

(d)

(e)

(f)

(g)
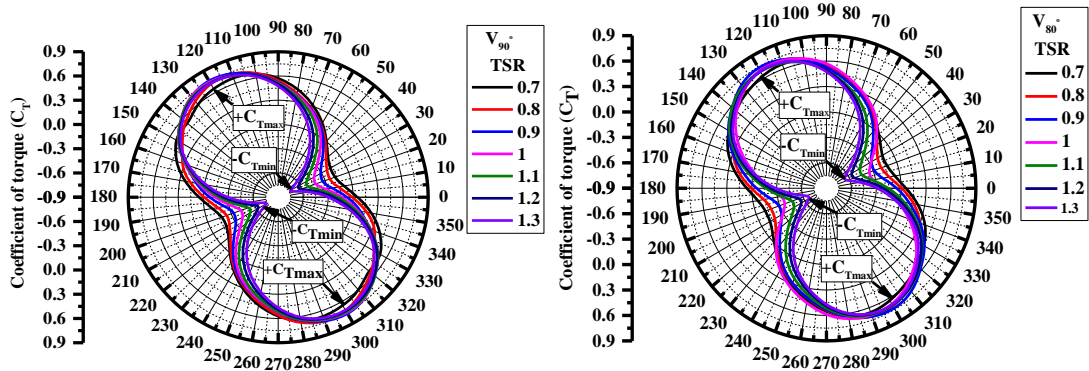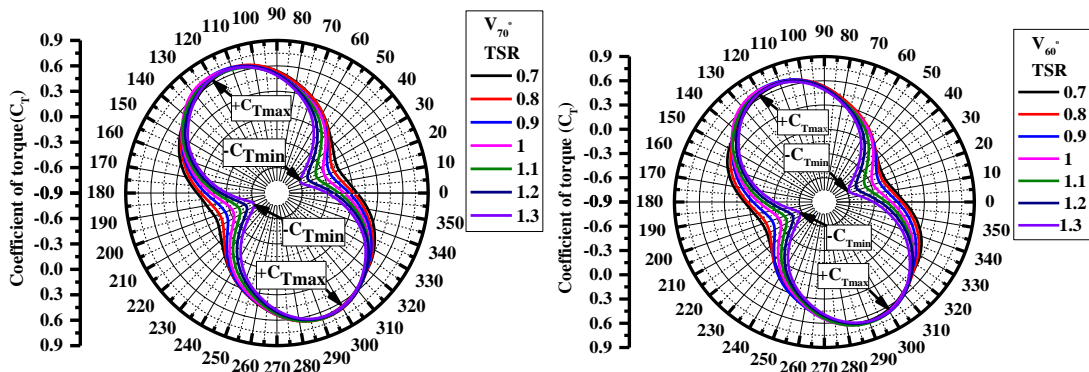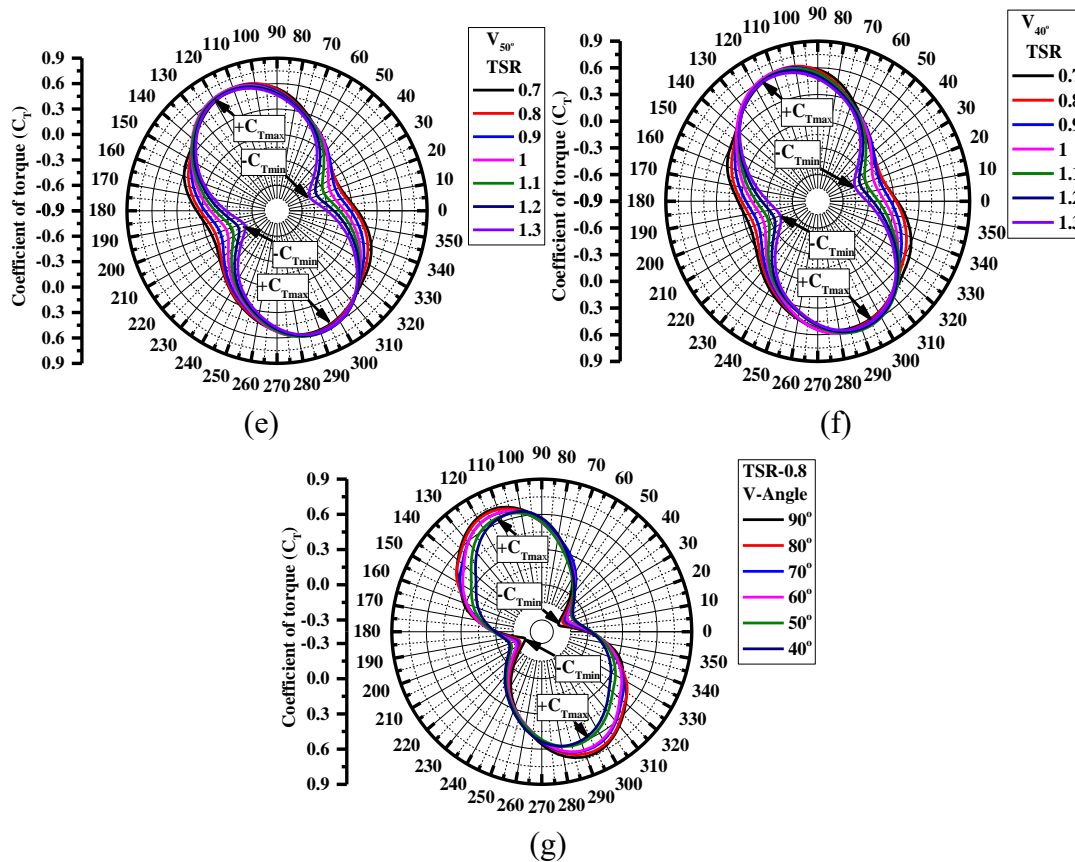
Figure 4.32 Variation of C_T with respect to rotor blade rotation (θ) using polar plots

4.7.3 Pressure and velocity contour plots for the rotor blades with different V-angles ($V_{90°-40°}$)

The present simulation uses a sliding mesh technique (SMT) five revolutions given to the turbine blade and rotates about 1° in each time step. The total time step for one complete revolution of the turbine blade is 360-time steps and the total 1800-time steps given for the five complete revolutions of the turbine blade. There are seven TSR (0.7-1.3) used in the present simulation with an increment of 0.1 and for each TSR, seven simulations were carried out. The transient simulations are carried out for all six-turbine blades with 7 TSR ($V_{90°-40°}$) then a total of 42 simulations were performed with a time step of 1° rotation in each time step. To understand the flow field around the turbine blade ($V_{90°-40°}$) post-processing is carried out to develop pressure contour plots and velocity contour plots at different angular positions such as 0º, 26º, and 109º respectively.

170

4.7.3.1 Pressure contours

Figures 4.33 (a-f) shows the pressure contour plots for rotor blades with different V-angles ($V_{90°-40°}$) at different angular positions (θ) such as 0°, 26° and 109° respectively. The direction of the fluid flow and direction of rotation of turbine blades are shown in Figures 4.33 (a-f). Several significant zones developed during the transient CFD simulation of turbine blades such as high-pressure zone, low-pressure zone, and very low-pressure zones are shown and the magnitude of pressure is shown in red (maximum pressure) and blue colours (Very low pressure) in the left side of the pressure contour plots.

The turbine blade rotates due to pressure difference between the advancing and returning blade profiles and various zones such as high-pressure zone, low-pressure zone, and very low-pressure zones are similar to the zones developed by previous researchers using Savonius hydrokinetic turbines (Kumar and Saini 2017b; a; Sarma, N. K. Biswas and Misra 2014; Talukdar et al. 2018; Zhang et al. 2017b; a) and it shows a similar trend for similar boundary conditions. Figures 4.33 (a-f) show the pressure contour plots for rotor blades $V_{90°}$-$V_{40°}$ at different angular positions such as $\theta=0°$, 26°, and 109° respectively. From pressure contour plots (Figures 4.33 (a-f)), the maximum pressure region on the upstream side of flow near the turbine blade surface is examined whereas the low-pressure region on the downstream side of the flow is observed (Zhang et al. 2017b; a).

On the rear side of the advancing and returning blade profile, a low-pressure region is observed and the very low-pressure zone is created at the tip of the advancing blade (Talukdar et al. 2018; Zhang et al. 2017b). Turbine blades begin to rotate due to this drop-in pressure around the turbine, allowing the Savonius water turbine to extract energy from the flowing water in an irrigation channel. The pressure difference between the advancing blade and returning blade should be maximum, then turbine blades tend to rotate in the anticlockwise direction in the present case (Zhang et al. 2017b; a).

In some of the angular positions such as $\theta=3^{\circ}$- 40° the turbine blade experiences the negative torque, similarly for the angular positions such as $\theta=50^{\circ}$-$182^{\circ,}$ the turbine is giving the positive torque and the C_{Tmax} is attained when the turbine blade is an angular position of 109°. The maximum pressure difference between the advancing and returning blade is increasing when the turbine blade angular position (θ) is in the range of $\theta=50^{\circ}$-182° and it is maximum at $\theta=109^{\circ}$ and the turbine blade with a V-angle of 80° is giving the better performance as compared to other turbine blades. In the pressure contour plots (Figures 4.33 (a-f)) three angular positions were presented such as 0°, 26° and 109° respectively the pressure acting on the advancing blade is maximum at a rotor blade rotation of 109° (Ostos et al. 2019a).

As the V-angle decreases from 90°-40° with an increment of 10° the width of arc on the returning blade profile increases and pressure acting on the returning blade increases), then the turbine's performance decreases. The bucket diameter is higher and the width of arc on the rotor bade is lower for the $V_{80^{\circ}}$ (rotor blade) than other blades. Further, it is also observed that the pressure difference between the advancing and returning blade is maximum when the rotor blade is at an angle of 109° as shown in Figure 4.33 (b) and the magnitude of pressure is 79.98 Pa. The turbine blade $V_{40^{\circ}}$ is having minimum performance as the advancing and returning blade bucket diameter is reduced at the advancing and returning profiles, and the width of arc on returning blade increased. Therefore, drag on the returning blade profile increases which leads to decreased performance.

(a)

(b)

(c)

(d)

174
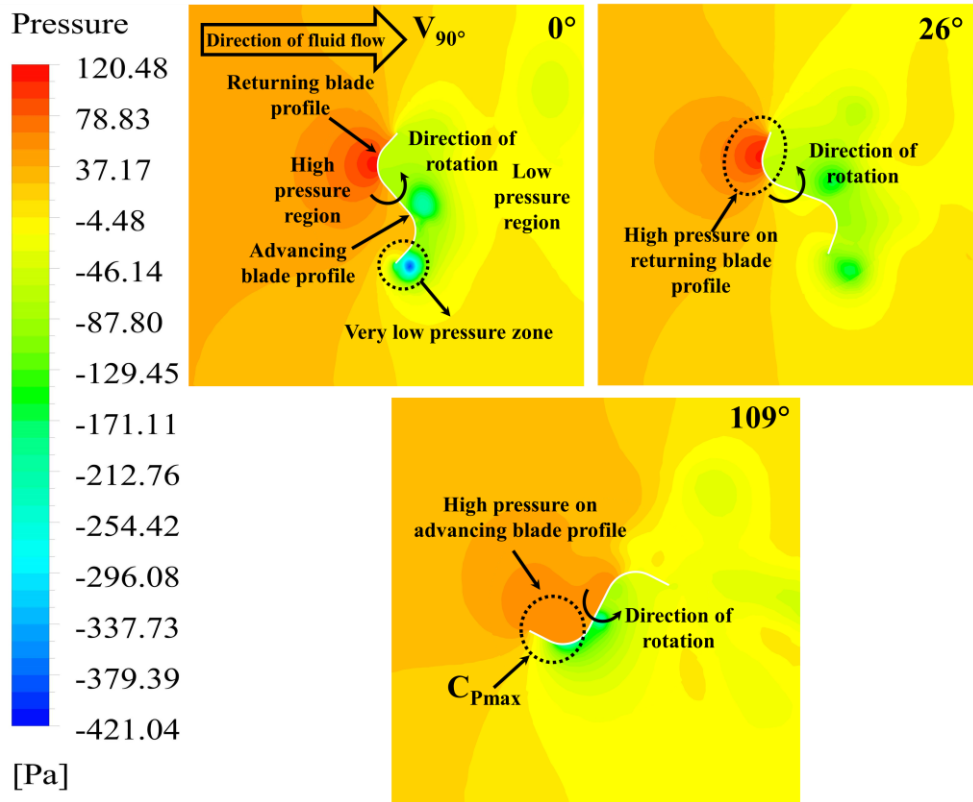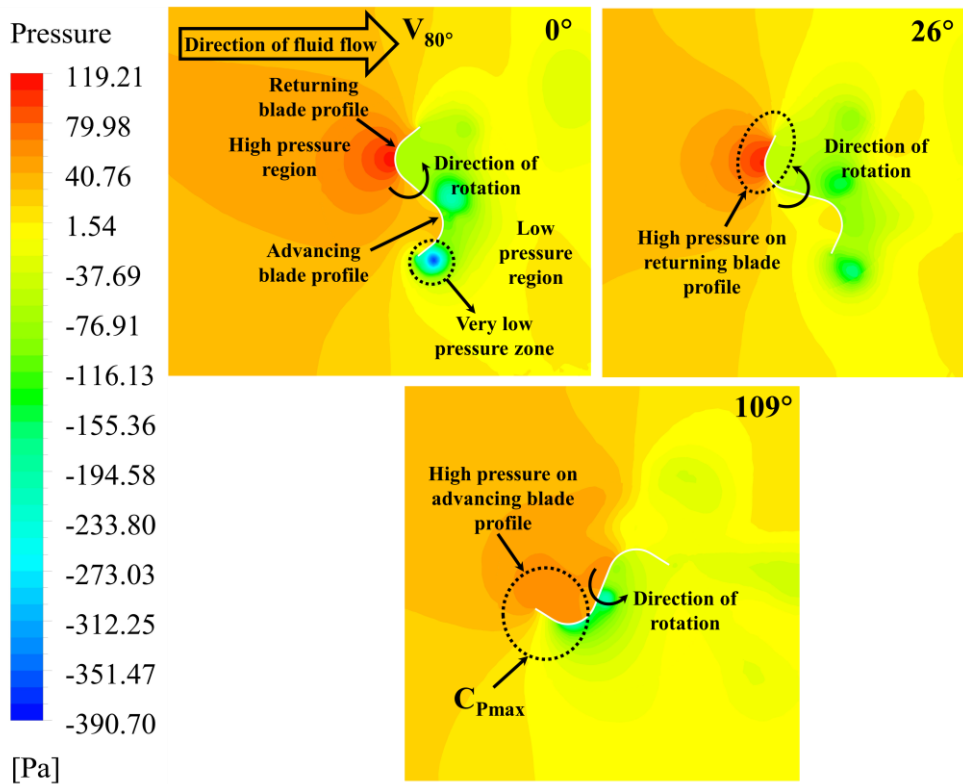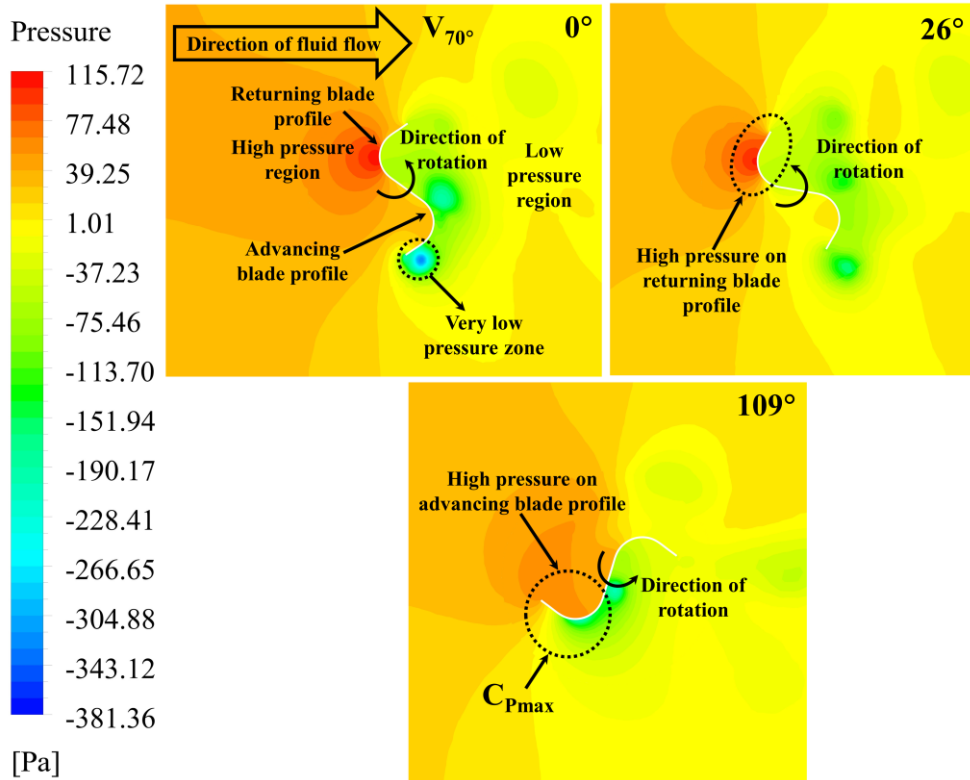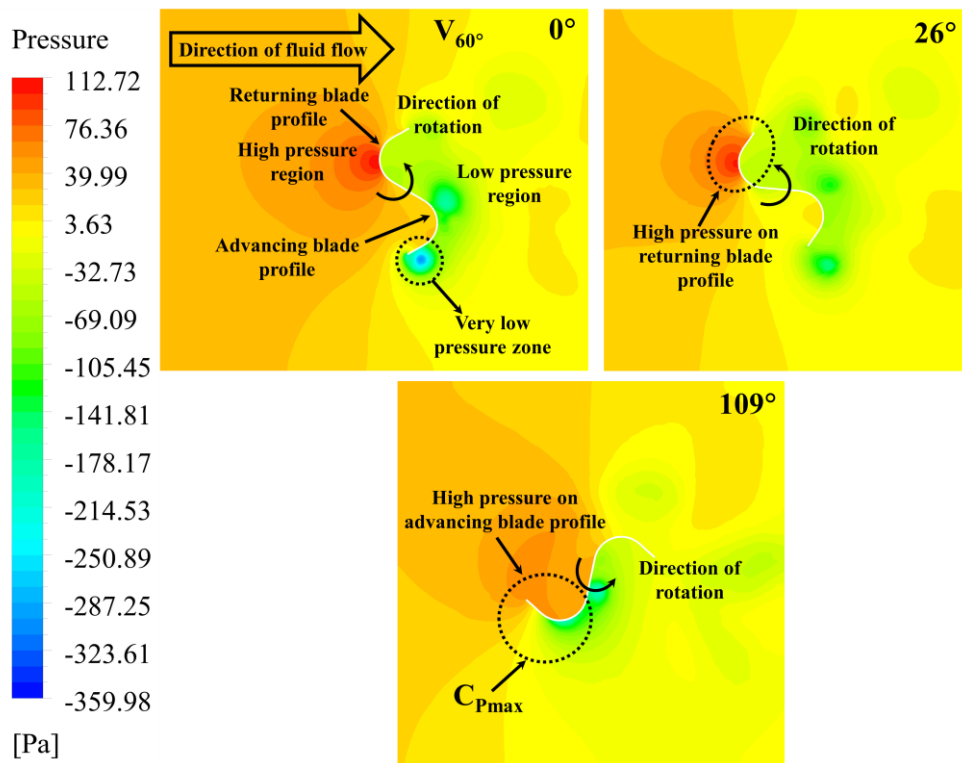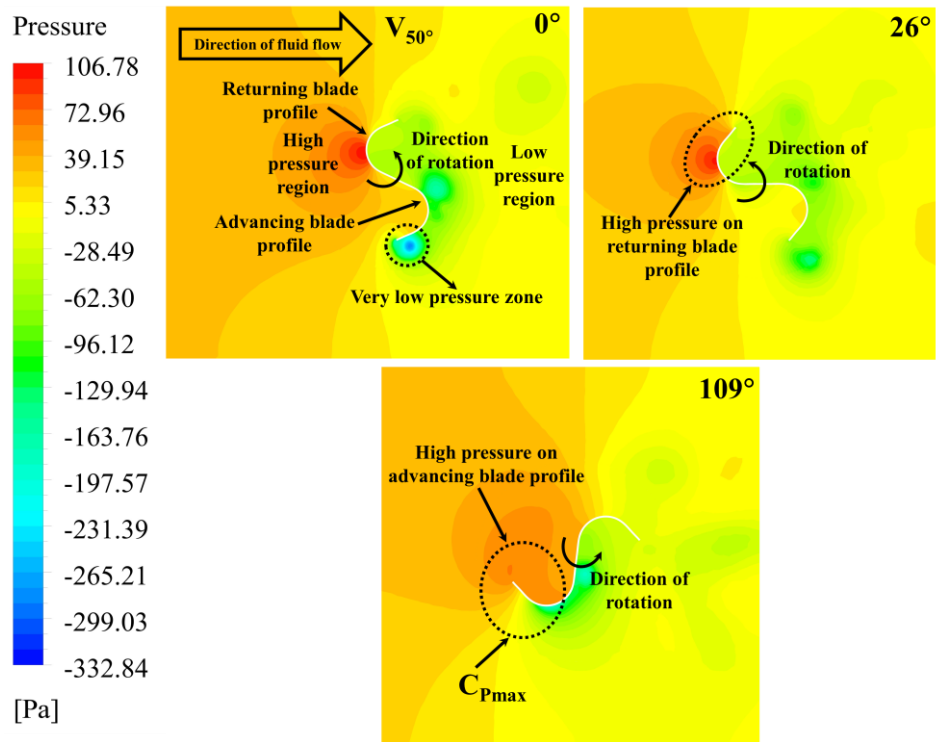
(e)
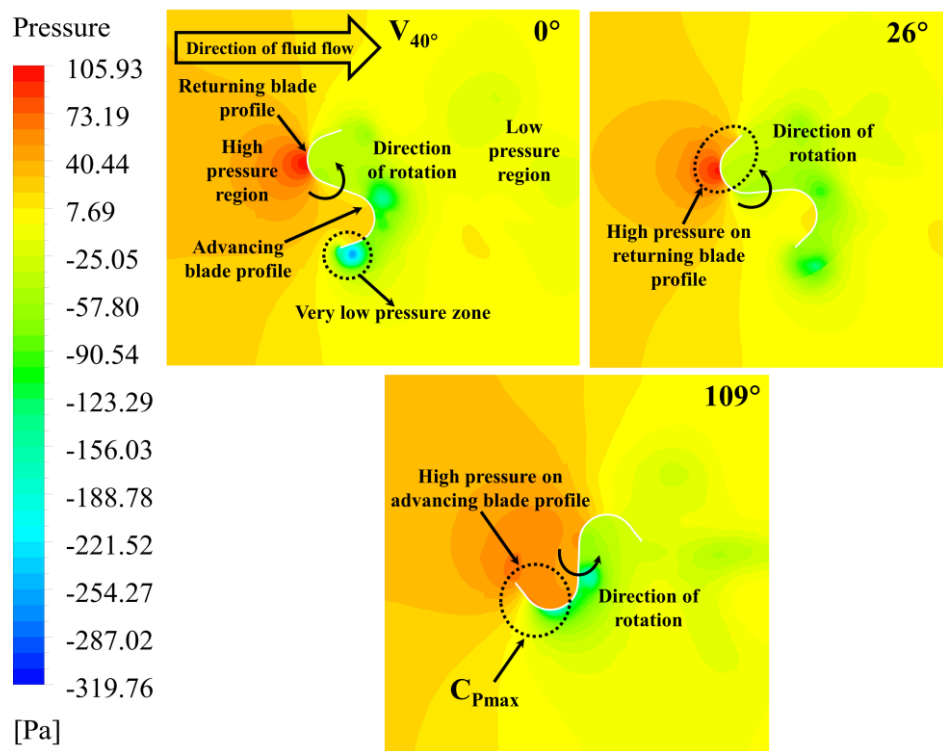
(f)

Figure 4.33 Pressure contour for rotor blade with a V-angle of θ=90°-40° at different

rotor blade positions (θ=0°, 26°, and 109°)

4.7.3.2 Velocity contours

Figures 4.34 (a-f) shows the velocity contour plots for rotor blades with different V-angles ranging from ($V_{90°}$-$V_{40°}$). Velocity contours plots deduce velocity differences within the flow region in various regions near the V-blades. A comparison is made to validate the velocity contour around the V-blades to show the similarities in the results. The various zones developed during the rotation of turbine blade during transient simulations are high-velocity zone at the tip of advancing blade, wake zone at the downstream side of the turbine blade and the direction of rotation of the turbine is in an anticlockwise direction and the direction of fluid flow is shown in Figures 4.34 (a-f). In the wake region, the flow velocity can be found to be significantly reduced.

The velocity contour plots were shown at three different angular positions such as 0°, 26°, and 109° for the rotor blades of $V_{90°-40°}$. In velocity contour plots, high velocity and low-velocity zones are represented by red and blue color in the left side of the velocity contour plots. It can be noted that for all V-blades such as $V_{90°-40°}$, high velocity is seen at the tip of the advancing blade. The zones developed in the simulation are similar to an earlier study carried out by various researchers for similar boundary conditions (Kumar and Saini 2016, 2017a; Talukdar et al. 2018; Zhang et al. 2017a). At the advancing blade tip, maximum velocity was found as 0.83 m/s for rotor blade with a V-angle of 80°.

(a)

(b)

(c)

(d)

178
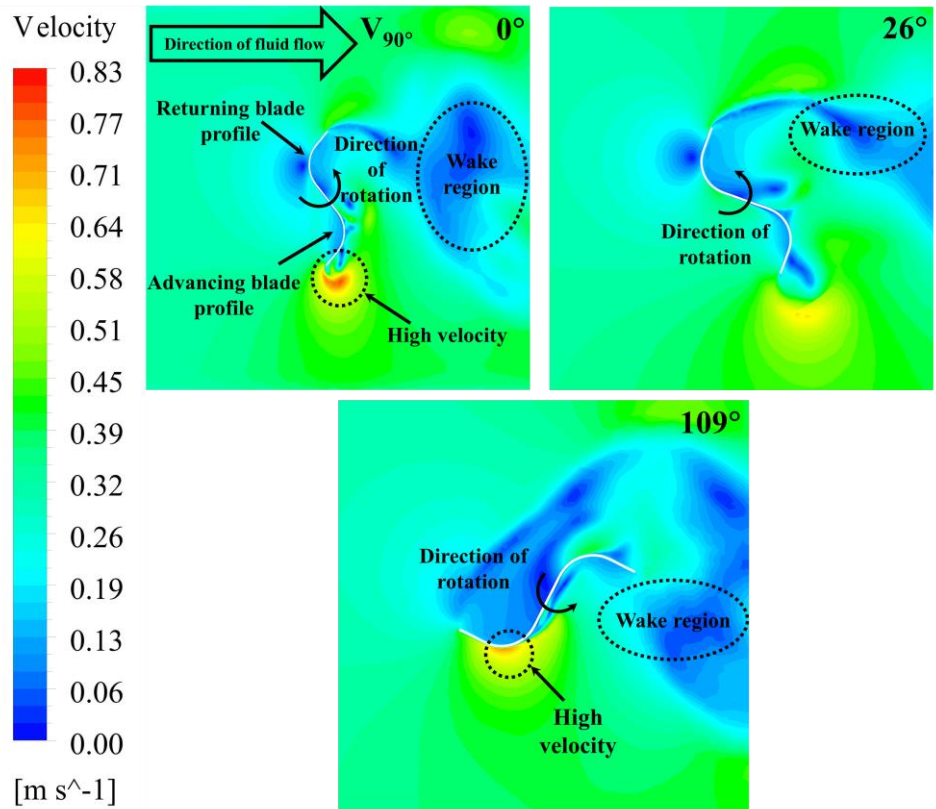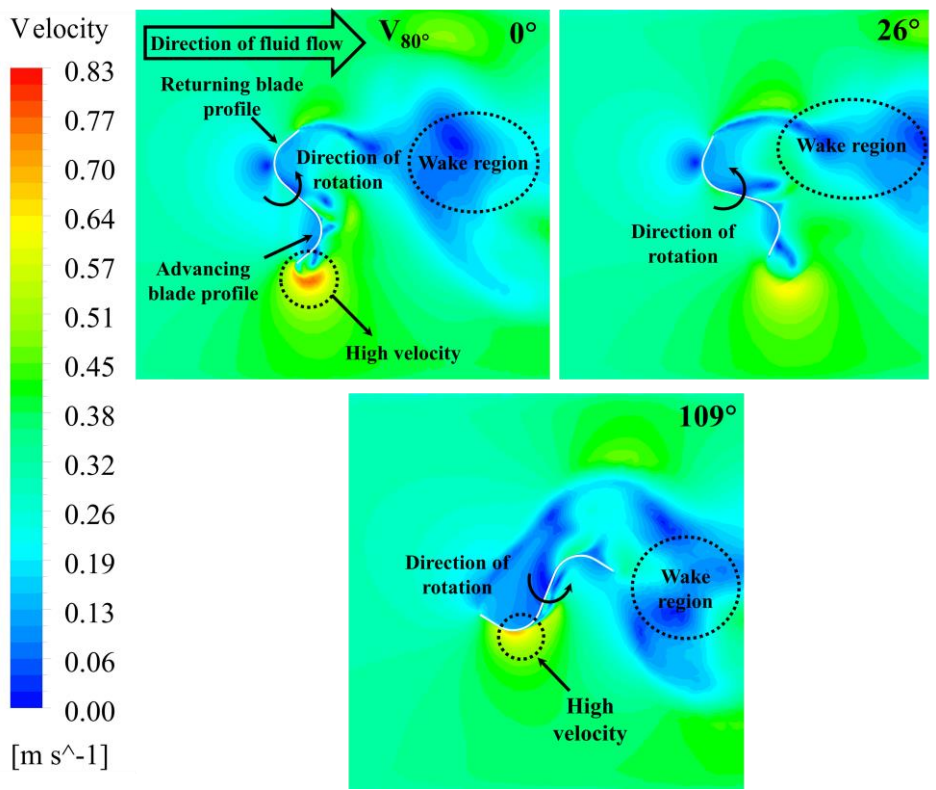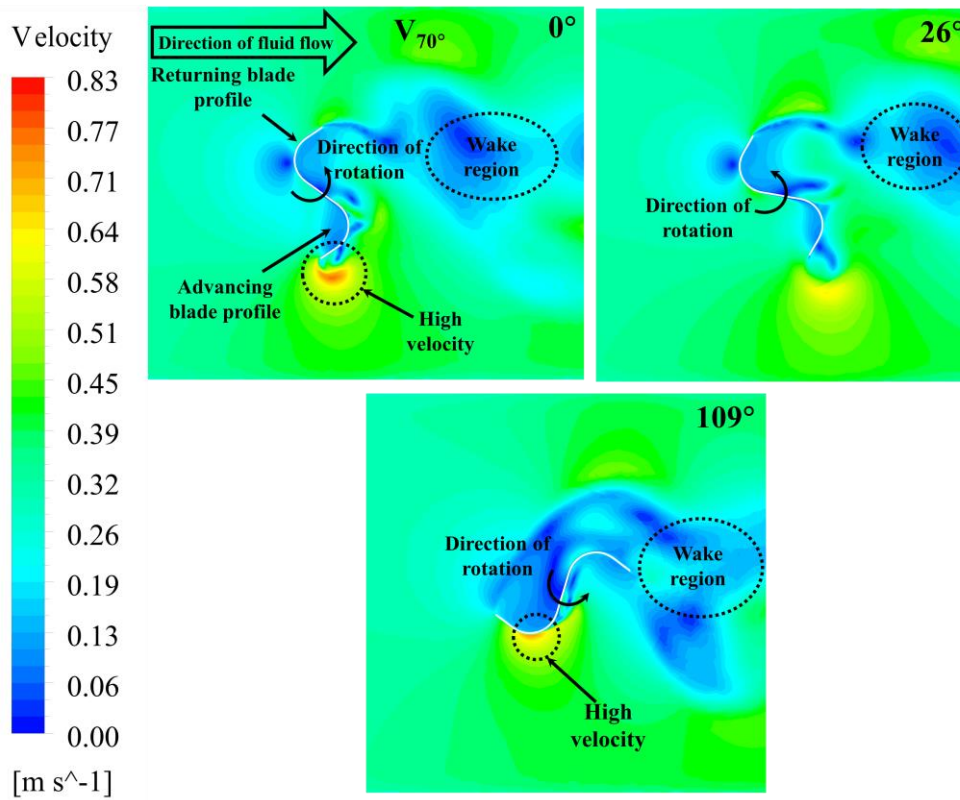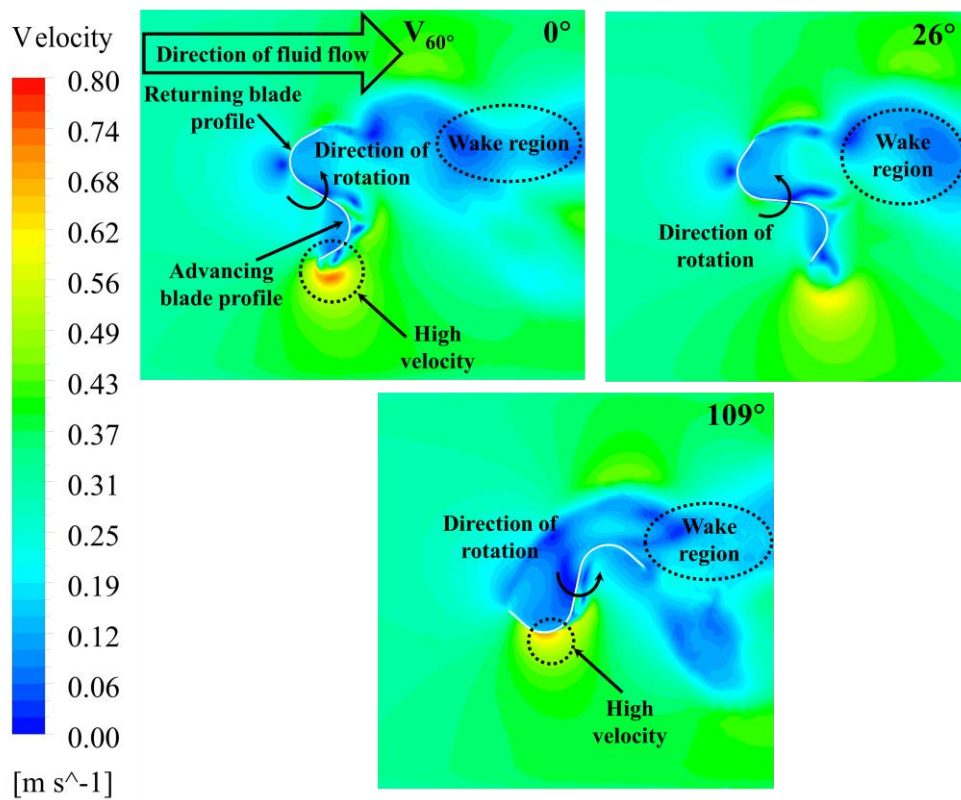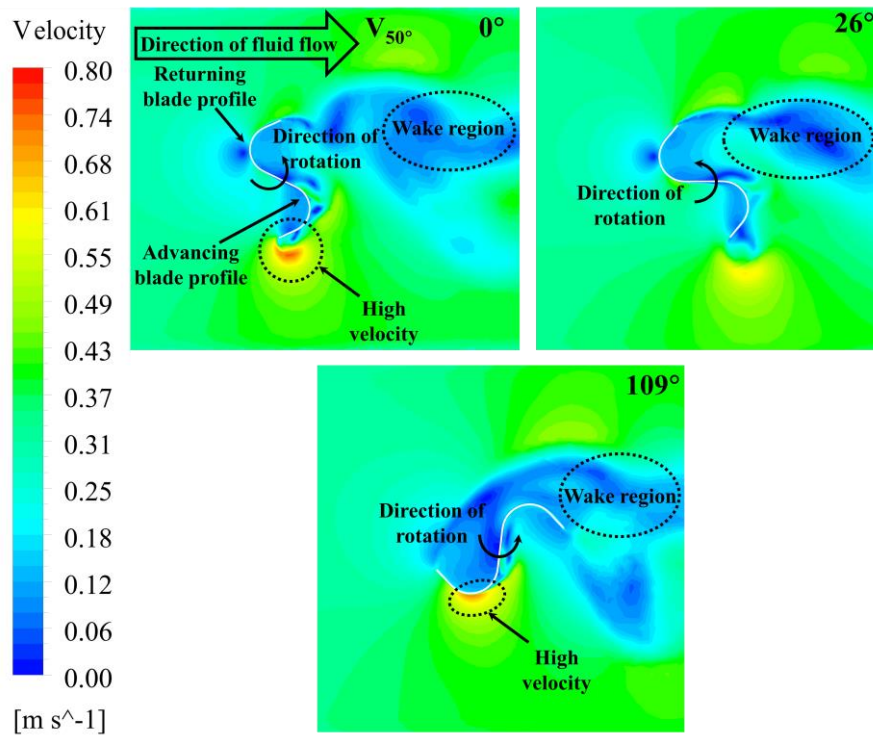
(e)
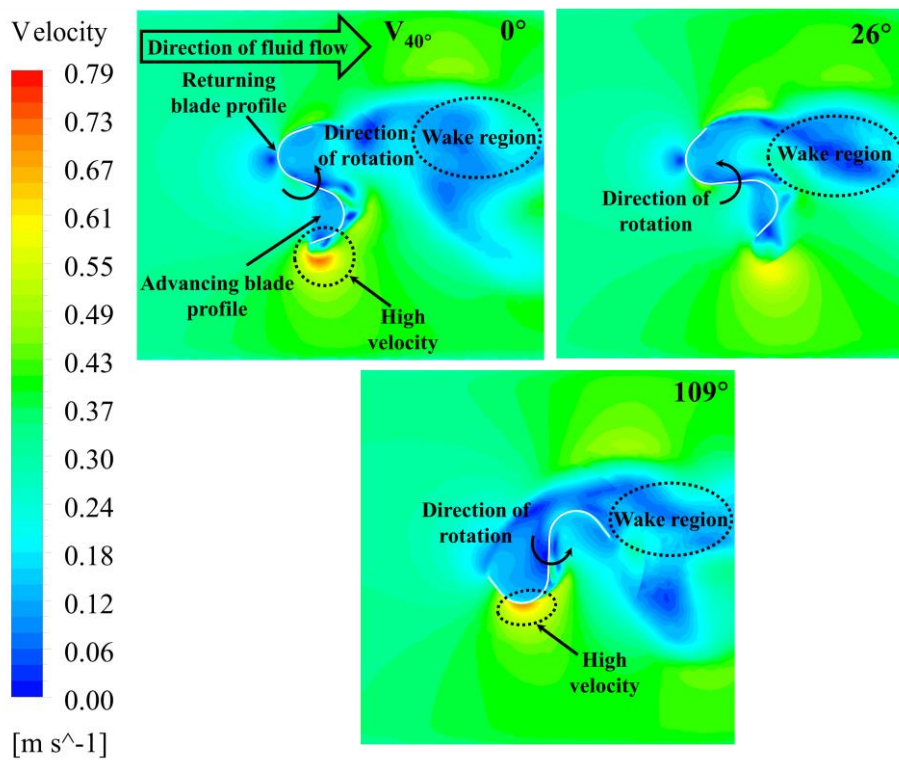
(f)

Figure 4.34 (a-f) Velocity contour plots for rotor blade with a V-angle of θ=90º- 40º

at different rotor blade positions (0º, 26º, and 109º)

4.7.3.3 Performance characteristics and effect of V-angle ($V_{90°\text{-}40°}$)

In this section the various performance parameters such as C_T and C_P were calculated. The variation of C_T and C_P with respect to TSR was studied in the range of 0.7-1.3. From the transient simulations, it is found that the turbine blade with a V-angle of $80°$ is having the better performance as compared to the other V-angles ($V_{90°}$, $V_{70°}$, $V_{60°}$, $V_{50°}$, and $V_{40°}$) with a velocity inlet of 0.3090 m/s. As the V-angle decreases from $70°$-$40°$ the width of a bucket on the advancing and returning blade decreases and the width of arc on V-blade (D_V) on the advancing and returning blade increases.

As the width of arc on V-blade (D_V) increases, the negative torque developed by the returning blade profile increases and net torque developed by the turbine decreases. Therefore, the turbine blade with a V-angle of $80°$ is considered as the optimum blade profile with a fixed aspect ratio (AR) of 0.7 and 0.0 overlap ratio (OR). This optimum blade profile of $V_{80°}$ obtained using transient CFD simulations is further investigated experimentally using multipurpose tilting water flume to study the effect of aspect ratio (AR) ranging from 0.7, 1.0, 1.25, 1.5 and 1.75 using two endplates and two endplate with one middle plate.

The depth (H_W) and velocity of water used for the CFD simulation are 70 mm and 0.3090 m/s. To study the effect of aspect ratio (AR) higher depth of water is required as the depth of water increases, velocity of water also increases due to an increase in discharge of water from the pump. To study the effect of aspect ratio (AR) using two endplates and middle plate, the depth of water and velocity of water maintained in the multipurpose tilting flume is 140 mm and 0.513 m/s.

4.7.4 Effect of aspect ratio (AR) on the performance of modified V-shaped rotor blade V_{80° using experimental investigation

4.7.4.1 Variation of C_T and C_P with respect to TSR on the performance of modified V-shaped rotor blade V_{80° by varying aspect ratio using two and three plates

The purpose of the endplate is to increase the turbine's efficiency by adding a lateral fin at top and bottom of the blades. These additional plates enhance the energy absorption from fluid flow to the rotating blades, by arresting more fluid locally at intersection of V-blade and endplate. This influences the power generated (C_P), by increasing the torque (C_T) (Patel et al. 2018). Inserting an additional lateral fin at middle of the V-blade (middle-plate) enhances the C_P by achieving additional fluid energy transfer, hence 7 % of additional C_P is observed with 0.7 of AR (Figures 4.35 (a-j)).

Effect of endplates on V-blade, with AR of 0.7 to 1.75 were investigated experimentally in order to determine the performance parameters. Effect of endplates on V-blade, with AR of 0.7 to 1.75 were investigated experimentally in order to determine the performance parameters. Experiments were carried out for two endplates and two endplates with one middle plate, in a multipurpose water flume with tilting facility, having a depth of water (H_W) equal to 140 mm, and the velocity of flow was 0.513 m/s. Figures 4.35 (a-j) represent C_T and $C_{P's}$ behavior with respect to TSR, at V-angle of 80° for AR 0.7 to 1.75 of a turbine. The results obtained follow a similar trend with other literature (Ramadan et al. 2020; Talukdar et al. 2018; Patel et al. 2016). The values of C_{Pmax} with respect to TSR for the turbine blades were presented in Table 4.12. It was found that the turbine blade with an aspect ratio of 1.75 shows better performance, and the value of C_{Pmax} were found to be 0.4114 and 0.4242, at TSR of 0.98 and 0.86 for the turbine blade with two endplates and two endplates with additional middle plate respectively.

The value of C_P depends on velocity of flow and the aspect ratio (AR). The increase in the pressure difference between the advancing and returning blade profiles of the turbine leads to the increase in value of C_P (Kumar and Saini 2017b; a) and it shows a maximum at AR of 1.75, with two endplates with one middle plate (3 plates) case. All

the turbine blades with a different aspect ratio were tested experimentally in a multipurpose tilting water flume at 140 mm depth of water. The power generated by turbine depends on the blade's geometry, where the smaller diameter of the blade influences RPM, and larger diameter of the blade influence torque.

When AR increased from 0.7 to 1.75 with a constant diameter of 72.6 mm, the height of the modified V blade changes from 50.82 to 127.05 mm. The blade geometry integrates more surface area of the blade with higher AR and enhances the C_P (Roy 2014a). In the case of a modified V-shaped turbine blade, with a V-angle of 80°, as the AR increases, the power developed by the turbine is also increased due to higher kinetic energy available with the flow of water because of static water pressure.

 This pressure increases linearly from the top surface of the water to the bottom surface, and a similar trend is observed by Patel et al. 2016 and Mahmoud 2012 using Savonius turbines. A modified V-shaped turbine blade acts as a bluff body, which causes a resistance for the flow of water in the channel. Therefore, water deflects its path towards the upward direction of the channel after hitting the modified V-shaped blade and follows the minimum resistance path. As the AR of the turbine blade decreases, kinetic energy utilization is also reduced, i.e., the turbine blade will not receive a sufficient load and stops before the threshold load. The power developed (P_{Rotor}) by the turbine decreases and similar observations was reported by Patel et al. 2016. The depth of water (H_W) available in the channel was 140 mm, hence the turbine with a lower aspect ratio (AR) will not utilize the total kinetic energy available from the water stream in channel.

 Figure 4.36 (a and b) shows the turbine performance parameters with the increase of AR from 0.7 to 1.75. The variation of C_P with respect to TSR for the present study was compared with previous researchers (Figure 4.37). It shows that the variation of C_T with respect to TSR in the present study follows a similar trend with other literatures for the case of Savonius water turbines at different blade profiles with varying input parameters (Golecha et al. 2011; Sarma, N. K. Biswas and Misra 2014; Talukdar et al. 2018). It was found that the turbine blade with an aspect ratio of 1.75 using two endplates with

one middle plate shows better performance, compared to other aspect ratios, and also using 2 plates is shown in Figures 4.36 (a and b). The comparison of C_{Pmax} with respect to TSR for present work and research carried out by various investigators with different blade profiles with different geometric parameters were presented in Table 4.13.

(a)

(b)

(c)

(d)

(e)

(f)

(g)

(h)

(i)

(j)
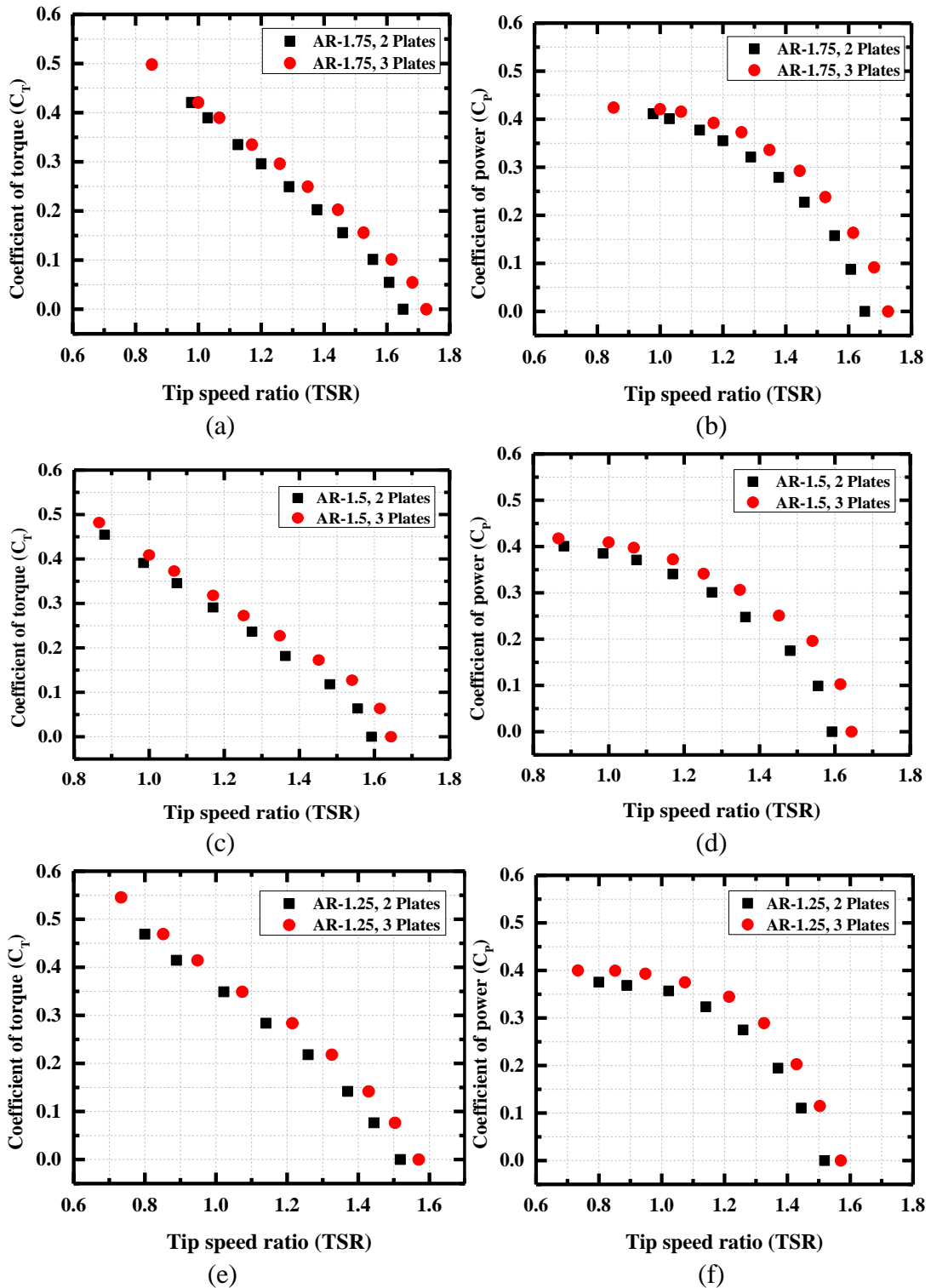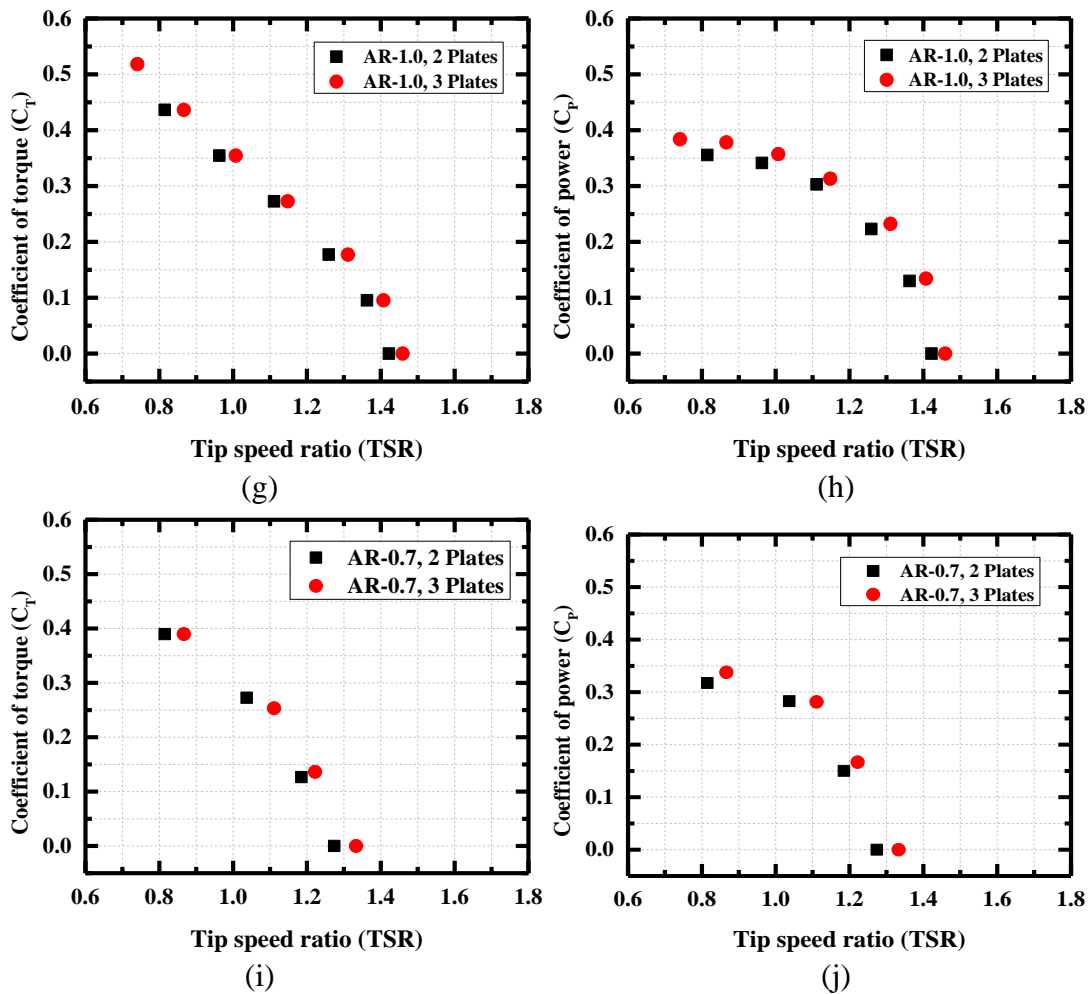
Figure 4.35 (a-j) Variation of C_T and C_P with respect to TSR for turbine blade with two endplates (top and bottom), two endplates with one middle plate and different AR (0.7-1.75)

(a)

(b)
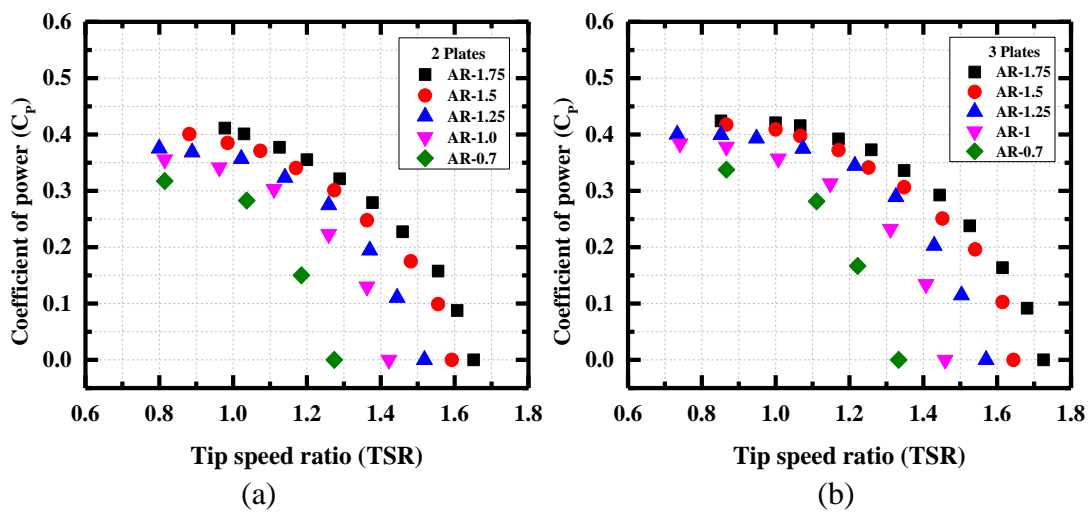
Figure 4.36 (a and b) Variation of C_T and C_P with respect to TSR for a turbine blade with two endplates and two endplates with one middle plate for different AR ranging from 0.7-1.75

Table 4.12 Experimental values of a turbine blade with a V-angle of 80° with different AR with two endplates and two endplates with the middle plate.

Sl. No	AR (Dimensionless)	OR (Dimensionless)	V_W (m/s)	2 Plate		3 Plate	
				C_{Pmax}	TSR	C_{Pmax}	TSR
1.	0.7	0.0	0.513	0.3174	0.83	0.3377	0.8665
2.	1.0	0.0	0.513	0.3555	0.82	0.3838	0.7406
3.	1.25	0.0	0.513	0.3753	0.8	0.4000	0.7332
4.	1.5	0.0	0.513	0.4007	0.89	0.4176	0.8665
5.	1.75	0.0	0.513	0.4114	0.98	0.4242	0.86

Table 4.13 Comparison of the present study with previously published data by various researchers

Researcher	Turbine blade profile	AR	OR	V_W	C_{Pmax}	TSR
Golecha et al. 2011 (water turbine)	Modified Savonius turbine	0.7	0.0	0.485	0.14	0.7
Sarma, N. K. Biswas and Misra 2014 (water turbine)	Three bladed convention type of Savonius turbine	0.7	0.0	0.9	0.39	0.77
Talukdar et al. 2018 (water turbine)	Two blades conventional type of Savoinius turbine	1.0	0.15	0.8	0.28	0.89
Talukdar et al. 2018	Two blades elliptical type of Savoinius turbine	1.0	0.15	0.8	0.17	0.89
Elbatran et al. 2017 (water turbine)	Modified Savonius rotor with ducted nozzle	0.7	0.0	0.46	0.27	0.73
Present study (CFD study) (Two endplates)	Modified V-shaped rotor blade with a V-angle of 80°	0.7	0.0	0.3090	0.2279	0.9
Present study (Experimental) (Two endplates)	Modified V-shaped rotor blade with a V-angle of 80°	1.75	0.0	0.513	0.4114	0.98
Present study (Experimental) (Two endplate with middle plate)	Modified V-shaped rotor blade with a V-angle of 80°	1.75	0.0	0.513	0.4242	0.86
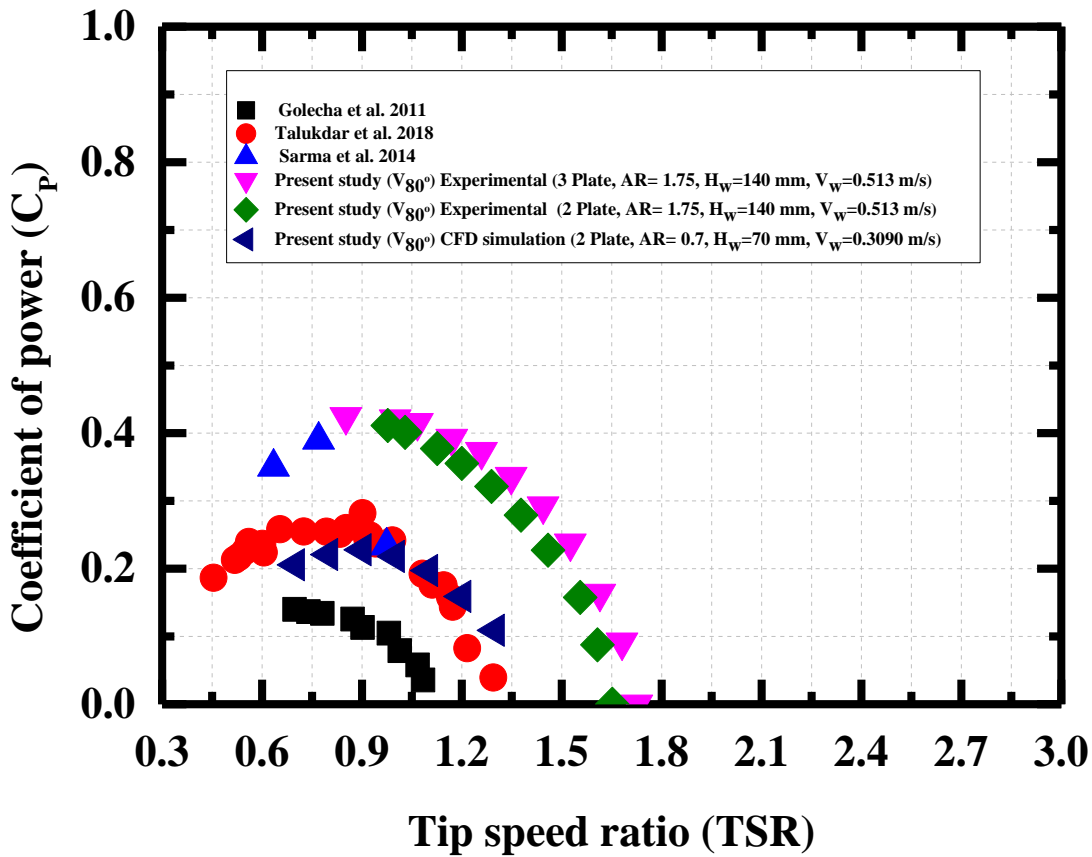
Figure 4.37 Variation of C_P with respect to TSR for the present study with previously published results (Golecha et al. 2011; Sarma et al. 2014; Talukdar et al. 2018)

4.8 Closure

This chapter provided the results and discussion of various parametric investigations such as the influence of bed slope, influence of taper on the performance of conventional Savonius hydrokinetic turbine blade profile using numerical analysis, development of Novel V-shaped rotor blade profile, the effect of overlap ratio (OR=0.0-0.3), the effect of V- angle (90°-40°) and effect of aspect ratio (AR=0.7-1.75) using experimental and three-dimensional numerical investigations. The next chapter deals with the conclusions of experimental, numerical investigation of different parametric studies of the present research work, key contributions, and scope of future work.

Chapter 5

CONCLUSIONS AND SCOPE FOR FUTURE WORK

Based on the research gap, various experimental and numerical investigations were carried out to increase the performance of the Savonius hydrokinetic turbine by using various parametric studies. Initially, the influence of bed slope on the performance of the Savonius hydrokinetic turbine blade was studied experimentally and, the effect of taper on the conventional turbine was studied numerically. Further to reduce the negative torque developed by the returning blade profile, the novel V-shaped blade rotor profile was developed, and the optimum blade profile was investigated further to study the effect of overlap ratio (OR=0.0-0.3), V-angle (90°-40°), and aspect ratio (0.7-1.75) using top, middle and bottom plates. The performance parameters such as C_T and C_P with respect to TSR were computed for all the investigations. The following are the conclusions of the various parametric studies.

5.1 Effect of bed slope on the performance of modified Savonius hydrokinetic turbine

A Savonius rotor of a geometrically scaled-down model is designed in the present investigation, and the experimental result is compared with the previous investigation (Golecha et al. 2011). Based on the present study, the following conclusions are made.

i.   For a bed slope of θ=0.5° it is observed that there is an increase of C_P and C_T values at a TSR of 0.92. Whereas for θ=1°, 1.5° and 2°, C_P and C_T values decreases due to partial submergence of the rotor.

ii.   Due to the decrease in water depth in the flume, the velocity of water increases, and TSR reduces, i.e., the water velocity is higher than the rotational speed of the turbine blade. The value of C_P and C_T decreases with respect to bed slope (θ= 1°, 1.5° and 2°)

iii. The velocity of water (V_w) in the flume increases due to change in bed slope angles (θ), the kinetic energy available in the channel increases, and inertia flow is dominating the gravity flow as the Froude number (Fr) reaches supercritical flow.

iv. Since $P_{Available}$ in the channel is more than the rotor's power, the C_P and C_T values decreased for bed slope angles $\theta=1°$, $1.5°$ and $2°$ due to a decrease in TSR. The Froude number (Fr) reaches supercritical value for at bed slope angle $\theta=1.5°$ and $2°$.

v. As the bed slope angle increases, torque and power developed by the turbine blade increases. At bed slope angle $\theta=2°$ the torque and power developed by the turbine is maximum due to an increase in Froude number (Fr>1).

5.2 Effect of taper on the performance of the Savonious hydrokinetic turbines with and AR and OR of 1.0 and 0.0

The CFD simulations are carried out for conventional and tapered Savonius turbine blade profiles with a water velocity of 0.5 m/s and zero bed slope. The angular velocity (ω) given to the rotating zone is based on the TSR (0.7–1.3) and computed the value of C_T by taking the average value of the last revolution of the turbine blade. The conclusions of the present work are as follows:

i. The C_{Tmax} and C_{Pmax} of the conventional turbine blade are higher as compared to the tapered turbine blade.

ii. The C_{Tmax} and C_{Pmax} of the conventional turbine blade are 0.3 at 0.7 TSR and 0.21 at 0.9 TSR.

iii. Since the cross-sectional area of the tapered turbine blade is lower and the exposed area of the turbine blade in the water is less as compared to the conventional turbine blade, there is a reduction in performance.

iv.   In the case of a tapered turbine blade, there is a loss of energy at the advancing blade's exit side, which leads to the degradation of performance.

v.   If the Savonius hydrokinetic turbine blade has a taper, then the performance of the turbine blade reduces. It is suggested from the present investigation that a turbine without a taper will give better performance than the turbine blade with a taper.

5.3 Novel V-shaped turbine blades V_1-V_5 with fixed V-angle, AR, and OR of 90°, 0.7 and 0.0. Effect of OR ranging from 0.0-0.3 with an increment of 0.05 by using rotor blade V_4

A numerical and experimental investigation was carried out on semi-circular and five different V-shaped rotor blade configurations (V_1-V_5) to determine the performance parameters such as C_{Pmax} and C_{Tmax} with respect to TSR with zero bed slope and without taper case. The validation of the experimental study was carried out with a numerical analysis using a sliding mesh technique with the same profile geometry models and operating conditions. The Effect of OR ranging from 0.0-0.3 with an increment of 0.05 using rotor blade V4 is also studied using the optimum rotor blade V_4 with similar inlet conditions. Finally, from the results obtained following conclusions are made:

i.   The optimum rotor blade profile V_4, obtained from the present investigation is having C_{Pmax} of 0.22 at a TSR of 0.87.

ii.   From the CFD results, it is found that the optimum rotor blade profile $V_{4\ is}$ having V-edge length 0.43 times the original length and an arc radius of 0.56 times the original length is giving better performance when compared with other rotor blade configurations (semi-circular, V_1, V_2, V_3, and V_5).

iii.   As the negative torque developed by the turbine blade V_4 is lower due to the lower arc at returning blade side, the performance of the turbine blade increases and reaches a maximum as compared to the semi-circular blade profile. The C_{Pmax} of V_4 is 19.3% higher than the semi-circular blade profile.

iv. All the modified V-shaped rotor blade with different overlap ratio ranging for 0.0-0.3 gives a C_{Tmax} at a TSR of 0.7 and is higher for 0.0 OR and least for 0.3 OR.

v. The turbine blade with zero overlap ratio is having better performance than that of turbine blades with overlap ratios (0.05, 0.1,0.15,0.2,0.25 and 0.3). The values of C_{Tmax} and C_{Pmax} are found to be 0.29 and 0.22 at a TSR of 0.7 and 0.9, respectively.

vi. With the increase in overlap ratio (OR) ranging from 0.05 to 0.3 with an increment of 0.05, the performance of the modified V-shaped turbine blades decreases with respect to OR.

vii. The presence of a gap (e) between the advancing and returning blades of the turbine blades reduces the performance. The overlap jet is acting in a parallel direction in between the turbine blade straight edges as the overlap jet effect is not acting on the rear side of the returning blade profile and increase of vorticity losses tends to degradation of performance of the turbine blade with overlap ratios (0.05-0.3).

viii. The turbine experiences the C_{Tmax} at $\theta = 120°$ and $300°$, whereas the minimum coefficient of torque (C_{Tmin}) is achieved at $\theta = 20°$ and $200°$ for the case of a turbine blade with zero overlap ratio.

5.4 CFD study of a turbine blade with different V-angles (V$_{90°-40°}$)

Three-dimensional transient simulations were carried out by ANSYS Fluent using sliding mesh technique for rotor blade V_4 to study the effect of V-angle ranging from V$_{90°-40°}$ with an AR of 0.7 and OR 0.0 and TSR range used for the CFD simulation is 0.7-1.3. In the present study, the inlet velocity of water is 0.3090 m/s given as inlet boundary condition, with zero bed slope, without taper case and angular velocity (ω) given to the rotating zone based on the tip speed ratio (TSR) ranging from 0.7-1.3.

The various performance parameters such as C_T and C_P with respect to TSR were calculated. The conclusions of the CFD simulations are as follows.

i. The turbine blade with a V-angle of 80° is giving better performance, and the values of C_{Tmax} and C_{Pmax} with respect to TSR were presented in Table 5.1 with an inlet water velocity (V_W) of 0.3090 m/s and 70 mm depth of water (H_W).

ii. The C_{Pmax} value of the modified V-shaped rotor blade profile with a V-angle of $80°$ is found to be 0.2279 at a TSR of 0.9. The rotor blade with a V-angle of $80°$ is having C_{Pmax} as compared to other blade profiles such as $V_{90°}$, $V_{70°}$, $V_{60°}$, $V_{50°}$ and $V_{40°}$ with a fixed aspect ratio of 0.7, straight edges and arc radius between the advancing and returning blade profiles.

iii. As the V-angle reduces from 70° to $40^{o,}$ the performance parameters such as C_T and C_P decreases with respect to TSR due to a decrease in bucket diameter of the turbine and increase in width of arc (D_V) on return blade. As the width of arc (D_V) increases, the negative torque developed by the returning blade increases, leading to a decrease in the overall performance of the turbine blade. The pressure is acting on the returning blade profile increases as the V-angle varying from 70° to 40° due to an increase in width of arc on returning blade profile side results in an increase in negative torque and reduction of C_{Pmax}.

iv. The maximum pressure difference between the advancing and returning side of the turbine blade is higher when the turbine blade is at an angle of position of 109° for the rotor blade with a V-angle of 80° as compared to other blade profiles such as $V_{90°}$, $V_{70°}$, $V_{60°}$, $V_{50°}$ and $V_{40°}$. At the advancing blade tip, maximum velocity was found as 0.83 m/s for rotor blade with a V-angle of $80°$.

Table 5.1 Simulation results of a rotor blade with a V-angle of 80° and inlet water velocity (V_w) of 0.3090 with an aspect ratio (AR) of 0.7

Sl. No	V-angle (Degrees)	AR	OR	H_W (mm)	C_{Tmax}	TSR	V_W (m/s)	C_{Pmax}	TSR
1.	80°	0.7	0.0	70	0.2940	0.7	0.3090	0.2279	0.9

5.5 Effect of aspect ratio using two endplates and two endplates with middle plate by experimental studies

The optimum turbine blade with a V-angle of 80° obtained by CFD simulations is fabricated with different AR ranging from 0.7-1.75 with two endplates and two endplates with one middle plate. The experimental investigation was carried out for a turbine blade with different AR from 0.7-1.75 using two endplates and two endplates with one middle plate in a multipurpose tilting flume with an inlet velocity of water (V_W) of 0.513 m/s and 140 mm depth of water (H_w). The performance parameters such as C_T and C_P are calculated with TSR. The conclusions for the effect of aspect ratio (AR) with two endplates and two endplates with one middle plate are given below.

   i.   As the turbine AR increases from 0.7-1.75, the energy conversion is increasing with respect to AR. Due to higher depth of water (H_W), turbine blade performance with higher AR is higher. Therefore, a turbine blade with higher AR is suitable for increasing efficiency.

  ii.   In the case of a modified V-shaped turbine blade with a V-angle of 80°, as the AR increases, the power developed (P_{Rotor}) by the turbine is increasing due to increased depth of water and utilization of kinetic energy existing in the channel is also increases. When the AR of the turbine blade decreases, kinetic energy utilization reduces, the turbine blade is not able to take much load, and it halts at lower load due to the loss of kinetic energy.

 iii.   Adding additional plate between the top and bottom endplates with thickness

same as that of the turbine blade (t=1 mm) increases the holding capacity of the fluid in the turbine during the rotation and increases the overall performance of the turbine. The maximum values of the C_P with respect to tip speed ratio (TSR) for a turbine blade with an AR=1.75 with two endplates and two endplates with a middle plate presented in Table 5.2.

iv. The C_{Pmax} of the turbine blade with a V-angle of 80°, AR=1.75, using top, middle and bottom plates is having a C_{Pmax} of 0.4242 at a TSR of 0.86. This rotor blade has shown a significant increase of performance by 86.13% at a tip speed ratio of 0.86 as compared to turbine blade with two endplates with an AR=0.7.

v.   In the present experimental investigation, the maximum available depth of water is 140 mm. Therefore, experimental investigation beyond 1.75 aspect ratio was not carried out due to the limitation of the pump capacity of the multipurpose tilting flume.

Table 5.2 Experimental results of C_{Pmax} values for the optimal two and three-plate turbine blades in relation to TSR.

Sl. No	AR	OR	H_w (mm)	V_w (m/s)	2-Plate		3-Plate	
					C_{Pmax}	TSR	C_{Pmax}	TSR
1.	1.75	0.0	140	0.513	0.4114	0.98	0.4242	0.86

5.6 Key contributions of the present work

Following are the key contribution of the present work.

i.   The effect of bed slope on the performance of Savonius turbine in irrigation channels is carried out to study the effect of Froude number and various forces acting and influence on the efficiency of the turbine blade.

ii. The novel modified V-shaped rotor blade was developed to reduce the negative torque and increase the turbine blade's C_P and C_T.

iii. The novel modified V-shaped rotor blade is further analyzed numerically to study the influence of overlap ratio (OR) on their performance, and various new zones

developed. The flow field around the turbine suggested that, modified V-shaped rotor blades performance reduces with overlap ratios (0.05-0.3).

iv. The optimum rotor blade V_4 with fixed V-angle of 90° is investigated further to study the effect of V-angle ranging from 90°-40° for the improvement of C_P and C_T.

v. The final rotor blade with and V-angle of 80° is used to study the effect of aspect ratio in higher depth of water case using two and three plates. This higher optimum rotor blade can be used for the utilization of kinetic energy available in irrigation channels.

vi. The effect of taper on the performance of Savonious Hydrokinetic turbine carried out. The present study suggested that when the taper is given to the turbine blade, and the performance of the turbine blade reduces.

5.7 Scope for future work

i. The present study can be extended to problems like taper turbine blade by maintaining a similar crossectional area of the turbine blade and bend irrigation channels with different bed angles.

ii. The performance of optimum rotor blade with three plates in varying bend angles of the irrigation channels.

iii. It is suggested that the present study may also be extended for further experimental investigation at a higher depth of water for the rotor blade with a V-angle of 80° to study the effect of aspect ratio beyond AR=1.75.

iv. It is suggested that the experimental and numerical investigations may be extended to study the effect of overlap ratio using optimum blade profile ($V_{80°}$) with an aspect ratio of 1.75 with turbine blade having two endplates and also two endplates with one mid-plate.

REFERENCES

Abraham, J. P., Plourde, B. D., Mowry, G. S., Minkowycz, W. J., and Sparrow, E. M. (2012). "Summary of Savonius wind turbine development and future applications for small-scale power generation." *J. Renew. Sustain. Energy*, 4(4).

Akwa, J. V., Alves Da Silva Júnior, G., and Petry, A. P. (2012a). "Discussion on the verification of the overlap ratio influence on performance coefficients of a Savonius wind rotor using computational fluid dynamics." *Renew. Energy*, 38(1), 141–149.

Akwa, J. V., Vielmo, H. A., and Petry, A. P. (2012b). "A review on the performance of Savonius wind turbines." *Renew. Sustain. Energy Rev.*, 16(5), 3054–3064.

Al-Bahadly, I. (2009). "Building a wind turbine for rural home." *Energy Sustain. Dev.*, 13(3), 159–165.

Al-Ghriybaha, M., and , Mohd Fadhli Zulkafli, Djamal Hissein Didane, S. M. (2019). "The effect of inner blade position on the performance of the Savonius rotor."

Alexander, A. J., and Holownia, B. P. (1978). "Wind Tunnel Tests On a Savonius Rotor." *J. Ind. Aerodyn.*, 3, 343–351.

Alipour, R., Alipour, R., Fardian, F., Koloor, S. S. R., and Petrů, M. (2020). "Performance improvement of a new proposed Savonius hydrokinetic turbine: a numerical investigation." *Energy Reports*, 6, 3051–3066.

Alizadeh, H., Jahangir, M. H., and Ghasempour, R. (2020). "CFD-based improvement of Savonius type hydrokinetic turbine using optimized barrier at the low-speed flows." *Ocean Eng.*, 202(August 2019), 107178.

Alom, N., and Saha, U. K. (2018). "Performance evaluation of vent-augmented elliptical-bladed savonius rotors by numerical simulation and wind tunnel experiments." *Energy*, 152, 277–290.

Alom, N., and Saha, U. K. (2019). "Influence of blade profiles on Savonius rotor performance: Numerical simulation and experimental validation." *Energy Convers. Manag.*, 186(October 2018), 267–277.

Altan, B. D., and Atilgan, M. (2010). "The use of a curtain design to increase the performance level of a Savonius wind rotors." *Renew. Energy*, 35(4), 821–829.

Altan, B. D., and Atilgan, M. (2012). "A study on increasing the performance of

Savonius wind rotors." *J. Mech. Sci. Technol.*, 26(5), 1493–1499.

ANSYS FLUENT 14.5 User's Guide. (2013). "Ansys Fluent Theory Guide." *ANSYS Inc., USA*, 15317(November), 724–746.

Antheaume, S., Maître, T., and Achard, J. L. (2008). "Hydraulic Darrieus turbines efficiency for free fluid flow conditions versus power farms conditions." *Renew. Energy*, 33(10), 2186–2198.

Balduzzi, F., Bianchini, A., Maleci, R., Ferrara, G., and Ferrari, L. (2016). "Critical issues in the CFD simulation of Darrieus wind turbines." *Renew. Energy*, 85, 419–435.

Basumatary, M., Biswas, A., and Misra, R. D. (2021). "Experimental verification of improved performance of Savonius turbine with a combined lift and drag based blade profile for ultra-low head river application." *Sustain. Energy Technol. Assessments*, 44(January), 100999.

Batten, W. M. J., and Müller, G. U. (2011). "Potential for using the floating body structure to increase the efficiency of a free stream energy converter." *34th IAHR Congr. 2011 - Balanc. Uncertain. Water a Chang. World, Inc. 33rd Hydrol. Water Resour. Symp. 10th Conf. Hydraul. Water Eng.*, (1), 2364–2371.

Birjandi, A. H., Bibeau, E. L., Chatoorgoon, V., and Kumar, A. (2013). "Power measurement of hydrokinetic turbines with free-surface and blockage effect." *Ocean Eng.*, 69, 9–17.

Boache, P. J. (1994). "Perspective: A method for uniform reporting of grid refinement studies." *J. Fluids Eng. Trans. ASME*, 116(3), 405–413.

Boyle, G. (2007). *Renewable electricity and the grid*.

Chen, C. A., Huang, T. Y., and Chen, C. H. (2015). "Novel plant development of a parallel matrix system of Savonius wind rotors with wind deflector." *J. Renew. Sustain. Energy*, 7(1), 1–15.

Chen, H., Zheng, Y., Zhou, D., Shen, P., and Liu, H. (2017). "Design and development of an eco-gate pump installation based on computational fluid dynamics." *Proc. Inst. Mech. Eng. Part C J. Mech. Eng. Sci.*, 231(14), 2636–2649.

Cleynen, O., Kerikous, E., Hoerner, S., and Thévenin, D. (2017). "Influence of flotation bodies on the power characteristics of a free-stream water wheel." *WIT Trans. Eng. Sci.*, 115, 55–60.

D'Alessandro, V., Montelpare, S., Ricci, R., and Secchiaroli, A. (2010). "Unsteady

Aerodynamics of a Savonius wind rotor: A new computational approach for the simulation of energy performance." *Energy*, 35(8), 3349–3363.

Doso, O., and Gao, S. (2020). "Application of Savonius Rotor for Hydrokinetic Power Generation." *J. Energy Resour. Technol.*, 142(1), 1–6.

El-Askary, W. A., Nasef, M. H., AbdEL-hamid, A. A., and Gad, H. E. (2015). "Harvesting wind energy for improving performance of savonius rotor." *J. Wind Eng. Ind. Aerodyn.*, 139, 8–15.

Elbatran, A. H., Ahmed, Y. M., and Shehata, A. S. (2017). "Performance study of ducted nozzle Savonius water turbine, comparison with conventional Savonius turbine." *Energy*, 134, 566–584.

Eshagh, M., Fatahian, H., and Fatahian, E. (2020). "Performance improvement of a Savonius vertical axis wind turbine using a porous deflector." *Energy Convers. Manag.*, 220(June), 113062.

F. Blackwell, Robert E. Sheldahl, L. V. F. Ben. (1977). "Wind Tunnel Performance Data for Two-and Three-Bucket Savonius Rotors." *J Energy*, 2(3), 160–164.

Ferrari, G., Federici, D., Schito, P., Inzoli, F., and Mereu, R. (2017). "CFD study of Savonius wind turbine: 3D model validation and parametric analysis." *Renew. Energy*, 105, 722–734.

Fujisawa, N., and Gotoh, F. (1992). "Visualization study of the flow in and around a Savonius rotor." *Exp. Fluids*, 12(6), 407–412.

Ghosh, A., Biswas, A., Sharma, K. K., and Gupta, R. (2015). "Computational analysis of flow physics of a combined three bladed Darrieus Savonius wind rotor." *J. Energy Inst.*, 88(4), 425–437.

Golecha, K., Eldho, T. I., and Prabhu, S. V. (2011). "Influence of the deflector plate on the performance of modified Savonius water turbine." *Appl. Energy*, 88(9), 3207–3217.

Golecha, K., Eldho, T. I., and Prabhu, S. V. (2012). "Study on the interaction between two hydrokinetic Savonius turbines." *Int. J. Rotating Mach.*, 2012(2012).

Gorban', A. N., Gorlov, A. M., and Silantyev, V. M. (2001). "Limits of the Turbine Efficiency for Free Fluid Flow." *J. Energy Resour. Technol.*, 123(4), 311.

Grinspan, A. S., Saha, U. K., Mahanta, P., Suresh Kumar, P., Ratna Rao, D. V, and Veda Bhanu, G. (2001). "Design development and testing of Savonius wind turbine rotor with twisted blades." *Proc. 28th Natl. Conf. Fluid Mech. Fluid Power*, (c), 428–

431.

Gunawan, B. (2017). *March 2017. Assess. Test. Hydrokinetic Turbine Perform. Eff. Open Channel Hydrodyn. An Irrig. Canal Case Study*.

Güney, M. S., and Kaygusuz, K. (2010). "Hydrokinetic energy conversion systems: A technology status review." *Renew. Sustain. Energy Rev.*, 14(9), 2996–3004.

Hand, B., and Cashman, A. (2020). "A review on the historical development of the lift-type vertical axis wind turbine: From onshore to offshore floating application." *Sustain. Energy Technol. Assessments*, 38(December 2019).

Hashemi, S. M., Moghimi, M., and Derakhshan, S. (2020). "Experimental and numerical study of a flapping-blade vertical-axis hydrokinetic turbine under free surface deformation and blockage effects." *Int. J. Environ. Sci. Technol.*

HAYASHI, T., LI, Y., and HARA, Y. (2005). "Wind Tunnel Tests on a Different Phase Three-Stage Savonius Rotor." *JSME Int. J. Ser. B*, 48(1), 9–16.

Herman Jacous Vermaak, Kazumba Kusakana, S. philip koko. (n.d.). "Status of micro-hydrokinetic river technology in rural applications: A review of literatute."

Hu, Y., Tong, Z., and Wang, S. (2009). "A new type of VAWT and blade optimization." *Int. Technol. Innov. Conf. 2009 (ITIC 2009)*, 14–14.

Iio, S., Katayama, Y., Uchiyama, F., Sato, E., and Ikeda, T. (2011). "Influence of Setting Condition on Characteristics of Savonius Hydraulic Turbine with a Shield Plate." 20(3), 224–228.

Irabu, K., and Roy, J. N. (2007). "Characteristics of wind power on Savonius rotor using a guide-box tunnel." *Exp. Therm. Fluid Sci.*, 32(2), 580–586.

Jaohindy, P., McTavish, S., Garde, F., and Bastide, A. (2013). "An analysis of the transient forces acting on Savonius rotors with different aspect ratios." *Renew. Energy*, 55, 286–295.

Kacprzak, K., Liskiewicz, G., and Sobczak, K. (2013). "Numerical investigation of conventional and modified Savonius wind turbines." *Renew. Energy*, 60, 578–585.

Kailash, G., Eldho, T. I., and Prabhu, S. V. (2012). "Performance study of modified savonius water turbine with two deflector plates." *Int. J. Rotating Mach.*, 2012, 1–12.

Kamoji, M. A., Kedare, S. B., and Prabhu, S. V. (2009a). "Performance tests on helical Savonius rotors." *Renew. Energy*, 34(3), 521–529.

Kamoji, M. A., Kedare, S. B., and Prabhu, S. V. (2009b). "Experimental investigations

on single stage modified Savonius rotor." *Appl. Energy*, 86(7–8), 1064–1073.

Kamoji, M. A., Kedare, S. B., and Prabhu, S. V. (2008). "Experimental investigations on single stage , two stage and three stage conventional Savonius rotor." (January), 877–895.

Kamoji, M. A., Kedare, S. B., and Prabhu, S. V. (2009c). "Experimental investigations on single stage modified Savonius rotor.pdf." *Appl. Energy*, 86.

Kang, C., Liu, H., and Yang, X. (2014). "Review of fluid dynamics aspects of Savonius-rotor-based vertical-axis wind rotors." *Renew. Sustain. Energy Rev.*, 33, 499–508.

Kassam, S. (2009). "IN-SITU TESTING OF A DARRIEUS HYDRO KINETIC TURBINE IN ln-Situ Testing of a Darrieus Hydro Kinetic Turbine in Gold Glimates Master of Science." University of Manitoba.

Kerikous, E., and Thévenin, D. (2019a). "Optimal shape and position of a thick deflector plate in front of a hydraulic Savonius turbine." *Energy*, 189.

Kerikous, E., and Thévenin, D. (2019b). "Optimal shape of thick blades for a hydraulic Savonius turbine." *Renew. Energy*, 134, 629–638.

Khan, M. J., Bhuyan, G., Iqbal, M. T., and Quaicoe, J. E. (2009a). "Hydrokinetic energy conversion systems and assessment of horizontal and vertical axis turbines for river and tidal applications: A technology status review." *Appl. Energy*, 86(10), 1823–1835.

Khan, M. J., Iqbal, M. T., and Quaicoe, J. E. (2008). "River current energy conversion systems: Progress, prospects and challenges." *Renew. Sustain. Energy Rev.*, 12(8), 2177–2193.

Khan, M. N. I., Tariq Iqbal, M., Hinchey, M., and Masek, V. (2009b). "Performance of savonius rotor as a water current turbine." *J. Ocean Technol.*, 4(2), 71–83.

Korprasertsak, N., and Leephakpreeda, T. (2015). *CFD-Based Power Analysis on Low Speed Vertical Axis Wind Turbines with Wind Boosters. Energy Procedia*, Elsevier B.V.

Kumar, A., and Saini, R. P. (2016). "Performance parameters of Savonius type hydrokinetic turbine - A Review." *Renew. Sustain. Energy Rev.*, 64, 289–310.

Kumar, A., and Saini, R. P. (2017a). "Performance analysis of a single stage modified Savonius hydrokinetic turbine having twisted blades." *Renew. Energy*.

Kumar, A., and Saini, R. P. (2017b). "Performance analysis of a Savonius hydrokinetic turbine having twisted blades." *Renew. Energy*, 113, 502–522.

Layeghmand, K., Ghiasi Tabari, N., and Zarkesh, M. (2020). "Improving efficiency of Savonius wind turbine by means of an airfoil-shaped deflector." *J. Brazilian Soc. Mech. Sci. Eng.*, 42(10).

Liu, W., and Xiao, Q. (2015). "Investigation on Darrieus type straight blade vertical axis wind turbine with flexible blade." *Ocean Eng.*, 110, 339–356.

Loots, I., Dijk, M. Van, Barta, B., Vuuren, S. J. Van, and Bhagwan, J. N. (2015). "A review of low head hydropower technologies and applications in a South African context." *Renew. Sustain. Energy Rev.*, 50, 1254–1268.

M.H. Mohamed, G. Janiga, E. Pap, D. T. (2010). "Optimization of Savonius turbines using an obstacle shielding the returning blade." *Renew. Energy*, 35(11), 2618–2626.

Mahmoud, N. H. (2012). "An experimental study on improvement of Savonius rotor performance." *Alexandria Eng. J.*, 51(1), 19–25.

Mereu, R., Federici, D., Ferrari, G., Schito, P., and Inzoli, F. (2017). "Parametric numerical study of Savonius wind turbine interaction in a linear array." *Renew. Energy*, 113, 1320–1332.

Moffat, R. J. (1988). "Describing the uncertainties in experimental results." *Exp. Therm. Fluid Sci.*, 1(1), 3–17.

Moghimi, M., and Motawej, H. (2020). "Developed DMST model for performance analysis and parametric evaluation of Gorlov vertical axis wind turbines." *Sustain. Energy Technol. Assessments*, 37(December 2019), 100616.

Mohamed, M. H., Janiga, G., Pap, E., and Thévenin, D. (2011). "Optimal blade shape of a modified Savonius turbine using an obstacle shielding the returning blade." *Energy Convers. Manag.*, 52(1), 236–242.

Mosbahi, M., Ayadi, A., Chouaibi, Y., Driss, Z., and Tucciarelli, T. (2019). "Performance study of a Helical Savonius hydrokinetic turbine with a new deflector system design." *Energy Convers. Manag.*, 194(April), 55–74.

Mosbahi, M., Ayadi, A., Chouaibi, Y., Driss, Z., and Tucciarelli, T. (2020a). "Performance improvement of a novel combined water turbine." *Energy Convers. Manag.*, 205(September 2019), 112473.

Mosbahi, M., Elgasri, S., Lajnef, M., Mosbahi, B., and Driss, Z. (2020b). "Performance enhancement of a twisted Savonius hydrokinetic turbine with an upstream deflector." *Int. J. Green Energy*, 00(00), 1–15.

Nakajima, Miyoshi, Iio, S., and Toshihiko Ikeda. (2008a). "Performance of Savonius Rotor for Environmentally Friendly Hydraulic Turbine." *J. Fluid Sci. Technol.*, 3(3), 420–429.

Nakajima, Miyoshi, Shouichiro Iio, and Toshihiko Ikeda. (2008b). "Performance of Double-step Savonius Rotor for Environmentally Friendly Hydraulic Turbine." *J. Fluid Sci. Technol.*, 3(3), 410–419.

Ostos, I., Ruiz, I., Gajic, M., Gómez, W., Bonilla, A., and Collazos, C. (2019a). "A modified novel blade configuration proposal for a more efficient VAWT using CFD tools." *Energy Convers. Manag.*, 180(November 2018), 733–746.

Ostos, I., Ruiz, I., Gajic, M., Gómez, W., Bonilla, A., and Collazos, C. (2019b). "A modifieOstos, I., Ruiz, I., Gajic, M., Gómez, W., Bonilla, A., & Collazos, C. (2019). A modified novel blade configuration proposal for a more efficient VAWT using CFD tools. Energy Conversion and Management, 180(November 2018), 733–746. https://doi.org." *Energy Convers. Manag.*, 180(November 2018), 733–746.

Patel, V., Eldho, T. I., and Prabhu, S. V. (2017). "Experimental investigations on Darrieus straight blade turbine for tidal current application and parametric optimization for hydro farm arrangement." *Int. J. Mar. Energy*, 17, 110–135.

Patel, V., Eldho, T. I., and Prabhu, S. V. (2019). "Performance enhancement of a Darrieus hydrokinetic turbine with the blocking of a specific flow region for optimum use of hydropower." *Renew. Energy*, 135, 1144–1156.

Payambarpour, S. A., Naja, A. F., and Magagnato, F. (2020). "Investigation of deflector geometry and turbine aspect ratio effect on 3D modi fied in-pipe hydro Savonius turbine : Parametric study." 148, 44–59.

Pham Long. (n.d.). "Riverine Hydrokinetic Technology : A Review."

Power, T. H. E., From, G., Currents, T., and Darrieus, B. Y. (1996). "Wrfc 1996." 1242–1245.

Puri, V., Chauhan, Y. K., and Singh, N. (2017). "A comparative design study and analysis of inner and outer rotor permanent magnet synchronous machine for power generation in vertical axis wind turbine using GSA and GSA-PSO." *Sustain. Energy Technol. Assessments*, 23(April), 136–148.

Qasemi, K., and Azadani, L. N. (2020). "Optimization of the power output of a vertical axis wind turbine augmented with a flat plate deflector." *Energy*, 202, 117745.

Quaranta, E. (2018). "Stream water wheels as renewable energy supply in flowing water: Theoretical considerations, performance assessment and design recommendations." *Energy Sustain. Dev.*, 45(August 2018), 96–109.

Ramadan, A., Nawar, M. A. A., and Mohamed, M. H. (2020). "Performance evaluation of a drag hydro kinetic turbine for rivers current energy extraction - A case study." *Ocean Eng.*, 195(October 2019), 106699.

Ramadan, A., Yousef, K., Said, M., and Mohamed, M. H. (2018). "Shape optimization and experimental validation of a drag vertical axis wind turbine." *Energy*, 151, 839–853.

Rourke, F. O., Boyle, F., and Reynolds, A. (2010). "Marine current energy devices : Current status and possible future applications in Ireland." 14, 1026–1036.

Roy, S. (2014a). "Aerodynamic performance evaluation of a novel savonius-style wind turbine through unsteady simulations and wind tunnel experiments." Indian Institute of Technology Guwahati.

Roy, S. (2015). "Flow physics around a Savonius-style wind turbine considering the influence of shaft." (May 2016).

Roy, S., and Ducoin, A. (2016). "Unsteady analysis on the instantaneous forces and moment arms acting on a novel Savonius-style wind turbine." *Energy Convers. Manag.*, 121, 281–296.

Roy, S. M. K. S. (2014b). "GTINDIA2014-8152." *Proc. ASME 2014 Gas Turbine India Conf.*, 1–7.

Roy, S., and Saha, U. K. (2013a). "Review of experimental investigations into the design, performance and optimization of the Savonius rotor." *Proc. Inst. Mech. Eng. Part A J. Power Energy*, 227(4), 528–542.

Roy, S., and Saha, U. K. (2013b). "Review on the numerical investigations into the design and development of Savonius wind rotors." *Renew. Sustain. Energy Rev.*, 24, 73–83.

Rumpfkeil, M. P., Verma, A. K., and Saini, R. P. (2015). "Efficiency Measurement Techniques of Hydro Kinetic Turbines : a Review." *Int. Conf. Hydropower Sustain. Dev.*, 268–285.

Runge, S., Stoesser, T., Morris, E., and White, M. (2018). "Technology Readiness of a Vertical-Axis Hydro-Kinetic Turbine." *J. Power Energy Eng.*, 06(08), 63–85.

S. J. Savonius, H. (1931). *S. J. Savonius, Helsinfors*.

Saad El-Deen, A. E., Nawar, M. A. A., Attai, Y. A., and Abd El-Maksoud, R. M. (2020). "On the enhancement of Savonius Bach-type rotor performance by studying the optimum stator configuration." *Ocean Eng.*, 217(April), 107954.

Saha, U. K., Thotla, S., and Maity, D. (2008). "Optimum design configuration of Savonius rotor through wind tunnel experiments." *J. Wind Eng. Ind. Aerodyn.*, 96(8–9), 1359–1375.

Saini, G., and Saini, R. P. (2018). "A numerical analysis to study the effect of radius ratio and attachment angle on hybrid hydrokinetic turbine performance." *Energy Sustain. Dev.*, 47, 94–106.

Saini, G., and Saini, R. P. (2020). "A computational investigation to analyze the effects of different rotor parameters on hybrid hydrokinetic turbine performance." *Ocean Eng.*, 199(October 2019), 107019.

Salleh, M. B., Kamaruddin, N. M., and Mohamed-kassim, Z. (2019). "Savonius hydrokinetic turbines for a sustainable river-based energy extraction : A review of the technology and potential applications in Malaysia." *Sustain. Energy Technol. Assessments*, 36(September), 100554.

Sarma, N. K. Biswas, A., and Misra, R. D. (2014). "Experimental and computational evaluation of Savonius hydrokinetic turbine for low velocity condition with comparison to Savonius wind turbine at the same input power." *Energy Convers. Manag.*, 83, 88–98.

Savonius, S. J. (1929). "Rotor adapted to be driven by wind or flowing water." *Patient*, 8.

Savonius, S. J. (1930). "Wind Rotor." *Patient*, 4.

Shaheen, M., and Abdallah, S. (2016). "Development of efficient vertical axis wind turbine clustered farms." *Renew. Sustain. Energy Rev.*, 63, 237–244.

Shaheen, M., and Abdallah, S. (2017). "Efficient clusters and patterned farms for Darrieus wind turbines." *Sustain. Energy Technol. Assessments*, 19, 125–135.

Shaheen, M., El-Sayed, M., and Abdallah, S. (2015). "Numerical study of two-bucket Savonius wind turbine cluster." *J. Wind Eng. Ind. Aerodyn.*, 137, 78–89.

Sharifian, A. (2014). "Influence of Blade Overlap and Blade Angle on the Aerodynamic Coefficients in Vertical Axis Swirling type Savonius Wind Turbine." (December).

Shashikumar C M, Ramesh, H., Vijaykumar, H., and Vasudeva, M. (2021). "Experimental and numerical investigation of novel V-shaped rotor for hydropower utilization." *Ocean Eng.*, 224, 108689.

Shaughnessy, B. M., and Probert, S. D. (1992). "Partially-blocked savonius rotor." *Appl. Energy*, 43(4), 239–249.

Shikha, Bhatti, T. S., and Kothari, D. P. (2003). "Wind energy conversion systems as a distributed source of generation." *J. Energy Eng.*, 129(3), 69–80.

Shikha, S., Bhatti, T. S., and Kothari, D. P. (2005). "Air concentrating nozzles: a promising option for wind turbines." *Int. J. Energy Technol. Policy*, 3(4), 394–412.

Sivakumar, A., Anandh, R., Anantharaman, A., and Suresh, M. (2018). "Multi Stage Power Generation in An Open Canal System by Accelerated Flow." *J. Informatics Math. Sci.*, 10(1–2), 313–320.

Takenori Ogawa, H. Y. (1986). "NII-Electronic Library Service." *Bull. JSME*, 29(253), 253–22.

Talukdar, P. K., Sardar, A., Kulkarni, V., and Saha, U. K. (2018). "Parametric analysis of model Savonius hydrokinetic turbines through experimental and computational investigations." *Energy Convers. Manag.*, 158(January), 36–49.

Tartuferi, M., D'Alessandro, V., Montelpare, S., and Ricci, R. (2015). "Enhancement of savonius wind rotor aerodynamic performance: A computational study of new blade shapes and curtain systems." *Energy*, 79(C), 371–384.

Tian, W., Mao, Z., Zhang, B., and Li, Y. (2018). "Shape optimization of a Savonius wind rotor with different convex and concave sides." *Renew. Energy*, 117, 287–299.

Tian, Z. M. andWenlong. (2016). "Effect of the blade arc angle on the performance of a Savonius wind turbine." *Adv. Mech. Eng.*, 89(5), 231–244.

Uchiyama, T., Gu, Q., Degawa, T., Iio, S., Ikeda, T., and Takamure, K. (2020). "Numerical simulations of the flow and performance of a hydraulic Savonius turbine by the vortex in cell method with volume penalization." *Renew. Energy*, 157, 482–490.

Vimal Patel, Ganapathi Bhat, T. I. Eldho, S. V. P. (2016). "Influence of overlap ratio and aspect ratio on the performance of Savonius hydrokinetic turbine." *Int. J. energy Res.*, 31(17 sept 2016), 135–147.

Vimal Patel, T.I. Eldho, S. V. P. (2018). "Theoretical study on the prediction of the hydrodynamic performance of a Savonius turbine based on stagnation pressure and

impulse momentum principle." *Energy Convers. Manag.*, 168(October 2017), 545–563.

Wahyudi, B., Soeparman, S., Wahyudi, S., and Denny, W. (2013). "A Simulation Study of Flow and Pressure Distribution Patterns in and around of Tandem Blade Rotor of Savonius (TBS) Hydrokinetic Turbine Model." *J. Clean Energy Technol.*, 1(4), 286–291.

Wahyudi, B., Soeparman, S., and Hoeijmakers, H. W. M. (2015). "Optimization design of Savonius diffuser blade with moving deflector for hydrokinetic cross flow turbine rotor." *Energy Procedia*, 68, 244–253.

Wong, K. H., Chong, W. T., Sukiman, N. L., Poh, S. C., Shiah, Y. C., and Wang, C. T. (2017). "Performance enhancements on vertical axis wind turbines using flow augmentation systems: A review." *Renew. Sustain. Energy Rev.*, 73(February), 904–921.

Yah, N. F., Oumer, A. N., and Idris, M. S. (2017). "Small scale hydro-power as a source of renewable energy in Malaysia: A review." *Renew. Sustain. Energy Rev.*, 72(May 2016), 228–239.

Zhang, B., Song, B., Mao, Z., and Tian, W. (2017a). "A novel wake energy reuse method to optimize the layout for Savonius-type vertical axis wind turbines." *Energy*, 121, 341–355.

Zhang, B., Song, B., Mao, Z., Tian, W., Li, B., and Li, B. (2017b). "A novel parametric modeling method and optimal design for Savonius wind turbines." *Energies*, 10(3).

Zhang, Y., Kang, C., Ji, Y., and Li, Q. (2019). "Experimental and numerical investigation of flow patterns and performance of a modified Savonius hydrokinetic rotor." *Renew. Energy*, 141, 1067–1079.

Zhao, H., Kang, C., Ding, K., Zhang, Y., and Li, B. (2020). "Transient startup characteristics of a drag-type hydrokinetic turbine rotor." *Energy Convers. Manag.*, 223(July), 113287.

Zhou, D., Chen, H., Zheng, Y., Kan, K., Yu, A., and Binama, M. (2019). "Development and numerical performance analysis of a pump directly driven by a hydrokinetic turbine." *Energies*, 12(22).

Zhou, D., and Deng, Z. (Daniel). (2017). "Ultra-low-head hydroelectric technology: A review." *Renew. Sustain. Energy Rev.*, 78(April), 23–30.

APPENDIX A

A.1 Uncertainty analysis

The uncertainties associated with the experimental settings and other derived quantities are estimated by the method suggested by Moffat (1986).

A.1.1 Uncertainties associated with the experimental settings
A.1.1.1 Actual discharge (Q_{Actual})

Depth of water H_W=70 mm, ΔH=0.2 mm

Width of the channel W_C=215 mm, ΔW_C=0.1 mm

Coefficient of discharge C_d=0.6, ΔC_d=0.01

$$Q_{Actual} = C_d \frac{2}{3} W_C \sqrt{2g} H_W^{3/2}$$

$$\frac{\Delta Q_{Actual}}{Q_{Actual}} = \left(\sqrt{\left(\frac{\Delta C_d}{C_d}\right)^2 + \left(\frac{\Delta W_C}{W_C}\right)^2 + \frac{3}{2}\left(\frac{\Delta H}{H}\right)^2} \right) \times 100$$

$$\frac{\Delta Q_{Actual}}{Q_{Actual}} = \left(\sqrt{\left(\frac{0.01}{0.6}\right)^2 + \left(\frac{0.1 \times 10^{-3}}{215 \times 10^{-3}}\right)^2 + \frac{3}{2}\left(\frac{0.2 \times 10^{-3}}{70 \times 10^{-3}}\right)^2} \right) \times 100$$

$$\frac{\Delta Q_{Actual}}{Q_{Actual}} = 1.7\%$$

A.1.1.2 Uncertainty of Velocity of water

$Q_{Actual} = A_C V_w$

$$V_W = \frac{Q_{Actual}}{A_C} = \frac{Q_{Actual}}{W_C H_w}$$

$A_C = W_C H_W$

Depth of water H_W=70 mm, ΔH=0.2 mm

Width of the channel W_C=215 mm, ΔW_C=0.1 mm

$$\frac{\Delta Q_{Actual}}{Q_{Actual}} = 1.7\%$$

$$\frac{\Delta A_c}{A_c} = \left(\sqrt{\left(\frac{\Delta W_C}{W_C} \right)^2 + \left(\frac{\Delta H_W}{H_W} \right)^2} \right) \times 100$$

$$\frac{\Delta A_c}{A_c} = \left(\sqrt{\left(\frac{0.1 \times 10^{-3}}{215 \times 10^{-3}} \right)^2 + \left(\frac{0.2 \times 10^{-3}}{70 \times 10^{-3}} \right)^2} \right) \times 100$$

$$\frac{\Delta A_c}{A_c} = 0.28\%$$

$$\frac{\Delta V_W}{V_W} = \left(\sqrt{\left(\frac{\Delta Q_{Actual}}{Q_{Actual}} \right)^2 + \left(\frac{\Delta W_C}{W_C} \right)^2 + \left(\frac{\Delta H_W}{H_W} \right)^2} \right) \times 100$$

$$\frac{\Delta V_W}{V_W} = \left(\sqrt{\left(0.017 \right)^2 + \left(\frac{0.1 \times 10^{-3}}{215 \times 10^{-3}} \right)^2 + \left(\frac{0.2 \times 10^{-3}}{70 \times 10^{-3}} \right)^2} \right) \times 100$$

$$\frac{\Delta V_W}{V_W} = 1.7\%$$

A.1.1.3 Uncertainty of angular velocity

$$\omega = \frac{2\pi N}{60}$$

$$N = 108, \ \Delta N = 1$$

$$\frac{\Delta \omega}{\omega} = \left(\sqrt{\left(\frac{\Delta N}{N} \right)^2} \right) \times 100$$

$$\frac{\Delta \omega}{\omega} = \left(\sqrt{\left(\frac{1}{108} \right)^2} \right) \times 100$$

$$\frac{\Delta \omega}{\omega} = 0.925\%$$

A.1.1.4 Uncertainty of Tip speed ratio

$$\text{Tip Speed Ratio } (\lambda) = \frac{\omega D_r}{2V_W}$$

$$\frac{\Delta \omega}{\omega} = 0.925\%$$

$$\frac{\Delta V_W}{V_W} = 1.7\%$$

$D_r = 72$ mm, $\Delta D_r = 0.1$ mm

$$\frac{\Delta \lambda}{\lambda} = \left(\sqrt{\left(\frac{\Delta \omega}{\omega}\right)^2 + \left(\frac{\Delta D_r}{D_r}\right)^2 + \left(\frac{\Delta V_W}{V_W}\right)^2} \right) \times 100$$

$$\frac{\Delta \lambda}{\lambda} = \left(\sqrt{(0.00925)^2 + \left(\frac{0.1 \times 10^{-3}}{72 \times 10^{-3}}\right)^2 + (0.017)^2} \right) \times 100$$

$$\frac{\Delta \lambda}{\lambda} = 1.94\%$$

A.1.1.5 Uncertainty of torque produced by rotor

$T_{Rotor} = (W_W - S_{SB}) g (R_{Shaft} + R_{Rope})$

$W_W = 10$ g, $\Delta W_W = 0.02$ g

$S_{SB} = 5$ g, $\Delta S_{SB} = 0.02$ g

$R_{Shaft} = 6$ mm, $\Delta R_{Shaft} = 0.01$ mm

$R_{Rope} = 1$ mm, $\Delta R_{Rope} = 0.01$ mm

$$\frac{\Delta T_{Rotor}}{T_{Rotor}} = \left(\sqrt{\left(\frac{\Delta W_W}{W_W}\right)^2 + \left(\frac{\Delta S_{SB}}{S_{SB}}\right)^2 + \left(\frac{\Delta R_{shaft}}{R_{shaft}}\right)^2 + \left(\frac{\Delta R_{Rope}}{R_{Rope}}\right)^2} \right) \times 100$$

$$\frac{\Delta T_{Rotor}}{T_{Rotor}} = \left(\sqrt{\left(\frac{0.02 \times 10^{-3}}{10 \times 10^{-3}}\right)^2 + \left(\frac{0.02 \times 10^{-3}}{5 \times 10^{-3}}\right)^2 + \left(\frac{0.01 \times 10^{-3}}{6 \times 10^{-3}}\right)^2 + \left(\frac{0.01 \times 10^{-3}}{1 \times 10^{-3}}\right)^2} \right) \times 100$$

$$\frac{\Delta T_{Rotor}}{T_{Rotor}} = 1.1\%$$

A.1.1.6 Uncertainty of torque available

$$T_{Available} = \left(\frac{1}{4} \rho H_R D_r{}^2 V_W{}^2 \right)$$

$\rho_W = 998$ kg/m^3, $\Delta \rho_W = 0.01$ kg/m^3

$H_R = 51.4$ mm, $\Delta H_R = 0.01$ mm

$D_r = 72$ mm, $\Delta D_r = 0.1$ mm

$$\frac{\Delta V_W}{V_W} = 1.7\%$$

$$\frac{\Delta T_{Available}}{T_{Available}} = \left(\sqrt{\left(\frac{\Delta \rho_W}{\rho}\right)^2 + \left(\frac{\Delta H_R}{H_R}\right)^2 + 2\left(\frac{\Delta D_r}{D_r}\right)^2 + 2\left(\frac{\Delta V_W}{V_W}\right)^2} \right) \times 100$$

$$\frac{\Delta T_{Available}}{T_{Available}} = \left(\sqrt{\left(\frac{0.01}{998}\right)^2 + \left(\frac{0.01 \times 10^{-3}}{50.4 \times 10^{-3}}\right)^2 + 2\left(\frac{0.1 \times 10^{-3}}{72 \times 10^{-3}}\right)^2 + 2\left(0.017\right)^2} \right) \times 100$$

$$\frac{\Delta T_{Available}}{T_{Available}} = 2.4\%$$

A.1.1.7 Uncertainty of Coefficient of torque

$$C_T = \frac{T_{Rotor}}{T_{Available}}$$

$$\frac{\Delta T_{Available}}{T_{Available}} = 2.4\%$$

$$\frac{\Delta T_{Rotor}}{T_{Rotor}} = 1.1\%$$

$$\frac{\Delta C_T}{C_T} = \left(\sqrt{\left(\frac{\Delta T_{Rotor}}{T_{Rotor}}\right)^2 + \left(\frac{\Delta T_{Available}}{T_{Available}}\right)^2} \right) \times 100$$

$$\frac{\Delta C_T}{C_T} = \left(\sqrt{\left(0.011\right)^2 + \left(0.024\right)^2} \right) \times 100$$

$$\frac{\Delta C_T}{C_T} = 2.6\%$$

A.1.1.8 Uncertainty of Coefficient of power

Coefficient of power $C_P = \lambda C_T$

$$\frac{\Delta C_T}{C_T} = 2.6\% \quad \text{and} \quad \frac{\Delta \lambda}{\lambda} = 1.9\%$$

$$\frac{\Delta C_P}{C_P} = \left(\sqrt{\left(\frac{\Delta C_T}{C_T}\right)^2 + \left(\frac{\Delta \lambda}{\lambda}\right)^2} \right) \times 100$$

$$\frac{\Delta C_P}{C_P} = \left(\sqrt{(0.026)^2 + (0.0194)^2} \right) \times 100$$

$$\frac{\Delta C_P}{C_P} = 3.24\%$$

List of Publications based on Ph.D. Research Work

Sl. No	Title of the Paper	Authors	Name of the journal/Conferences/ Symposium., No., Pages	Month & Year of publication	Category*
1.	Studies on application of vertical axis hydro turbine for sustainable power generation in irrigation channels with different bed slopes	Shashikumar C M, Ramesh H, Vijaykumar H, Vasudeva M	Renewable Energy and international journal-Elsevier, Volume 163, Pages 845-857	4th September 2020	1
2.	Numerical investigation of conventional and tapered Savonius hydrokinetic turbines for low-velocity hydropower application in an irrigation channel	Shashikumar C M, Vijaykumar H, Vasudeva M	Sustainable Energy Technologies and Assessment-Elsevier, Volume 43, Pages 100871	19th Nov 2020,	1
3.	Experimental and numerical investigation of novel v-shaped rotor for hydropower utilization	Shashikumar C M, Ramesh H, Vijaykumar H, Vasudeva M	Ocean Engineering Journal-Elsevier Volume 224, Pages 108689	20th, Feb 2021	1
4.	Numerical and experimental investigation of modified V-shaped turbine blades for hydrokinetic energy generation	Shashikumar C M, Vasudeva M	Renewable Energy and international journal-Elsevier, Volume 177, Pages 1170-1197	27th, May 2021	1
5.	CFD investigation of unsteady three-dimensional Savonius hydrokinetic turbine in irrigation channel with varying positions for hydro power application	Shashikumar C M, Vijaykumar H, Vasudeva M	AIP Conference Proceedings, Volume 2316, Pages 030028	16th, Feb 2021	3
6.	CFD analysis of V-shaped rotor blades for hydropower application in irrigation channels	Shashikumar C M, Vijaykumar H, Vasudeva M	International Conference on Advanced materials, Energy & Environmental Sustainability (ICAMEES-2018), UPES, Dehradun-248007, India	Dec, 2018	4
7.	CFD study of vertical axis water turbine for hydropower application in an irrigation channel	Shashikumar C M, Vijaykumar H, Vasudeva M	International Symposium on "Advanced Materials for Industrial and Societal Applications	Dec 2019	4
8.	CFD study of conventional and tapered Savonius turbines for hydropower application in rural areas	Shashikumar C M, Vijaykumar H, Vasudeva Madav	International Mechanical Engineering Congress (IMEC) 2019	Nov 2019	4

9.	Numerical study of novel V-shaped rotor blades with different overlap ratios for hydropower application	Shashikumar C M, Vijaykumar H, Vasudeva Madav	11th International Exergy, Energy and Environment Symposium (IEEES-11), SRM University, Chennai	July 2019	4
10.	CFD investigation of unsteady three-dimensional Savonius hydrokinetic turbine in irrigation channel with varying positions for hydropower application	Shashikumar C M, Vijaykumar H, Vasudeva Madav	International Conference on "Advanced Trends in Mechanical & Aerospace Engineering" (ATMA -2019) at Dayananda Sagar University, Bangalore-560068, India.	Nov, 2019	4

Category: 1: Journal paper, full paper reviewed   2: Journal paper, Abstract reviewed

3: Conference/Symposium paper, full paper reviewed   4: Conference/Symposium paper, abstract reviewed 5: others (including papers in Workshops, NITK Research Bulletins, Short notes etc.)

(If the paper has been accepted for publication but yet to be published, the supporting documents must be attached.)

Shashikumar C M
Research Scholar

Dr. Vasudeva M
Research Guide

04-08-2021
Name & Signature, with
Date

Name & Signature, with
Date

BIODATA

NAME: Shashikumar C M
DATE OF BIRTH: 26-05-1984
Mobile No.: +919886226899
Email: shashi.auto@gmail.com

ADDRESS:

S/O Manjunathachar, Kasthurabha Road, Near Bank of Baroda, Channarayapatna, Hassan district, Karnataka State, India-573116.

QUALIFICATION:

Examination	Board/Institute	Year
Ph. D (course work)	NITK, Surathkal	2016
M.Tech (Thermal Engg.)	NITK, Surathkal	2010-12
B.E. (Automobile Engg)	Visveswaraiah Technological University, Belgaum, Malnad College of Engineering, Hassan	2003-07

EXPERIENCE:

SL. no	Name of the college/Institute	Designation	From	To
1.	KVGCE, Sullia	Assistant professor	24-02-2008	04-07-2015

ACHIEVEMENTS:

1. Received **Best Paper Award** for the research paper entitled "**Numerical study of novel V-shaped rotor blades with different overlap ratios for hydropower application**", presented at 11[th]International Exergy, Energy and Environment Symposium (IEEES-11) held during 14 - 18, July 2019, organized by Department of Automobile Engineering, School of Mechanical Engineering SRMIST, Kattankulathur, Tamil Nadu, INDIA. https://www.nitk.ac.in/best-paper-award-to-mr-shashikumar-c-m